Downloaded from orbit.dtu.dk on: May 05, 2023

DTU Library

The Structure of Individual Nanoparticles and Hot Electron Assisted Chemistry at Surfaces

Gavnholt, Jeppe

Publication date:
2009

Document Version
Publisher's PDF, also known as Version of record

Link back to DTU Orbit

Citation (APA):
Gavnholt, J. (2009). *The Structure of Individual Nanoparticles and Hot Electron Assisted Chemistry at Surfaces*. Technical University of Denmark.

General rights
Copyright and moral rights for the publications made accessible in the public portal are retained by the authors and/or other copyright owners and it is a condition of accessing publications that users recognise and abide by the legal requirements associated with these rights.

- Users may download and print one copy of any publication from the public portal for the purpose of private study or research.
- You may not further distribute the material or use it for any profit-making activity or commercial gain
- You may freely distribute the URL identifying the publication in the public portal

If you believe that this document breaches copyright please contact us providing details, and we will remove access to the work immediately and investigate your claim.

The Structure of Individual Nanoparticles and Hot Electron Assisted Chemistry at Surfaces

Ph.D. Thesis

Jeppe Gavnholt

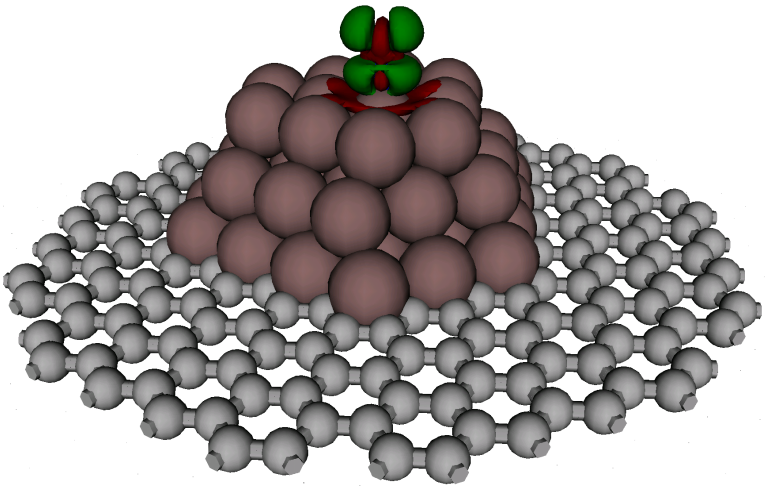

Supervisor: Jakob Schiøtz
Danish National Research Foundation's
Center for Individual Nanoparticle Functionality
Department of Physics
Technical University of Denmark

31 January 2009

Preface

This thesis is submitted in candidacy for the Ph.D. degree at the Technical University of Denmark (DTU). The work has been carried out from February 2006 to January 2009 at the Danish National Research Foundation's Center for Individual Nanoparticle Functionality (CINF), Department of Physics, with Associate Professor Jakob Schiøtz as supervisor. The studies have been a part of the Ph.D. program of Mathematics, Physics and Informatics at DTU.

I sincerely thank my supervisor for an enthusiastic and motivating supervision of my work. I thank all colleagues at the Center for Individual Nanoparticle Functionality (CINF) and Center for Atomic-scale Materials Design (CAMD) for making it an interesting and pleasant place to work. I particularly thank my office mates, Thomas Olsen, Vivien Petzold, Carsten Rostgaard and Heine A. Hansen. I also thank the computer staff, Jens Jørgen Mortensen, Marcin Dulak and Ole Holm Nielsen for always providing help with computer and software issues. Furthermore I wish to thank Professor Angel Rubio from Universidad del Pais Vasco, San Sebastian, Spain for a fruitful collaboration and for two interesting stays in San Sebastian.

Finally, I warmly thank my wife, Lucia Gavnholt, for being a constant motivation and for making life more than research.

Jeppe Gavnholt
Danish National Research Foundation's Center for Individual Nanoparticle Functionality
Department of Physics
Technical University of Denmark
31 January 2009

Abstract

The aim of this thesis is to gain a fundamental insight to different aspects of heterogeneous catalysis by developing theoretical models of catalytic processes, and applying them to describe real systems. The first considered aspect is the structure of the catalyst. Solid catalysts typically consist of small nanometer sized particles. A method to calculate detailed structural information of crystalline nano-particles has been developed and applied to Ruthenium particles in the diameter range from 2 nm to 5 nm. The detailed structural information is important in relation to the catalytic properties of the particles, since many catalytic reactions are known to be highly structure sensitive. The ammonia synthesis activity of the Ruthenium particles is investigated and the optimal particle size is found to be 3 nm in diameter. The second considered aspect of heterogeneous catalysis is that of hot electron mediated chemical processes at surfaces, where a hot electron is an electron with an energy above the Fermi level. This is approached in two different ways. The first approach is based on potential energy surfaces, which are used to estimate the coupling between the hot electrons and the vibrational modes of molecules at the surface. The method is applied to different diatomic molecules adsorbed on transition metal surfaces, and it is seen to qualitatively reproduce experimentally observed relations between electron flux and desorption rates. The second approach is to apply time-dependent density functional theory to model hot electrons colliding with molecular resonances. This approach is seen provide supplementary information on the resonances.

Resumé

Målet med denne afhandling er at opnå fundamental indsigt i forskellige aspekter af heterogen katalyse ved at udvikle teoretiske modeller af katalytiske processer, og anvende dem i beskrivelsen af virkelige systemer. Det første aspekt, som betragtes, er strukturen af en katalysator. Katalysatorer på fast form består typisk af små partikler i nanometer størrelse. En metode til at beregne detaljeret information om strukturen af krystalliske nano-partikler er blevet udviklet og anvendt på ruthen partikler med en diameter mellem 2 nm og 5 nm. Den detaljerede information om strukturen er vigtig med hensyn til de katalytiske egenskaber af partiklerne, da mange katalytiske reaktioner vides at være yderst følsomme overfor strukturen. Ruthen-partiklernes aktivitet i ammoniak-syntesen undersøges og en diameter på 3 nm findes at være den optimale størrelse. Det andet aspekt af heterogen katalyse, som betragtes, er kemiske processer ved overflader, som fremmes af varme elektroner. En varm elektron er en elektron med en energi, der ligger over Fermi-niveauet. Dette anskues på to forskellige måder. Den første tilgang baserer sig på potentiel energi-overflader, som anvendes til at estimere koblingen mellem de varme elektroner og de vibrationelle tilstande i et molekyle ved overfladen. Metoden anvendes på forskellige diatomige molekyler ved overflader af overgangsmetaller, og den ses kvalitativt at reproducere eksperimentelt observerede sammenhænge mellem elektron-fluksen og desorptions-raten. Den anden tilgang er at anvende tidsafhængig tæthedsfunktional-teori til at modellere kollisioner mellem varme elektroner og molekylære resonanser. Denne tilgang ses at give supplerende information om resonanserne.

Contents

List of Figures

List of Tables

Chapter 1

Introduction

The topic of this thesis is within the field of heterogeneous catalysis. A catalyst is a substance, which changes the kinetics of a chemical reaction, ie. the speed at which a reaction happens, without being consumed by the reaction. The effect of a catalyst can be illustrated in a simple way as shown on Fig. 1.1. Without the catalyst the energy barrier between the reactants and the products is very high, which results in a low rate of forming products. The effect of the catalyst is to lower this barrier, such that rate increases. As the rate typically depends exponentially on the energy barrier this increase in rate can be enormous. In the case of heterogeneous catalysis the reacting species and the catalyst are on different forms. This work only considers the situation of a solid catalyst and reactants and products on gas form.

Heterogeneous catalysis plays an important role in todays modern society. Some of the most important applications are in the fuel production, fertilizer production and in the cleaning of car and factory exhaust. These very large scale applications means that the interest for optimizing and developing new and better catalysts is huge, since the potential economic consequences are enormous.

This thesis deals with two different aspects of catalyst optimization on the very basic level. The first part has to do with how large a part of the catalyst that effectively lowers the barrier of the reaction, ie. how large a part of the catalyst actually contributes to the catalytic activity. I introduce this part in Sec. 1.1. The second part considers a more direct and controlled way of getting the reactants to pass the barrier. This is the field of hot electron induced chemistry, which I will introduce in Sec. 1.2.

1.1 The structure of nanoparticles

The catalytic reactions on a solid catalyst occurs on the surface of the catalyst, so typically the catalyst material is split into very small (nanometer sized) particles, such that the surface to volume ratio becomes very high. However, it turns out that the catalytic activity is not simply proportional to the surface area. Single crystal experiments have revealed that step sites can have up to 9 orders of magnitude larger activity than flat surface sites in the splitting of the Nitrogen molecule[23]. Computations have verified

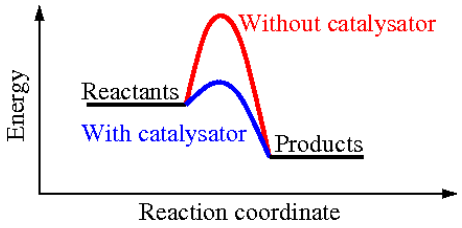

Figure 1.1: A catalyst lowers the barrier between reactants and products, such that the reaction rate increases.

these observations[73]. Obviously the total activity of a particle will then be completely dominated by the presence of these highly active sites.

The ability of calculating the catalytic activity of nanoparticles is very desirable, since this could provide better understanding of the mechanisms, which results in high catalytic activity. Such an understanding could hopefully be applied to guide experiments in the attempts of improving catalysts. However, as the catalytic activity is extremely structure sensitive, such a calculation requires the ability of obtaining detailed structural information of the particles.

In this thesis I will present a model to obtain detailed structural information of nanoparticles. This includes the effect of finite number of atoms and a finite temperature. I will focus on Ruthenium which crystallizes in the hcp structure. However, the methodology presented here could also be applied on other metals.

1.2 Hot electron femtochemistry at surfaces

Typically a catalyst does not completely remove the barrier between the reactants and the products. Ordinarily the remaining barrier is passed due the random motion of the atoms, which will always be present at a finite temperature. However, this random motion will occur in all directions, ie. one cannot direct the energy towards the desired reaction path. An increase in temperature will increase the energy present to overcome the barrier to the products. However, it may also destabilize the catalyst itself.

Hot electron femtochemistry can potentially provide a way of directing energy directly into the desired motion, such that high catalytic activity at low temperatures and high selectivity can be achieved. The idea is to send hot electrons (electrons with an energy above the Fermi energy) toward the intermediate species adsorbed on the surface of the catalyst. If the energy of the electron fits with the energy of a certain resonance in the species, the electron may loose some of its energy to certain vibrational modes of the species. By tuning the energy of the hot electrons it is theoretically possible to partially control which vibrational modes that get excited, and hence the motion of the species.

The effect has been demonstrated experimentally by Bonn et al,[8] who where able to form CO_2 from CO and O on a Ruthenium (001) surface with the help of hot electrons. This is normally not possible beause the CO will desorb before the CO_2 formation as

the temperature is raised. The effect is explained by the hot electrons injecting energy into vibrational modes of the adsorbed O, which means that the barrier to forming CO_2 can be overcome at a lower temperature. Many other experiments have also revealed the capability of hot electrons to cause desorption of molecules adsorbed on a surface[8, 11, 14, 29, 56, 76, 87, 88, 96].

In this thesis I will present an approach to predicting the energy transfer from a hot electron to vibrational energy in a molecule in a given system. This will include a calculation of the potential energy surface (PES) of the molecule in its ground state and of the excited molecule. To the extend it is possible the approach will be compared to experiments in order to test the validity of the approach. I will also discuss another approach, where the entire event of a hot electron interacting with an adsorbed molecule is simulated in real-time. This approach will provide supplementary information, which will extend the insight on the process.

1.3 Outline of the thesis

Chapter 2 gives an introduction to the density functional methods applied in this work. This includes ordinary density functional theory (DFT), delta self-consistent field (ΔSCF) and time-dependent density functional theory (TDDFT).

Chapter 3 gives an overview of the developed method of obtaining the structure of individual nanoparticles. This includes a discussion of the applied approximations.

Chapter 4 describes some of the results obtained regarding the structure of Ruthenium nanoparticles. This includes an estimation of the optimal particle diameter of Ruthenium with respect to ammonia synthesis activity. Furthermore it includes some considerations regarding the influence of the substrate and gases on the structure.

Chapter 5 gives an overview of one approach to predicting the energy transfer from hot electrons to vibrations in an adsorbed molecule. This includes an example of a PES calculation and the prediction of the rate of hot electron mediated desorption.

Chapter 6 considers a completely different approach to considering the interaction between hot electrons and a molecular resonance. The approach is based on time evolution TDDFT calculations on the entire event of a hot electron hitting an adsorbed molecule.

Chapter 7 summarizes the obtained results and conclusions. Furthermore it provides a few thoughts on some possible future work.

Chapter 2

Theory and methods

In this chapter I will provide a short overview of the density functional methods I have applied in this work. It covers a broad spectrum of issues and should not be considered a complete reference. Instead the reader is provided with references a long the way, which will contain more detailed information.

In the following I will start in Sec. 2.1 by presenting the fundamental electronic structure problem and show why this cannot be handled directly except in the case of very small systems. In Sec. 2.2 I then show how the ground state part of the problem is reformulated and solved within density functional theory (DFT). The simple, but not fully justified, approach of delta self-consistent field (ΔSCF) of handling excited states is described in Sec. 2.3. This will include an introduction to the extensions to ΔSCF made during this work, which makes it applicable in relation to molecular resonances near surfaces. In Sec. 2.4 I will briefly introduce time-dependent density functional theory (TDDFT), which is an in principle exact approach to describing time-varying electronic structure problems, including excited state properties. Finally in Sec. 2.5 I will touch upon some of the different practical approaches to implementing a density functional scheme, and in Sec. 2.6 I list the calculational parameters applied in the calculations performed in this work. Throughout the chapter I will apply atomic units, ie. $m_e = \hbar = e^2 = 1$.

2.1 The Schrödinger equations

The famous Schrödinger equations were discovered in 1926[95], and constitutes the description of all matter. For a system of N electrons the time-dependent Schrödinger equation can be written in the form

$$i\frac{\partial}{\partial t}\Psi(\underline{\mathbf{r}},t) = \hat{H}(\underline{\mathbf{r}},t)\Psi(\underline{\mathbf{r}},t), \tag{2.1}$$

where $\underline{\mathbf{r}} = (\mathbf{r}_1, \mathbf{r}_2 ... \mathbf{r}_N)$ and $\Psi(\underline{\mathbf{r}},t)$ is the many-particle wave-function, whose absolute square ($|\Psi(\underline{\mathbf{r}},t)|^2$) is interpreted as the probability of finding the electrons at the positions $\underline{\mathbf{r}}$. $\hat{H}$ is the Hamiltonian of the system, which I will return to in a short while.

In Eq. (2.1) only the electrons are considered, ie. the nuclei are treated separately and their influence on the electronic system is only provided through the Hamiltonian as it

will soon be obvious. This is by far the most applied approach in electronic structure calculations. In TDDFT, which I will consider in Sec. 2.4 it is Eq. (2.1) which is reformulated into a density description.

In the case of a time-independent Hamiltonian the variables in Eq. (2.1) can be separated and the position-dependent part will take the form of an eigenvalue equation:

$$\hat{H}(\underline{\mathbf{r}})\Psi_i(\underline{\mathbf{r}}) = E_i\Psi_i(\underline{\mathbf{r}}), \tag{2.2}$$

where i is an index used to distinguish the different solutions. This is known as the time-independent Schrödinger equation. The ground state ($i = 0$) part of Eq. 2.2 is reformulated in DFT as I will explain in Sec. 2.2, whereas the ΔSCF method of Sec. 2.3 tries to estimate the E_i's of the higher lying states.

For a system of electrons the Hamiltonian, $\hat{H}$ of Eqs. (2.1) and (2.2) has the form

$$\hat{H} = \hat{T} + \hat{U}_{ee} + \hat{U}_{ext}, \tag{2.3}$$

where $\hat{T}$ is the kinetic energy

$$\hat{T} = -\frac{1}{2}\sum_{i=1}^{N}\nabla_i^2, \tag{2.4}$$

$\hat{U}_{ee}$ gives the electron-electron interaction

$$\hat{U}_{ee} = \sum_{i<j}\frac{1}{|\mathbf{r}_i - \mathbf{r}_j|}. \tag{2.5}$$

and $\hat{U}_{ext}$ is the external potential. The ionic potential is treated as an external potential and if the ions are the only source to an external potential we have that

$$\hat{U}_{ext} = -\sum_{i=1}^{N}\sum_{j=1}^{N_{ion}}\frac{Z_j}{|\mathbf{r}_i - \mathbf{R}_j|}, \tag{2.6}$$

where $\mathbf{R}_j$ is the position and $Z_j e$ the charge of ion no. j. N_{ion} is the number of ions.

2.1.1 The exponential wall

Before I move on to describing how the Schrödinger equations are reformulated in density functional theory I will motivate this reformulation by illustrating the problem of solving the Schrödinger equations directly. If we consider a system of N electrons and want to describe the wavefunction with p parameters in each dimension, we find that a total of $M = p^{3N}$ parameters are needed to contain the many-particle wavefunction. If we have 100 electrons and just use the very relaxed condition of $p = 3$ we find that $M = 3^{3\cdot 100} \approx 10^{143}$. Obviously this constitutes an exponential wall, which severely limits the number of electrons it is possible to handle, when one attempts to represent the many-particle wavefunction directly.

2.2 Density Functional Theory

In this section I provide a basic introduction to density functional theory (DFT), which was first put on a formal basis by Hohenberg and Kohn in 1964[54] and later in 1965 Kohn and Sham[67] pioneered a practical approach to applying the theory of Hohenberg and Kohn. I start in Sec. 2.2.1 by presenting the basic theorem of Hohenberg and Kohn and then in Sec. 2.2.2 I present the practical approach of Kohn and Sham. Finally in Sec. 2.2.3 I consider the central issue in DFT, the approximation and evaluation of the unknown exchange-correlation functional.

2.2.1 The Hohenberg-Kohn theorem

The objective in DFT is to avoid considering the many-particle wavefunction by considering the ground state density instead. This is made possible by the fundamental theorem of Hohenberg and Kohn, which states that there is a one-to-one correspondence between the external potential and the ground-state density for a system with a non-degenerate ground state.[54] This means that one in principle can derive the ground-state wavefunction from a given ground-state density, since the external potential uniquely determines the ground-state wavefunction. The Rayleigh-Ritz variational principle can then be applied to obtain a new expression for the ground state energy.[9]

$$E_0 = \min_\Psi \langle \Psi | \hat{H} | \Psi \rangle = \min_\Psi \langle \Psi | \hat{T} + \hat{U}_{ee} + \hat{U}_{ext} | \Psi \rangle, \tag{2.7}$$

where $\hat{H}$ is the Hamiltonian from Eq. (2.3). By applying the Hohenberg-Kohn theorem we find that

$$\begin{aligned} E_0 &= \min_{n'(\mathbf{r})} \langle \Psi[n'(\mathbf{r})] | \hat{T} + \hat{U}_{ee} + \hat{U}_{ext} | \Psi[n'(\mathbf{r})] \rangle \\ &= \min_{n'(\mathbf{r})} \left[T[n'(\mathbf{r})] + U_{ee}[n'(\mathbf{r})] + U_{ext}[n'(\mathbf{r})] \right] \\ &= \min_{n'(\mathbf{r})} E[n'(\mathbf{r})], \end{aligned} \tag{2.8}$$

where $T[n'(\mathbf{r})]$ is the kinetic energy of the electrons, $U_{ee}[n'(\mathbf{r})]$ is the electron-electron interaction energy and $U_{ext}[n'(\mathbf{r})]$ is the external potential energy contribution

$$U_{ext}[n'(\mathbf{r})] = \int v_{ext}(\mathbf{r}) n'(\mathbf{r}) d\mathbf{r}. \tag{2.9}$$

$E[n'(\mathbf{r})]$ is the total energy. The exact form of $T[n'(\mathbf{r})]$ and $U_{ee}[n'(\mathbf{r})]$ is not known, so in order to make progress Hohenberg and Kohn wrote the total energy operator as follows[54]

$$E[n'(\mathbf{r})] = T_{HK}[n'(\mathbf{r})] + U_{ES}[n'(\mathbf{r})] + U_{ext}[n'(\mathbf{r})] + E_{XC}[n'(\mathbf{r})], \tag{2.10}$$

where $T_{HK}[n'(\mathbf{r})]$ is the kinetic energy of non-interacting electrons, $U_{ES}[n'(\mathbf{r})]$ the classical electrostatic energy

$$U_{ES}[n'(\mathbf{r})] = \frac{1}{2} \int \int \frac{n'(\mathbf{r}) n'(\mathbf{r}')}{|\mathbf{r} - \mathbf{r}'|} d\mathbf{r}' d\mathbf{r}, \tag{2.11}$$

$U_{ext}[n'(\mathbf{r})]$ is unchanged from before and $E_{XC}[n'(\mathbf{r})]$ is the exchange-correlation energy functional, which gives all the electron-electron interaction effects not covered by the classical electrostatic term. The approximation of this is the subject of Sec. 2.2.3.

2.2.2 Kohn-Sham formulation of DFT

Eventhough the Hohenberg-Kohn theorem enables us to write all ground-state properties of a system as a functional of the ground-state density it does not provide us with a way of finding the ground-state density or a way of evaluating properties from this density. Kohn and Sham made progress on the former by introducing an effective potential, $v_{eff}(\mathbf{r})$, such that they were able to form a set of self-consistent single-particle equations, known as the Kohn-Sham equations[67]

$$\left[-\frac{1}{2}\nabla^2 + v_{eff}(\mathbf{r}) - \epsilon_i\right]\psi_i(\mathbf{r}) = 0 \tag{2.12}$$

$$n(\mathbf{r}) = \sum_{i=1}^{N} |\psi_i(\mathbf{r})|^2 \tag{2.13}$$

$$v_{eff}(\mathbf{r}) = v_{ext}(\mathbf{r}) + \int \frac{n(\mathbf{r}')}{|\mathbf{r}-\mathbf{r}'|}d\mathbf{r}' + v_{XC}(\mathbf{r}), \tag{2.14}$$

where the exchange-correlation contribution to the effective potential, $v_{XC}(\mathbf{r})$, is given as the functional derivative of the exchange-correlation energy with respect to the density

$$v_{XC}(\mathbf{r}) = \frac{\partial E_{XC}[n'(\mathbf{r})]}{\partial n'(\mathbf{r})} \tag{2.15}$$

Eqs. (2.12)-(2.14) gives the exact solution to the ground state part of the time-independent Schrödinger equation (Eq. (2.2) with $i = 0$). However, it is important to note that the energy eigenvalues of Eq. (2.12), ϵ_i, are not the true electron energies. The Kohn-Sham equations provide a practical approach to finding the ground-state density. First one must quess a density and then Eqs. (2.12)-(2.14) are applied iteratively until a self-consistent density, $n(\mathbf{r})$ is reached. When this has been done the ground state energy of the system can be calculated as

$$\begin{aligned} E_0 &= T_{HK}[n(\mathbf{r})] + U_{ES}[n(\mathbf{r})] + U_{ext}[n(\mathbf{r})] + E_{XC}[n(\mathbf{r})] \qquad (2.16)\\ &= \sum_{i=1}^{N}\epsilon_i - \int v_{eff}(\mathbf{r})n(\mathbf{r})d\mathbf{r} + \frac{1}{2}\int\int\frac{n(\mathbf{r})n(\mathbf{r}')}{|\mathbf{r}-\mathbf{r}'|}d\mathbf{r}'d\mathbf{r} + \int v(\mathbf{r})n(\mathbf{r})d\mathbf{r} + E_{XC}[n(\mathbf{r})], \end{aligned}$$

where Eqs. (2.9) and (2.11) have been inserted and $T_{HK}[n(\mathbf{r})]$ has been found using Eq. (2.12) and the fact that

$$T_{HK}[n(\mathbf{r})] = \sum_{i=1}^{N}\langle\psi_i| - \frac{1}{2}\nabla^2|\psi_i\rangle. \tag{2.17}$$

However, the Kohn-Sham iterative scheme and the final energy evaluation both require the ability of evaluating the unknown exchange-correlation functional, $E_{XC}[n(\mathbf{r})]$. This will be the subject of the next section. The Hartree approximation corresponds to setting the exchange-correlation energy equal to zero.[66]

2.2.3 The exchange-correlation functional

The exchange-correlation functional, $E_{XC}[n(\mathbf{r})]$, contains all electron-electron interactions beyond the classical electrostatic repulsion. The approach of estimating this term is the central issue of all DFT calculations and much work has gone into finding different approximations. This has led to the presence of a wide variety of different exchange-correlation functionals which vary in accuracy, complexity, computational effort and simply which type of systems they are suited for. A lot of effort is still put into the hunt for better and faster exhange-correlation functionals. Here I will only provide a brief description of the type of functionals I have applied in my work.

Local density approximation

The simplest and perhaps most direct approach of estimating $E_{XC}[n'(\mathbf{r})]$ is the Local Density Approximation (LDA), which assumes the exchange-correlation energy to be local in the sense that the contribution to it from each point in space only depends on the density in that point.[67]

$$E_{XC}^{LDA}[n(\mathbf{r})] = \int n(\mathbf{r})\epsilon_{XC}^{hom}(n(\mathbf{r}))d\mathbf{r}. \tag{2.18}$$

The relation between the density and exchange-correlation energy is taken to be that of the homogeneous electron gas, ie. it can be found with a higher accuracy method. An example of such a calculation is the one performed by Ceperley and Alder[17] in 1980, who used a quantum Monte Carlo approach.

Naturally, one would only expect good results from this approximation, when the electron density varies slowly. However, this approach gives surprisingly good results, even in cases with quite rapidly varying electron densities. Bond lengths are estimated within 1-2% of the correct value[86]. One of the reasons the LDA gives these good results is that it at least the correct solution to one physical system, i.e. the constant density electron gas, which ensures the sum rule for the exchange-correlation hole to be obeyed at all times. The sum rule basically states that the probability of finding an electron at $\mathbf{r}'$ given an electron has been found at $\mathbf{r}$ integrated over $\mathbf{r}'$ must be equal to $N-1$, where N is the number of electrons in the system. A problem with the LDA is that it has a tendency to overestimate binding energies in the order of 10-15%[86].

Generalized gradient approximation

The natural way to go in an attempt of improving the LDA is to include a dependence of the gradient of the electron density on the exchange-correlation functional.

$$E_{XC}[n(\mathbf{r})] = \int f_{XC}(n(\mathbf{r}), \nabla n(\mathbf{r}))d\mathbf{r}. \tag{2.19}$$

This is normally termed a Gradient Expansion Approximation (GEA). However the sum rule for the exchange-correlation hole is generally not satisfied under the GEA, since no physical system is described by such functionals. In order to get good results, it is then necessary to constrain the functional form of f_{XC}, such that the exchange-correlation

end up obeying the sum rule. With such constraints the GEA is normally termed the Generalized Gradient Approximation (GGA).

The most applied GGA functional today is the Perdew-Burke-Ernzerhof (PBE) functional which was presented in 1996.[85] In most of the GGA DFT-calculations made during this work the so-called revised Perdew-Burke-Ernzerhof (RPBE) GGA-functional developed by Hammer et al. has been used[43]. This functional has in most cases been chosen, because it gives good results for molecular binding to transition metal surfaces[43].

2.3 ΔSCF

The purpose of the delta self-consistent field (ΔSCF)[47, 62] method is to utilize the framework of DFT to make a simple estimation of excitation energies. As the name indicates the excitation energy is calculated as the difference between to self-consistent calculations, typically with one of them being an ordinary DFT calculation and the other a modified DFT calculation, which tries to find the electron density of the excited state. The modification consists of a change in the occupation numbers of the Kohn-Sham states as I will explain in Sec. 2.3.1. The ΔSCF method has a formal justification in cases, where the excited state corresponds to the lowest state of a given symmetry.[40] More recently Görling[38] extended the Kohn-Sham formalism to include excited states, such that the formal justification of ΔSCF becomes more general. However, a special unknown orbital-dependent exchange-correlation potential should be used for the excited states. In practical implementations, included the ones performed in this work, standard exchange-correlation potentials from ground state DFT are typically applied. The true justification of ΔSCF should come from testing its performance compared to experimental results.

Our objective with the ΔSCF method has been to apply it to find the energies of molecular resonances at surfaces. This requires some extensions to the method as I will show in Sec. 2.3.2. We have chosen to name this extended version the linear expansion ΔSCF method. The method has been published in Paper II and the following should just be considered a supplement to that.

2.3.1 Modifications to DFT

When performing an ordinary DFT calculation the density is constructed from the lowest lying orbitals (Eq. (2.13)), corresponding to placing the electrons in those orbitals. The only modification of ΔSCF is to take one of these electrons and place it in a higher lying orbital, such that Eq. (2.13) becomes

$$n(\mathbf{r}) = \sum_{i \neq s}^{N} |\psi_i(\mathbf{r})|^2 + |\psi_e(\mathbf{r})|^2, \tag{2.20}$$

where one electron has been moved from the s'th Kohn-Sham orbital to the e'th. Naturally we must have that $s \leq N$ and $e > N$. With this change the system will reach a different self-consistency, but except from that the calculation goes completely as an ordinary DFT calculation.

Only a minor modification in the calculation of the total energy is required. The Hartree term, U_{ES}, and the external potential term, U_{ext}, only depend on the density, as it is also the case for the exchange-correlation term, U_{XC}, in the case of an orbital-independent functional. This means that the evaluation of these terms is completely unchanged. The Hohenberg-Kohn kinetic energy term, T_{HK}, only changes with respect to which eigenvalues that are summed. Of course one must sum the eigenvalues corresponding to the occupied Kohn-Sham orbitals. A bit extra care would have to be taken in the case of an orbital-dependent exchange-correlation functional. However, this should be quite straightforward as all the occupied orbitals are still well-known.

There is an arbitrary choice which has to be made when applying Eq. (2.20) and that is the values of s and e, ie. which orbitals to move the electron from and to. The choice of these of course depends on the excitation one wants to consider. One should keep in mind that the ΔSCF method is only applicable in situations where the choices of s and e are obvious. Another issue with the ΔSCF method is the problem of directly considering different magnetic states, such as singlet and triplet states, as it is explained in Ref. [110] and in Paper II. In some cases the issue can be handled with the use of the multiplet sum method.[110]

The only true justification of the ΔSCF method is given through testing. In Paper II we show that the method gives quite reasonable results in the calculation of different excitation energies in the N_2 and CO molecules. By reasonable I mean significantly better than just taking Kohn-Sham eigenvalue differences and with an accuracy close to that of TDDFT. We also show that the excited state potential energy surfaces upon variation of the inter-atomic distance in the N_2 molecule agree very well with those of TDDFT.

2.3.2 The linear expansion ΔSCF method

The purpose of the linear expansion ΔSCF method is to find the energies of resonances. The method is suited for a Newns-Anderson[1, 80] type system as illustrated on Fig. 2.1, where the resonance can be identified as coming from a localized orbital, ϕ. The resonance is a result of a broadening and perhaps shift of the localized level, which happens because it has been brought close enough to a wide band of states for there to be a weak coupling. This corresponds well to the situation of the molecular resonance in a molecule adsorbed on a surface. The criteria here being that the molecular level does not couple too well with the surface states, such that the resonance no longer can be identified directly from an original molecular level.

The direct way of applying the ΔSCF method to the problem of finding the resonance energy in such a system would be to perform a self-consistent calculation where one electron has been taken from the Fermi level and placed in the Kohn-Sham orbital which resembles the molecular orbital the most. This, however, gives rise to several problems as it was also pointed out by Hellman et al.[47] and Behler et al.[4] First of all the hybridization of the molecular level gives some arbitrariness to the choice of which Kohn-Sham orbital to occupy, as several Kohn-Sham orbitals will be similar to the molecular orbital. Just taking the one with the largest overlap with the molecular orbital is also not ideal as this will give discontinuities if one tries to map out potential energy surface of the resonance and

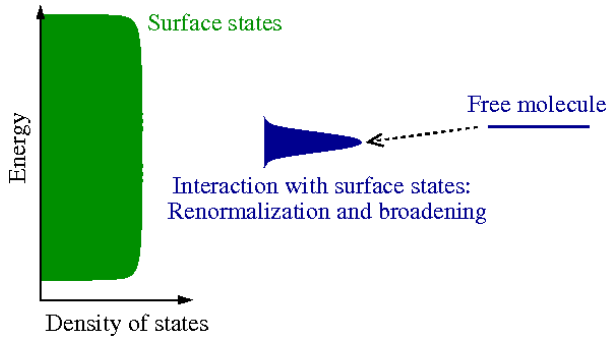

Figure 2.1: Newns-Anderson model.[1, 80] When a localized orbital in a molecule is brought near a metallic surface, such that the orbital interacts with a broad band of surface states, it will shift its energy and broaden.

provide some unfortunate system size dependencies. The solution we propose in Paper II is to place the excited electron in a linear combination of Kohn-Sham states, ie. to evaluate the density as

$$n(\mathbf{r}) = \sum_{i=1}^{N-1} |\psi_i(\mathbf{r})|^2 + \sum_{i,j=N}^{M} a_i^* a_j \psi_i^*(\mathbf{r})\psi_j(\mathbf{r}), \tag{2.21}$$

where the expansion coefficient are chosen such that the occupied state will resemble the molecular state, ϕ, as much as possible:

$$a_i = \frac{\langle\psi_i|\phi\rangle}{(\sum_i |\langle\psi_i|\phi\rangle|^2)^{1/2}}, \tag{2.22}$$

where ψ_i is the i'th Kohn-Sham orbital.

The total energy evaluation is still not very different from that of ordinary DFT. In the case of an orbital-independent exchange-correlation functional only the Hohenberg-Kohn kinetic energy, T_{HK}, changes a bit in its evaluation. The occupied orbital is not an eigenfunction (Kohn-Sham orbital), so it does not have an eigenvalue. Instead its contribution is evaluated as $\sum_{i=N}^{M} |a_i|^2 \epsilon_i$ (see Paper II for further details).

The method described here is an 'ad hoc' method in the sense that it lacks formal justification. The only way of really justifying the method is through comparisons with experimental results. In chapter 5 I will comment on the results of such comparisons. It seems that the method performs quite well for the type of systems considered here.

2.4 Time-dependent Density Functional Theory

Time-dependent density functional theory (TDDFT) should not be considered a mere extension to DFT but rather a theory of its own, which is based on some of the same ideas and principles as DFT. It is important to stress that, as DFT, TDDFT is in principle

an exact theory which only inaccuracies lie in the ability of approximating the exchange-correlation functional and of course the practical limitations of concrete implementations. As in DFT one avoids the many-particle wavefunction by using the density as the basic variable from which all observables are calculated.

In the following I will start in Sec. 2.4.1 by mentioning the TDDFT equivalent of the Hohenberg-Kohn theorem, the Runge-Gross theorem. I then move on to the more practical issue of finding the density by presenting the time-dependent Kohn-Sham equations in Sec. 2.4.2. Finally I will touch upon the central issue of approximating the exchange-correlation functional in Sec. 2.4.3.

2.4.1 The Runge-Gross theorem

The Hohenberg-Kohn theorem in DFT is only applicable to the ground state, which can be found through a variational principle with respect to the total energy of the system. Naturally this approach is not directly applicable to a time-dependent system where 1) the system will in general not be in the ground state and 2) the total energy is not a conserved quantity, so no variational principle can be based on it. However, through the definition of an analogy to the total energy, the quantum mechanical action, whose stationary points corresponds to physical solutions, Runge and Gross[93] were in 1984 able to prove a theorem relating the time-varying external potential with the time-varying density. This is today known as the Runge-Gross theorem.

The Runge-Gross theorem states that if two external potentials $v(\mathbf{r}, t)$ and $v'(\mathbf{r}, t)$ differ by more than a only time-dependent constant, $c(t)$, then they cannot provide the same time-varying density. On mathematical form this looks as

$$v(\mathbf{r}, t) \neq v'(\mathbf{r}, t) + c(t) \Rightarrow n(\mathbf{r}, t) \neq n'(\mathbf{r}, t). \tag{2.23}$$

This means that it in principle is possible to, for a given density, $n(\mathbf{r}, t)$, to find the external potential up to a time-dependent constant and hence the wavefunction up to a purely time-dependent phase. It is in other words justfiable to use the density as the basic variable, since all observables in principle can be calculated from the density. It is here important to notice that finding the value of an observable at a certain time may require knowledge of the density at all past times, whereas it will be enough to know the many-particle wavefunction at that certain time.

2.4.2 Time-dependent Kohn-Sham equations

As it is the case for DFT practical progress is made in TDDFT by establishing an complementary system of non-interacting particles, whose density matches the one of the real system. This is ensured through an effective potential, $v_{eff}(\mathbf{r}, t)$, which is defined to give the right density. With this picture in mind it is possible to write the time-dependent

Scrödinger equation for the non-interacting electrons:

$$i\frac{\partial}{\partial t}\psi_i(\mathbf{r},t) = \left[-\frac{1}{2}\nabla^2 + v_{eff}(\mathbf{r},t)\right]\psi_i(\mathbf{r},t) \tag{2.24}$$

$$n(\mathbf{r},t) = \sum_{i=1}^{N} |\psi_i(\mathbf{r},t)|^2 \tag{2.25}$$

$$v_{eff}(\mathbf{r},t) = v_{ext}(\mathbf{r},t) + \int \frac{n(\mathbf{r}',t)}{|\mathbf{r}-\mathbf{r}'|}d\mathbf{r}' + v_{XC}(\mathbf{r},t), \tag{2.26}$$

where v_{ext} is the external potential and v_{XC} is the exchange-correlation contribution to the effective potential, which is not simple the functional derivative of the exchange-correlation energy as in DFT. However, van Leeuwen[102] in 1998 managed to write it as a functional derivative of the exchange-correlation part of a an action functional he defined.

The time-dependent Kohn-Sham equations (Eqs. (2.24)-(2.26)) are not solved through the same self-consistency procedure as for the Kohn-Sham equations in DFT. Instead they constitute an initial value problem, where the Kohn-Sham orbitals are evolved over time from some given starting point. This time-evolution is not straightforward as the Hamiltonian is also time-dependent, but by dividing the time-evolution into a range of small steps and applying one of several existing evolution techniques[27, 74] it is possible to perform the evolution numerically.

2.4.3 The exchange-correlation functional

The central issue in all TDDFT calculation is the ability to approximate the exchange-correlation functional, on which the accuracy of the calculation is completely dependent. This approximation is, however, much more involved in TDDFT compared to ordinary DFT as the TDDFT exchange-correlation functional is not only non-local in space but also time. In fact it depends on both the density to all prior times and the initial state, ie. the exchange-correlation functional contains a memory effect where a change in the density now will influence the density evolution at all later times. Obviously this makes it a monumental task to establish a good exchange-correlation functional. None-the-less a lot of work has been and is being put into creating functionals which incorporates both the non-locality in space and time[24, 71, 98]. However, here I will only consider the simplest approach to approximating the exchange-correlation functional as it is only these simple functionals I have applied in my work.

Adiabatic approximation

The simplest approach to approximating the exchange-correlation functional is simply to ignore the non-locality time, such that the functional only becomes dependent on the density right now.[27]

$$v_{xc}^{adiabatic}[n](\mathbf{r},t) = v_{xc}[n](\mathbf{r})|_{n=n(t)}. \tag{2.27}$$

This is known as the adiabatic approximation. Any functional from ordinary DFT can be applied in TDDFT through this adiabatic approximation. In the case of the local

density approximation the exchange-correlation functional has the abbreviation ALDA, which is short for adiabatic local density approximation.[109] ALDA is probably the most commonly used adiabatic approximation, since the non-locality in time is more severe than the non-locality in space, such that it does not improve results significantly to apply a GGA.

2.5 Implementation

During the work presented in this thesis I have applied three different implementations of density functional theory. I have used the plane-wave code Dacapo[22, 43] and the real-space code GPAW,[39, 77] which are both run with the python modules provided in the Atomic Simulation Environment[2, 3] (ASE). Furthermore I have applied the real-space code Octopus,[16, 83] which has a lot of functionalities related to TDDFT calculations. This section is meant as a brief description of those issues related to the practical implementation, where there has been made different choices in the different codes. I will start in Sec. 2.5.1 by describing how infinite periodic systems are treated. In Sec. 2.5.2 I mention the different ways the wavefunctions can be represented and finally in Sec. 2.5.3 I consider the issue of treating the core electrons in an efficient way.

2.5.1 Periodic systems

When considering systems of bulk materials the ability of restricting the description to a limited unit cell and then apply periodic boundary conditions is of absolute importance. This is also true for systems in surface science, where the surfaces will be periodic in two of the three dimensions. This is complicated a bit by the fact that the wavefunctions not necessarily hold the same periodicity as the external potential. On the contrary it is given by Bloch's theorem that the wavefunctions can be written as a product of an exponential and a function, $f_i(\mathbf{r})$, which has the same periodicity as the external potential:

$$\psi_i(\mathbf{r}) = \exp(i\mathbf{k}\cdot\mathbf{r})f_i(\mathbf{r}). \tag{2.28}$$

Due to Bloch's theorem it is still possible to limit the description to a unit cell, which contains the periodicity of the external potential. The only price is that it necessitates a sampling of the possible $\mathbf{k}$-values, the so-called $\mathbf{k}$-space sampling of the 1. Brilliuon zone. The consequence is limited by the fact that the $\mathbf{k}$-space sampling is easily parallelized as the eigenvalue problem can be solved independently for each $\mathbf{k}$-point. The density of the sampling is system dependent and convergence tests should be performed whenever a new type of system is taken under consideration.

All the three codes, Dacapo, GPAW and Octopus provide the possibility of considering periodic systems in this manner. For Dacapo it is only possible to handle periodic systems because of the way wavefunctions are represented as it will be evident in Sec. 2.5.2.

2.5.2 Representing the wavefunctions

When putting wavefunctions on numerical form is is necessary to choose some way of representing them. In practice this means to choose a basis set for the wavefunctions. In this section I will mention the 3 most applied approaches to this.

Plane wave basis set

The DACAPO code uses plane waves with reciprocal lattice vectors of the periodic unit cell, $\mathbf{G}_j$, as the basis set:

$$f_i(\mathbf{r}) = \sum_j c_j \exp(i\mathbf{G}_j \cdot \mathbf{r}). \tag{2.29}$$

I write $f_i(\mathbf{r})$ instead of $\psi_i(\mathbf{r})$ because it, of course, only is the periodic part in Eq. 2.28, which is represented by the plane waves. The periodic nature of this basis makes periodic boundary conditions the only possibility.

Naturally, it is not possible to have an infinite basis set. In practice the basis set is limited by setting an energy cut-off, where all plane waves with an energy above this cut-off is removed from the basis. The optimal value of the energy cut-off is system dependent and must be determined through a convergence test, whenever a new type of system is taken under consideration.

Grid

The perhaps most intuitive approach to representing a function is by holding its value in a sufficiently dense grid of positions in space. This is the so-called real-space grid basis, which both GPAW and OCTOPUS implements. The big advantage of this approach the ability to effectively parallelize big systems through a division of the considered space into different domains. This only requires limited communication between domains sharing boundaries. The most significant disadvantage is the so-called egg-box effect, which is an artificial variation of the observables as the position of the grid is varied. As it is the case for the energy cut-off in the plane wave basis set, the grid-point distance has to be subjected to a convergence test, whenever a new type of system is taken under consideration.

Localized orbitals

A third approach to representing wavefunctions is to use some set of localized orbitals. That could for example be gaussians or a set of atomic wavefunctions. The advantage of this approach is that it is possible to get quite reasonable results with a rather small basis. The disadvantage being that there is no systematic way of improving the basis set as one can with plane waves by increasing the cut-off energy or with a real-space grid by making it denser. Another disadvantage is that the basis set often will be bound to the positions of the considered atoms, which complicates force evaluations as the displacement of the basis set also has to be accounted for.

Both GPAW and Octopus offer the possibility of converging density and wavefunctions within a localized basis set before the calculation is continued on the real-space grid.

2.5.3 Treating core electrons

The chemical properties of an atom is almost completely determined by the outermost lying electrons, the so-called valence electrons. This leaves an enormous potential for making calculations more effective by leaving all core electrons out of the calculations. However, the biggest advantage lies in the possibility of smoothing out the valence electron wavefunctions, which vary very rapidly in the core regions, because of the criterion of orthogonality to all core electron wavefunctions. Such a smoothing makes it much easier to represent the wavefunctions, ie. a much smaller basis set can be applied. In the following I will mention some different approaches to performing this smoothing.

Pseudo-potentials

In the pseudo-potential method the nuclei potentials and core electrons are replaced with soft pseudo potentials.[42] This replacement is accompanied by a replacement of the true valence wave functions with pseudo wave functions. The point of the pseudo potentials is to design them such that the pseudo wave functions are node-less and smooth, which will make them easier to represent. In the generation of pseudo potentials at least two basic guidelines are typically followed[84]:

(i) The pseudo potential should give the true eigenvalues for the valence electrons for the isolated atom.

(ii) Beyond some given core radius the pseudo wave functions and the true valence wave functions should coincide.

Often a third socalled norm-conserving criteria is added[42]. This criteria states that the pseudo wave function and the true valence wave function should have the same integrated charge over the core region.

When using the Octopus code I have applied norm-conserving pseudo-potentials developed by the Fritz-Haber institute[26], which have been generated using the Troullier-Martins scheme.[99] The Dacapo code applies ultra-soft Vanderbilt pseudo-potentials,[103] which do not fulfill the norm-conserving criteria. This is done to preserve the freedom of making even smoother wavefunctions.

Projector Augmented Wave method

The projector augmented wave[5, 6, 69] (PAW) method was invented by Blöchl and is implemented by GPAW. The approach is similar to the pseudo-potential approach in the sense that core radii are chosen for each atom. Outside these the pseudo wavefunctions coincide with the real ones and inside the pseudo wavefunctions are smoothened. The big difference is, however, that one in the PAW formalism establishes a transformation

between the pseudo wavefunctions and the real ones, such that the real wavefunctions can be found from the pseudo wavefunctions. I will leave all technical details to the articles of Blöchl[5, 6] and just mention some of the advantages compared to the pseudopotential approach. First of all it gives much better control of the error induced by the approximation. By converging all parameters it is possible get the accuracy of an all-electron implementation. Secondly the PAW approach gives some extra information on the system, since all the correct wavefunctions can be generated. This can for example by applied to extract the total electron density, which can be benefitial in for example a Bader analysis.[48]

2.6 Calculational details

All the density functional calculations performed as a part of this work have been performed on rather similar systems. They all include a transition metal, in most cases Ruthenium, and in many cases they also include a diatomic molecule (N_2, CO or NO). Because of this similarity it has not been necessary to vary the used parameters in the calculations much. In this section I provide the parameters I have used in the three codes, Dacapo, GPAW and Octopus.

2.6.1 Dacapo

I have mainly applied Dacapo in the calculations related to the structure of nanoparticles. Exchange-correlation effects are described with the revised Perdew-Burke-Ernzerhof (RPBE)[43] functional.

The optimal energy cut-off and k-point density was found through ordinary convergence tests. I have used an energy cut-off of 350 eV, and in all periodically repeated directions the number of k-points has been set such that it multiplied with the unit cell length in that direction is bigger than 25. For convergence reasons an electronic temperatures of 0.1 eV have been applied. Since the wavefunctions in Dacapo are represented as a linear combination of plane waves it is only possible to apply periodic boundary conditions to the unit cell. When calculating on slabs the have all been separated with at least 10 Å of vacuum in order to avoid interactions between the slabs.

2.6.2 GPAW

The ΔSCF methods of Sec. 2.3 was implemented in the GPAW code, so all presented ΔSCF calculations have been made with GPAW. In most calculations the revised Perdew-Burke-Ernzerhof (RPBE) functional is used to describe exchange-correlation effects. This functional has been chosen, because it is optimized to provide a good description of molecules adsorbed on transition metal surfaces.[43, 70] In a few cases the local density approximation (LDA) has been applied, because the results are compared to TDDFT calculations using the adiabatic local-density approximation (ALDA).

The optimal grid-spacing and k-point density was found through ordinary convergence tests. I have used a grid-spacing of 0.18 Å, and in all periodically repeated directions the

number of k-points has been set such that it multiplied with the unit cell length in that direction is bigger than 25. For convergence reasons an electronic temperatures of 0.1 eV has been applied.

Many of the ΔSCF calculations are performed on diatomic molecules on flat transition metal surfaces. In those calculations the size of the unit cell is set, such that it corresponds to a coverage of 0.25.

2.6.3 Octopus

Octopus has been applied in all the TDDFT calculations presented in this thesis. Exchange-correlation effects are approximated with the adiabatic local-density approximation (ALDA) Because of the simple nature of this approximation we should not expect to get good quantitative numbers, but the hope is that it provides qualitatively good results. Hopefully it will in the future become feasible to apply better approximations, which also account for the non-locality in time of the exchange-correlation functional. I have not applied the adiabatic version of a generalized gradient approximation, since the localization in time is more severe than the localization in space.

A variety of different propagators for the Kohn-Sham equations are implemented in Octopus. Before performing full calculations I ran a number of test calculations with each propagator in order to find the one most suited for the type of systems I consider. For the different propagators I compared the maximally allowed value for the timestep, before the propagation starts to diverge. This comparison revealed a combination of the exponential midpoint rule[53] and a Krylov subspace approximation to the exponential matrix operator[52] to be the preferred choice. With this propagator it was possible to use a timestep of 0.001 fs, so this propagator and this timestep has been applied in all calculations presented here.

The grid-spacing was found through an ordinary convergence test of the total energy. Here I found the results to be converged at a grid-spacing of 0.18 Å.

When performing ground state calculations on the systems containing Ruthenium it turned out to be quite hard to get the calculations to converge. However, by applying Broyden mixing[10] of the 7 preceding densities in each self-consistency cycle and using an electronic temperature of 0.1 eV it was possible to get slow convergence.

Chapter 3

Finding the shape of a nanoparticle

In this chapter I consider problem of theoretically finding the detailed structure of a nanoparticle of a given size. I start in Sec. 3.1 by describing the simple classical approach to finding structures of crystalline particles, the socalled Wulff construction, and consider the limitations of this approach with respect to finding reactivity. In Sec. 3.2 I discuss the issue of equilibrium shape vs kinetic shape, ie. whether or not given particles have had time enough to reach their equilibrium structures. In Sec. 3.3 I focus on avoiding the limitations of the Wulff construction by taking a more general approach. I start with the first attempts in my project of finding the structure, which failed due to unrealistic requirements on the computational time, but they serve as a justification and inspiration to limit the configurational space significantly. I then describe in more detail how this is done. Naturally the model requires the ability of calculating the energy of the nano-particle in different structures. High-accuracy methods, such as DFT, are not directly applicable for this purpose, due to the required computational effort. In Sec. 3.4 I consider the problem of getting computationally easy but sufficiently accurate estimates of the energies. The obtained structures and the energies of these are combined in Sec. 3.5 to calculate average properties of the cluster. The whole first part of this chapter only considers the structure and properties of particles floating in vacuum. In Secs. 3.6 and 3.7 I describe how one can approach more realistic conditions by including the effects of a substrate and the presence of a gas. A small part of this chapter describes work I did in my master project[37] prior to the beginning of my ph.d. However, I still include this here in order to provide a more complete picture. In my master I performed the molecular dynamics simulations and first Monte Carlo simulations of Sec. 3.3, I developed the EMT potential of Sec. 3.4.1 and I performed the potential energy vs free energy consideration of Sec. 3.5.2. Paper I also contains a description of some of the issues discussed in this chapter, and this can be considered supplementary to that.

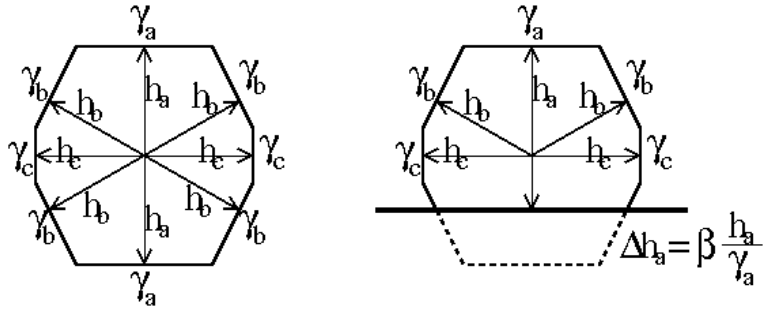

Figure 3.1: Left panel: Illustration of the Wulff construction of a 2-dimensional crystal with three different facets (a, b and c). The distances from the center to the facets (h_a, h_b and h_c) are proportional to the free surface energies (γ_a, γ_b and γ_c). Right panel: The effect of the substrate is included by changing the distance to the substrate-particle interface by $-\beta\frac{h_a}{\gamma_a}$, where β is the interface adhesion energy.

3.1 The Wulff construction

The Wulff theorem[19, 60, 108] was first discovered by G. Wulff in 1901 and is a simple approach to finding the equilibrium structure of a crystal. The idea is to minimize the surface free energy, $\int \gamma dA$, with respect to the shape of the particle. If the surface energy, γ, is independent of the direction then the optimal shape is naturally just a sphere. However, as a crystal has different facets with different energies, the optimal shape may look very non-spherical. Wulff's theorem tells us how to construct the optimal shape by ensuring that the normal distance from the center to each facet is proportional to the surface energy as illustrated on Fig. 3.1. The figure illustrates the situation for a 2-dimensional crystal, but it is of course easily extended to 3 dimensions.

If the particle is placed on a substrate, then it will influence the equilibrium structure of the particle. This is handled in the Wulff construction by changing the distance to the substrate-particle interface by $-\beta\frac{h_a}{\gamma_a}$, where β is the interface adhesion energy. This is also illustrated on Fig. 3.1.

Obviously it is necessary to know the surface energies of the different crystal facets, before it is possible to make the Wulff construction. Experimentally it is very hard to measure surface energies[7, 100], so typically surface energies are obtained through calculations[104]. With these surface energies, the proportionality factor between the surface energies and the distances is just varied until the constructed shape has the desired volume. This is the procedure I will apply in Sec. 3.1.1 for Ruthenium. In Sec. 3.1.2 I will then discuss those limitations of the Wulff construction, which are especially relevant when trying to estimate the catalytic activity of a particle.

Table 3.1: Energies of different Ruthenium facets. The basis vectors for the Miller indices are the standard hcp basis vectors.

Facet	γ_{surf} (eV/Å^2)	γ_{surf} (J/m^2)
(001)	0.176	2.82
(100)	0.197	3.16
(011)	0.199	3.19
(201)	0.203	3.25
(102)	0.210	3.36
(110)	0.221	3.54
(111)	0.221	3.54

3.1.1 The Wulff construction for Ruthenium

In this section I will describe how I have made the Wulff construction for Ruthenium, which forms a hcp crystal. The first step is to calculate surface energies of all the different facets, which will be present. In principle one would have to calculate the energy of all facets in order to know which ones are present, but as this is not possible one has to limit it to the most likely ones. I calculate the energy of one facet by constructing a four layer slab in DACAPO using the experimental lattice constants, $a = 2.7059$ Å and $c = 4.2815$ Å. The parameters of the calculations can be found in Sec. 2.6.1. I then relax the top layer of atoms and obtain the surface energy as:

$$\gamma_{surf} = \frac{\frac{1}{2}(E_{unrelaxed} - E_{bulk}) - (E_{unrelaxed} - E_{relaxed})}{A}, \tag{3.1}$$

where $E_{unrelaxed}$ and $E_{relaxed}$ are the energies of the slab before and after the relaxation respectively, E_{bulk} is the energy of the same number of atoms sitting in bulk Ruthenium and A is the area of one of the facets of the slab. The factor half is there because the slab has two sides, so the surface energy of one side is half the total surface energy. The $E_{unrelaxed} - E_{relaxed}$ term is the correction due to the relaxation. I only relax the first layer of atoms on one of the sides, instead of relaxing both sides of the slab, in order to minimize the effect of having a slab of limited size. The obtained surface energies are summarized in Table 3.1.

The Wulff construction obtained from the energies of Table 3.1 is shown on Fig. 3.2 together with illustrations of the different facets.

3.1.2 Limitations of the Wulff construction

The Wulff construction is capable of giving a good estimation of the overall shape of crystalline nanoparticles, but it is not sufficient when trying to determine the detailed structure of nanoparticles. This is very important when calculating the catalytic activity of a particle, because it depends a lot on the detailed structure. This has for example been shown by Dahl et al,[23] who found that the catalytic activity of splitting a Nitrogen

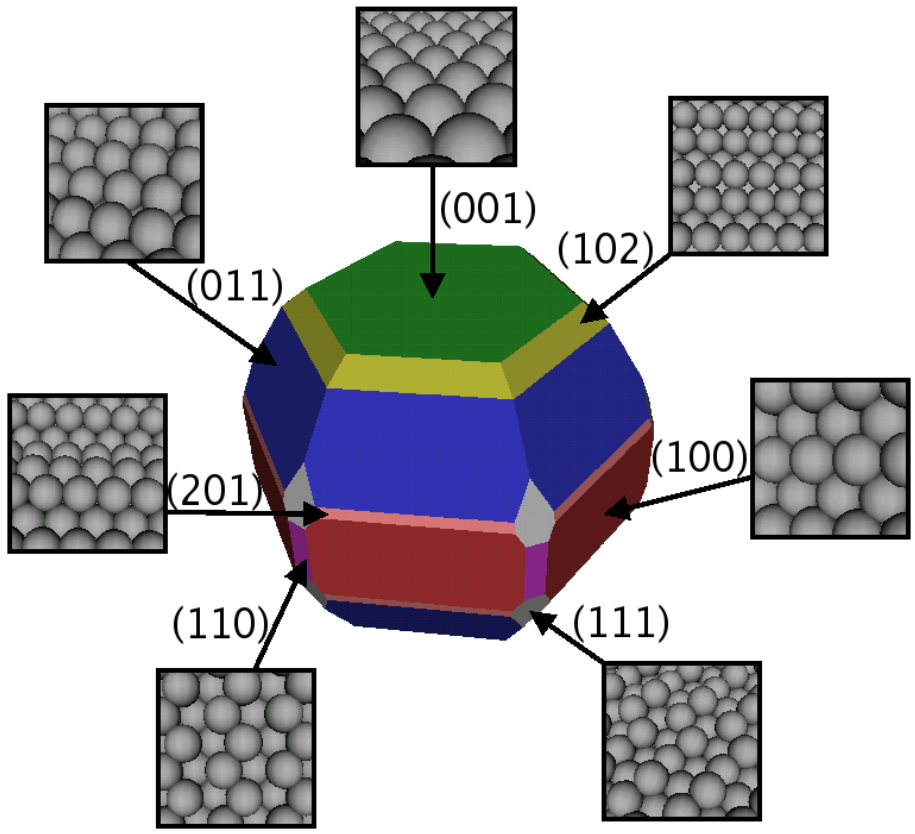

Figure 3.2: The Wulff construction of a Ruthenium crystal based on the facets and energies of Table 3.1. The basis vectors for the Miller indices are the standard hcp basis vectors.

molecule is up to 8 orders of magnitude higher at a Ruthenium step site compared to a close-packed (001) surface site. This means that the catalytic activity of the particles, at least for some reactions, will be completely dominated by the presence of a few catalytic active sites. Especially important is that the highly active sites often will be step sites. The reason for that is two-fold. First of all there is the d-band model[44, 45], which relates the catalytic activity to the position of the d-band center, which will shift depending on the coordination of the surface atom. Step sites have low coordinated surface atoms, which often gives a favourable positioned d-band. Secondly step-sites provide the geometrical freedom for adsorbates to bind to several surface atoms. Typical examples of reactions, where step sites indeed are the most active, are reactions which are limited by the splitting of a diatomic molecule, such as N_2-splitting in the ammonia synthesis[73]. As Fig. 3.3 shows the Wulff construction may not provide the presence of any step sites, ie. the presence of these are completely dominated by the limitations of the Wulff construction. In the following I will list some of the inadequacies of the Wulff construction, with respect to detailed structure calculations.

First of all the Wulff construction does not include finite size effects, it just assumes

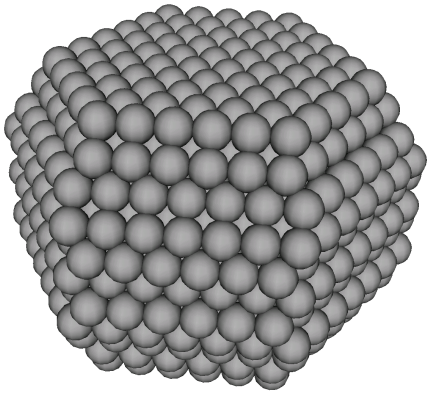

Figure 3.3: Example of how one could try to estimate the structure of a finite cluster based on the Wulff construction of Ruthenium (see Fig. 3.2). Due to the finite size of the cluster it is only possible to include the 3 dominating types of facets of the Wulff construction. It is seen that this cluster does not provide any step sites.

that the material is completely homogeneous, except for the directional dependence of the surface energy. One finite size effect is that the possible distances from the center of the particle to a facet is discrete, due to the finite distance between atomic layers, ie. it is not possible set the distances such that they all fulfill the Wulff construction. Another finite size effect is the finite number of atoms, which acts as another restriction when trying to create structures close to the Wulff construction. It is not unlikely that this is very important for the presence of step sites, because they may be provided by a mismatch between the actual number of atoms and the number needed in order to make a near-Wulff construction.

Secondly the Wulff construction does not include any edge effects. For small particles the number of edge atoms becomes comparable to the number of surface atoms, so it is possible that edge energies will have an influence on the optimal structure of the particle.

Finally the Wulff construction only estimates the structure with the lowest energy, ie. it does not include the effect of a finite temperature. A finite temperature will make the cluster change between different configurations over time, ie. it may spend time in configurations with a higher number of active sites than the ground state configuration, which could influence the time-averaged catalytic activity of the cluster.

3.2 The time it takes to reach equilibrium shape

Before I move on to describing the model that accounts for the finite size and edge effects that the Wulff construction ignores, I will touch upon another important issue in relation to the shape of nanoparticles. Both the Wulff construction and the model I will describe in the remainder of this chapter try to find the equilibrium structure of a particle, ie. the

shape the particle will obtain after being left alone for sufficiently long time. However, the models do not estimate what a sufficiently long time is, which means that in some situations the equilibrium shape may be completely irrelevant, since the particle may not have had enough time to reach the equilibrium shape. It is for example well-known that the shape of a macroscopic crystal typically is dominated by the growth rate of the different facets and hence the conditions under which the crystal has been made.[49]

The problem of how long it takes to reach equilibrium shape has been treated to some extent in the literature. In 1951 Herring[50] showed that the relaxation time is proportional to the particle radius to the fourth power, $\tau \propto R^4$. Later Kern[64] considered the more specific situation of a crystal relaxing from a cubic shape and he also found a proportionality between the relaxation time and the particle radius to the fourth power. However, more recent kinetic Monte-Carlo simulations indicate that this relation only hold for high temperatures[20, 79]. At lower temperatures the relaxation time is dominated by the rate of nucleation on the facets, ie. the time it takes before a number of atoms have randomly moved on to the top of a facet. In this case the relaxation time is significantly prolonged.

In Sec. 3.3.1 I describe some molecular dynamics simulations I have performed on Ruthenium nanoparticles. Here I found that particles below a diameter of 1 nm will reach equilbrium within 1 ns at a temperature of 1000 K. At room temperature it has to be a bit smaller particles before they will reach equilibrium within 1 ns. With the Herring estimation on the relaxation time I then find that $\tau \approx 10^4 \cdot 1 \text{ ns} = 10 \ \mu\text{s}$ for a particle with a diameter of 10 nm at a temperature of 1000 K. This is a very short time-scale compared to the time-scale of typical experiments, so this could indicate that it is reasonable to only consider the equilibrium shapes of Ruthenium particles below a diameter of 10 nm. However, this estimate does not include the nucleation of facets effect mentioned above and 1000 K is a quite high temperature compared to most experiments, so one should use this result very carefully. When comparing to experiments it is always important to keep in mind that the particles may not have had sufficient time to equilibrate.

3.3 Generating an ensemble of structures

In section 3.1.2 I described some of the limitations of the Wulff construction. The model, which I will describe in the following sections, tries to incorporate all the mentioned issues with the Wulff construction. The issues of finite size and edge effects are handled by building structures up of individual atoms instead of a geometrical shape as in the Wulff construction. The issue of finite temperature is handled by generating an ensemble of structures instead of just the ground state structure. In this section I will only describe how the ensembles of structures are created, whereas Secs. 3.4 and 3.5 will deal with the problem of calculating the energies of the structures in the ensemble and applying those to obtain the average structural properties, respectively.

The final model contains some rather restrictive conditions on the structure of a nanoparticle. In the following I will start in Sec. 3.3.1 by trying to justify this with the help of my first failed attempts of generating representative ensembles of structures.

In Sec. 3.3.2 I will then provide a more detailed description of the final model. When I in the following talk about relevant structure I mean structures, which a particle could obtain at temperatures below 1200 K, ie. temperatures significantly below the melting point of Ruthenium.

3.3.1 Limiting the configurational space

In this part I will try to give a chronological description of the development towards the method of generating ensembles of structures, which will be the subject of Sec. 3.3.2. The EMT potential, which will be described in Sec. 3.4.1, has been applied to get energies in the methods of this section. The estimated DFT method of section 3.4.2 is only applicable for certain structures, and therefore only applicable after a limitation of the configurational space has been justified.

Molecular dynamics simulations

The most direct method of finding the structure of a cluster is to perform a long molecular dynamics simulation and then sample the configurational space it goes through. I have performed constant temperature Langevin dynamics calculations for different cluster sizes and temperatures. The problem with this approach is that the computational effort restricts the simulation time to the nanosecond scale, which turns out to be way too short a time to get sufficiently around in configurational space for most cluster sizes and temperatures. For very small clusters, on the order 40 to 80 atoms, and temperatures around 1000 K it was possible to reach the same equilibrium structures from different starting points within a nanosecond.

Monte Carlo simulations

In the molecular dynamics simulations a lot of computational time is spend between jumps over barriers, where the atoms just vibrate around a local minimum. This can be avoided by jumping directly between local minima using a Monte Carlo scheme. I have made an implementation of the Metropolis Monte Carlo algorithm, which is a quite simple stochastic algorithm used to generate equilibrium ensembles of states for a given system at a given temperature[63]. The algorithm consists of many iterations, where a new configuration is suggested in each of these. The cluster changes to this configuration with a certain acceptance probability, p_{acc}. The criterion of detailed balance has to be fulfilled in order for the Metropolis algorithm to give valid results.[81] This criterion states that the probability of going from configuration a to configuration b should be the same as the probability of going from configuration b to configuration a, i. e.

$$K(b|a)f(a) = K(a|b)f(b) \Leftrightarrow p_{acc}(b|a)p_{sugg}(b|a)f(a) = p_{acc}(a|b)p_{sugg}(a|b)f(b), \qquad (3.2)$$

where $f(a)$ is the probability of being in configuration a, $K(b|a)$ is the probability of moving to configuration b when sitting in configuration a, $p_{sugg}(b|a)$ is the probability of suggesting configuration b when sitting in configuration a and $p_{acc}(b|a)$ is the probability

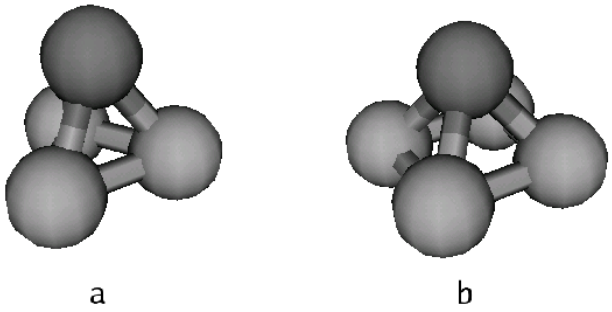

Figure 3.4: In a close-packed structure all atoms will be supported by at least 3 neighboring atoms sitting as illustrated on the left panel or 4 neighboring atoms sitting as illustrated on the right panel.

of accepting a suggested jump from configuration a to configuration b. Equation (3.2) is fulfilled if the following acceptance probability, $p_{acc}(b|a)$ is used

$$p_{acc}(b|a) = \min\left[1, \frac{p_{sugg}(a|b)f(b)}{p_{sugg}(b|a)f(a)}\right]. \tag{3.3}$$

Here I desire a Boltzmann distribution of the configurations, i.e

$$\frac{f(b)}{f(a)} = \exp\left(\frac{E_a - E_b}{k_B T}\right) = \exp\left(\frac{-\Delta E}{k_B T}\right), \tag{3.4}$$

where E_a is the energy of configuration a, k_B is the Boltzmann constant and T is the simulated temperature. The expression for the acceptance probability is then obtained by combining Eqs. (3.3) and (3.4)

$$p_{acc}(b|a) = \min\left[1, \frac{p_{sugg}(a|b)}{p_{sugg}(b|a)} \exp\left(\frac{-\Delta E}{k_B T}\right)\right]. \tag{3.5}$$

A correct ensemble will then be obtained by using this acceptance probability and performing so many iterations that the system has moved sufficiently through the relevant parts of the configurational space, such that a representative set of structures is obtained.

Only close-packed configurations

The crucial part of the Metropolis algorithm is how to find the structures, which should be suggested in each iteration. The experience from the molecular dynamics simulations was that all local minima are close-packed structures in the sense that all atoms are supported by neighboring atoms sitting in a triangle or a square in the manner illustrated on Fig. 3.4. Naturally atoms may be supported by several triangles or squares. All hcp-structures, fcc-structures and structures with stacking faults fulfill this criterion. Because the molecular dynamics simulations only gives these close-packed structures it should be reasonable

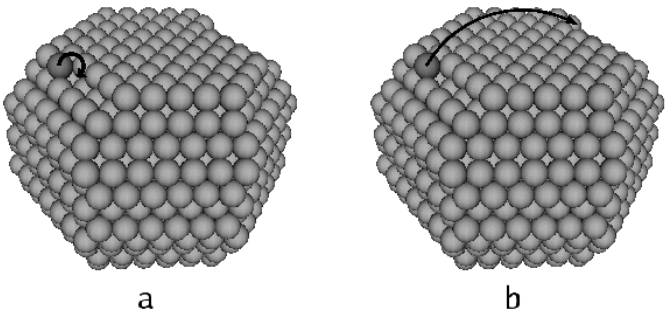

Figure 3.5: The two implemented ways of generating a suggested configuration in the Monte Carlo Metropolis algorithm. On the left panel a random surface atom is moved to a random neighboring position, which is supported as illustrated on Fig. 3.4. On the right panel a random surface atom is moved to a random supported site anywhere on the cluster.

to restrict the configurational space in the Metropolis algorithm to this. However, this restriction also rules out the possibility of making icosahedral clusters. For Copper this has been seen to be the preffered structure theoretically[101] as well as experimentally[91] for clusters below approximately 3.8 nm in diameter. For a 55 atoms gold cluster DFT calculations have also predicted it to be the preferred structure[41]. I did not observe the icosahedral configuration in the molecular dynamics simulations on Ruthenium. The reason of that could be that Ruthenium is an hcp metals, whereas Copper and Gold are fcc metals.

The suggested configuration in each step of the Metropolis algorithm is generated by moving one random surface atom to another random place on the surface, where it will be supported as illustrated on Fig. 3.5. The two panels illustrate two different implementations. In the first the atom is only moved to a neighboring site, whereas in the second it can move to any place on the cluster. The second implementation turned out to be a bit more successful than the other. It should be mentioned that the probabilities, $p_{sugg}(a|b)$ and $p_{sugg}(b|a)$, of Eq. (3.5) are easily calculated from the number of surface atoms and supported surface sites of the current and suggested structures.

The results obtained by carrying out simulations for a number of different cluster sizes and at different temperatures using this implementation of the Metropolis algorithm was that it gives good results for clusters up to 2 nm in diameter with a temperature of 1000-1200 K. By good results I mean that it would give the same equilibrium structures from different starting points, within reasonable computing times. The high temperature is not a big problem since lower temperature ensembles is easily generated by weighting the obtained structures differently using Boltzmann factors. However, clusters with 2 nm in diameter are quite small, and the aim was to be able to describe also larger particles.

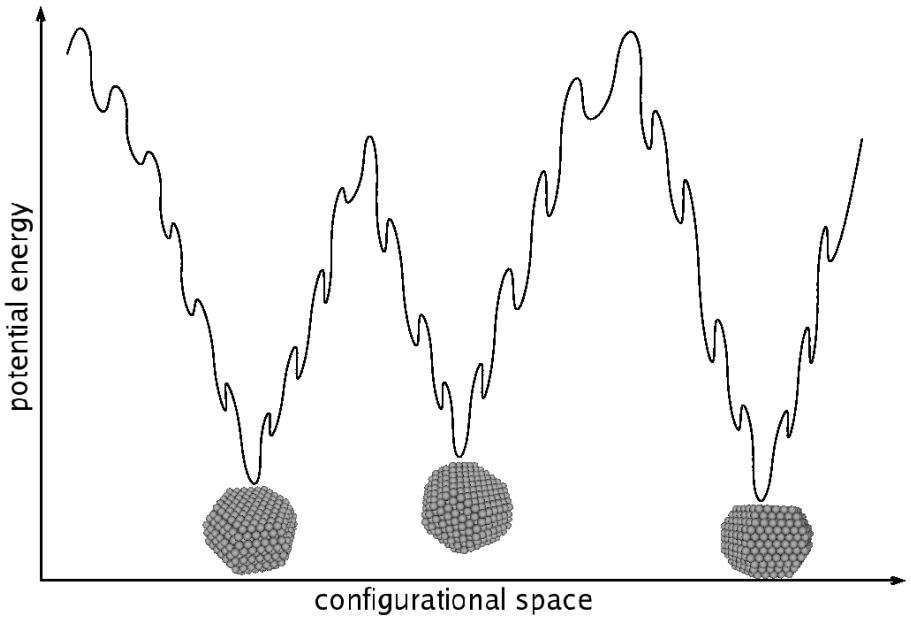

Figure 3.6: The configurational space contains some very deep local minima as illustrated on the figure. The high barriers arise because it is very expensive to start a new layer on the facets.

Only hcp structures

One result of the Monte Carlo Metropolis calculations was that almost none of the relevant structures for clusters above 1.5 nm in diameter contain any stacking faults. This means that it is reasonable to limit the configurational space even further to only include pure hcp-structures. This has the advantage that the implementation becomes much simpler and that the computational effort can be lowered. Furthermore it has the advantage that it becomes possible to use the estimated DFT potential of Sec. 3.4.2 to calculate the energies of structures. As I will argue in Secs. 3.4.2 and 3.4.3 this potential probably performs better for this purpose. However, this extra constraint on the structure did not make it possible to treat significantly larger particles with the Metropolis algorithm.

3.3.2 Generating only relevant structures

The problem that arise, when the Metropolis algorithm of Sec. 3.3.1, is applied to particles over 2 nm in diameter is that the simulation gets stuck in very deep local minima, which it cannot get out of within reasonable computational times. These deep minima all have very similar features, as it is illustrated on Fig. 3.6. They are completely dominated by three different facets, (001), (011) and (100), except that some atoms may be missing along a few edges or, more rarely, a group of atoms are placed on top of one of the facets.

Obviously it is necessary for a method to be able to jump more directly between these

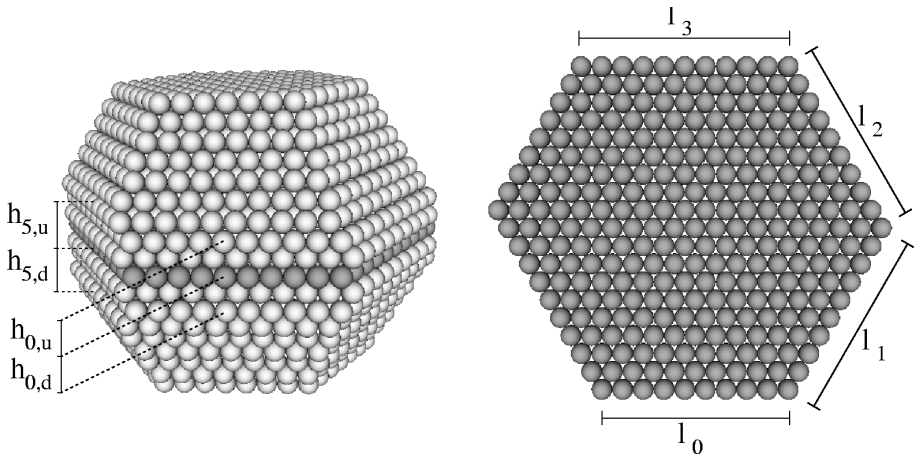

Figure 3.7: The definition of the 16 parameters $\{l_0 - l_3, h_{0,u} - h_{5,u}, h_{0,d} - h_{5,d}\}$ *describing the cluster shape.* $\{l_0 - l_3\}$ *are the dimensions of the basal plane whereas* $\{h_{0,u} - h_{5,u}\}$ *and* $\{h_{0,d} - h_{5,d}\}$ *are the number of layers up and down to the edges between the (001)-surfaces and (011)-surfaces. The figure is the same as Fig. 4 in paper I.*

very deep local minima in order for the method to be able to handle larger particles. The way I chose to do this was to split the process of generating an ensemble of structures up in two parts. One part where one finds the relevent deep local mininma and a second part where one searches through all the relevant parts of each of these deep local minima. In the following I will describe the method. A supplementary description can be found in Paper I, where a flowchart of the method is also provided.

First part: Overall cluster shapes

All the deep local minima are build from the same facets, as illustrated on Fig. 3.7. By parametizing the shape in the way illustrated on the figure it becomes easy to jump between the deep local minima, since one just have to vary the 16 parameters $\{l_0 - l_3, h_{0,u} - h_{5,u}, h_{0,d} - h_{5,d}\}$. The Metropolis Monte Carlo algorithm (see Sec. 3.3.1) is used to search through the parameter space. This algorithm is applied in order to only stay within relevant parts of the parameter space. In order to apply the Metropolis algorithm one has to assign an energy to each set of parameters. This is done by building the cluster from the parameters and then removing atoms along a edge or adding atoms on a facet, until the cluster has the correct number of atoms, and then calculate the energy. One should continue iterating through in the Metropolis algorithm for a sufficient amount of time. This has been tested by comparing different calculations on the same cluster. If they agree within the desired uncertainty then it is concluded that the simulations have run for sufficiently long time.

By running the algorithm at different simulation temperatures I found that 1200 K seems to be the optimal trade-off between being able to move through parameter space

and not spending too much time in irrelevant parts of it. The temperature does not have any physical relevance, as the aim is just to find all relevant sets of parameters.

It turns out that it is not necessary to take all the found sets of parameters to the second part, since a lot of them has too high an energy to be relevant. Tests have shown that one can disregard all sets of parameters which have an energy, which is more than 3 eV above the energy of the set of parameters with the lowest. This test is presented in Paper I, and was performed by checking the result's dependence on this cut-off energy. At 3 eV the results had converged.

Second part: Removing/adding atoms to the overall shape

The second part of the method is to take each deep minimum found in the first part and search through the relevant parts of them. In practice this means to take each set of parameters, build the cluster from these parameters and then find the different ways one can remove or add atoms to make the number of atoms fit the desired. This is done in a combinatorial way. First the algorithm finds the ways one can remove/add 1, 2, 3, ... N atoms from/to the same part of the cluster. N being the number of atoms that should be removed from/added to the cluster in order to make the number of atoms fit the desired. For each these groups of atoms it is calculated how a removal/addition of the atoms changes the energy of the cluster. Secondly the algorithm goes through the different ways one can combine these groups, such that the number of atoms sums up to N. In this way one also include the different ways one can remove/add atoms from/to different parts of the cluster. In case of an overwhelming number of possibilities a random sample is chosen. The change in energy from the removal/addition of several groups of atoms is just the sum of the changes given by the individual groups, since they are placed on different parts of the cluster. This makes it easy and fast to get the energy of all the structures.

It turns out that it is not necessary to find all the ways one can remove or add atoms, because many of the resulting structures have too high an energy. Figure 3.8 illustrates the difference between relevant and irrelevant ways of removing/adding atoms. As the figure indicates it is only necessary to consider removal of atoms from the edges of the cluster and it is only necessary to consider addition atoms of atoms in one group on one of the facets. That structures with holes are irrelevant is not so surprising, since it requires a lot of energy to break nearest neighbor bonds between the atoms. However, I have tested this claim by performing Metropolis Monte Carlo simulations on several clusters, where only the outermost layer of atoms was allowed to move.

3.4 Calculating the energy of a given structure

In order to weight the different configurations collected in the ensemble it is absolut necessary to be able to calculate the energy of the cluster in these configurations. Since the clusters can be quite large, up to thousands of atoms, it is not possible to apply high-accuracy methods, such as DFT, directly. Instead the first possibility I explored was to develop a EMT potential[18, 58, 59, 82] for Ruthenium, which I will consider in Sec.

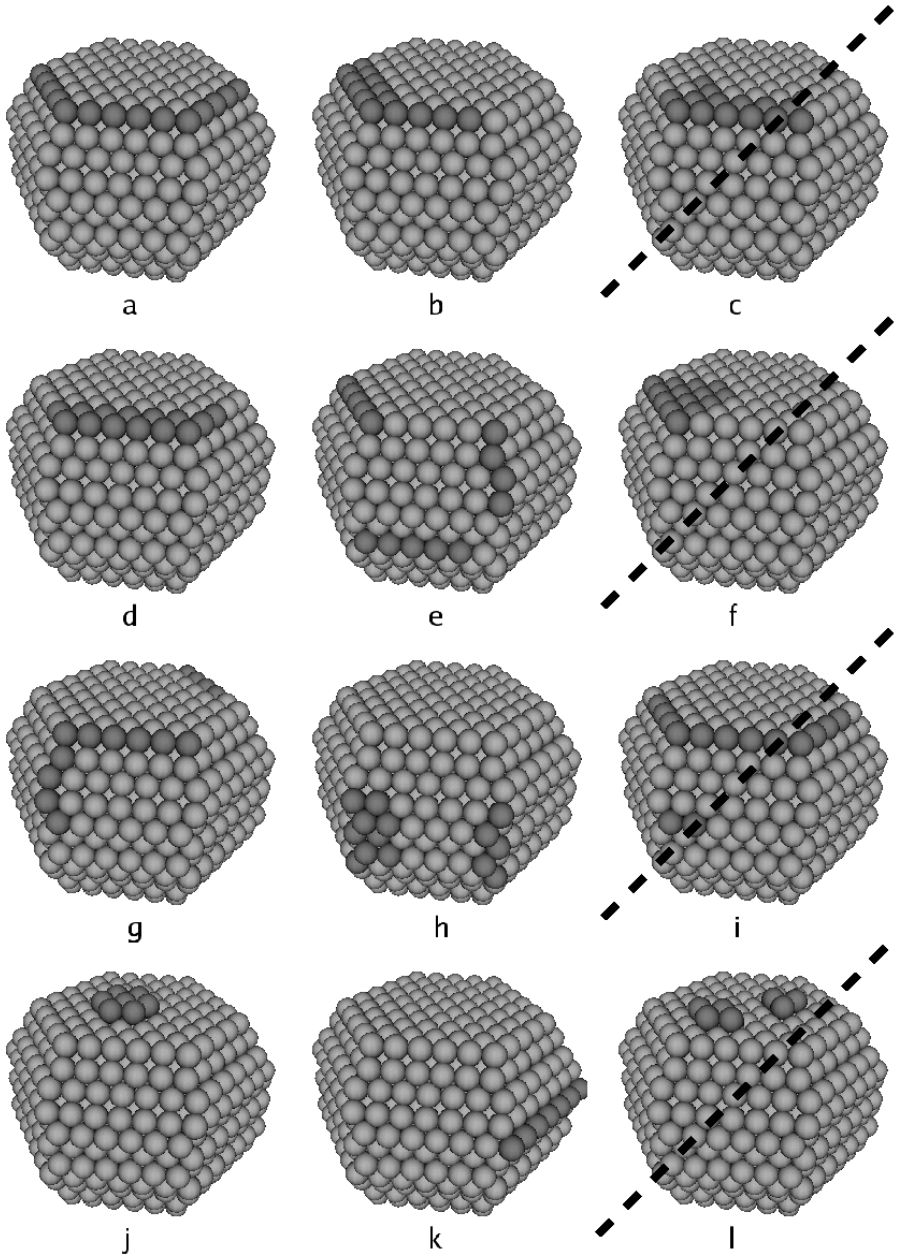

Figure 3.8: Examples of ways atoms can be removed (panel a-i) or added (panel j-l). The grey atoms indicate the removed/added atoms. The configurations with dotted lines across are examples of configurations, which are not included in the ensemble, since the energies of those are too high. Only configurations where maximally one row is partially removed is included. Atoms are only added to a single facet in a single island.

3.4.1. This potential was applied in all initial attempts of making a method for creating ensembles of structures, which I described in Sec. 3.3.1. As it became evident that it is possible to significantly restrict the configurational space it also became possible to consider a different approach to calculating the energy, where the total energy is pieced together from different surface energies, obtained through DFT slab calculations. I will describe this in Sec. 3.4.2. Finally I will compare the two approaches in Sec. 3.4.3.

3.4.1 EMT potential

EMT provides an expression for the total energy, which is not much more complicated to evaluate than a simple pair interaction model. EMT can be approached in different ways, but here I will follow the approach of Jacobsen et al[59]

The basic idea in the effective medium theory is to get the energy of an atom in any system by first calculating the energy in a well known reference system, the effective medium, and then perform an approximation of the energy difference between the actual system and the reference system. The total energy of the system, E, can then be written as

$$E = \sum_i E_{c,i} + \left(E - \sum_i E_{c,i} \right), \tag{3.6}$$

where $E_{c,i}$ is the energy of atom nr i in the reference system. The initial choice of reference system was the homogeneous electron gas.[82] Here a reference system of close-packed atoms has been used, ie. a system where each atom has 12 nearest neighbors. The correction term can be evaluated at an accuracy comparable to that of DFT, but also at a comparable computational cost[18, 58]. Here the correction term is evaluated using a simple pair interaction model.[59]

I will leave the reader to Ref. [59] for all the details. The final result is simply that the potential for a one-component system can be parameterized by 6 different parameters, E_0, V_0, s_0, η_2, κ and λ, which are defined in Ref. [59]. It is possible to assign values to these parameters using different physical arguments, but here the values have been found through a fitting procedure, where the properties of the potential are optimized to agree as well as possible with the desired. Table 3.2 lists the properties the potential was fitted to and how well the optimized potential performs with respect to these properties. The optimized values of the parameters are: $E_0 = -6.3505$ eV, $V_0 = 12.3052$ eV, $s_0 = 1.4984$ Å, $\eta_2 = 3.9452$ Å^{-1}, $\kappa = 6.5612$ Å^{-1} and $\lambda = 6.7015$ Å^{-1}.

The target values have in all cases, except for $E_{coh,hcp} - E_{coh,fcc}$, been taken from the literature (see the table caption). Experimental values have been used for the lattice constants, the cohesive energy and the elastic constants. DFT calculation results for unrelaxed surface energies have been used as target values for the surface energies. I calculated the target value for $E_{coh,hcp} - E_{coh,fcc}$ using the DFT code DACAPO.

3.4.2 Applying DFT surface energies

The idea in this approach is to calculate the total energy of the cluster as the sum of surface energies for the individual atoms. The individual surface energies are then found

Table 3.2: Properties of the optimized effective medium theory potential for ruthenium compared to the target values. [1] *Taken from Ref. [25],* [2] *Taken from Ref. [65],* [3] *Taken from Ref. [28],* [4] *Taken from Ref. [104],* [5] *Found by performing density functional theory calculations.*

Property	Optimized value	Target value	Deviation (%)
a (Å)	2.690	2.710[1]	0.74
c/a	1.630	1.579[1]	3.2
$E_{coh,hcp}$ (eV)	6.383	6.620[2]	3.6
c_{11}	9.112	9.014[3]	1.1
c_{12}	2.600	3.009[3]	14
c_{13}	1.849	2.695[3]	31
c_{33}	10.89	10.00[3]	8.9
c_{44}	2.511	2.894[3]	13
c_{66}	3.257	3.002[3]	8.5
γ_{0001} (eV/atom)	1.903	1.574[4]	21
$\gamma_{10\bar{1}0A}$ (eV/atom)	3.762	3.201[4]	18
$\gamma_{10\bar{1}0B}$ (eV/atom)	4.737	3.669[4]	29
$E_{coh,hcp} - E_{coh,fcc}$ (eV)	0.019	0.109[5]	83

using DFT energies. This approach is only feasible because it turns out that it is only necessary to consider pure hcp-clusters, which are dominated by a few facets as discussed in Sec. 3.3.

The energies of the individual surface atoms are chosen to be a function of the number and position of the nearest neighbors and is estimated by calculating the DFT energy of the slabs shown on Fig. 3.9. This is done with the DACAPO code, using the parameters given in Sec. 2.6.1. The grey atoms on the figure indicate the atoms whose energies are estimated from that slab calculation. The procedure is as follows:

- First the energy of the flat surface atoms (panel a-d) are determined. The total surface energy is distributed such that the individual energies are proportional to the missing number of nearest neighbors, in the cases with more than one type of surface atom.

- Secondly the energies of the edge atoms are determined from the slabs on panel e-h by first giving the flat surface atoms the energy determined in the last step. The remaining surface energy is then distributed amongst the edge atoms, again with the energy being proportional to the missing number of nearest neighbors.

- Thirdly the step energies are determined using the slabs on panel i-l, in exactly the same manner as in the last step.

Naturally, this procedure does not assign an energy to atoms in all possible configurations of nearest neighbors. For all other configurations the energy is just proportional to the

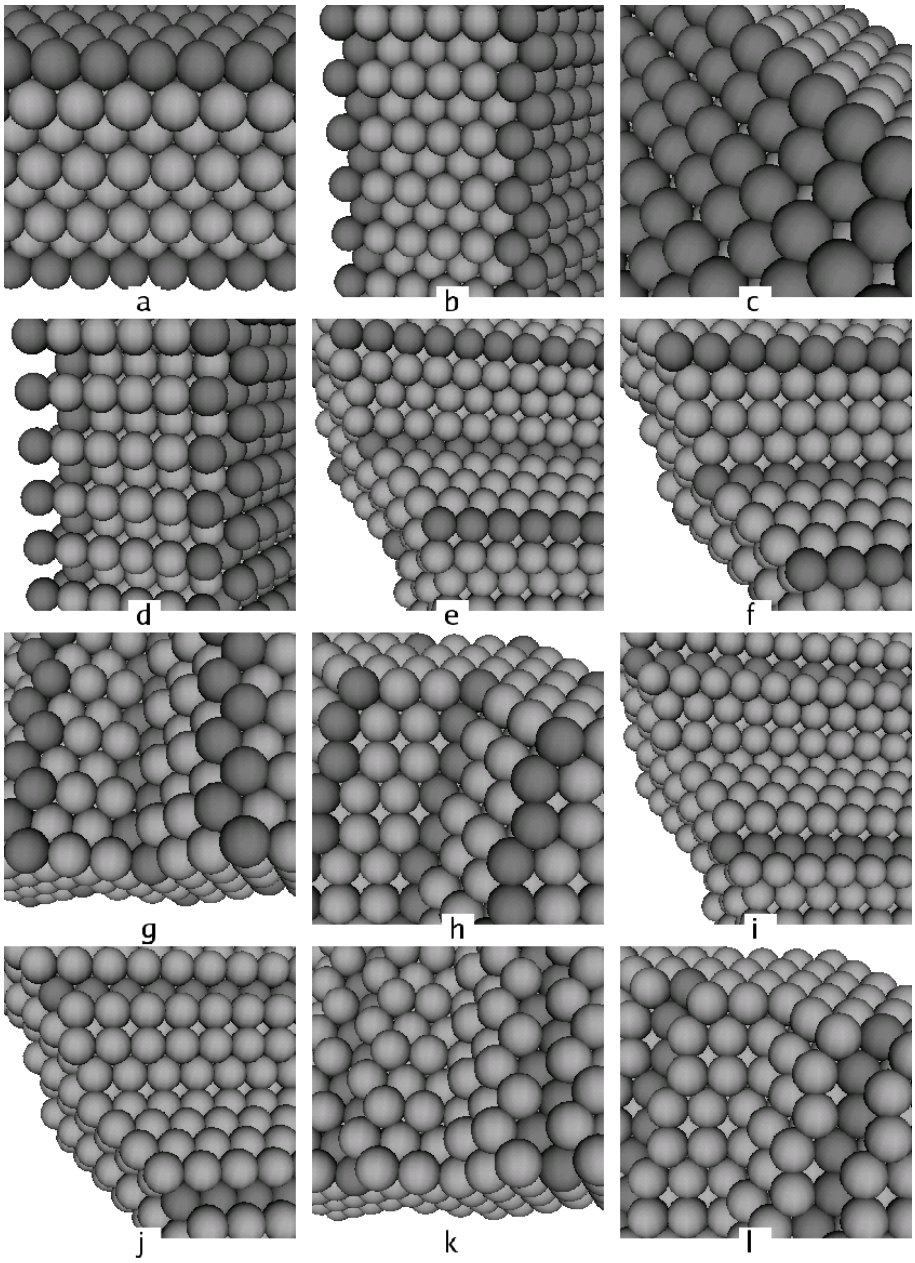

Figure 3.9: The slabs used to make the estimated DFT potential. The grey atoms indicate the atoms, whose energy is estimated by that slab calculation. The slabs on panel a-d gives the energy of flat surface atoms. The slabs on panel e-h gives the energy of edge atoms. The slabs on panel i-l gives the energy of step atoms.

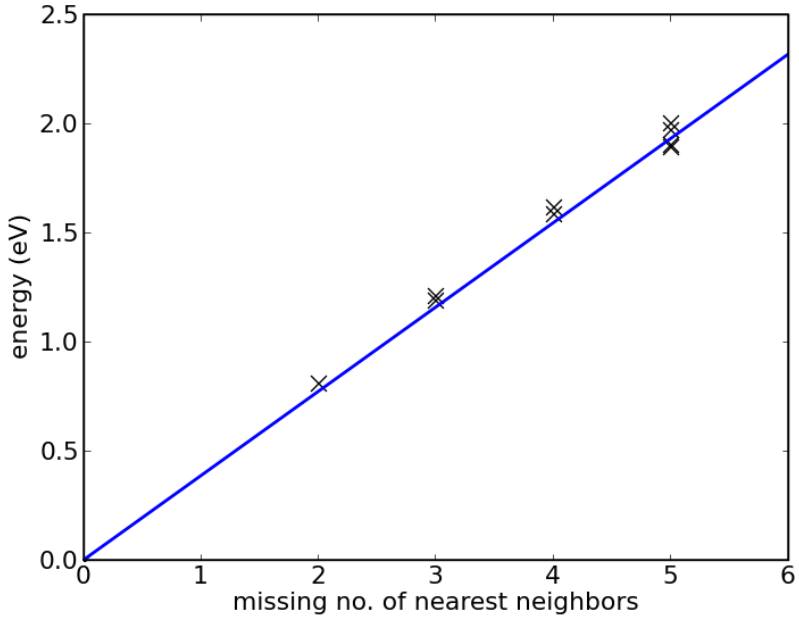

Figure 3.10: The surface energy as a function of the missing number of nearest neighbors. The X's indicate the energies found from the slabs on Fig. 3.9. The blue line is the linear fit, which is applied to atoms not covered by the slabs on Fig. 3.9.

missing number of nearest neighbors. The proportionality factor is determined by fitting to the energies found in the previous procedure as illustrated on Fig. 3.10.

3.4.3 Comparing EMT potential with DFT approach

The big advantage of the EMT potential, compared to the DFT approach, is of course that it can be used to calculate the energy of the cluster in any configuration, as well as the forces on the atoms. However, as Table 3.2 reveals, it is quite inaccurate with respect to surface energies. Even more worrying is that the EMT potential underestimates the difference in energy between a completed edge and an edge with a missing row of atoms by approximately a factor of 7. The EMT potential gives a difference of 0.015 eV/atom for the edge between the (001) and the (011) facets, whereas DFT calculations gives an energy difference of 0.1 eV/atom. This is crucial for the purpose of this work because an edge with a missing row of atoms contains a lot of catalytic important step sites.

In paper I we also performed some comparisons of the two different ways of calculating cluster energies. Here we concluded that it gives a larger error to use a EMT potential than the error of the estimated DFT approach. In the paper we also applied the estimated DFT approach to calculating the energies of two slabs, which we did not use in the construction of the estimated DFT potential. Here we found that the error was on the order of 0.01

eV/atom.

Because of these results I decided to apply the estimated DFT potential to all the calculations presented in the next chapter and in Paper I.

3.5 Obtaining properties

When a representative and sufficiently large ensemble of structures has been generated for a given cluster and all the energies of the structures are known it is possible to find the time-averaged properties of the cluster. I will describe how this is done in Sec. 3.5.1. The calculation applies the potential energies of the structures, where the free energy should be used. I discuss the consequences of that in Sec. 3.5.2.

3.5.1 Boltzmann averaging

The average properties of a cluster are calculated using simple Boltzmann averaging

$$\langle O \rangle = \frac{\sum_i O_i w_i \exp\left[-\frac{E_i}{k_B T}\right]}{\sum_i w_i \exp\left[-\frac{E_i}{k_B T}\right]}, \tag{3.7}$$

where $\langle O \rangle$ is the average of property O and the sum goes over all configurations in the ensemble. O_i, w_i and E_i is the value of property O, the weighting factor and energy of configuration number i. The weighting factor is used to include symmetrically equivalent structures and to compensate in the cases where only a random sample of configurations is included, as described in Sec. 3.3.2. In all the examples of this thesis the property, O_i, has been the number of a specific site, but in principle it could be any structural property of the cluster.

3.5.2 Potential energy vs free energy

The energy, E_i, of Eq. (3.7) should be the free energy of configuration i. This can easily be realized from the fact that each configuration is representative of a local minimum in configurational space and should be weighted by the number of states in that local minimum. In principle the free energy could be estimated by performing a vibrational analysis of each configuration. However, this is not practically feasible, so in all calculations the potential energy is simply used instead, which naturally will give rise to an error in the results. In order to get an estimate of the error involved I performed very long constant temperature molecular dynamics simulations on a 79 atoms Ruthenium cluster at a temperature of 2000 K, where I sample the configurations it goes through. Figure 3.11 shows the two configurations with the lowest energy. By comparing the amount of time the simulation spends in the two configurations with what I would expect by weighting the configurations with the Boltzmann factors I find a deviation of approximately 5%. This is of course only one example, but this could indicate that the approximation of applying the potential energy instead of the free energy is not too severe.

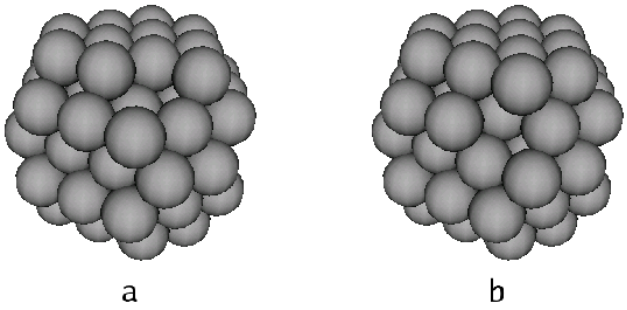

Figure 3.11: The two lowest energy configurations of a 79 atom Ru cluster. These are used in an estimation of the consequence of applying the potential energy instead of the free energy.

3.6 Including substrate

So far I have only considered floating particles, ie. particles which are not in contact with any substrate. Real particles used in catalysis are of course always supported in some way, so it is desirable include the substrate in the model. It is definitely not unlikely that the symmetry break and the restrictions of the configurational space inflicted by a substrate could influence the presence of catalytic active sites.

The simplest approach to including the effect of a substrate is to introduce a fictive plane as illustrated on Fig. 3.12. The energy of the configuration is then lowered by the interaction energy between the substrate and the particle, which will be proportional to the number of atoms in the lowest layer of the particle. The figure illustrates a situation where the substrate surface is parallel to the close-packed planes of the particles, but the same approach could in principle be applied for any other orientation. On Fig. 3.7 I introduced 16 parameters to describe the overall shape of the particle. When including the substrate it is necessary to include an extra parameter, which gives the position of the substrate plane relative to the particle. Except from that the calculations can be performed in exactly the same manner as for the floating particles. The size of the interaction between the substrate and the particle has to be chosen before generating the ensemble of structures. This can either be calculated by other means, be determined experimentally or one can generate an ensemble of structures for a range of different adhesion energies.

3.7 Including gas effects

So far I have only considered the structure of particles in vacuum. However, as I am interested the catalytic properties of the particles it is more relevant to know the structure in the presence of gas. A gas may change the structure because it will bind differently to different sites, which can change the costs of creating the different sites. The gas can promote a certain type of site if it binds stronger to that site. This effect can quite easily

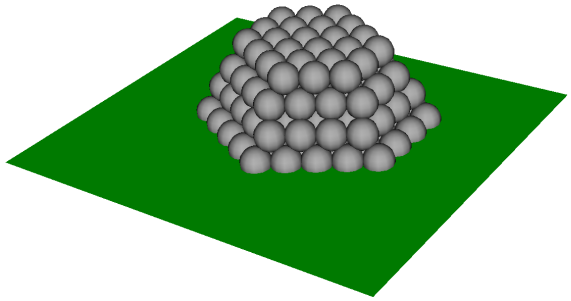

Figure 3.12: The effect of the substrate can be estimated by including a fictive plane in the calculations. All the atoms at the substrate lower their energy by the adhesion energy.

be included in the model of this chapter by changing the energy of all sites in this way

$$F_i = F_{i,vac} - \theta_{i,gas} \cdot F_{i,binding}, \tag{3.8}$$

where F_i is the free energy of site i, $F_{i,vac}$ is the free energy in vacuum, $\theta_{i,gas}$ is the coverage of gas on site i and $F_{i,binding}$ is the free binding energy

$$F_{i,binding} = F_{i,vac} + F_{gas} - F_{i,ads}, \tag{3.9}$$

where F_{gas} is the free energy of the gas molecule and $F_{i,ads}$ is the free energy of the site with an adsorbed molecule.

When the change in free energy, $\theta_{i,gas} \cdot F_{i,binding}$, of Eq. (3.8) is known for all sites it is easy to get the change in energy of all structures by summing up for all the sites present on the structures. With this modified energy the ensemble of structures can be found in exactly the same manner as for the particles in vacuum. In the following I will describe how the free binding energy, $F_{i,binding}$, and the coverage, $\theta_{i,gas}$, can be calculated for a given temperature and a given gas pressure. For simplicity I only consider the presence of one gas.

3.7.1 The free binding energy

In order to obtain the free binding energy of Eq. (3.9) it is necessary to include entropy contributions.

$$F_{i,binding} = E_{i,vac} + E_{gas} - TS_{gas} - E_{i,ads} + TS_{ads} = E_{i,vac} + E_{gas} - E_{i,ads} + Tk_B \log\left(\frac{q_{ads}}{q_{gas}}\right), \tag{3.10}$$

where E is the potential energy, T is the temperature, S is the entropy, q is the partition function and k_B is the Boltzmann constant. It has been assumed that the vibration of the gas and the surface is completely decoupled, such that the vibrational contribution from the surface to the entropy is unchanged upon adsorption and can be disregarded. This is reasonable, since the masses of the surface atoms and the gas atoms are typically very different.

The potential energies are easily estimated with the use of DFT. Unless the molecule is quite loosely bound to the surface there will only be a vibrational contribution to partition function, q_{ads}, which is calculated as[19]

$$q_{ads} = \prod_i \frac{e^{-\frac{1}{2}\frac{\hbar\omega_i}{k_B T}}}{1 - e^{-\frac{\hbar\omega_i}{k_B T}}}, \tag{3.11}$$

where ω_i is the frequency of the i'th vibrational mode. These can be estimated through an ordinary normal mode analysis[30]. The partion function of the gas consists of a translational, rotational and vibrational part

$$q_{gas} = q_{trans} q_{rot} q_{vib}, \tag{3.12}$$

where q_{vib} is evaluated as in Eq. (3.11), with the vibrational frequencies of the gas molecule. The translational contribution, q_{trans}, is given as[19]

$$q_{trans} = \frac{1}{p}\frac{(2\pi m)^{3/2}(k_B T)^{5/2}}{h^3}, \tag{3.13}$$

where m is the mass of the molecule. In the case of a diatomic molecule at all relevant temperatures the rotational contribution is given as[19]

$$q_{rot} = \frac{8\pi^2 I k_B T}{h^2}, \tag{3.14}$$

where I is the moment of inertia.

3.7.2 The coverage

The coverage, $\theta_{i,gas}$, of Eq. (3.8) can be estimated by assuming equilibrium between the gas and the adsorbed molecules, ie. by assuming that the adsorption rate equals the desorption rate.

$$k_+ \theta_{i,*} = k_- \theta_{i,gas} \Rightarrow \theta_{igas} = \frac{k_+/k_-}{1 + k_+/k_-}, \tag{3.15}$$

where k_+ and k_- are the adsorption and desorption reaction constants, respectively. $\theta_{i,*}$ is the coverage of free sites, ie. $\theta_{i,*} + \theta_{i,gas} = 1$.

The reaction constant of adsorption can be estimated from transition state theory[19]

$$k_+ = \frac{k_B T}{h} \frac{q_T}{q_{gas}} = \frac{k_B T}{h} \frac{q_{T,0}}{q_{gas}} e^{-\frac{E_{T-g}}{k_B T}}, \tag{3.16}$$

where q_T is the partition function of the transition state. In the last equality the energy scale of the transition state partition function is shifted, such that it is calculated with respect to the energy of the transition state. E_{T-g} is the energy difference between a molecule in the transition state and in the gas phase. Similarly one gets the reaction constant of desorption.

$$k_- = \frac{k_B T}{h} \frac{q_{T,0}}{q_{ads}} e^{-\frac{E_{T-a}}{k_B T}}, \tag{3.17}$$

where E_{T-a} is the energy difference between a molecule in the transition state and in the adsorption state. The ratio is then

$$k_+/k_- = \frac{q_{ads}}{q_{gas}} e^{\frac{E_{g-a}}{k_B T}}, \tag{3.18}$$

where E_{g-a} is the binding energy. The partition functions, q_{ads} and q_{gas}, are calculated from Eqs. (3.11) and (3.12). The coverage can then be calculated by inserting Eq. (3.18) in Eq. (3.15).

Chapter 4

The presence of active sites on Ru-nanoparticles

The last chapter was devoted to describing and justifying the developed model for calculating the detailed structure of Ruthenium particles. In this chapter I will present some of the results, which have been obtained through the application of this model. I will start in Sec. 4.1 by showing the most interesting sites with respect to many catalytic reactions, ie. the different types of step sites on a hcp crystal. In Sec. 4.2 I will assume no influence from the substrate and present gases on the particle structure when estimating the presence of step sites. This section will include a rough estimate of the ammonia synthesis activity as a function of the particle sizes. In Sec. 4.3 I consider the inclusion of a substrate and in Sec. 4.4 I consider the effect of having CO gas present. All density functional calculations presented in this chapter have been made with the DACAPO code, with the parameters given in Sec. 2.6.1.

4.1 Step sites on a hcp-cluster

For many catalytic reactions the step sites are much more catalytic active than flat surface sites and closed edge sites. This is for example in the case in ractions where the rate limiting step is the splitting of a diatomic, such as the ammonia synthesis, where the rate is determined by the splitting of N_2. This can be understood by combining a electronic structure analysis with a geometrical consideration. According to the d-band model[44, 45] low-coordinated surface atoms will typically have a more favourable electronic structure for splitting a diatomic molecule, since the d-band center for low-coordinated surface atoms is more favourably aligned with the anti-bonding state of the molecule. Step sites contain low-coordinated surface atoms. Step sites furthermore have the geometrical advantage that it is possible for a diatomic molecule to bind to several surface atoms on them.

Figure 4.1 shows the four types of step sites on a hcp cluster, which I will consider in the remainder of this chapter. All four steps sites can be found at an edge between two facets by removing one row of atoms. The figure also shows the corresponding completed edges. The right panel indicates where the edges are found on a hcp cluster.

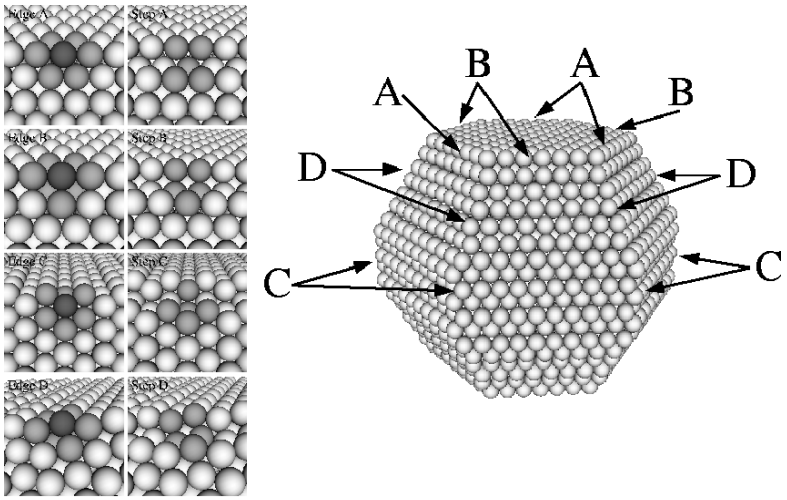

Figure 4.1: Definitions of the 4 types of edge sites and the 4 types of step sites present on a Ruthenium particle. The grey scale indicate the definitions of the sites. The edge sites are defined by the the dark grey atom having exactly the light grey atoms as the nearest neighbors. The steps sites are defined by an empty site having exactly the light grey atoms as nearest neighbors. The right panel indicate the positions of the different sites on the cluster. The figure is similar to Fig. 8 in paper I.

4.2 Floating Ru-particles

In this section I will present the results obtained with respect to the presence of the 4 types of step sites from Sec. 4.1 on Ruthenium nanoparticles. I consider particles in the diameter range from 2 nm to 5 nm. By calculating the barrier of N_2 dissociation on the four types of step sites I will also come with a rough estimate of the relation between the size of the particles and the catalytic activity under the ammonia synthesis.

4.2.1 Number of step sites vs no. of atoms

Figure 4.2 shows the average number of step sites as a function of the number of atoms in a Ruthenium particle. In the upper panel the number of atoms is varied from 396 to 416, which corresponds to a particle with approximately a diameter of 1.8 nm. The number of step sites is here seen to depend heavily on the exact number of atoms, the addition or removal of a single atom completely changes the number of sites. In the lower panel of Fig. 4.2 the particles are larger, the number of atoms is varied from 1000 to 1009. The diameter of these particles is approximately 2.7 nm. In this case the lines seem significantly more continuous, ie. an added or removed atom will not change the structure as significantly. This indicates that the size at which single atoms begin to play a crucial role on the overall structure lies in the diameter range between 2 nm to 3 nm.

The black and blue lines on Fig. 4.2 are at temperatures of 300 K and 1200 K,

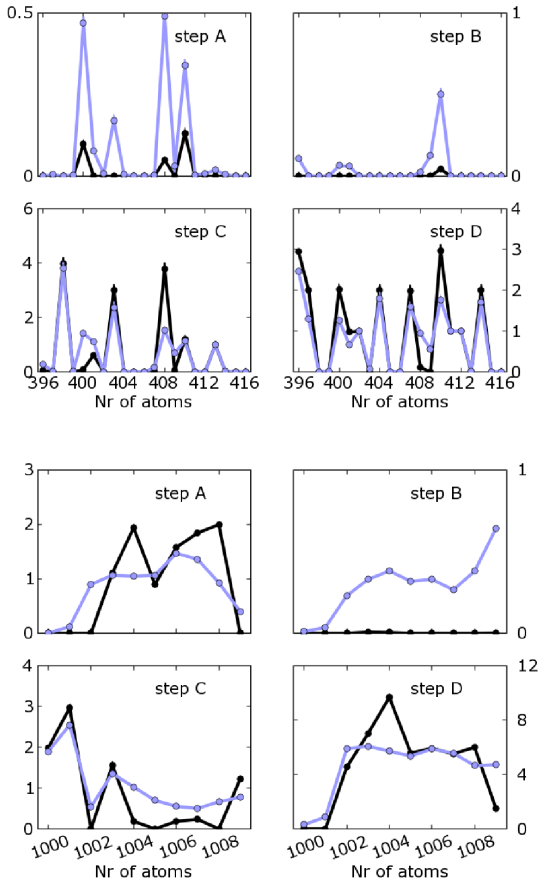

Figure 4.2: Number of step sites as a function of the number of atoms. The step sites are defined on Fig. 4.1. Upper panel considers clusters in the range from 396 to 416 atoms and the lower panel clusters in the range from 1000 to 1009 atoms. The black and blue lines are for a temperature of 300 K and 1200 K, respectively. The graphs are also shown on Figs. 9 and 10 in paper I.

respectively. The role of the temperature is seen to be rather limited, it does not increase the number of step sites significantly as one might expect. However, the temperature seem to smear out some of the dependence on the number of atoms. This is especially clear for the larger particles in the lower panel of Fig. 4.2.

Another interesting thing to note is that at 300 K many of the numbers are nearly integers, which indicates that the results are dominated by a single structure in the ensemble, the ground state. However, at 1200 K this domination is, as expected, significantly smaller, and many non-integer values are seen.

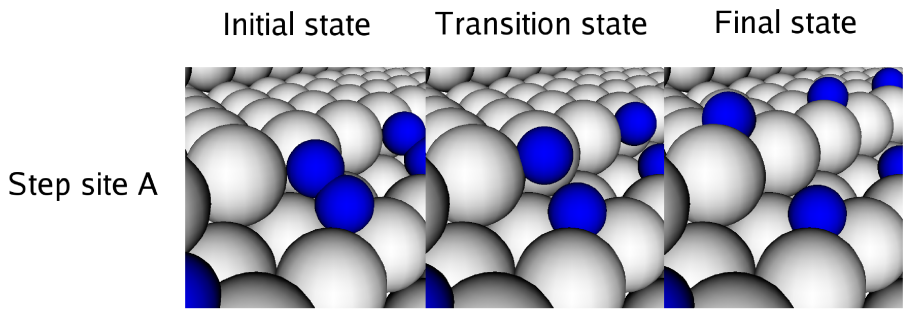

Figure 4.3: The initial, final and transition state configuration for the dissociation of N_2 on step site A, which is defined on Fig. 4.1. Similar plots for all 4 step sites is shown on Fig. 12 in paper I.

4.2.2 The barrier for N_2 dissociation

The purpose of calculating the detailed structure of the nano-particles is to apply it to estimate the catalytic activity of them. In order to do that it is necessary to also find the catalytic activity of the different sites, which are present on the particle and which will provide a significant contribution to the total activity. As an example of that I will consider the ammonia synthesis, which has the dissociation of the Nitrogen molecule as the rate limiting step[15, 55]. Step sites are known to be the most catalytic active for this reaction, as I explained in Sec. 4.1, so here I will only consider the four step sites given in that section.

I will only make a very simple estimate of the ammonia synthesis rate, which is based solely on the barrier for Nitrogen dissociation.

$$r = A \cdot \exp\left(-\frac{E_a}{k_B T}\right), \tag{4.1}$$

where k_B is the Boltzmann constant, T is the temperature and A is the prefactor, which depends on the equilibrium constants of the other reaction steps and the gas pressures. However, as I will only consider qualitative trends I will assume that the prefactor is the same on all the sites. A quantitative analysis would require a much more involved analysis such as the one done by Logadóttir et al.[73] for the B_5-site (step site B here). E_a is the barrier height with respect to the gas phase level. This is done because the adsorbed molecular state is in equilibrium with the gas phase at experimentally relevant gas pressures and temperatures.[73]

The barriers, E_a, are calculated using the DFT code DACAPO by finding the configurations of adsorbed Nitrogen and dissociated Nitrogen, ie. the initial and final configurations on Fig. 4.3, which shows the situation for step site A. These configurations are found by fixing the positions of the surface atoms while making local minimizations of the Nitrogen atom positions. It should be noted that the initial position is not the preferred configuration of an adsorbed Nitrogen molecule, which would be the molecule standing on-top of

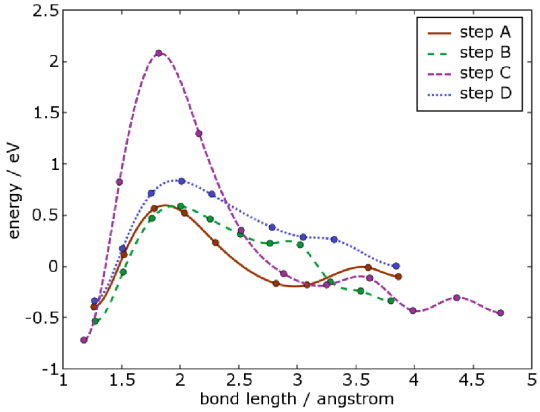

Figure 4.4: The energy as a function of the N_2 bond length for the four step sites of Fig. 4.1. Dots correspond to a DFT calculation. The lines are cubic splines connecting the dots. The figure is the same as Fig. 13 in paper I.

the surface atom. However, the barrier for rotating the molecule down is smaller than the barrier for dissociation[73, 78], so it is reasonable to use that as the starting points. The paths between the initial states and the final states are found by minimizing the position of the molecule for a number of different fixed bond lengths of the molecule. This gives the energy as a function of the bond length, which is shown on Fig. 4.4 for the four step sites. The energy barriers can then directly be extracted from these data and inserted in Eq. (4.1).

4.2.3 Catalytic activity vs cluster size

With values for the single site activities and the number of sites on a cluster it is straightforward to multiply these and get the total activity of the cluster. I have calculated the presence of step sites on a large number of particles in the diameter range from 2 nm to 5 nm, and displayed the results on Fig. 4.5. Each point is an average of approximately 60 clusters. The error bars indicate the range of cluster sizes and the standard deviations of the results obtained from the 60 clusters in the x and y directions, respectively. The results show that the relation between cluster size and the number of step sites is rather complex, and very different for the four different types of sites. The presence of step sites A and B is significantly lower than the presence of step site C and D, and their trend is also less smooth. Step site C shows a decreasing density as the particles gets larger in the considered range, whereas step site D shows a clear maximum.

By combining the data from Fig. 4.5 with the single site activities obtained from Eq. (4.1) one gets the relation between catalytic activity pr volume catalyst as a function of particle size, which is shown on Fig. 4.6. Very interestingly this indicates an optimal size for the Ruthenium particles with respect to the ammonia synthesis at a diameter of

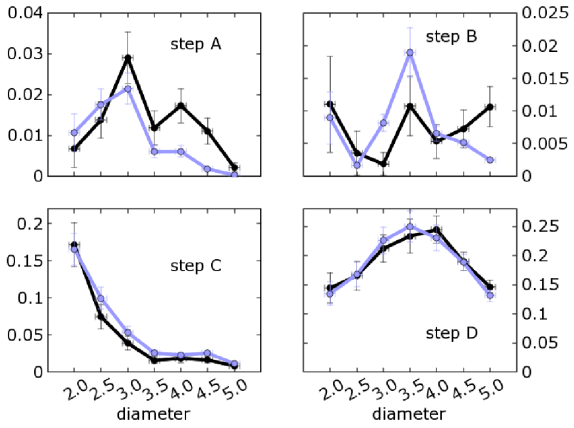

Figure 4.5: The number of step sites pr volume as a function of the cluster diameter for the 4 steps sites on Fig. 4.1. The unit on the y-axes is nm^{-3}. Each point is an average of approximately 60 cluster calculations. The error bars indicate the size distribution of the 60 particles and and the standard deviation of the obtained number of sites on the x- and y- axes, respectively. The black and blue lines are for 300 K and 1200 K, respectively. The figure is the same as Fig. 11 in paper I.

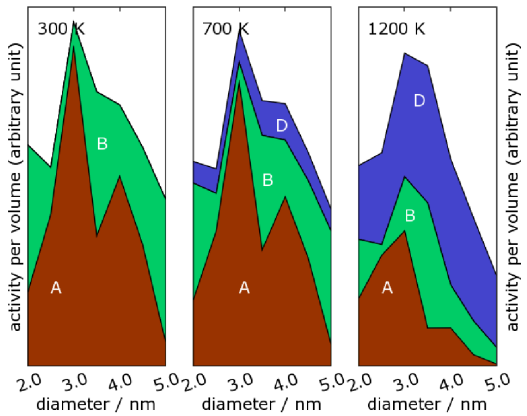

Figure 4.6: Ammonia synthesis activity pr volume Ruthenium as a function of the particle diameter at 300 K, 700 K and 1200 K. The different colors indicate the contributions from the different step sites of Fig. 4.1. The figure is the same as Fig. 14 in paper I.

3 nm. This maximum is rather constant as the temperature is varied. These results are consistent with experimental findings, which show the catalytic activity can increase when very small particles are sintered together.[57]

Another interesting observation is that several types of sites give significant contributions to the activity. Step site C is irrelevant due to the high dissociation barrier there,

but the barriers for step site A and B are so close that they both contribute significantly. At higher temperatures step site D also becomes important due to the higher presence of that site. Naturally, the barrier height difference gets less important as the temperature is raised.

4.3 Substrate effects

In Sec. 3.6 I decribed a simple approach to including the effect of an substrate when calculating the structure of a particle. I have implemented this approach under the assumption that the close-packed (001) facets are parallel to the substrate. Figure 4.7 shows the found ground state structures for a 500 atoms Ruthenium cluster at a range of different adhesion energies. As one would expect the particle is seen to get flatter as the adhesion energy is increased. These preliminary calculations do not indicate that the substrate has a huge impact on the absolut number of step sites present on the particles. However, due to limited time it has not been possible to make calculations on a larger number of particles. This is necessary in order to see how the substrate influences the relation between the particle size and the number of sites. It would be especially interesting to see if the optimal particle diameter is changed.

4.4 Ru-particles with presence of CO gas

In Sec. 3.7 I described an approach to including the effect of a gas on the structure of the particles. In this section I will consider the example of Ruthenium particles in the presence of carbonmonooxide (CO). First I will describe how the adsorption energies and vibrational frequencies are calculated. Then I will apply these values to obtain the coverage of CO as a function of temperature and pressure. Unfortunately, due to limited time it was not possible to calculate ensembles of structures with the inclusion of gas effects. However, the results will indicate that the presence of a CO gas could have a large impact on the number of step sites.

4.4.1 Adsorption energies and vibrational frequencies

The adsorption energy and the vibrational frequencies of the adsorbed molecule have to be calculated for each type of site present on the surface, as shown in Sec. 3.7. I have performed calculations for the 9 types of sites shown on Fig. 4.8. The calculations are all performed on surfaces which consist of periodic repetitions of the site in question. For simplicity I will assume that the CO molecules do not dissociate, ie. they will only be molecularly adsorbed. In all cases the molecule prefer to sit on-top with the Carbon atom pointing downwards. Matters are complicated by the fact that the adsorption energy depends on the coverage of molecule, ie. in principle the calculations should be performed for a range of different coverages. However, for simplicity I assume a coverage of $\frac{1}{2}$ for most sites. Preliminary calculations revealed that a coverage of 1 is not attainable for at least the flat surface sites, so I will just assume a maximum coverage of $\frac{1}{2}$. One exception

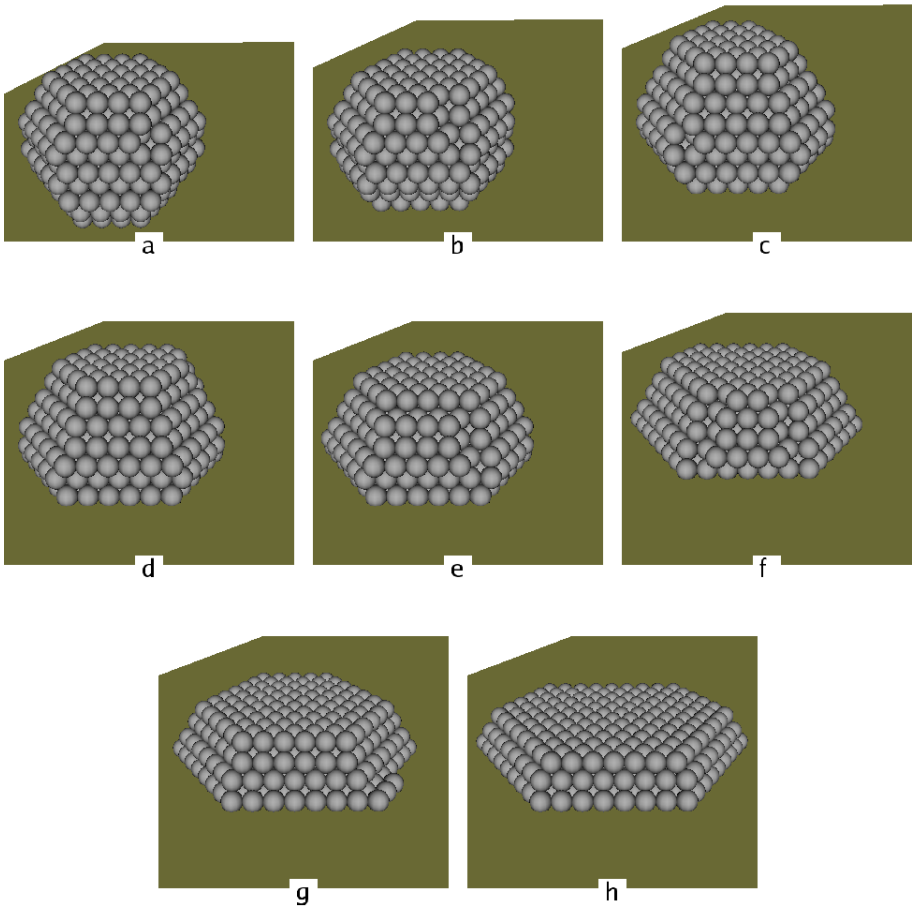

Figure 4.7: The found ground state structure for a 500 atoms Ruthenium cluster at different adhesion energies with the substrate. Panel a-h are for adhesion energies of 0.0, 0.3, 0.6, 0.9, 1.2, 1.5, 1.8, 2.1 eV/atom, respectively.

is the (011) surface, where a coverage of $\frac{1}{2}$ is also not attainable, so here I consider a coverage of $\frac{1}{4}$. The second exception is the corner site, where the calculation can only be performed for a coverage of 1.

All calculations have been made with the DACAPO code. The calculational details are given in Sec. 2.6.1. The adsorption configuration is found by minimizing the energy with respect to the positions of the atoms in the molecule and the top layer of the surfaces. The vibrational frequencies are then easily found by an ordinary normal mode analysis.[30]

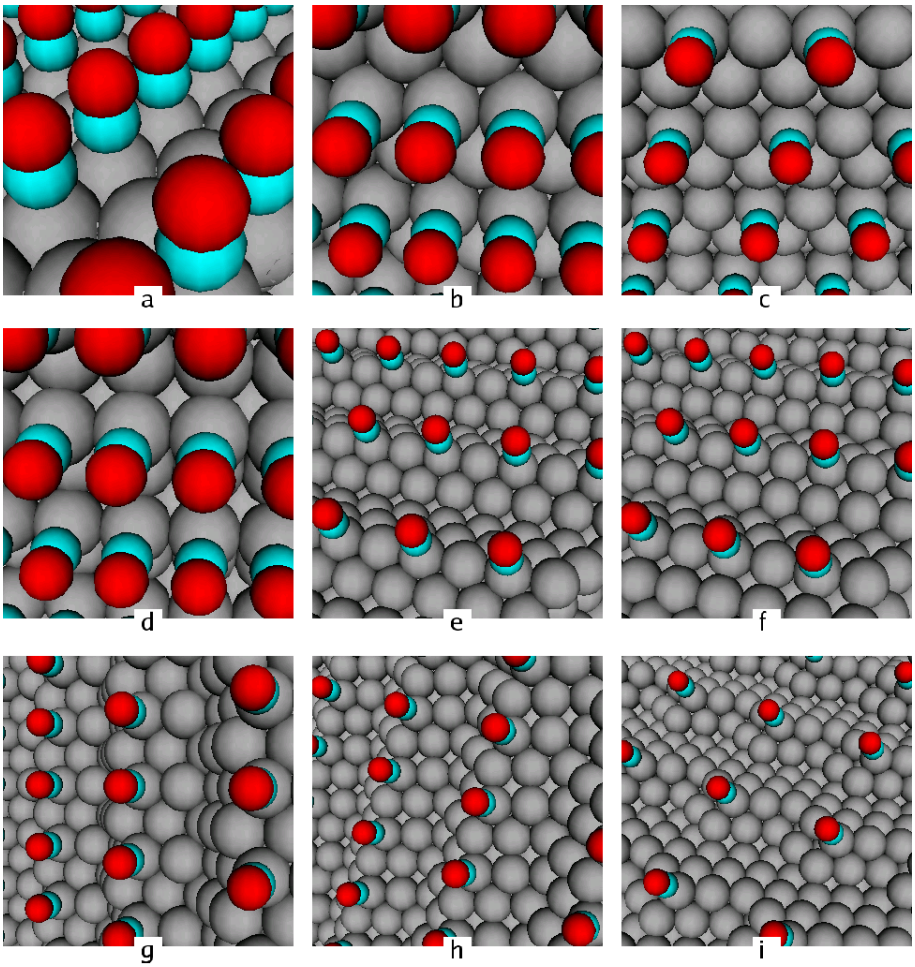

Figure 4.8: The unit cells used to calculate the adsorption energies and vibrational frequencies of CO on 9 different Ruthenium surface sites: Panel a: (001), panel b: (100)A, panel c: (011), panel d: (100)B, panel e: Edge site A, panel f: Edge site B, panel g: Edge site C, panel h: Edge site D and panel i: corner site. Blue and red atoms are Carbon and Oxygen, respectively.

4.4.2 CO coverage

When the adsorption energies and vibrational frequencies are known, the coverage can be calculated as described in Sec. 3.7.2. Figure 4.9 shows the coverage as a function of temperature and pressure for the 9 different sites in Fig. 4.8. The graphs clearly show that it is harder to remove CO from the edge sites compared to the flat surface sites. This is a reflection of the fact that CO binds stronger to the edge sites.

Figure 4.10 shows the correction, $\theta_{i,gas} \cdot F_{i,binding}$, to the site energy in Eq. (3.8) as a function of the temperature. It is seen that as long as there is CO present on the particle

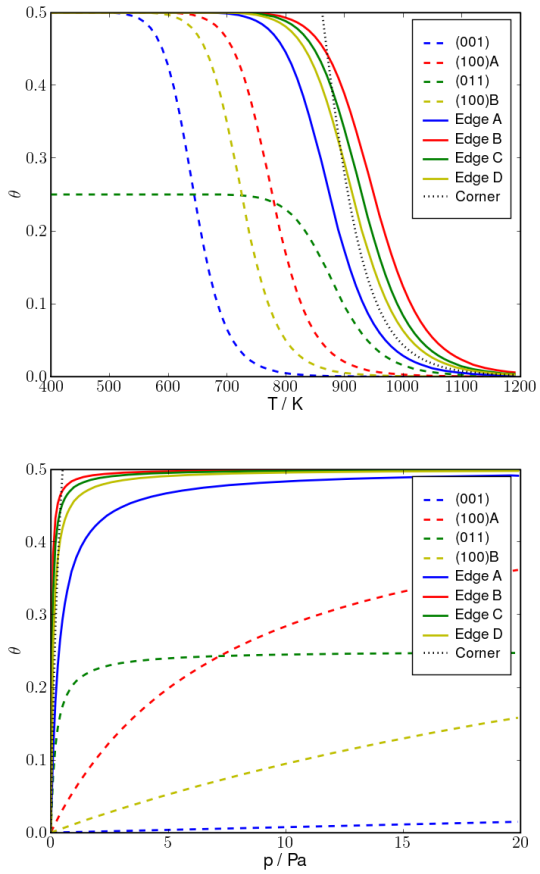

Figure 4.9: The coverage of CO, $\theta_{i,gas}$, on the 9 different surface sites of Fig. 4.8. Upper panel: As a function of temperature at a CO gas pressure of 100 Pa. Lower panel: As a function of CO gas pressure at a temperature of 700 K.

the correction term will be larger for edge sites compared to flat surface sites, which means that edge sites are promoted under the presence of CO gas. Since steps consist of two rows of edges this means that the gas most likely will increase the number of step sites. The difference in the correction term is on the order of 0.1-0.2 eV, which is high compared to the thermal energy at most temperatures, so the effect will probably be significant.

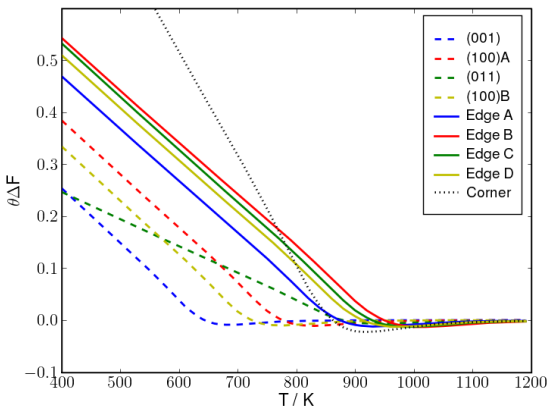

Figure 4.10: The correction, $\theta_{i,gas} \cdot F_{i,binding}$, to the site energy in Eq. (3.8) as a function of the temperature for the 9 different surface sites of Fig. 4.8.

Chapter 5

Hot electron femto-chemistry at surfaces

In the description of many catalytic reactions it has proven to be a good approximation to separate the electronic and nuclear motion, because the electronic relaxation often will happen on a shorter timescale than the motion of the nuclei. This means that it is possible to describe the nuclei motion from the ground state potential energy surfaces, which are significantly easier to calculate than it is to solve the full quantum mechanical problem with both nuclei and electrons. This is known as the Born-Oppenheimer approximation. However, there are situation where this approximation breaks down. Either because the nuclei motion is very fast or because excited electrons are present in the system.

In this chapter I consider the problem of describing catalytic processes under the influence of deliberately created high-energy electrons, ie. hot electrons. Throughout the chapter I will focus on systems with diatomic molecules on transition metal surfaces, but the model and some of the results are more generally applicable. I start out by considering the experimental ways of exciting electrons in Sec. 5.1. Then in Sec. 5.2 I will describe how excited electrons can influence the rate of catalytic reaction and some ways of estimating these rates. It turns out that potential energy surfaces (PES) are still very helpful. However, it is not sufficient to know the ground state PES, but also the PES's of molecular resonances. In Sec. 5.3 I consider the calculation of such PES's and the features they reveal. The PES's will in Sec. 5.4 be applied to estimate desorption rates. Finally I will give an outlook with some of the perspectives of this field. All density functional calculations presented in this chapter have been made with the GPAW code, with the parameters given in Sec. 2.6.2.

5.1 Creating hot electrons

In order to have excited electrons present, which can influence the catalytic process, it is of course necessary to create them. In this section I will describe two different approaches to doing this and some of the properties of the excited electrons in each. First I consider excitation with the use of laser light in Sec. 5.1.1. In Sec. 5.1.2 I will describe how the

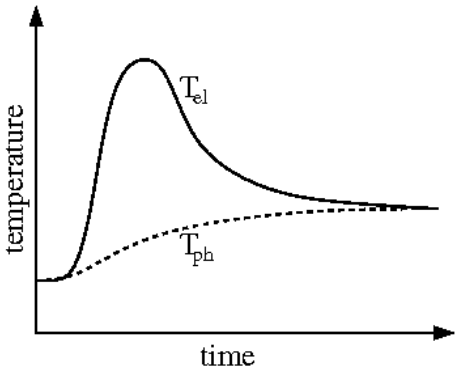

Figure 5.1: Electron temperature, T_{el}, and phonon temperature, T_{ph} in a metallic surface after a femtosecond laser pulse hits it. The electron temperature quickly becomes very high, on a femtosecond timescale. The equilibration of the electron and phonon temperatures happen on a picosecond timescale.

electrons can be created by applying a bias to a three layer junction.

5.1.1 Femtosecond laser pulses

The by far most applied approach to generating hot electrons is the use of femtosecond pulsed laser[8, 11, 14, 29, 56, 76, 87, 88, 96], which is capable of generating very high intensity, but very short, pulses of light. When such a pulse hits a metal surface it will excite a large number of electrons. Because of the very high density of excited electrons, the electron-electron scattering length will be very short, which results in a very rapid thermalization of the hot electrons.[31] However, it takes significantly longer for the electrons and phonons to equilibriate, ie. for approximately a picosecond the electronic temperature will be much higher than the phonon temperature as illustrated on Fig. 5.1. The electronic temperature can be much higher than the melting temperature of the metal. At these high temperatures one may have a lot of electrons, which can interact with some molecular resonance as shown on Fig. 5.2. This interaction can lead to extra motion of the nuclei in the molecule, such that a catalytic process may be initiated.

The advantage of generating the electron in this way is that it gives a high density of excited electrons, which means that the possibility of them making a significant influence on the catalytic rate is high. The disadvantage, however, is that it does not leave the possibility of targeting any desired molecular resonance. The thermalization of the electrons means that the lower lying molecular resonances always will be influenced by a higher number of excited electrons than the higher lying resonances.

5.1.2 MIM/MOS devices

A very different approach to creating excited electrons was proposed by Gadzuk in 1996[34]. His idea was to make a three layered Metal-Insulater-Metal (MIM) junction as depicted

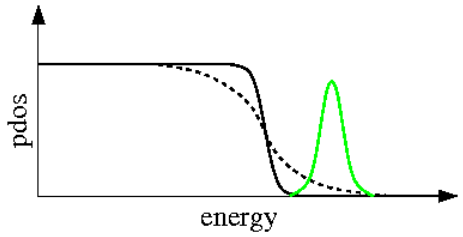

Figure 5.2: The black and dotted lines illustrate the Fermi distribution of the electrons at a low and high temperature, respectively. The green line illustrate a molecular resonance. At a high electron temperature some of the electrons have an energy, which matches the energy of the resonance.

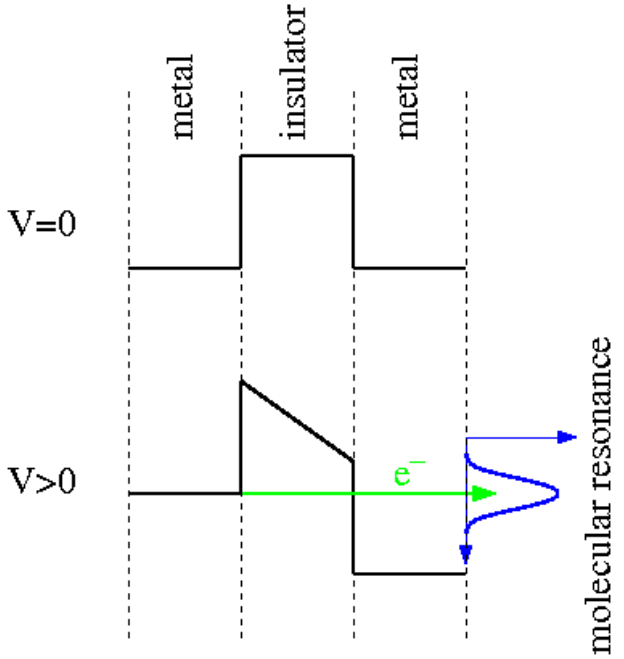

Figure 5.3: The energy bands in a metal-insulator-metal (MIM) device. The lines in the metals indicate the Fermi levels and the line in the insulator indicates the position of the first valence band. The insulator band gap constitutes a barrier for the electrons. At finite bias the Fermi levels of the metals are shifted with respect to each other and an electron tunneling through the insulator will have an energy above the Fermi level in the other metal. This electron may reach the surface of the metal and interact with a molecular resonance at the surface.

on Fig. 5.3. The top panel sketches the potential energy through the junction. The barrier arrises because of the large band gap of the insulator. The lower panel illustrates

the situation, when a finite bias has been applied over the junction. Due to the bias, an electrical field builds up in the insulator, which causes a difference in the Fermi energy of the two metals. If the insulating layer is sufficiently thin, electrons will be able to tunnel from the left metal to the right, where the electrons will have an energy above the Fermi level, ie. they will be hot. The electrons may reach the surface of the right metal without scattering, if the metal layer is also made very thin. At the surface the electrons can interact with a resonance of an adsorbed molecule.

The advantage of generating excited electrons in this manner is the great, at least theoretically, possibility of controlling the energy of the excited electrons. In principle it should be possible to target the energy of any molecular resonance simply by changing the applied bias. The disadvantage, however, is that it will not be possible to generate a high density of hot electrons, which means that for many systems the effect of the hot electrons will probably be insignificant.

Even though this device was suggested back in 1996, there has not been many attempts of realizing it. However, recently Thomsen et al[97] have made a Metal-Oxide-Semiconductor (MOS) device, which comprise a promising candidate for future femto-chemistry experiments. In this device the left metal of Fig. 5.3 has been replaced with highly doped Silicon for technical reasons. The insulating layer is oxidized Silicon.

5.2 Inducing chemistry

In this section I will describe the mechanisms that lead to nuclei motion in an adsorbed molecule, and possibly a catalytic reaction, from the presence of excited electrons in the surface. I will start in section 5.2.1 by giving a classical picture, where nuclei motion is treated using classical mechanics. Eventhough I later will argue that in many cases the motion of the nuclei cannot be treated classically, the picture is still benefical, since it provides an intuitive understanding of the mechanisms involved. In section 5.2.2 I will consider a more involved quantum mechanical approach, which is expected to provide more reliable results. Throughout this section I will focus on desorption induced by hot electrons, since it is the type of reaction, which has been seen in most femtochemistry experiments[11, 14, 29, 56, 76, 87, 88, 96]. However, the concepts presented are generally applicable, such that for example dissociation induced by hot electrons can be described in the same manner.

5.2.1 Classical picture

As mentioned in the beginning of this chapter, the motion of nuclei can in many different catalytic reactions be described by the ground state potential energy surface of the nuclei. By ground state I mean with respect to the electronic degree of freedom, ie. the electronic system is assumed to relaxed at all times. Naturally, this is a bad approximation when considering systems with excited electrons. However, one approach to including the electronic effects is to have several PESs and then include the electronic effects as shifts between the different PESs. In the following I will describe how this approach can be used to understand both single electron and multiple electron processes.

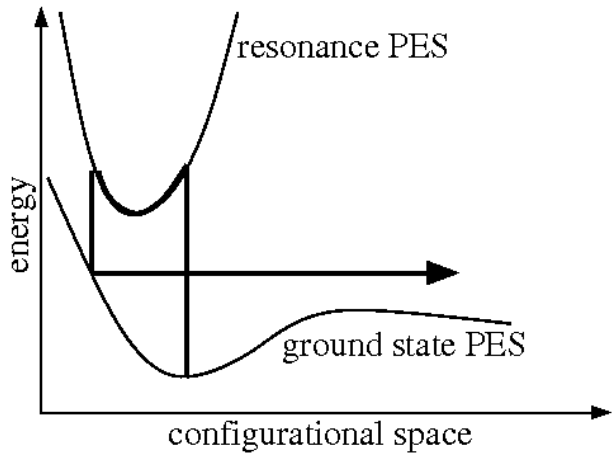

Figure 5.4: Desorption induced by electron transitions (DIET). The system sits in the ground state as an electron hits the resonance, which causes molecular motion due to the shifted minimum of the resonance PES. When the electron leaves the resonance the molecule may have enough energy to pass the desorption barrier.

DIET mechanism

Desorption induced by electronic transitions (DIET) was observed experimentally already in 1988 by Buntin et al[12] who observed the desorption of NO from a Platinum (111) surface. In 1989 the same authors proposed an explanation of the mechanism behind.[13] The picture consists of two PESs as illustrated on Fig. 5.4, where the first PES is the energy of the system with relaxed electrons (ground state) as a function of nuclei position and the second PES is the energy of the system when the adsorbed molecule is electronically excited. To start with the whole system is relaxed, ie. it sits at the bottom of the ground state PES. At some point a hot electron may excite the adsorbed molecule such that the system jumps to the excited PES, where it is not located at the minimum, ie. the nuclei will start to move. The nuclei may move to a different part of the PES before the excitation of the molecule decays and the system is brought back to the ground state PES. This may be at a point where the energy is quite high, above the desorption energy, such that the molecule can desorb from the surface.

DIMET mechanism

Figure 5.4 illustrates a situation where a single hot electron causes a desorption event. In some cases, however, it may require several electrons in order to get desorption as it was observed by Misewich et al[75] in 1992. This is known as desorption induced by multiple electronic transitions (DIMET) and is illustrated on Fig. 5.5 As seen the mechanism is very similar to the DIET mechanism except from the fact that the molecule is excited several times in the DIMET mechanism. Experimentally the DIMET mechanism is distinguished from the DIET mechanism by varying the intensity of the applied laser

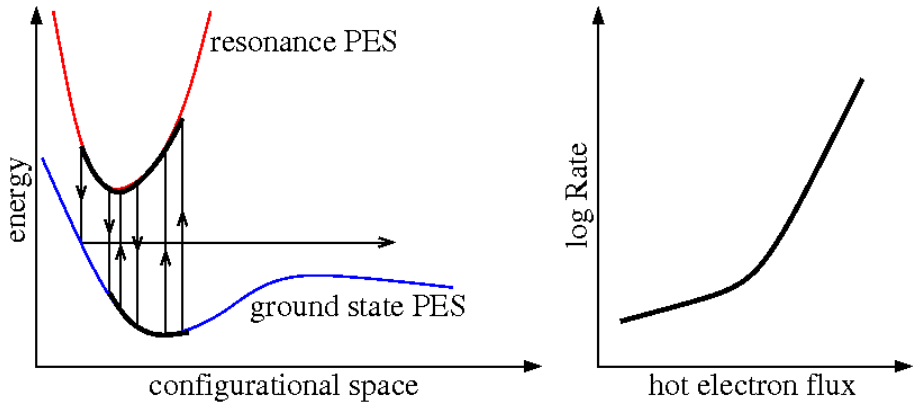

Figure 5.5: Left panel: Desorption induced by multiple electronic transitions (DIMET). Electrons will hit and leave the resonance several times before the molecule has enough energy to pass the desorption barrier. Right panel: Experimental observations of the DIET and DIMET regimes. At low hot electron fluxes single electron processes dominate and the desorption rate is proportional to the flux. At high fluxes multiple electron processes dominate and the desorption rate becomes proportional to the rate to a higher power.

light, ie. the number of generated hot electrons. In case of a dominating DIET mechanism the desorption rate will be proportional to the light intensity. With a dominating DIMET mechanism the desorption rate will follow a power-law dependence to the intensity, the higher number of electrons needed to desorb a molecule the higher the power will be. This is also illustrated on Fig. 5.5.

5.2.2 Quantum description

In Paper III we argue that it is not reasonable to treat the nuclei motion classically in the type of systems we consider here, because the molecular resonances are quite shortlived, approximately 1 fs. We base this on an approximative evaluation of the action, $S = \int dt L(\dot{x}(t), x(t))$, on a classical trajectory of 1 fs in a quadratic potential with a frequency and initial potential energy, which fit calculated values. Here we find that $|S| \approx \hbar$, where the classical limit corresponds to $|S| \gg \hbar$.

Instead of treating the nuclear motion classically we then consider a Newns-Anderson[1, 80] type Hamiltonian to treat the interaction of the resonant state with the substrate states. This is inspired by the work of Jacobsen et al[105] and Gadzuk.[32] However, as they only consider a 1-dimensional system, we extend their approach to 2 dimensions in Paper III, which enables us to consider for example both the internal stretch and the distance to the surface of a diatomic molecule. Paper III provides a detailed description of the model, so here I will only discuss the basic assumptions and some of the properties of the model.

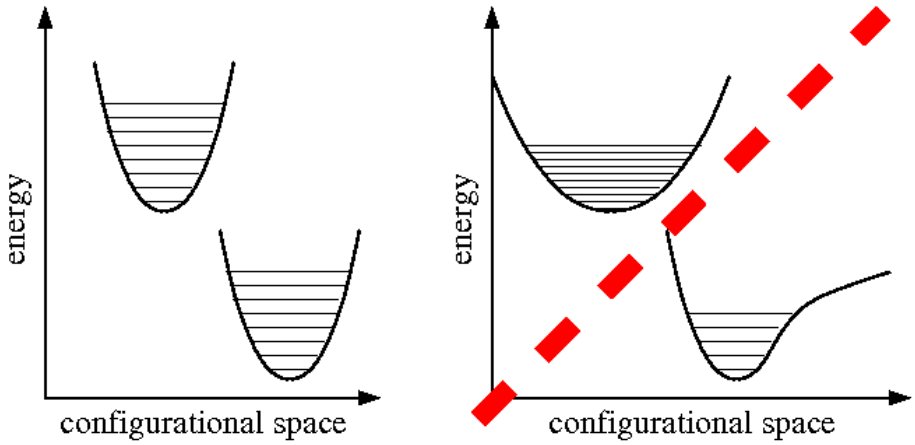

Figure 5.6: Illustration of the assumption made by the quantum model of Sec. 5.2.2. Left panel: The ground state and resonance PESs are assumed to be quadratic with the same vibrational frequencies. Right panel: The more general situation of non-quadratic PESs with different frequencies cannot be handled in the model.

Assumptions

The important outcome of the model is that it enables us to estimate the probability, $P_{n_i,n_j}(\epsilon_i)$, that an electron with a certain energy, ϵ_i, will scatter of the molecule and excite the (n_i, n_j) vibrational mode of the 2-dimensional system, ie. that it transfers an energy of $\hbar\omega_i n_i + \hbar\omega_j n_j$ into vibrational energy. However, the evaluation of this model requires some rather strict assumptions about the system. First of all the system is assumed to be in the wide band limit, which means that the couplings between substrate states and the molecular state is slow varying in energy and that the density of states is constant in the vicinity of the resonance. This assumption is simply wrong, so one can only hope the important physics is still captured and that a comparative test of the results of this model will justify this assumption. Secondly it is assumed that the ground state PES and the resonance PES are quadratic and only differ by a translation in configurational space, ie. with the same vibrational frequencies. This is illustrated on Fig. 5.6. In Sec. 5.3 I will show through an example that this may be a reasonable assumption for the type of systems considered here.

Input

Several parameters are needed in order to calculate $P_{n_i,n_j}(\epsilon_i)$ for a given system in this model. First of all there are the vibrational frequencies, ω_i and ω_j, of the different normal modes, which gives the possible transfers of energy, $\hbar\omega_i n_i + \hbar\omega_j n_j$. Secondly one needs the slopes of the resonance PES in the directions of the normal modes, which gives the coupling between the electrons and the molecular vibrational modes. This is the only part of the excited state PES needed, because the model assumes that the ground state PES

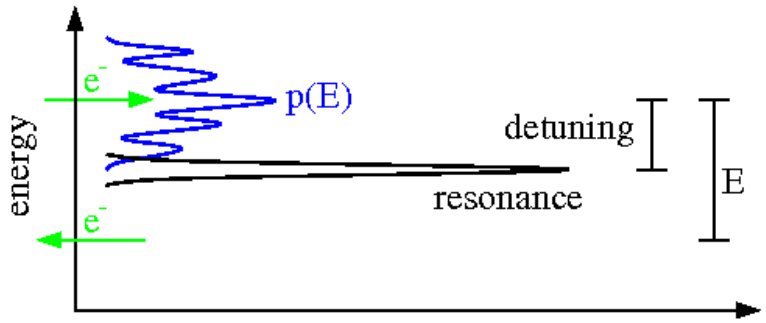

Figure 5.7: The optimal energy of a hot electron with respect to the probability, $p(E)$, of the electron delivering an energy, E, to the molecule is detuned with repect to the position of the resonance. The detuning is approximately $\frac{1}{2}E$. The multiple peaked features in $p(E)$ is only observed for small resonance widths.

and resonance PES have the same shape. Finally one needs the energy, ϵ_a, and width, Γ, of the resonance.

Properties

One of the interesting properties of the model is the detuning effect, which seen from Fig. 2 in Paper III and also illustrated on Fig. 5.7. The detuning effect means that the probability of an electron delivering an energy of E to the molecule is highest, when the electron has an energy above the center of the resonance. The optimal energy lies approximately $\frac{1}{2}E$ above the resonance energy. Physically this can be understood by realizing that the electron not only must excite the molecule at an energy of ϵ_i, but it must also be able to leave the molecule at an energy ϵ_f. Since $\epsilon_i - \epsilon_f = E$, the optimal trade-off can be found at $\epsilon_i = \epsilon_a + \frac{1}{2}E$. Examples of the size of the detuning effect for different systems are listed in Tables III and IV in Paper III.

Another interesting effect is the peaked feature of the probability, $p(E)$, which is also illustrated on Fig. 5.7. This feature is only seen for small resonance widths. For large resonance widths the sidebands become washed out and the probability distribution takes the form of a Lorentzian. Both cases are illustrated on Fig. 2 in Paper III.

Coupling DIET and DIMET regimes

It is quite straightforward to treat the DIET regime in this model, if we assume that a molecule will desorb as soon as it has a vibrational energy above the desorption. For small molecules this is probably a quite reasonable assumption, since the vibrational decay time is in the order of picoseconds, whereas the vibrations are on a femtosecond timescale, ie. the molecule will vibrate back and forth many times before losing the vibrational energy. The DIET regime is then treated by finding the probability that the electron will transfer an energy above the desorption energy to the molecule: $\epsilon_i - \epsilon_f > E_{des}$. The rate of

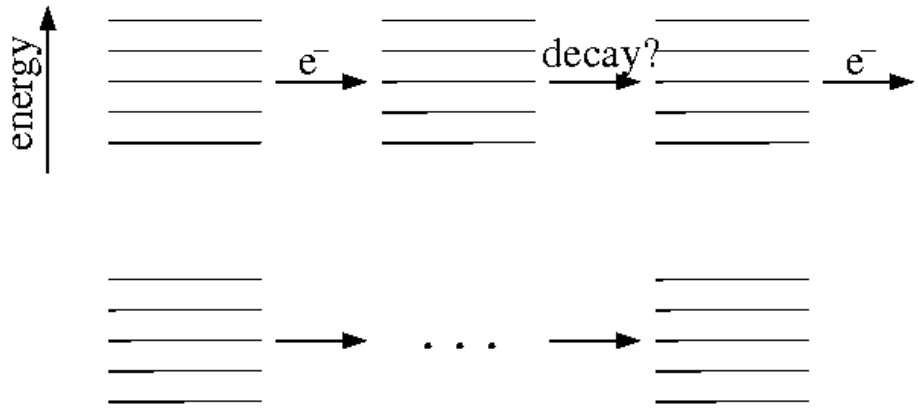

Figure 5.8: Including multiple electron processes in the model. The 5 thin lines indicate the 5 vibrational states up to desorption of the molecule. The thick black lines indicate the probability distribution of the vibrational states. First the system is in the ground state. Then an electron hits resonance, which changes the probability distribution. Then some time passes where the vibrations may decay. Then another electron hits. This is continued until the probability of an electron desorbing the molecule is constant, such that the desorption rate can be calculated.

desorption is simply the flux of hot electrons times this probability.

A simple way of including the DIMET regime, where hot electrons hits the molecule at equally spaced timeintervals, Δt, is illustrated on Fig. 5.8. The probability of the molecule sitting in the lowest vibrational state is unity in the beginning. Then the first hot electron hits the molecule, which spreads the probability distribution of the vibrational state of the molecule. The vibrational excitations will decay before the next electrons comes with a probability of $1 - e^{-\Delta t/T_{vib}}$, where T_{vib} is the vibrational decay time, which again changes the probability distribution. Then the second electron comes, which gives a new probability distribution, where the probability of each vibrational state is found as a sum of all the probabilities times the probability that the electron will cause a shift to that vibrational state. This is continued until the probability distribution has converged. In each step all probabilities at vibrational states above the desorption energy are removed. From the converged probability distribution the probability of an electron changing the vibrational state to something above the desorption energy can then be calculated. The desorption rate is then this probability times the electron flux.

5.3 Potential energy surfaces

For the classical as well as the quantum description approaches described in Sec. 5.2 it is necessary to have some information about the resonance PES and the ground state PES. Because of the difficulty involved when trying to calculate the resonance PES most results so far have been based on model potentials[32, 33, 35, 36, 46, 94]. In this section I will

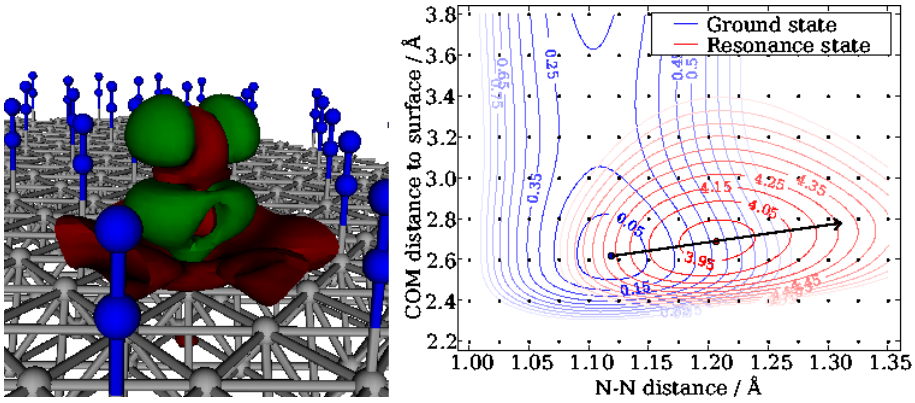

Figure 5.9: Linear expansion ΔSCF calculation on the $2\pi^*$-resonance in a Nitrogen molecule on a Ruthenium (001) surface. Left panel: The change in electron density upon excitation of the molecule. The green and red contour surfaces indicate higher and lower density, respectively. The density change is just shown within one unit cell, whereas the atomic positions have been repeated. Right panel: The ground state and resonance PESs as a function of the center of mass (COM) distance to the surface and the inter-atomic bond length in the Nitrogen molecule. The dots show where actual calculations have been performed. The black arrow indicates a possible classical trajectory of the system on the resonance PES. These illustrations can also be found on Figs. 2 and 5 in paper II.

start by giving an example of a resonance PES calculated using the method of Sec. 2.3.2 and paper II. Afterwards I will comment on the expected accuracy of these.

5.3.1 PESs for N_2 on Ru (001)

In Paper II we calculated a 2-dimensional cut of the ground state PES and 2π-resonance PES for N_2 on a Ruthenium (001) surface. The molecule sits vertically on a top site, and the two dimensions are the interatomic distance in the molecule and the center of mass distance to the surface. These dimensions are the most important, because the gradient of the resonance PES for symmetry reasons must be zero in the other directions, ie. the direct electron couplings to vibrations in the other directions are zero. The results are also shown on Fig. 5.9.

One interesting feature of the PESs is that the minimum of the resonance PES lies further from the surface than the ground state PES. This contradicts the traditional picture[13], where it is assumed that the excited, and hence charged, molecule will be attracted to the surface, because of the image charge effect. The increase in center of mass distance to the surface upon excitation can be explained by the fact that the resonance corresponds to an anti-bonding state in the molecule. This means that the molecular bond is weakened upon excitation such that the Nitrogen atoms will go further apart. The calculated PESs indicate that this effect is substantially larger than the image charge attraction. This is illustrated on Fig. 5.10.

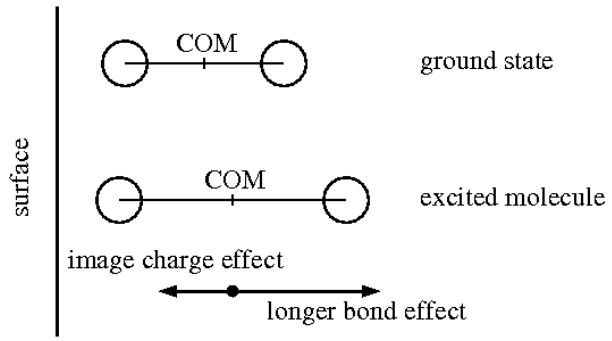

Figure 5.10: The center of mass (COM) of the molecule shifts outwards upon excitation as seen on Fig. 5.9. This is because the bond length increases significantly more than the molecule shifts inwards due to the image charge.

Table 5.1: The vibrational frequencies of N_2 on a Ru (001) surface in the ground state and in the resonance. The values have been obtained from the PESs of Fig. 5.9.

	Ground state (eV)	Resonance (eV)
COM	0.13	0.22
N-N distance	1.69	1.45

Another thing that can be extracted from the PESs of Fig. 5.9 are the vibrational frequencies of the minima. These are given in Table 5.1. As seen from the table the frequencies with respect to the N-N distance are quite close. As we show in Paper III this is the by far most important vibrational mode with respect to transferring energy into vibrational motion. This indicates that the approximation of Sec. 5.2.2 that the vibrational frequencies of the ground state and resonance minima are equal is reasonable for this type of system. The center of mass (COM) vibrational modes deviate somewhat, but they are still within a factor 2 of each other.

5.3.2 Validation

Even though the linear expansion ΔSCF method intuitively seems reasonable it lacks fundamental justification and therefore requires justification through comparisons with experiments and higher accuracy methods. This is not straightforward for these excitation energies of molecules at metallic surfaces, since it is very hard to gain comparable data from experiments and since it is a very difficult to perform accurate calculations of resonance energies in periodic metallic systems. The best experimental estimations of the energy of molecular resonances at surfaces come from inverse photo-emission spectroscopy (IPES)[61, 89, 90, 92], where electrons are send towards the system in question, ie. a surface with a specific molecule adsorbed on it. The electrons will place themselves in states at the surface while emitting a photon to compensate for the loss of energy. By measuring

Table 5.2: Comparison of the $2\pi^*$ resonance energies for different diatomic molecules on different surfaces found by spatially constrained DFT, ordinary ΔSCF, linear expansion ΔSCF and experiments. The experimental results have been obtained from inverse-photoemission spectroscopy (IPES) measurements: [a]Johnson and Hulbert[61], [b]Reimer et al[89], [c]Reimer et al[90], [d]Rogozik and Dose[92]. All energies are in eV. These results are also given in Table 1 in paper II.

System	Constrained DFT	ΔSCF (orig.)	ΔSCF (this work)	Experiment
N_2 on Ni(001)	2.2	3.5	4.0	4.4^a
CO on Ni(001)	2.2	3.2	4.2	$4.0^a/4.5^b$
NO on Ni(001)	2.2	0.6	1.4	$1.6^a/1.5^c$
CO on Ni(111)	2.8	4.3	4.4	4.4^c
NO on Ni(111)	2.7	0.5	1.4	1.5^b
CO on Pd(111)	4.6	4.1	4.9	4.7^d
CO on Pd step	2.8	3.2	4.5	4.0^d

the emitting photons one gets information on the amount energy the electrons looses and hence the energy of the states they get into. Such experiments are capable of revealing the presence of molecular resonances and their energy can also be estimated quite well. In Paper II we performed comparisons between the ΔSCF method and IPES experiments from the literature. The results are reproduced on Table 5.2. The table also compares the linear expansion ΔSCF results with results we obtain by applying the ordinary ΔSCF method and the constrained DFT method.[106, 107] The ordinary ΔSCF method corresponds to just forcing an electron into the Kohn-Sham orbital with the largest overlap with the molecular orbital in question. In the constrained DFT method one applies an extra fictive potential, which is varied until some constraint on the density is fulfilled. When calculating the energy one compensates for this fictive potential. This can be done in several ways. The results in the table are obtained by applying a step-like potential which goes down between the molecule and the surface, and varying the strength until an extra electron sits on the molecule. Se Paper II for further details. The results indicate that the linear expansion ΔSCF method works quite well, predictions are within 0.5 eV, which is much better than the two other methods.

The IPES measurements only estimates the resonance energy at the minimum of the ground state PES, ie. it does not provide any information on the shape of the resonance PES. In order to get an idea of the ability of the ΔSCF approach to getting the shape of excited state PESs correct we also perform some ΔSCF calculations on the Nitrogen molecule in Paper II. For molecules it is also possible to perform quite accurate linear response TDDFT (lrTDDFT) calculations. From Fig. 5.11 it is seen that the ΔSCF and lrTDDFT calculated PESs obtained by varying the N-N distance for different excitations in the molecule have very similar shapes, ie. the ΔSCF approach is seemingly capable of estimating the shapes of excited state PESs accurately. Especially interesting is that

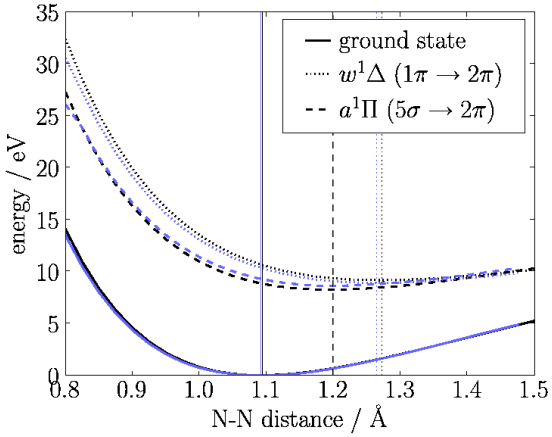

Figure 5.11: The ground state PES and two excited state PESs for the Nitrogen molecule. The black lines are obtained using the ΔSCF method and the blue lines are obtained using linear response TDDFT. The graphs are also shown on Fig. 6 in paper II.

the shifts of the minima are predicted very well. Whether or not these results can be transferred to the molecular resonance PESs at surfaces is still an open question.

5.4 Desorption of CO and NO on transition metal surfaces

By combining PESs calculated as in Sec. 5.3 with the model of Sec. 5.2.2 it is possible to calculate the probability of a hot electron transferring a certain amount of vibrational energy to the molecule. In paper III we did this for CO and NO on four different close-packed transition metal surfaces. Figure 5.12 shows the rate of a single hot electron transferring an energy, which is higher than 1.5 eV and 1.0 eV for CO and NO, respectively. The rates are plotted as a function of the resonance width. We assume that the electron flux is uniformly spread in energy with a value of 1 electron$\cdot eV^{-1} \cdot s^{-1}$. We treat the resonance width as an unknown parameter, since we can only get a rough estimate of it from the projected density of Kohn-Sham states.

The graphs on 5.12 reveal that the rates depend heavily on the resonance width. Another seen feature is that it is significantly easier to transfer energy to CO compared to NO. One should however keep in mind that in traditional femtochemistry experiments, where the hot electrons are generated using a femtosecond laser pulse, the density of hot electrons with an energy at the molecular resonance depends heavily on the energy of the resonance. This is due to the thermalization of the electrons as illustrated on Fig. 5.2. The molecular resonance for CO lies significantly higher than for NO, which can be seen on Table 5.2. This means that in otherwise comparable situations the flux of hot electrons with the right energy will be much lower for CO compared to NO.

A comparison of the different metals indicate that Platinum and Palladium provide the highest transfer of energy, whereas Rhenium and Ruthenium give much smaller transfer

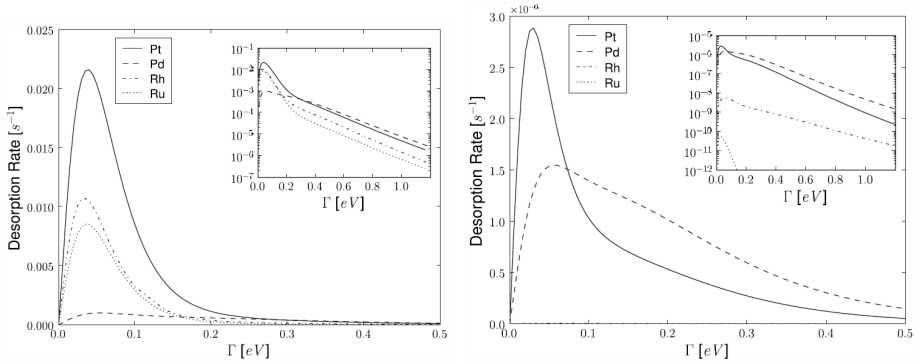

Figure 5.12: The rate of transferring a certain amount of energy to vibrations in a molecule on 4 different transition metal surfaces as a function of the resonance width. It is assumed that the electron flux is uniformly spread in energy with a value of 1 electron·$eV^{-1} \cdot s^{-1}$. Left panel: The rate of transferring at least 1.5 eV to the CO molecule. Right panel. The rate of transferring at least 1.0 eV to the NO molecule.

of energy, especially in the case of NO.

The rates of Fig. 5.12 cannot be compared directly to any experimental observations for several reasons. First of all is it very hard to estimate the electron flux in the experiments, where the hot electrons are generated from femtosecond laser pulses. Secondly it is not possible to detect how often a certain energy has been transferred to the molecule. However, it is possible to compare trends in the model to trends in experiments. Figure 5.13 shows the calculated trend for desorption of NO on a Pt(111) surface as a function of the hot electron flux. The different lines are for different energies of the hot electrons. Desorption is assumed to occur each time the vibrational energy of the molecule exceeds the desorption energy. This is not unreasonable, since the timescale of the molecule loosing its vibrational energy to the surface is much longer than the timescale of single vibrations. The resonance width is assumed to be 0.8 eV as estimated from the projected density of Kohn-Sham states. The experimental desorption energy of 1.29 eV[21] has been used. Multiple electron effects are accounted for as described in Sec. 5.2.2. For low hot electron fluxes the desorption rate is dominated by single electron events, so the rate is proportional to the flux (The DIET regime). At higher fluxes multiple electron events dominate and the rate becomes proportional to the flux to a higher power (The DIMET regime). The graph has a striking similarity to experimental observations[51]. This shows that the model at least is capable of qualitatively reproducing reality.

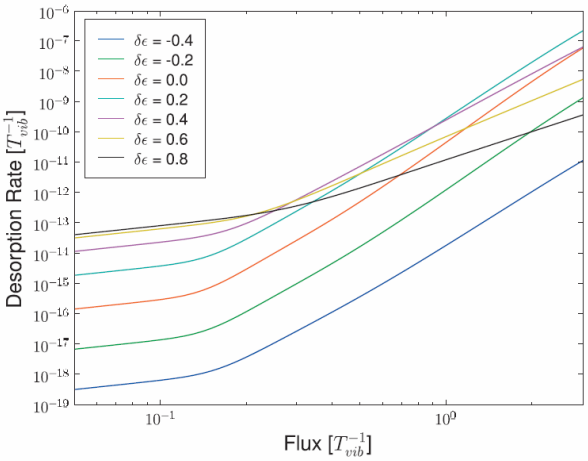

Figure 5.13: Desorption rate of NO on a Pt (111) surface as a function the hot electron flux for different hot electron energies ($\delta\epsilon$ is the detuning with respect to the position of the resonance). The model is seen to reproduce the shift between the DIET and DIMET regimes seen experimentally[51] very well.

Chapter 6

Studying molecular resonances with TDDFT

It is a very challenging task to build a model, which is capable of predicting the influence on the catalytic rate from hot electrons in a given system. There are several reasons for that. First of all there are a lot of detailed information, which is simply not possible to gain from experiments, which limits the possibility of comparing models with the real systems. In chapter 5 I for example show calculated energy surfaces of the resonance, where it is possible to compare the resonance energy with inverse photoemission spectroscopy (IPES) measurements, but where it is still very hard to validate the overall shape. Secondly models will often include parameters, which are very hard to calculate, such that crude estimates must be applied. In chapter 5 I for example discussed influence of the resonance lifetime, which we can only give crude estimates of.

One way of attacking these issues is to approach the same problem from different angles. This hopefully provides the possibility of comparisons, which can act as a sanity check of he achieved results. Furthermore it may be possible that the different approaches can supplement each other, ie. provide good estimates of parameters which cannot be estimated in the other model.

Time-dependent density functional theory (TDDFT) is a good alternative approach to model hot-electron femtochemistry, because it constitutes an exact framework to describing non-equilibrium processes. The price of course being that it is necessary to approximate a very complex exchange-correlation functional, which is non-local in both time and space. In this chapter I will describe the progress made in applying TDDFT to describing hot electron femtochemistry at surfaces. I start in Sec. 6.1 by presenting the basic idea. Then in Sec. 6.2 I will consider the issue of the hot electron being in some arbitrary unknown state. The different properties of the resonances, which can be estimated from this approach is the subject of Sec. 6.3. The system in mind in all presented calculations is a Nitrogen molecule adsorbed on a Ruthenium surface, but all the presented concepts are generally applicable. This chapter should be considered supplementary to Paper IV.

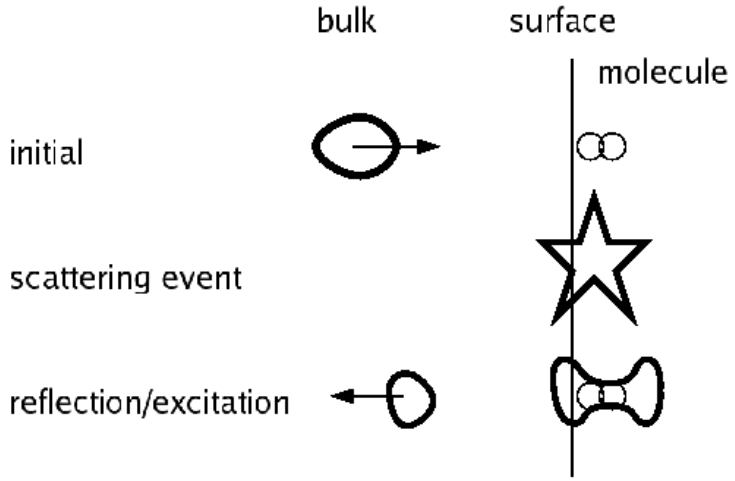

Figure 6.1: The basic approach to studying molecular resonance with TDDFT. A hot electron is placed inside the bulk material with a momentum towards the molecule at the surface. The hot electron position is then evolved over time until some point after it has scattered of the molecule/surface. This will result in some of the hot electron exciting the molecule and some of it being reflected.

6.1 The basic idea

TDDFT provides the possibility of simulating the time evolution of the electronic density, ie. it makes it possible to simulate the entire event of a hot electron coming from inside a surface and hitting an adsorbed molecule at the surface. This includes simulation of the electron scattering of the molecule or the electron going into a molecular resonance and the subsequent decay of the resonance. This is sketched on Fig. 6.1 On Fig. 6.2 I have applied this idea and show an example of how a hot electron orbital evolves over time, when it is send towards an adsorbed molecule.

In this case the surface is just included as a step like potential as illustrated on the left panel and the molecule is a Nitrogen molecule standing vertical on the surface. The starting orbital of the hot electron is made by taking a random un-occupied Kohn-Sham state and multiply it with a complex exponential factor to give it the momentum towards the surface. In the example it is seen that most of the hot electron orbital is simply reflected at the surface, but a small part of it is seen to stay at the molecule in the $2\pi^*$-orbital. The figure also indicates that it is possible to clearly distinguish between these two parts of the wavefunction, ie. it seems possible to determine a excitation probability by squaring and integrating the part of the wavefunction, which stays at the molecule. If the reflected parts of the wavefunction did not start to interfere with the molecule again it would probably also be possible to continue the calculation and follow the decay of the excitation. All calculations presented here have been made with the Octopus code, with the parameters given in Sec. 2.6.3.

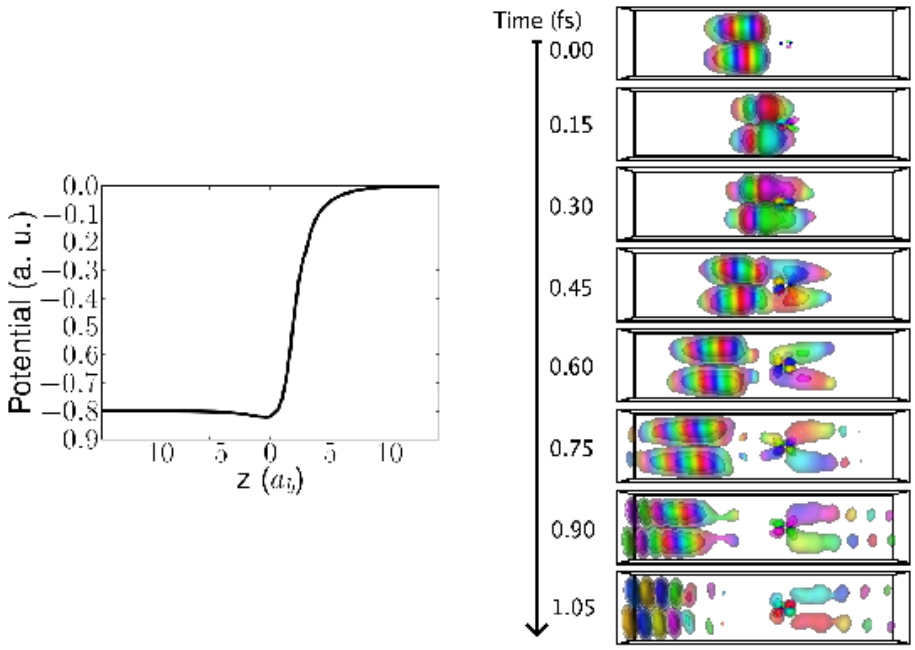

Figure 6.2: An example of a TDDFT calculation of a hot electron hitting a Nitrogen molecule from inside a surface. The surface is represented by the step-like potential shown on the left panel. The right panel shows the hot electron orbital at different times, where the color grading indicates phase. The initial hot electron orbital is constructed as a Kohn-Sham eigenfunction times an exponential factor to give it a momentum towards the molecule. The two small dots show the positions of the Nitrogen atoms. The same data is shown on Figs. 1 and 2 in paper IV.

6.2 The hot electron wavefunction

In the example of a calculation given in Sec. 6.1 the starting orbital of the hot electron was chosen rather randomly. Undoubtedly the obtained results will depend strongly on this arbitrary choice, so clearly a more systematic approach must be taken in order to get some more general information on the molecular resonance. Here this will take the form of a hypothesis on the relation between the hot electron orbital and the probability of exciting the molecular resonance, which I present in Sec. 6.2.1. Then I will test this hypothesis on a very simple system in Sec. 6.2.2. Finally in Sec. 6.2.3 I will apply this approach to a more realistic system.

6.2.1 The assumptions

It seems reasonable to assume that the probability of a hot electron exciting an adsorbed molecule is related to how well the energy of the hot electron fits the energy of the resonance. More precisely this can be expressed as an overlap between the energy representa-

tion of the hot electron and the energy representation of the resonance:

$$MO = \int R(\epsilon)W(\epsilon)d\epsilon, \tag{6.1}$$

MO is the excitation probability. I choose this abbreviation because the maximum overlap (MO) between the hot electron orbital and the molecular orbital in question, during the time evolution is interpreted as the excitation probability. $W(\epsilon)$ is the amount of the hot electron that has the energy ϵ, ie.

$$W(\epsilon) = \sum_i |\langle\phi|\psi^i_{KS}\rangle|^2\delta(\epsilon - \epsilon^i_{KS}). \tag{6.2}$$

Equation (6.2) is only approximative, since the Kohn-Sham eigenvalues are not adequate to describe excitation energies, ie. the renormalisation of the Kohn-Sham eigenvalues by the exchange-correlation kernel is completely ignored. $R(\epsilon)$ is the energy representation of the resonance. In the following I will assume this to be a Lorentzian

$$R(\epsilon) = \alpha_{res}\frac{(\Gamma/2)^2}{(\epsilon - \epsilon_{res})^2 + (\Gamma/2)^2}, \tag{6.3}$$

such that it corresponds to an exponentially decaying resonance. The three parameters ϵ_{res}, Γ and α_{res} corresponds to properties of the resonance and will be the subject of Sec. 6.3.

6.2.2 A simple system

In order to test the approximations of Eqs. (6.1)-(6.3) it is necessary to carry out a range of calculations with different starting orbitals for the hot electron and compare the results for the excitation probability with those obtained by inserting Eqs. (6.2) and (6.3) in Eq. (6.1). Since the three parameters, ϵ_{res}, Γ and α_{res}, of Eq. (6.3) are unknown it is necessary to estimate those through fitting, ie. significantly more than three calculations are required in order to avoid overfitting.

The first system I considered was the one indicated on Fig. 6.2, where the surface is just included as a step like potential and the molecule is a Nitrogen molecule standing vertically on the surface. This simple system was chosen, because of its simplicity, such that it is possible to carry out a lot of calculations in order to get a good feel for the possibilities and limitations of this approach. The biggest advantage is probably that this system does not contain any electrons inside the surface, so it is not necessary to worry about the created hot electron orbitals being orthogonal to the other occupied orbitals. Table 6.1 lists the 38 different starting orbitals for the hot electron, which were used. It is important to stress that all orbitals are created with a Π symmetry, such that they can interact with the $2\pi^*$-orbitals of the Nitrogen molecule. Without this symmetry there is no interaction and the excitation probability is zero.

Figure 6.3 summarizes the results obtained from the 38 calculations. The left panel shows $R(\epsilon)$ and $W(\epsilon)$ of Eqs. (6.2) and (6.3) for 7 different calculations, where the hot

Table 6.1: The 38 different starting orbitals for the hot electron orbital used in Sec. 6.2.2. The orbitals are divided into 5 groups. Within each group the orbitals only differ by the exponential factors, $e^{ip_0 z}$, they have been multiplied with, ie. the size of the momentum they have towards the molecule. Group 1, 2 and 3 consist of a gaussian wavefunction in the z-direction with Δp's of 0.1, 0.2 and 0.4 a.u., respectively. In the radial direction they are given by the a 1. order Bessel function, where the first node fits the unit cell boundary. Group 4 and 5 consist of two different Kohn-Sham eigenfunctions.

Illustration					
p_0-values	0.2 0.4 0.6 0.8 1.0 1.2 1.4	0.2 0.4 0.6 0.7 0.8 0.9 1.0 1.2 1.4 1.6	0.2 0.4 0.6 0.8 1.0 1.2 1.4	0.2 0.4 0.6 0.8 1.0 1.2 1.4	0.2 0.4 0.6 0.8 1.0 1.2 1.4

electron orbitals only differ by the applied momentum. From this it is obvious how the energy of the hot electron orbital is increased as the momentum is increased, which will give rise to a peaked feature if the overlap between $R(\epsilon)$ and $W(\epsilon)$ is plotted against the applied momentum.

The right panel on Fig. 6.3 shows these peaked features for all performed calculations. The black lines are the direct found excitation probabilities and the grey curves are the excitation probabilities found by inserting Eqs. (6.2) and (6.3) in Eq. (6.1). The values of ϵ_{res}, Γ and α_{res} in Eq. (6.3) are determined through a least squares fitting to be $\epsilon_{res} = 9.8$ eV above the Fermi energy, $\Gamma = 1.4$ eV and $\alpha_{res} = 5.4 \cdot 10^{-3}$. The least squares fitting procedure is a bit tricky due to the presence of several local minima, so the fitting procedure involves starting minimizations from a range of different offsets.

The reasonable good agreement between the directly obtained and the calculated excitation probabilities indicates that the assumptions made in Eqs. (6.1)-(6.3) are reasonable and that ϵ_{res}, Γ and α_{res} are true properties of the resonance, which I will consider in Sec. 6.3.

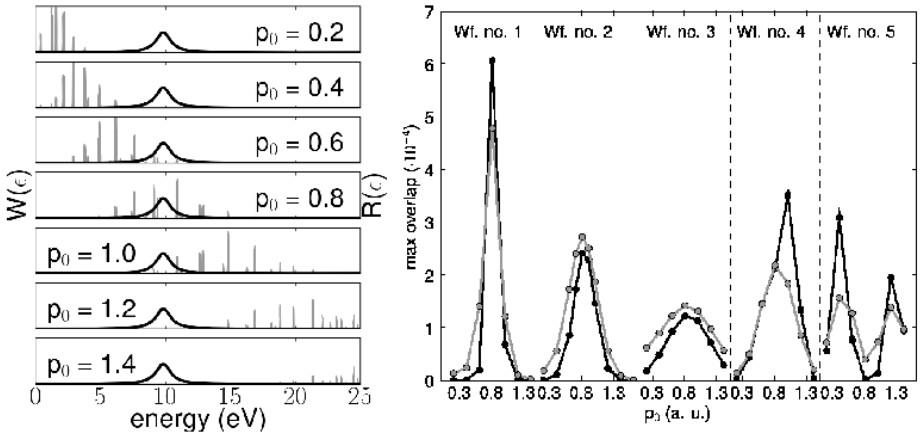

Figure 6.3: Left panel: $R(\epsilon)$ and $W(\epsilon)$ of Eqs. (6.2) and (6.3) for the 7 hot electron orbitals of group 1 in Table 6.1. The delta functions in $W(\epsilon)$ have been replaced with gaussians with a width of 0.1 eV. Right panel: The excitation probability as a function of the hot electron orbitals. The black and grey lines are the direct found excitation probabilities and the excitation probabilities found by inserting Eqs. (6.2) and (6.3) in Eq. (6.1), respectively. The values of ϵ_{res}, Γ and α_{res} in Eq. (6.3) have been fitted to give the best agreement. These data are also plotted on Figs. 6 and 7 in paper IV.

6.2.3 A more realistic system

The simple system of Sec. 6.2.2 is good for testing the approximations of Sec. 6.2.1, but it is not very realistic and cannot be used to estimate properties of real physical systems. In order to get closer to a more realistic description I now consider the system shown on Fig. 6.4, which consists of a 20 atoms Ruthenium cluster and an adsorbed Nitrogen molecule. This system is a simple model of a Nitrogen molecule adsorbed on a close-packed Ruthenium (001) surface. The three layers of the cluster each correspond to a close-packed layer.

The big practical difference between this system and the one of Sec. 6.2.2 lies in the generation of the starting orbitals for the hot electron. In this system there are a lot of electrons inside the cluster, ie. one must carefully make sure that the hot electron orbitals are orthogonal to these electrons. However, it is still preferable to have starting orbitals for the hot electron, which is reasonably localized in energy, such that the fitting of ϵ_{res}, Γ and α_{res} in Eq. (6.3) will be tremendously eased. If they are not reasonably localized in energy there will be no peaked features, which act as important guidelines in the fitting procedure. The solution I chose was to start by choosing the hot electron orbitals and then make the other orbitals orthogonal through an ordinary Gram-Schmidt orthogonalization procedure. The hot electron orbitals are created as a linear combination of some of the Kohn-Sham orbitals of the 20 atoms cluster without a molecule times a

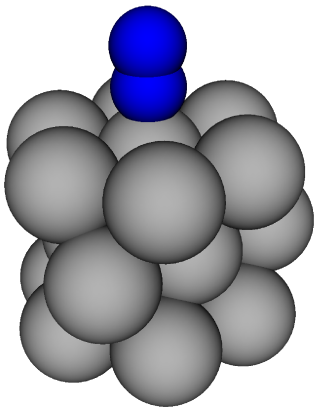

Figure 6.4: The 20 atoms Ruthenium cluster with an adsorbed Nitrogen molecule, which is studied in Sec. 6.2.3.

complex exponential factor to give them a momentum towards the surface. The linear combination is found by projecting the Kohn-Sham orbitals onto a function, which is reasonably localized in energy. Here I choose

$$\Psi(r,\theta,z) = J_1(\tfrac{r}{r_0})e^{i\theta}e^{-\frac{(z+3.3)^2}{3.3^2}}, \tag{6.4}$$

where $J_1(r)$ is a Bessel function of the first kind, r, θ and z are the usual semipolar coordinates and the equation is in atomic units.[72] The first node of $J_1(\frac{r}{r_0})$ lies at $r = 8a_0$ and $z = 0$ is the position of the highest layer of the cluster. The Bessel function is necessary in order to give the orbital the required Π-symmetry, such that it can interact with the $2\pi^*$-orbitals of the Nitrogen molecule. 13 different starting orbitals for the hot electron is made by multplying with 13 different exponential factors.

The results of the 13 calculations are summarized in Fig. 6.5, where the black line indicates the directly found excitation probabilities and the grey line indicates the excitation probabilities found by inserting Eqs. (6.2) and (6.3) in Eq. (6.1).

Again the values of ϵ_{res}, Γ and α_{res} in Eq. (6.3) are determined through a least squares fitting. For this system I find that $\epsilon_{res} = 4.9$ eV above the Fermi energy, $\Gamma = 0.36$ eV and $\alpha_{res} = 1.9 \cdot 10^{-3}$. The agreement between the directly found and the calculated excitation probabilities is also seen to be quite good for this system, indicating that the assumptions of Eqs. (6.1)-(6.3) are also reasonable in this more realistic system.

6.3 Resonance properties

In Sec. 6.2 I explained how it is possible to obtain true properties of a resonance, which are apparently only system dependent and not dependent on the starting orbital of the hot electron, by sending a range of differently prepared hot electrons towards the resonance. In this section I will discuss these properties and the reliability of the obtained values.

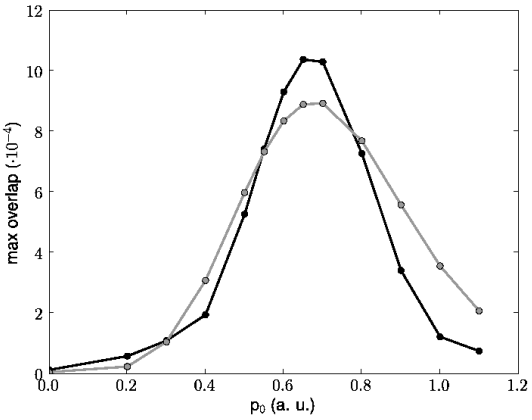

Figure 6.5: The excitation probability as a function of the applied momentum to the hot electron orbital for the system considered in Sec. 6.2.3. The black and grey lines are the direct found excitation probabilities and the excitation probabilities found by inserting Eqs. (6.2) and (6.3) in Eq. (6.1), respectively. The values of ϵ_{res}, Γ and α_{res} in Eq. (6.3) have been fitted to give the best agreement. These data are also plotted on Fig. 10 in paper IV.

6.3.1 Energy

The energy of the resonance, ϵ_{res} in Eq. (6.3), expresses the position of the resonance. For the simple system of Sec. 6.2.2 I found a value of $\epsilon_{res} = 9.8$ eV above the Fermi energy. This may seem a bit high, but one should keep in mind that the Fermi energy in this system lies at the highest occupied molecular orbital (HOMO) of the molecule. Another consequence of the missing electrons in the surface is that it is not possible to create an image charge, which would lower the resonance. The 9.8 eV is in the same range as the lowest lying excitations in the Nitrogen molecule, which seems reasonable.

In the more realistic system of Sec. 6.2.3 I found a value of $\epsilon_{res} = 4.9$ eV above the Fermi energy. The projected density of states for the $2\pi^*$-orbitals is shown on Fig. 6.6 and indicates a position of the resonance between 2 and 3 eV above the Fermi energy. This is quite different from the 4.9 eV, which indicates that the TDDFT results cannot be explained solely by the energy of the molecular orbital in the ground state Hamiltonian. In fact the results agree much better with inverse photoemission spectroscopy (IPES) measurements performed for Nitrogen on Nickel,[61] where the resonance is found 4.4 eV above the Fermi energy. ΔSCF calculations made as described in Paper II indicate that the difference in energy between having a Ruthenium and a Nickel surface is minor. The fact that the TDDFT results seem to agree better with a ΔSCF description can be understood by realizing that the energy of the hot electron should fit the position of the resonance when the resonance is getting occupied and not the position of the resonance when the system is in the ground state.

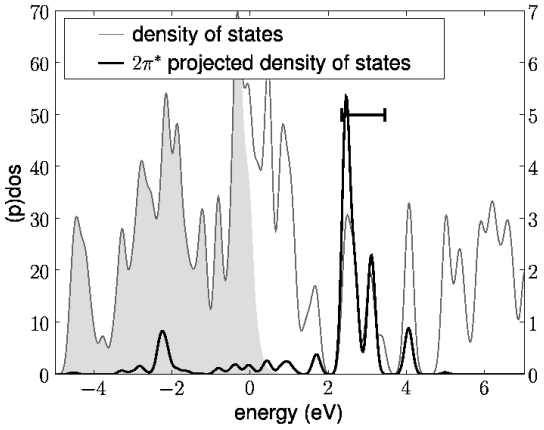

Figure 6.6: The density of states and projected density of states (pdos) for the Ruthenium cluster with a Nitrogen molecule shown on Fig. 6.4. The light grey area indicate the occupied states. The inserted bar has a length of 1.1 eV. The figure is the same as Fig. 14 in paper IV.

6.3.2 Width

In Sec. 6.2 I also obtained values for the widths of the resonances, Γ in Eq. (6.3). However, these widths are determined through probing by some hot electrons, which are very delocalized in energy. This can for example be seen on the left panel of Fig. 6.3. This means that the obtained values probably are determined with a large uncertainty. In Sec. 6.3.4 I will show that the obtained values of Γ does not fit well with other estimations of the excitation lifetimes, which is consistent with a large uncertainty on the values of Γ.

6.3.3 Cross-section

The α_{res} values in Eq. (6.3) is obviously proportional to the excitation probabilities, ie. they must be closely related to the resonance cross-sections. If we assume that the hot electron are evenly distributed on the unit cell cross section then it is reasonable to expect that the resonance cross-section, σ_{res} is the product of α_{res} and the unit cell cross-section, A_{system}:

$$\sigma_{res} = \alpha_{res} \cdot A_{system}. \tag{6.5}$$

A more accurate description would take into account that the hot electrons are not distributed evenly across the unit cell cross-section, but I will not do that in this crude approximation. This could explain the small tendency to a systematic deviation of some of the points on the right panel of Fig. 6.3.

By applying Eq. 6.5 to the more realistic system of Sec. 6.2.3 I find that $\sigma_{res} = 0.88$ Å^2. In the calculation it is assumed that A_{system} equals the area filled by 7 atoms in a Ruthenium (001) surface as the top layer of the cluster holds 7 atoms.

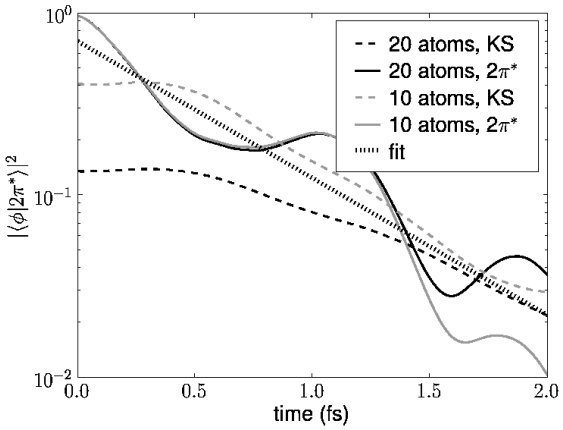

Figure 6.7: The overlap between an excited electron and the $2\pi^*$ orbitals of a Nitrogen molecule adsorbed on a Ruthenium cluster. The four calculations differ by the state of the excited electron and/or the size of the Ruthenium cluster. The excited electron is either placed in the Kohn-Sham (KS) orbital with the largest overlap to the molecular orbital or it is placed directly in a $2\pi^*$ orbital of the molecule. The Ruthenium cluster either has 10 or 20 atoms. The inserted fit corresponds to an excitation lifetime of 0.6 fs. The data is also plotted on Fig. 12 in paper IV.

6.3.4 Lifetime

In Sec. 6.3.2 I discussed the found widths of the resonances, which can be directly coupled to lifetimes of the excitations. However, the lifetime can also be estimated in other ways. Figure 6.7 shows the overlap between an excited electron and the corresponding molecular orbital as a function of time for four different calculations. The four calculations differ by the choice of the excited state and/or the size of the Ruthenium cluster. However, they all consider the $2\pi^*$ excitation of a Nitrogen molecule adsorbed on Ruthenium. In all four calculations it is possible to follow how the excitation decays over time. The decay is seen to be reasonably exponential with approximately the same lifetime for the four calculations. The included fit in the figure corresponds to a lifetime of $\tau = 0.6$ fs. This is equivalent to an uncertainty in the resonance energy of $\Delta E = \hbar/\tau = 1.1$ eV.

Another way of estimating the lifetime of the resonance is to consider the projected density of Kohn-Sham states. This was done on Fig. 6.6 where a bar of 1.1 eV is also inserted for comparison. The two estimates are seen to agree quite well, which indicates that the simple projected density of Kohn-Sham states estimation is reasonable. However, the width of $\Gamma = 0.36$ eV found in Sec. 6.2.3 is far from the two other estimates, which is consistent with the expectation of a large uncertainty on the Γ-values.

6.4 Future possibilities

In all the calculations presented in this paper all atoms have been fixed and only electrons have been allowed to move. This offers the possibility of studying the properties of the resonance, but it does not provide any information on the dynamics induced by electrons hitting the resonance. However, TDDFT also provides the possibility of studying coupled ion-electron dynamics.[68] It would be very interesting to apply this approach to the systems considered here and investigate whether or not such a framework can give sufficiently accurate estimations of the induced dynamics. This would allow for comparisons with results obtained by the method of chapter 5.

Chapter 7

Summary and outlook

This thesis is concerned with two different aspects of heterogeneous catalysis. The first part is focused on calculating the detailed structure of catalytic nanoparticles. This is very important since many catalytic reactions are extremely structure sensitive, ie. the catalytic activity of nanoparticles can only be truly understood when the structure of the nanoparticles is understood. I will summarize the results of this part in Sec. 7.1. The second part considered the field of hot electron assisted femtochemistry, which potentially provides the possibility of placing energy in certain vibrational states of adsorbed species. This could be applied to enhancing selectivity in reactions or to increasing the catalytic activity without increasing the temperature. I summarize the results of this part in Sec. 7.2.

7.1 The structure of nanoparticles

The classical approach to obtaining the structure of crystalline particles, the Wulff construction, cannot be applied in the case of catalytic nanoparticles, since it does not provide sufficiently detailed information. It provides an estimation of overall structure, but the catalytic activity is governed by the presence of special active sites. Instead I have developed a significantly different approach to obtaining the structure of a nanoparticle, with focus on Ruthenium nanoparticles, which crystallizes in a hcp structure.

The approach is to generate a large representative ensemble of structures for the nanoparticle. Each structure is build up from individual atoms, such that finite size effects are included in the description. Preliminary attempts of generating representative ensembles have shown that it is reasonable to heavily restrict the configurational space, since all relevant structures will be dominated by the same facets as the Wulff construction. This restriction makes it possible to consider particles up to at least 5 nm in diameter. The energy of each structure is estimated by summing up the surface energy of all the atoms. The surface energies are estimated with the help of DFT calculations. The potential energy is applied instead of the free energy. However, tests indicate that the consequence of this approximation is rather limited. The ensemble of structures can be used to calculate average properties of the cluster by a simple Boltzmann averaging.

Ensembles of structures have been calculated for a lot of Ruthenium particles in the diameter range from 2 nm to 5 nm. For the smallest particles the number of interesting step sites is heavily dependent on the exact number of atoms. When the particles become bigger than 3 nm in diameter this dependence on single atoms is smaller. An increased temperature does not influence the presence of step sites significantly, it just smooths out some of the size dependence. The ammonia synthesis activity was estimated for the Ruthenium particles. This indicated that the optimal size is 3 nm in diameter. The effect of the substrate and a gas on the structure can quite easily be included in the model. Results indicate that the presence of carbonmonooxide will promote the presence of step sites.

Unfortunately time did not permit a thorough investigation of the effect of the substrate and gas on the structure of the particles. In the future it would be very interesting to continue this analysis. It is possible that the reactants in some cases promote the presence of the active sites. It would be interesting to understand such effects in more detail. It would also be interesting to apply the same methodology to other materials than Ruthenium in order investigate the material dependence on the presence of active sites.

7.2 Hot electron femtochemistry at surfaces

Most theoretical investigations of the energy transfer from hot electrons to vibrational energy in adsorbed molecules are based on model potential energy surfaces, since it is difficult to calculate potential energy surfaces of excited molecules at surfaces. In this thesis I presented an extended version of the ΔSCF method, which can be used to calculate such potential energy surfaces. The method has been applied to different diatomic molecules adsorbed on different transition metal surfaces. Comparisons with inverse photo-emission spectroscopy (IPES) experiments and TDDFT calculations indicate that the ΔSCF approach provides reasonable results. The calculations also reveal that the minimum of the resonance PESs for these diatomic molecules lie further away from the surface compared to the minimum of the ground state PESs. This is in contradiction to the typical assumption that the creation of an image charge will attract the excited molecule to the surface. The molecule is moved away from the surface because the bond length increases as the anti-bonding state of the molecule becomes occupied.

The obtained PESs can be used to estimate the coupling between the hot electrons and the vibrational modes of the molecule. In this way it is possible to estimate the probability of an electron transferring a certain amount of energy into vibrational energy. By combining these probabilities it is also possible to estimate multi-electron effects, as long as the electrons hit the molecule at different times. The method was applied to the desorption of NO on Pt (111). This revealed a striking resemblance to experimental observations, where the desorption rate follow a power-law relation to the hot electron flux. In the regime where single electron events dominate the power is 1, whereas the power changes to a higher number when multiple electron events begin to dominate.

I also presented a more direct approach to studying the interaction between hot electrons and molecular resonances. This is based on TDDFT calculations, where the entire

event of a hot electron hitting a molecular resonance is simulated. By doing this for a range of different hot electrons it is possible to extract different properties of the resonance. The found resonance energy seems to agree quite well with ΔSCF calculations. The approach also provided an approximation to the cross-section area of the resonance. A value of the resonance width is also estimated, but it is given with a very large uncertainty. However, the resonance width can also be estimated by considering the decay of an excited molecule at a surface. The result of such a calculation turned out to agree quite well with a simple projected density of Kohn-Sham states approach. In all calculations I considered a Nitrogen molecule adsorbed on a Ruthenium surface, but the developed methodology is of general applicability. In the future it would be interesting to include the coupling between the electron motion and ionic motion. This would provide a direct estimation of the energy transfer to ionic motion, which could be compared to experiments and results obtained by other approaches.

Bibliography

[1] Anderson, P. W. Localized magnetic states in metals. *Physical Review 124* (1961), 41–53.

[2] ASE is a freely available collection of python modules for manipulation of atoms, analyzing simulations, visualization etc. (see `wiki.fysik.dtu.dk/ase`).

[3] Bahn, S. R., and Jacobsen, K. W. An object-oriented scripting interface to a legacy electronic structure code. *Computing in Science and Engineering 4* (2002), 56–66.

[4] Behler, J., Delley, B., Reuter, K., and Scheffler, M. Nonadiabatic potential-energy surfaces by constrained density-functional theory. *Physical Review B 75* (2007), 115409.

[5] Blöchl, P. E. Projector augmented-wave method. *Physical Review B 50* (1994), 17953.

[6] Blöchl, P. E., Först, C. J., and Schimpl, J. Projecter augmented wave method: ab-initio molecular dynamics with full wave functions. *Bulletin of Materials Science 26* (2003), 33.

[7] Boer, F. R. d., Boom, R., Mattens, W. C. M., Miedema, A. R., and Niessen, A. K. *Cohesion in metals: transition metal alloys*. North-Holland, 1988.

[8] Bonn, M., Funk, S., Hess, C., Denzler, D. N., Stampfl, C., Scheffler, M., Wolf, M., and Ertl, G. Phonon- versus electron-mediated desorption and oxidation of CO on Ru(0001). *Science 285* (1999), 1042–1045.

[9] Bransden, B. H., and Joachain, C. J. *Quantum Mechanics*. Prentice Hall, 2000.

[10] Broyden, C. G. A class of methods for solving nonlinear simultaneous equations. *Mathematics of Computation 19* (1965), 577–593.

[11] Budde, F., Heinz, T. F., Loy, M. M. T., Misewich, J. A., de Rougemont, F., and Zacharias, H. Femtosecond time-resolved measurement of desorption. *Physical Review Letters 66* (1991), 3024.

[12] Buntin, S. A., Richter, L. J., Cavanagh, R. R., and King, D. S. Optically driven surface reactions: Evidence for the role of hot electrons. *Physical Review Letters 61* (1988), 1321.

[13] Buntin, S. A., Richter, L. J., King, D. S., and Cavanagh, R. R. State-resolved evidence for hot carrier driven surface reaction: Laser-induced desorption of NO from Pt(111). *Journal of Chemical Physics 91* (1989), 6429.

[14] Cai, L., Xiao, X., and Loy, M. M. T. Femtosecond laser desorption of CO from the Pt(111) surface. *Surface Science Letters 464* (2000), 727.

[15] Cao, Z., Wan, H., and Zhang, Q. Density functional characterization of N_2 dissociation on the step of ruthenium clusters. *Journal of Chemical Physics 119* (2003), 9178–9180.

[16] Castro, A., Appel, H., Oliveira, M., Rozzi, C. A., Andrade, X., Lorenzen, F., Marques, M. A. L., Gross, E. K. U., and Rubio, A. Octopus: a tool for the application of time-dependent density functional theory. *Physica Status Solidi B 243* (2006), 2465–2488.

[17] Ceperley, D. M., and Alder, B. J. Ground state of the electron gas by a stochastic method. *Physical Review Letters 45* (1980), 566–569.

[18] Chetty, N., Stokbro, K., Jacobsen, K. W., and Nørskov, J. K. Ab initio potential for solids. *Physical Review B 46* (1992), 3798–3809.

[19] Chorkendorff, I., and Niemantsverdriet, J. W. *Concepts of modern catalysis and kinetics*. Wiley, 2003.

[20] Combe, N., Jensen, P., and Pimpinelli, A. Changing shapes in the nanoworld. *Physical Review Letters 85* (2000), 110–113.

[21] Croci, M., Felix, C., Vandoni, G., harbich, W., and Monot, R. Chemisorption and macroscopic diffusion of NO on Pt(111). *Surface Science 307* (1994), 460.

[22] Dacapo is a freely available plane-wave density functional theory code, which is a part of the CAMPOS software (see `wiki.fysik.dtu.dk/dacapo`).

[23] Dahl, S., Logadottir, A., Egeberg, R. C., Larsen, J. H., Chorkendorff, I., Törnqvist, E., and Nørskov, J. K. Role of steps in N_2 activation on Ru(0001). *Physical Review Letters 83* (1999), 1814–1817.

[24] Dobson, J. F., Bunner, M. J., and Gross, E. K. U. Time-dependent density functional theory beyond linear response: an exchange-correlation potential with memory. *Physical Review Letters 79* (1997), 1905–1908.

[25] Elliot, S. *The physics and chemistry of solids*. Wiley, 1998.

[26] Pseudo potentials from the Fritz-Haber institute are available on the website `www.abinit.org/Psps/?text=../Psps/LDA_FHI/fhi`.

[27] Fiolhais, C., Nogueira, F., and Marques, M., Eds. *A primer in density functional theory*. Springer-Verlag Berlin Heidelberg New York, 2002.

[28] Fisher, E. S., and Dever, D. Temperature dependence of elastic moduli of ruthenium, rhenium, cobalt, dysprosium. *Trans. Met. Soc. AIME 239* (1967), 48–57.

[29] Fournier, F., Zheng, W., Carrez, S., Dubost, H., and Bourguignon, B. Ultrafast laser excitation of CO/Pt(111) probed by sum frequency generation: Coverage dependent desorption efficiency. *Physical Review Letters 92* (2004), 216102.

[30] Frederiksen, T., Paulsson, M., Brandbyge, M., and Jauho, A. P. Inelastic transport theory from first-principles: methodology and applications for nanoscale devices. *Physical Review B 75* (2007), 205413.

[31] Frischkorn, C., and Wolf, M. Femtochemistry at metal surfaces: Nonadiabatic reaction dynamics. *Chemical Reviews 106* (2006), 4207–4233.

[32] Gadzuk, J. W. Inelastic resonance scattering, tunneling, and desorption. *Physical Review B 44* (1991), 13466.

[33] Gadzuk, J. W. Resonance-assisted, hot-electron-induced desorption. *Surface Science 342* (1995), 345.

[34] Gadzuk, J. W. Resonance-assisted hot electron femtochemstry at surfaces. *Physical Review Letters 76* (1996), 4234.

[35] Gadzuk, J. W. Role of secondary electrons in hot-electron femtochemistry at surfaces using tunnel junctions. *J. Vac. Sci. Technol. A 15* (1997), 1520.

[36] Gadzuk, J. W., Richter, L. J., Buntin, S. A., King, D. S., and Cavanagh, R. R. Laser-excited hot-electron induced desorption: a theoretical model applied to NO/Pt(111). *Surface Science 235* (1990), 317.

[37] Gavnholt, J. Shape and functionality of individual nanoparticles. *Master Thesis* (2006).

[38] Görling, A. Density-functional theory beyond the Hohenberg-Kohn theorem. *Physical Review A 59* (1999), 3359–3374.

[39] GPAW is a freely available real-space density functional theory code, which is a part of the CAMPOS software (see `wiki.fysik.dtu.dk/gpaw`).

[40] Gunnarson, O., and Lundqvist, B. I. Exchange and correlation in atoms, molecules, and solids by the spin-density-functional formalism. *Physical Review B 13* (1976), 4274–4298.

[41] Häkkinen, H., and Moseler, M. 55-atom clusters of silver and gold: Symmetry breaking by relativistic effects. *Computational Materials Science 35* (2006), 332–336.

[42] Hamann, D. R., Schlüter, M., and Chiang, C. Norm-conserving pseudopotentials. *Physical Review Letters 43* (1979), 1494–1497.

[43] Hammer, B., Hansen, L. B., and Nørskov, J. K. Improved adsorption energetics within density functional theory using revised Perdew-Burke-Ernzerhof functionals. *Physical Review B 59* (1999), 7413–7421.

[44] Hammer, B., and Nørskov, J. K. Electronic factors determining the reactivity of metal surfaces. *Surface Science 343* (1995), 211–220.

[45] Hammer, B., and Nørskov, J. K. Why gold is the noblest of all the metals. *Nature 376* (1995), 238–240.

[46] Harris, S. M., Holloway, S., and Darling, G. R. Hot electron mediated photodesorption: A time-dependent approach applied to NO/Pt(111). *Journal of Chemical Physics 102* (1995), 8235.

[47] Hellman, A., Razaznejad, B., and Lundqvist, B. I. Potential-energy surfaces for excited states in extended systems. *Journal of Chemical Physics 120* (2004), 4593–4602.

[48] Henkelman, G., Arnaldsson, A., and Jónsson, H. A fast and robust algorithm for bader decomposition of charge density. *Computational Mateterials Science 36* (2006), 354–360.

[49] Henry, C. R. Morphology of supported nanoparticles. *Progress in Surface Science 80* (2005), 92–116.

[50] Herring, C. *The Physics of Powder Metallurgy.* McGraw-Hill, New York, 1951.

[51] Ho, W. Femtosecond laser-induced dynamical quantum processes on solid surfaces (DQPSS). *Surface Science 363* (1996), 166.

[52] Hochbruck, M., and Lubich, C. On Krylov subspace approximations to the matrix exponential operator. *SIAM journal on numerical analysis 34* (1997), 1911–1925.

[53] Hochbruck, M., and Lubich, C. On Magnus integrators for time-dependent Schrödinger equations. *SIAM journal on numerical analysis 41* (2003), 945–963.

[54] Hohenberg, P., and Kohn, W. Inhomogeneous electron gas. *Physical Review 136* (1964), B864–B871.

[55] Honkala, K., Hellman, A., Remediakis, I. N., Logadottir, A., Carlsson, A., Dahl, S., Christensen, C. H., and Nørskov, J. K. Ammonia synthesis from first-principles calculations. *Science 307* (2005), 555–558.

[56] Howe, P. T., and Dai, H. L. Translational energy distribution in hot electron mediated photodesorption: a one-dimensional quantum mechanical calculation of NO/Pt(111) and SO_2/Ag(111). *Surface Science 451* (2000), 12.

[57] Jacobsen, C. J. H., Dahl, S., Hansen, P. L., Törnqvist, E., Jensen, L., Topsøe, H., Prip, D. V., Møenshaug, P. B., and Chorkendorff, I. Structure sensitivity of supported ruthenium catalysts for ammonia synthesis. *Journal of Molecular Catalysis A 163* (2000), 19–26.

[58] Jacobsen, K. W., Nørskov, J. K., and Puska, M. J. Interatomic interactions in the effective-medium theory. *Physical Review B 35* (1987), 7423–7442.

[59] Jacobsen, K. W., Stoltze, P., and Nørskov, J. K. A semi-empirical effective medium theory for metals and alloys. *Surface Science 366* (1996), 394–405.

[60] Johnson, C. A., and Chakerian, G. D. On the proof and uniqueness of Wulff's construction of the shape of minimum surface free energy. *J. Math. Phys. 9* (1965), 1403–1404.

[61] Johnson, P. D., and Hulbert, S. L. Inverse-photoemission studies of adsorbed diatomic molecules. *Physical Review B 35* (1987), 9427–9436.

[62] Jones, R. O., and Gunnarson, O. The density functional formalism, its applications and prospects. *Reviews of Modern Physics 61* (1989), 689–746.

[63] Kalos, M. H., and Whitlock, P. A. *Monte Carlo methods.* John Wiley and sons, 1986.

[64] Kern, R. *Morphology of Crystals.* Terra Scientific Pub. Company, Tokyo, 1987.

[65] Kittel, C. *Introduction to solid state physics.* Wiley, 1976.

[66] Kohn, W. Nobel lecture: Electronic structure of matter - wave functions and density functionals. *Reviews of Modern Physics 71* (1998), 1253–1266.

[67] Kohn, W., and Sham, L. J. Self-consistent equations including exchange and correlation effects. *Physical Review 140* (1965), A1133–A1138.

[68] Kreibich, T., and Gross, E. K. U. Multicomponent density-functional theory for electrons and nuclei. *Physical Review Letters 86* (2001), 2984–2987.

[69] Kresse, G., and Joubert, D. From ultrasoft pseudopotentials to the projector augmented-wave method. *Physical Review B 59* (1999), 1758.

[70] Kurth, S., Perdew, J. P., and Blaha, P. Molecular and solid-state tests of density functional approximations: LSD, GGAs, amd meta-GGAs. *International Journal of Quantum Chemistry 75* (1999), 889–909.

[71] Kurzweil, Y., and Baer, R. Time-dependent exchange-correlation current density functionals with memory. *Journal of Chemical Physics 121* (2004), 8731–8741.

[72] Lengths in Bohr radii and energies in Hartree.

[73] Logadóttir, Á., and Nørskov, J. K. Ammonia synthesis over a Ru(0001) surface studied by density functional theory. *Journal of Catalysis 220* (2003), 273–279.

[74] Marques, M. A. L., Ullrich, C. A., Nogueira, F., Rubio, A., Burke, K., and Gross, E. K. U., Eds. *Time-dependent density functional theory.* Springer, Berlin Heidelberg, 2006.

[75] Misewich, J. A., Heinz, T. F., and Newns, D. M. Desorption induced by multiple electronic transitions. *Physical Review Letters 68* (1992), 3737.

[76] Misewich, J. A., Kalamarides, A., Heinz, T. F., Höfer, U., and Newns, D. M. Vibrationally assisted electronic desorption: Femtosecond surface chemistry of O_2/Pd(111). *Journal of Chemical Physics 100* (1994), 736.

[77] Mortensen, J. J., Hansen, L. B., and Jacobsen, K. W. Real-space grid implementation of the projector augmented wave method. *Physical Review B 71* (2005), 35109.

[78] Mortensen, J. J., Morikawa, Y., Hammer, B., and Nørskov, J. K. Density functional calculations of N_2 adsorption and dissociation on a Ru(0001) surface. *Journal of Catalysis 169* (1997), 85–92.

[79] Mullins, W. W., and Rohrer, G. S. Nucleation narrier for volume-conserving shape changes of faceted crystals. *J. Am. Ceram. Soc. 83* (2000), 214–216.

[80] Newns, D. M. Self-consistent model of hydrogen chemisorption. *Physical Review 178* (1969), 1123–1135.

[81] Nightingale, M. P., and Umrigar, C. J. *Quantum Monte Carlo methods in physics and chemistry.* Kluwer Academic Publishers, 1999.

[82] Nørskov, J. K., and Lang, N. D. Effective-medium theory of chemical binding: Application to chemisorption. *Physical Review B 21* (1980), 2131–2136.

[83] Octopus is a freely available real space time-dependent density functional theory code (see `www.tddft.org/programs/octopus/`).

[84] Payne, M. C., Teter, M. P., Allan, D. C., Arias, T. A., and Joannopoulos, J. D. Iterative minimization techniques for ab initio total-energy calculations: molecular dynamics and conjugate gradients. *Reviews of Modern Physics 64* (1992), 1045–1097.

[85] Perdew, J. P., Burke, K., and Ernzerhof, M. Generalized gradient approximation made simple. *Physical Review Letters 77* (1996), 3865–3868.

[86] Perdew, J. P., Chevary, J. A., Vosko, S. H., Jackson, K. A., Pederson, M. R., Singh, D. J., and Fiolhais, C. Atoms, molecules, solids and surfaces: Applications of the generalized gradient approximation for exchange and correlation. *Physical Review B 46* (1992), 6671–6687.

[87] Prybyla, J. A., Heinz, T. F., Misewich, J. A., Loy, M. M. T., and Glownia, J. H. Desorption induced by femtosecond laser pulses. *Physical Review Letters 64* (1990), 1537.

[88] Prybyla, J. A., Tom, H. W. K., and Aumiller, G. D. Femtosecond time-resolved surface reaction: Desorption of CO from Cu(111) in less than 325 fsec. *Physical Review Letters 68* (1992), 503.

[89] Reimer, W., Fink, T., and Küppers, J. Inverse photoemission of CO, H and H/CO adsorbed at Ni(001) surfaces. *Surface Science 186* (1987), 55–66.

[90] Reimer, W., Fink, T., and Küppers, J. Inverse photoemission spectroscopy of H, CO, and NO adsorbed at Ni(001) and Ni(111) surfaces. *Surface Science 193* (1988), 259–270.

[91] Reinhard, D., Hall, B. D., Berthoud, P., Valkealahti, S., and Monot, R. Size-dependent icosahedral-to-fcc structure change confirmed in unsupported nanometer-sized copper clusters. *Physical Review Letters 79* (1997), 1459–1462.

[92] Rogozik, J., and Dose, V. The role of the 2π level in CO chemisorption on metal surfaces. *Surface Science 176* (1986), L847–L851.

[93] Runge, E., and Gross, E. K. U. Density-functional theory for time-dependent systems. *Physical Review Letters 52* (1984), 997–1000.

[94] Saalfrank, P., Boendgen, G., Finger, K., and Pesce, L. Photodesorption of no from a metal surface: quantum dynamical implications of a two-mode model. *Journal of Chemical Physics 251* (2000), 51.

[95] Schrödinger, E. An undulatory theory of the mechanics of atoms and molecules. *Physical Review 28* (1926), 1049–1070.

[96] Struck, L. M., Richter, L. J., Buntin, S. A., Cavanagh, R. R., and Stephenson, J. C. Femtosecond laser-induced desorption of CO from Cu(100): Comparison of theory and experiment. *Physical Review Letters 77* (1996), 4576.

[97] Thomsen, L. B., Nielsen, G., Vendelbo, S. B., Johansson, M., Hansen, O., and Chorkendorff, I. Ultralarge area MOS tunnel device for electron emission. *Physical Review B 76* (2007), 155315.

[98] Tokatly, I. V., and Pankratov, O. Local exchange-correlation vector potential with memory in time-dependent density-functional theory: The generalized hydrodynamics approach. *Physical Review B 67* (2003), 201103.

[99] Troullier, N., and Martins, J. L. Efficient pseudopotentials for plane-wave calculations. *Physical Review B 43* (1991), 1993–2006.

[100] Tyson, W. R., and Miller, W. A. Surface free energies of solid metals: Estimation from liquid surface tension measurements. *Surface Science 62* (1977), 267–276.

[101] Valkealahti, S., and Manninen, M. Instability of cuboctahedral copper clusters. *Physical Review B 45* (1992), 9459–9462.

[102] van Leeuwen, R. Causality and symmetry in time-dependent density-functional theory. *Physical Review Letters 80* (1998), 1280–1283.

[103] Vanderbilt, D. Soft self-consistent pseudopotentials in a generalized eigenvalue formalism. *Physical Review B 41* (1990), 7892–7895.

[104] Vitos, L., Ruban, A. V., Skriver, H. L., and Kollár, J. The surface energy of metals. *Surface Science 411* (1998), 186–202.

[105] Wingreen, N. S., Jacobsen, K. W., and Wilkins, J. W. Inelastic scattering in resonant tunneling. *Physical Review B 40* (1989), 11834.

[106] Wu, Q., and Voorhis, T. V. Direct optimization method to study constrained systems within density-functional theory. *Physical Review A 72* (2005), 024502.

[107] Wu, Q., and Voorhis, T. V. Direct calculation of electron transfer parameters through constrained density functional theory. *Journal of Physical Chemistry A 110* (2006), 9212–9218.

[108] Wulff, G. Zur Frage der Geschwindigkeit des Wachsturms under Auflosung der Kristallflachen. *Z. Krist. 34* (1901), 449–530.

[109] Zangwill, A., and Soven, P. Density-functional approach to local-field effects in finite systems: Photoabsorption in the rare gases. *Physical Review A 21*, 5 (1980), 1561–1572.

[110] Ziegler, T., Rauk, A., and Baerends, E. J. On the calculation of multiplet energies by the Hartree-Fock-Slater method. *Theor. Chim. Acta 43* (1977), 261–271.

Included papers

Paper I on page 97

Gavnholt, J. and Schiøtz, J., Structure and reactivity of ruthenium nanoparticles, *Physical Review B, 77* (2008), 035404

Paper II on page 109

Gavnholt, J., Olsen, T., Engelund, M. and Schiøtz, J., Δ self-consistent method to obtain potential energy surfaces of excited molecules on surfaces, *Physical Review B, 78* (2008), 075441

Paper III on page 121

Olsen, T., Gavnholt, J. and Schiøtz, J., Hot-electron-mediated desorption rates calculated from excited-state potential energy surfaces, *Physical Review B, 79* (2009), 035403

Paper IV on page 135

Gavnholt, J., Rubio, A., Olsen, T., Thygesen, K. S. and Schiøtz, J., Hot electron assisted femtochemistry at surfaces - a TDDFT approach, *submitted*

Paper I

PHYSICAL REVIEW B **77**, 035404 (2008)

Structure and reactivity of ruthenium nanoparticles

Jeppe Gavnholt and Jakob Schiøtz*
Center for Individual Nanoparticle Functionality (CINF), Department of Physics, Technical University of Denmark, DK-2800 Kongens Lyngby, Denmark
(Received 6 July 2007; published 3 January 2008)

We present a method for obtaining detailed structural information of ruthenium nanoparticles in at least the diameter range from 1.5 to 5 nm. The method is based on an ensemble approach where a large number of low-energy structures are collected in an ensemble, from which average properties can be extracted using Boltzmann averaging. The method is used to obtain the number of catalytic active step sites present on the surface of the ruthenium particles. We find that the presence of highly catalytic active step sites does not depend significantly on the temperature within a relevant temperature range; the presence of step sites is mainly a function of the lowest energy shape of the cluster, i.e., a function of the number of atoms. By combining the structural information with estimations of the single site activities in the ammonia synthesis, we find that the optimal particle diameter is approximately 3 nm. The single site activities are estimated by using density functional theory to calculate the barrier of the rate limiting step, the dissociation of a nitrogen molecule.

DOI: 10.1103/PhysRevB.77.035404 PACS number(s): 61.46.Df, 82.33.Hk, 82.20.Wt

I. INTRODUCTION

Within the past decade, it has become possible to make reasonably accurate theoretical estimations of adsorption energies of individual molecules and barrier heights for the different part reactions in a variety of different catalytic processes.[1–14] This success has been made possible by the use of density functional theory and the increase in computer power. The adsorption energy and barrier height information can be combined with either a mean-field kinetic model[11] or a kinetic Monte Carlo model,[12] where interactions between surface species can be included, to obtain the catalytic activity of single sites. The development of these methods has given much insight to the fundamental processes governing many catalytic reactions. One of the things that has been realized is that some catalytic reactions, such as the ammonia synthesis, is completely dominated by a few highly active sites. Dahl *et al.*[13] show that the sticking coefficient of a nitrogen molecule on a ruthenium surface drops at least 9 orders of magnitudes, when the steps are blocked by Au atoms. This is supported by density functional theory calculations, which show that the barrier of the N_2 dissociation is much lower at a step site than at a flat surface site. This proves that the detailed structure of the catalyst is of vital importance for at least some catalytic reactions. It is then necessary not only to find the single site activity in order to make theoretical estimates of a catalyst's activity but also to make some estimate of the catalyst's detailed surface structure.

Honkala *et al.*[14] made such an estimate of the catalytic activity of ruthenium clusters in the ammonia synthesis and found beautiful agreement with experiments, i.e., between a factor 3 and 20 in difference. However, the structure estimation was only applicable for a few cluster sizes and did not include temperature effects. In this paper we take the step further and develop a method, which can systematically treat all cluster sizes between at least 1.5 and 5 nm in diameter, and which gives the temperature dependence on the structure. We hope that such a model will provide further insight to the factors governing the presence of highly active sites. In this paper, we have focused on ruthenium clusters. However, the model can be directly applied to other hcp metals, and with minor modifications, it could be applied to other crystal structures as well. We have chosen to study ruthenium since this is known to be one of the best catalysts for the ammonia synthesis.

The main principle of the method is for a given cluster size to collect a large ensemble of possible and relevant configurations for the cluster. Average properties of the cluster can then be calculated using simple Boltzmann averaging over the ensemble. In order to do that, we need the energy and the property we want to average of each cluster in the ensemble. In this paper, we have focused on calculating the average number of catalytic active sites; however, in principle, the ensemble could be used to calculate other properties as well. In the following two sections, we describe the method. First, we describe the model for obtaining the energy, and second, we go through the configuration generation and the Boltzmann averaging. In this part, we will also discuss the limitations and approximations of the method. Finally, we present the results, where we look at the number of catalytic active sites as a function of cluster size. Here, we will also carry out calculations on the barrier size for the dissociation of nitrogen at different sites in order to link the obtained structures to actual catalytic activities for the ammonia synthesis. The dissociation of nitrogen is the rate limiting step in the ammonia synthesis, i.e., knowledge of the barrier height for this dissociation will enable us to make a simple approximation of the ammonia synthesis rate.

II. ENERGY OF A CLUSTER

Both in the process of finding the relevant cluster configurations and in the following Boltzmann averaging, it is of absolute importance that we are able to calculate the energy of the different cluster configurations. Since this paper fo-

 ©2008 The American Physical Society

cuses on large clusters with up to 4000 atoms in size, it is not possible to apply high-accuracy methods such as density functional theory directly for this task. We need a method which can compute the energy of a 4000 atom cluster within a few tenths of a second, such that it is possible to obtain energies of many different structures within a reasonable time of computation. One possibility is to optimize an effective medium theory (EMT) potential for ruthenium, as described by Jacobsen *et al.*[15,16] Another possibility is to assign an energy to each atom in the cluster depending on the configuration of nearest neighbors, where the total energy is then simply the sum of all these atomic energies. The individual atomic energies should then be estimated from density functional theory (DFT). This turned out to be the preferred method for this type of calculations, so in the following, we will describe this method in more detail. Afterward, we argue why this is the preferable method by making a comparison to the above-mentioned effective medium approach.

All the DFT calculations presented in this paper are based on a plane-wave expansion of the wave functions, a revised Perdew-Burke-Ernzerhof (RPBE) description of exchange and correlation effects,[17] and ultrasoft pseudopotentials.[18] Plane waves with energy up to 350 eV are used. The self-consistent electron density is determined by iterative diagonalization of the Kohn-Sham Hamiltonian, Fermi population of the Kohn-Sham states using a temperature of 0.1 eV, and Pulay mixing of the resulting electronic density.[19] All total energies have been extrapolated to zero temperature. Slabs have been separated by at least 10 Å in all calculations. The DFT calculations are made with the DACAPO software.[20]

A. Description of the method

The simplest way to assign an energy to each atom is to let the energy depend solely on the number of nearest neighbors. DFT is then used to obtain a relation between the energy and the number of nearest neighbors. However, since different surfaces in many cases contain atoms with the same number of neighbors, we extend this model a bit, such that the atomic energy not only depends on the number of nearest neighbors but also the configuration of these. In this way, we preserve the freedom to assign different energies to different surfaces. However, we also restrict ourselves to find energies of nonstrained hcp structures. As it will be argued in the next section, this is sufficient for our purpose.

We illustrate the method by the example shown in Fig. 1 where we assign energies to the atoms sitting on the (0001) and $(10\bar{1}1)$ surfaces and the edge between them. Furthermore, we include the step formation energy. First, the bulk energy is determined by doing a standard lattice parameter optimization using DFT. Here, we found the lattice parameters $a=2.7529$ Å and $c=4.3595$ Å, which are 1.7% and 1.8% above the experimental values. The lattice parameter values obtained here have been used in all the following calculations. Furthermore, the found bulk energy has been subtracted from the following results, such that all energies are the total surface energies. After this, the surface energies are determined by calculating the energies of the slabs shown in panels (a) and (b) in Fig. 1. All atoms with 12 nearest neighbors are considered as bulk atoms, i.e., they are assigned zero energy. All the energies are then placed on the rest of the atoms. For the (0001) surface, this is straightforward since all the remaining atoms sit in the same configuration, so the energy is just distributed evenly. However, for the $(10\bar{1}1)$ surface, there are two different types of surface atoms. In this case, we choose to distribute the surface energy proportional to the missing number of nearest neighbors. After this, we find the edge energy by calculating the energy of the slab shown in panel (c) in Fig. 1, which consists of repeated edges between the (0001) surface and the $(10\bar{1}1)$ surface. From the figure, it is clear that two types of atoms have not been assigned an energy, the ones in the inner and the ones in the outer edge. Again, we distribute the remaining energy among these atoms, proportionally to the number of missing nearest neighbors. Finally, we can find the step formation energy by calculating the energy of the slab shown in panel (d) in Fig. 1, where a step has been formed at the edge by removing a row of atoms. Here, there is only one type of atom, which has not been assigned an energy. By assigning the remaining energy to these, we ensure that the model gives correct step formation energies.

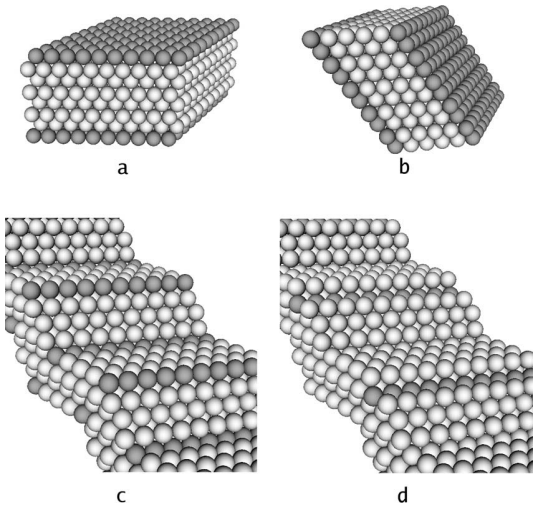

FIG. 1. Some of the surfaces for which energies have been calculated using DFT. The calculations are used to determine the energy of the gray atoms. Panel (a) shows the close-packed surface (0001). Panel (b) shows the $(10\bar{1}1)$ surface. The surfaces on panels (c) and (d) are repeated edges between the (0001) surface and the $(10\bar{1}1)$ surface with and without a step, respectively.

We did these calculations for the $(10\bar{1}0A)$, (0001), and $(10\bar{1}1)$ surfaces and all the edges between these since the ruthenium clusters almost entirely consist of these low-energy surfaces. Furthermore, we included the $(10\bar{1}0B)$ surface. Naturally, there will still be atoms sitting on the clusters in other configurations than those included here. These atoms have been assigned an energy based on the number of nearest neighbors alone. We obtain a relation between the energy and the number of nearest neighbors by averaging the already calculated energies. The atoms which are assigned an energy in this way are mainly corner atoms, i.e., it is a small part of the total energy.

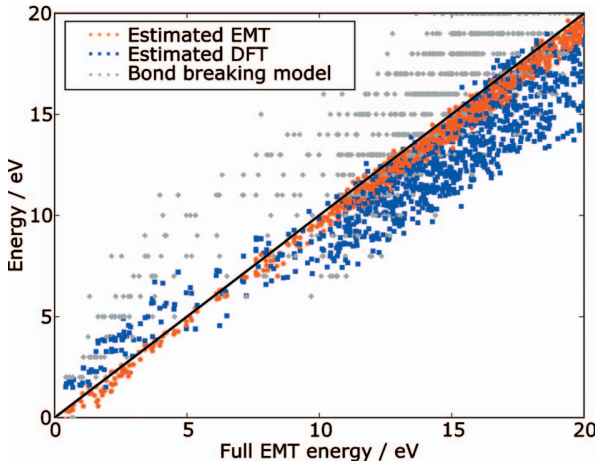

FIG. 2. (Color) A comparison between the energy obtained using four different methods. The estimated EMT, the estimated DFT, and the simple bond breaking model are all compared to the full EMT energy. Each point corresponds to a certain configuration of a 10 046 atom cluster. Points on black line indicate perfect agreement between the full EMT energy and the method in question. Energies are relative to the energy of the found ground state configuration. From this, we conclude that the estimated DFT is the preferred method in our situation (see text).

B. Test of the method

Since it is impossible to calculate the DFT energy of a large cluster, it is hard to test the accuracy of this method directly. So, instead we optimized an EMT potential for ruthenium.[21] With this potential, we went through all the same calculations as for the DFT potential and established an estimated EMT potential. With these three potentials, the estimated DFT, the estimated EMT, and the full EMT, we calculated the energy of a lot of different configurations of a 10 046 atom cluster. In Fig. 2, we have plotted the obtained energies using the estimated DFT and the estimated EMT versus the full EMT energy. For comparison, we also included a simple bond breaking model, where the energy is proportional to the number of broken nearest neighbor bonds. The figure shows that the estimated EMT model and the full EMT potential have better agreement than any of the others. From this, we conclude that the main difference between the full EMT potential and the estimated DFT potential is due to the change from EMT to DFT and not due to using the estimated DFT values instead of the exact values. In other words, calculating the cluster energy as a sum of atomic energies, which are estimated from surface calculations, is a better approximation than calculating the cluster energy using the EMT potential instead of the accurate DFT potential.

Another advantage of the estimated DFT model is that we are sure to get the high-accuracy DFT step formation energies at the edges, which are the most important energies in this case, since these step edge sites typically are the most catalytic active, as we will argue for later. These steps are badly described in the EMT model.

Finally, we tested the estimated DFT potential by calculating the energy of the $(30\bar{3}1)$ and $(1\bar{1}00)$ surfaces, which was not used in estimating the individual atomic energies. The results are shown in Table I, from which it is seen that the error per surface atom is very low, on the order of 0.01 eV/surface atom. All cluster energies in the following are determined using the estimated DFT model.

TABLE I. Comparison between full DFT surface energy and the estimated DFT surface energy of two surfaces, which were not used in the development of the estimated DFT potential.

Surface	Full DFT (eV/atom)	Estimated DFT (eV/atom)	Error (eV/atom)
$(30\bar{3}0)$	2.525	2.536	0.011
$(1\bar{1}00)$	2.377	2.371	−0.006

III. NUMBER OF SITES ON A CLUSTER

In this section, we present the developed method for finding the number of times a specific site occurs on a cluster of a given number of atoms. First, we go through the method of obtaining a ensemble of configurations for the cluster, and then we show how this ensemble can be used to obtain the number of sites at a given temperature using simple Boltzmann factor averaging. Finally, we perform some testing of the method.

A. Generating an ensemble

Clusters of several thousand atoms in size have almost endless different possible configurations, so it is completely impossible to calculate the energy of them all. Instead, we need a method which only searches through relevant configurations, i.e., configurations of low energy. The obvious choice in such a situation is some sort of Monte Carlo method, and we have in fact tried using the Metropolis algorithm. All close-packed configurations were allowed and the energy of each configuration was calculated using the EMT potential. By all close-packed configurations, we mean hcp and fcc including all possible stacking faults. Each new configuration was generated by moving one atom from one part of the cluster to another. The algorithm was able to find configurations with stacking faults, but they were too high in energy to contribute significantly to the ensemble.

The problem using such a method is that the potential energy surface contains many local minima with very high barriers between them, which can make the time it takes to search through a sufficient amount of the configurational space much too high except for the smallest clusters, unless one makes sure it is possible to jump directly through these barriers. Also, an algorithm based on genetic optimization was implemented, but it suffered from the same problems.

The limitations of these methods, however, inspired a way around the problems since they showed that all these low-energy configurations, in which the simulations got stuck, have some common characteristics. They are all clusters, which almost only consist of the (0001), $(10\bar{1}1)$, and $(10\bar{1}0)$ surfaces, possibly with some atoms missing near the edges or

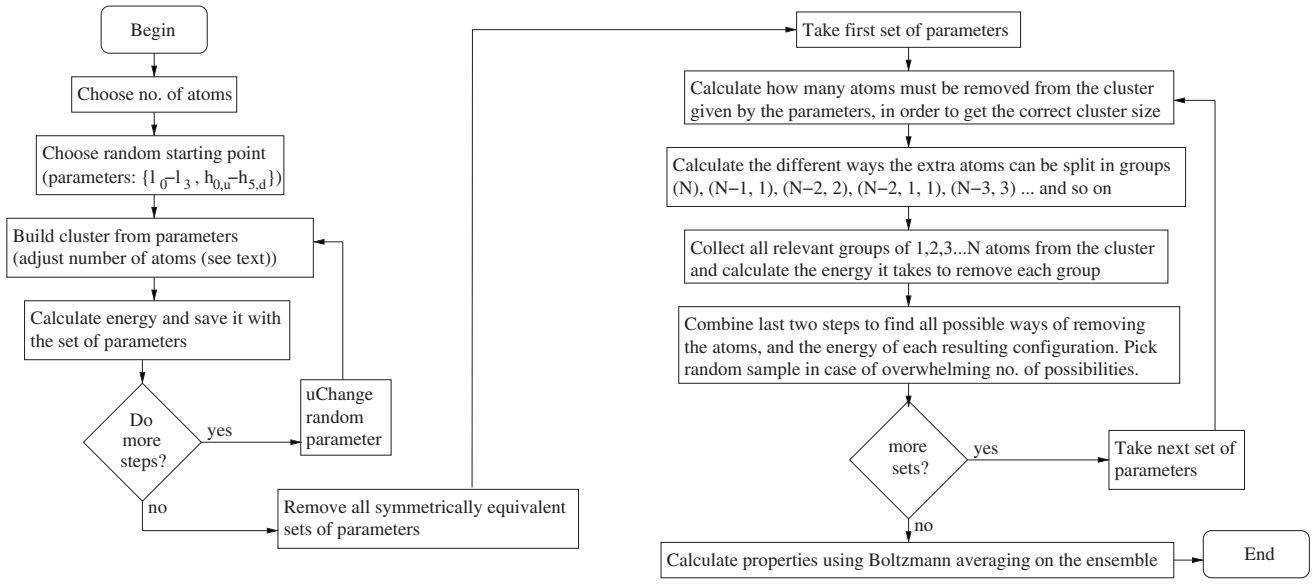

FIG. 3. Flowchart of the algorithm that collects an ensemble of relevant structures for a given cluster.

in a few cases a couple of adatoms placed on one of the surfaces. Because of this, we can restrict ourselves to search through configurations with these characteristics. The reason that only configurations with these characteristics are relevant is that the energy it takes to break a nearest neighbor bond is close to 0.5 eV, which is much higher than the thermal energy at all relevant temperatures. So, all odd configurations with holes in the surface or other cuts in the surface are way too high in energy.

We have not investigated the energy of non-close-packed structures, for example, structures with internal stress, which could be relevant for the smallest nanoparticles. However, high-resolution transmission electron microscopy studies of industrial Ru-based catalysts have shown nanoparticles with a regular hcp crystal structure.[14,22]

After having gained these experiences, we chose to divide the generation of the ensemble of structures into two steps. First, we find all the relevant clusters, which only consist of the (0001), $(10\bar{1}1)$ and $(10\bar{1}0)$ surfaces and with a number of atoms close to the desired cluster size. For each relevant cluster, we then adjust the number of atoms. If the number of atoms is too large, we search through the different ways one can remove the excess number of atoms; otherwise, we search through the ways one can add the lacking number of atoms.

A flowchart of the method is shown in Fig. 3, the details are described in the following sections.

1. Finding relevant cluster shapes

The first step is done by describing all relevant clusters through 16 parameters $\{l_0-l_3, h_{0,u}-h_{5,u}, h_{0,d}-h_{5,d}\}$, which are defined on Fig. 4. The total height of the cluster is not included since that is governed by the number of atoms. Any cluster only consisting of the (0001), $(10\bar{1}1)$, and $(10\bar{1}0)$ surfaces can be described by these 16 parameters. With this parametrization, it is now possible to escape the large barriers in the potential energy surface, i.e., it is possible to do a Metropolis Monte Carlo search through the configurational space, where one of the parameters is changed between each step. The energies used in the algorithm are not the energies of the cluster given by the 16 parameters since these cluster may not consist of the right number of atoms. Instead, the extra or lacking numbers of atoms have been removed or added at a favorable position on the cluster before calculating the energy.

Through a testing phase, it was found that a simulation temperature of 2 eV is optimal in this type of simulations. At this temperature, the simulations move rather freely between all relevant sets of parameters without spending too much time in irrelevant sets of parameters. The algorithm is run for a sufficient amount of steps, typically around 50 000, and then we pick out the sets of parameters with an energy below 5 eV above the lowest found energy. This limit was set to 5 eV since the removal and/or adding of extra and/or lacking

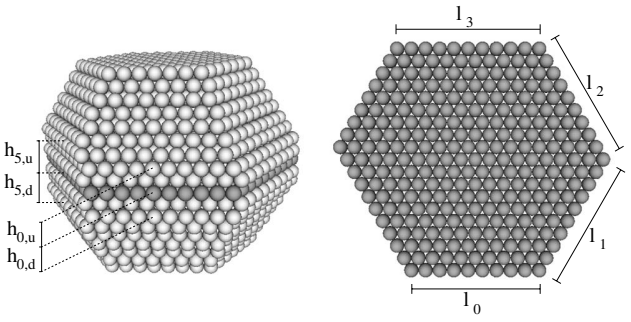

FIG. 4. The definition of the 16 parameters $\{l_0-l_3, h_{0,u}-h_{5,u}, h_{0,d}-h_{5,d}\}$ describing the cluster shape. $\{l_0-l_3\}$ are the dimensions of the basal plane, whereas $\{h_{0,u}-h_{5,u}\}$ and $\{h_{0,d}-h_{5,d}\}$ are the number of layers up and down to the edges between the (0001) surfaces and $(10\bar{1}1)$ surfaces.

atoms may not have been done in the optimal way; i.e., in the next part where we search through all the ways one can do this removal and/or adding, we may find lower energy configurations within these 16 parameters. After some testing, we found that it sometimes is possible to find configurations with up to 2 eV lower energy, i.e., by setting a 5 eV limit, we are reasonably sure to get all configurations with up to 3 eV higher energy than the ground state configurations. Later, we will see that this is enough.

We continue the simulations until we are confident that all relevant sets of parameters have been collected. This we test by looking at how many rotation symmetric and mirror symmetric pairs we have collected. Here, we find that more than half of all the symmetric versions are found, i.e., we feel confident that we rarely miss all the symmetric versions of a relevant configuration. After this, the collected set is reduced, such that it only contain symmetrically different clusters.

2. Removing excess atoms

After having collected all relevant sets of parameters, we then go through each set of parameters one by one and figure out how many different configurations each set of parameters correspond to, i.e., typically how many ways we can remove the excess number of atoms. Here, we only go through the ways to remove extra atoms since it is by far the most common situation and since the algorithm is very similar to the one that finds the ways to add lacking atoms.

If the excess number of atoms is N, then one could remove all N atoms from one part of the cluster but one could also remove $N-1$ atoms from one part and 1 from another or $N-2$ from one part and 2 from another and so forth. Furthermore, one could remove from three, four, five, and so on different parts of the cluster. In order to include all these possibilities, we start out by collecting all the ways one can remove one atom, a group of two atoms, a group of three atoms, and so on up to a group of N atoms. By a group, we mean atoms sitting next to each other. We only collect groups sitting near the edges, as illustrated in Fig. 5, since all others give too high an energy to be relevant.

After this, we go through all the different ways you can remove groups of atoms such that it adds up to N atoms, i.e., one group of N atoms, two groups of $N-n$ and n atoms, and so forth up to N groups of 1 atom. For each of these different ways, we use the already obtained data on the different ways the different group sizes can be removed and go through all combinations. In some cases, when N is large, the number of combinations is overwhelming. In these cases, we take a random set of combinations out, typically a set of 10 000 combinations for each group combination. In these cases, each of the random combinations are assigned a weighting factor of the number of configurations divided by 10 000, which is used in the Boltzmann averaging later such that we get the correct weighing between the configurations when we calculate properties of the clusters. Figure 5 shows a few different configurations for a 1670 atoms cluster. Panel (d) shows the found ground state configuration.

When we have gone through this for all the relevant sets of parameters, we have a huge set of configurations, which is a representative segment of all possible configurations with an energy below a certain limit value.

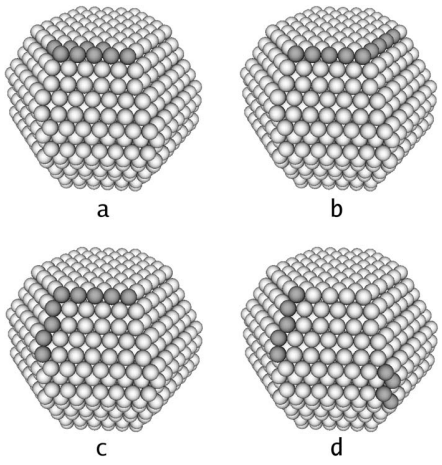

FIG. 5. Some different ways, one could remove nine atoms (gray) from a cluster. (a)–(c) show examples where all removed atoms are in one group. (d) shows an example where the atoms are removed in two groups (one of five and one of four atoms). The configuration shown in (d) is the found ground state configuration for a 1670 atom cluster.

B. Calculating properties

After having generated the ensemble of configurations, we can start calculating properties of the cluster. This is done using simple Boltzmann averaging, where the average value of a property O is calculated as

$$\langle O \rangle = \frac{\sum_i O_i w_i \exp\left[-\frac{E_i}{k_B T}\right]}{\sum_i w_i \exp\left[-\frac{E_i}{k_B T}\right]}, \tag{1}$$

where the sum goes over all configuration in the ensemble. O_i, w_i, and E_i are the value of property O, the weighting factor, and the energy of configuration number i. The weighting factor is the weighting factor introduced in the last section multiplied by a symmetry correction, which is the number of rotations and mirrorings which will result in a new configuration. This is included since the ensemble of configurations has been reduced such that configurations which only differ by a rotation or mirroring are removed. T is the temperature at which we want to know the average. The only property we calculate the average of here is the number of some specific sites. However, we could calculate many other properties of the clusters as well.

This way of averaging the configurations rely on the approximation that it is reasonable to only include configurations which are local minima on the potential energy surface in our ensemble. Ideally, we should also include the different entropies of the different minima. However, we used the developed EMT potential (see Sec. II) and compared a long constant temperature molecular dynamics simulation with

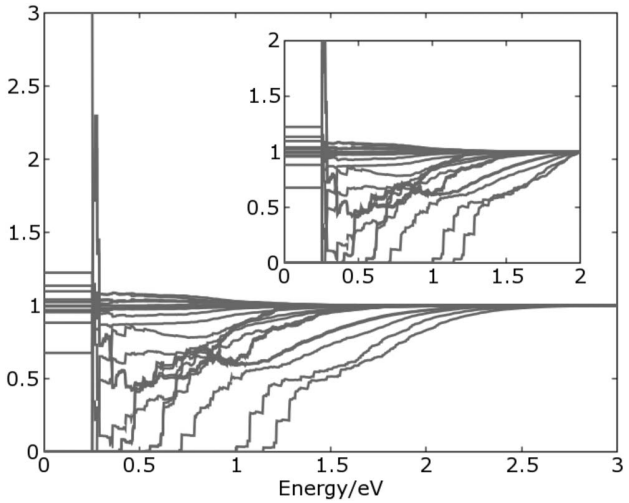

FIG. 6. Only configurations with a energy below a limit value are saved and used in the further calculations. The graph shows the found number of sites divided by the found number of sites with a limit energy of 3 eV above the ground state level for a 4000 atoms cluster as a function of the limit energy. Each line corresponds to a certain site type. The inset shows the same thing where the found number of sites are divided by the found number of sites with a limit energy of 2 eV instead of 3 eV. The asymptotic behavior when approaching 3 eV shows that 3 eV is a sufficiently high limit, whereas the inset shows that a limit of 2 eV is insufficient.

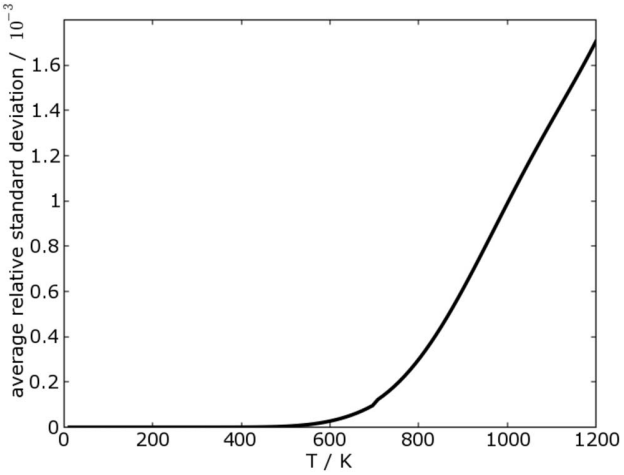

FIG. 7. An estimation of the statistical uncertainty in the calculations. The abundance of 22 different sites has been estimated in three completely independent calculations on a 4000 atoms cluster. For each site, the three estimations on the number of sites have been used to calculate the relative standard deviation. The graph shows the average of these relative standard deviations taken over the 22 different sites as a function of temperature. The low values (below 2×10^{-3} show that the statistical error is negligible).

the ensemble approach for a small cluster of 79 atoms and found that the difference was below 5%. This indicates that the curvatures of the different local minima are sufficient alike, such that the entropy does not vary much from minimum to minimum, i.e., the approximation seems valid.

C. Testing the method

When we collect configurations for the ensemble, we only include configurations which have an energy below a certain limit value. This is done to keep the amount of data down and is justified by the fact that low-energy configurations are more relevant than higher-energy configurations. In order to set this limit value, we made a calculation on a 4000 atom cluster and calculated the number of sites at 1200 K for 22 different types of sites with many different limit values. We chose this large cluster and this high temperature since we wanted an upper boundary on the limit value. Figure 6 shows the found number of sites relative to the found number of sites at a limit value of 3 eV as a function of the limit value. The graph clearly indicates asymptotic behavior toward 1 as the limit value goes toward 3 eV, i.e., we conclude that a limit value of 3 eV above the found ground state energy is sufficient. This is the limit value we have used in all further calculations. The inset in Fig. 6 shows the same plot, but here the number of sites is taken relative to the number of sites at a limit value of 2 eV. This graph does not show the same asymptotic behavior, i.e., a limit value of 2 eV is not sufficient.

There are two parts of the method that rely on random sampling. First of all, there is the Monte Carlo part where we expect we have found all relevant sets of parameters. Furthermore, there is the second part where we rely on random sampling of configurations. In order to check the statistical uncertainty that come from these random samplings, we made three separate simulations on a 4000 atoms cluster. For all three ensembles, we calculated the relative standard deviation on the number of sites for 22 different sites. Figure 7 shows the average of these relative standard deviations as a function of temperature. It is seen that the average relative standard deviation is below 2×10^{-3} at all temperatures below 1200 K, i.e., we conclude that the statistical error is negligible.

IV. CALCULATING THE REACTIVITY

When calculating the catalytic activity of a cluster, one should ideally pick out every type of surface site present on the cluster and calculate the contribution to the catalytic activity from each of these. However, since the catalytic activity is completely dominated by a few highly active sites, we can neglect the contribution from all other sites and only focus on these. In the following, we present the obtained results. First, we show the size dependence of the number of active sites. Second, we combine these results with obtained barrier heights for the dissociation of nitrogen in order to see how the ammonia synthesis activity depends on the cluster size.

A. Number of active sites

In the dissociation of nitrogen, we expect the dominating sites to be step sites since they possess low-coordinated surface atoms, which from the *d*-band model[23,24] are predicted

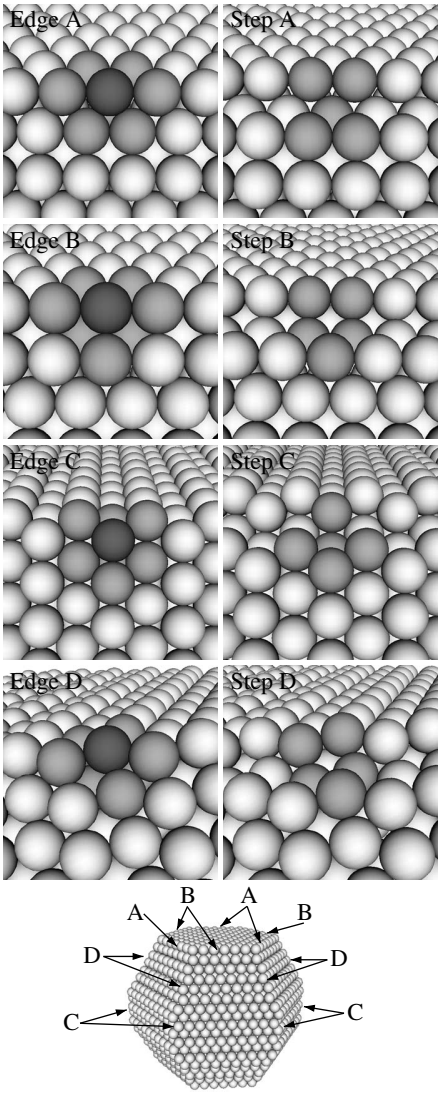

FIG. 8. Definitions of four different edges. Completed edges are seen to the left and stepped edges to the right. The color differences indicate the definitions of the sites. A completed edge site is defined by a dark gray atom having exactly the nearest neighbors sitting as the light gray atoms does. A stepped edge site is defined by a free position having exactly the nearest neighbors sitting as the light gray atoms. Edges A and B connect the (0001) surfaces and $(10\bar{1}1)$ surfaces. Edge C connects two $(1010A)$ surfaces. Edge D connects two $(10\bar{1}1)$ surfaces. Step site B is known as the B_5 site.

to give the largest weakening of the bond. Furthermore, the nitrogen molecule can bind to more surface atoms at the foot of a step.[13] For this reason, we have focused our analysis in the four step sites shown in Fig. 8. These step sites are most likely to be found at the edges of the cluster, so for comparison we have also shown the same edges without the step in Fig. 8.

Figure 9 shows the average number of these four step sites as a function of the number of atoms in the cluster in the range between 396 and 416 atoms. The black and gray lines correspond to temperatures of 300 and 1200 K, respectively. From the graphs, it is clear that this is a regime where

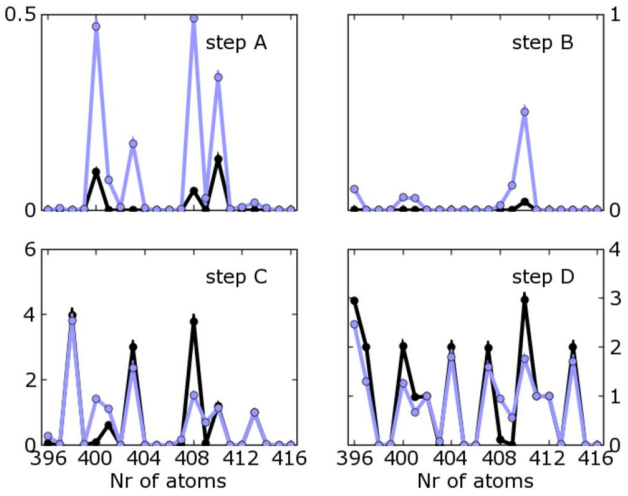

FIG. 9. (Color online) The number of step sites as a function of the number of atoms in the cluster. The four step sites are defined in Fig. 8. The black curve is at a temperature of 300 K, whereas the gray (light blue) is at 1200 K. 400 atoms corresponds to a cluster with approximately 1.8 nm diameter.

the addition or removal of a single atom has a huge impact on the properties of the cluster. This is an expected behavior at the nanometer scale and is one of the many challenges and opportunities that comes when decreasing the size of structures down to a few nanometers.

The black lines in the graphs of Fig. 9 also show that the average number of sites is near integer at 300 K. This indicates that the ground state configuration dominates at this temperature such that the integer values are the number of step sites in the ground state configuration. At 1200 K, the points are not so bound to the integer values, i.e., at this temperature, the higher-energy configurations are important as well. However, the graphs indicate a rather small temperature dependence on the number of sites.

Figure 10 shows the average number of these four step sites as a function of the number of atoms in the cluster in the range between 1000 and 1009 atoms. These graphs show less rapid variations in the average number of sites indicating that the single atom influence on the properties begin to loose the importance at these cluster sizes. This may be the first estimation of the size at which the properties of a cluster will cease to change dramatically due to the addition or removal of a single atom.

From the graphs in Fig. 10, it is also seen that the tendency toward having near integer values of the average number of sites at 300 K is not so big at these larger clusters. That is not so surprising since the number of possible configurations is much higher at larger clusters, i.e., the ground state configuration will be less dominant. Furthermore, it is seen from the graphs that a higher temperature has a stronger tendency to smear out the size effects rather than increasing the number of step sites as one might intuitively expect.

When performing real experiments, it is unfortunately impossible to measure the exact number of atoms in the clusters that are present on a sample. So in order to present some results which are more comparable to experiment, we need to

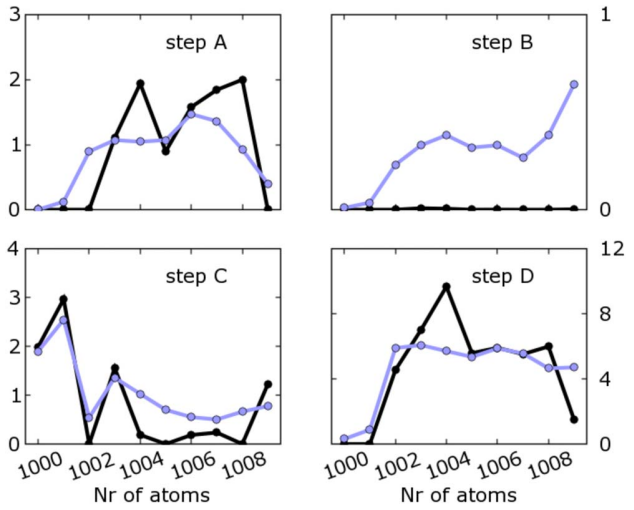

FIG. 10. (Color online) The number of step sites as a function of the number of atoms in the cluster. The four step sites are defined in Fig. 8. The black curve is at a temperature of 300 K, whereas the gray (light blue) is at 1200 K. 1000 atoms corresponds to a cluster with approximately 2.7 nm diameter.

do some averaging over several cluster sizes. Figure 11 shows the number of step sites per volume at 300 K and at 1200 K as a function of cluster diameter. Each point is an average of approximately 60 different clusters evenly distributed in the diameter range of ±0.1 nm around the desired diameter. All cluster sizes in the range contribute equally to the average, no attempt is made to take into account that some cluster sizes, for example, corresponding to closed shells, might be more abundant since this would depend on

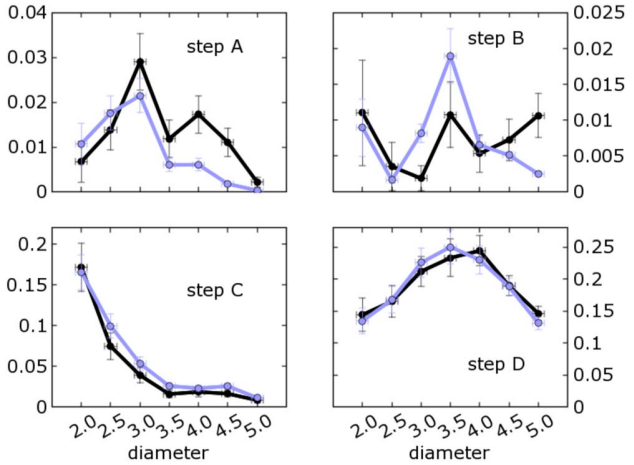

FIG. 11. (Color online) The number of step sites per volume as a function of the cluster diameter. The four step sites are defined in Fig. 8. The black curve is at a temperature of 300 K, whereas the gray (light blue) is at 1200 K. Each point is an average of approximately 60 different clusters. The uncertainty in the diameter indicates the spread in cluster sizes, whereas the uncertainty in the number of sites is the average standard deviation of the number of sites obtained from the 60 different clusters. The unit in the y axis is nm^{-3}.

the details of how the clusters were produced.

The figures clearly indicate that the size dependency is different for the different types of sites. For step site A, there is apparently a maximum at 3 nm, which is more significant at 1200 K compared to 300 K. For step site B, there seems to be a maximum at a diameter of 3.5 nm. However, the curve is not very smooth, especially at 300 K, the variations are large. For step site C, the curve seems to increase monotonically for decreasing cluster size, whereas for step site D, the curve is smooth with a maximum around 3.5–4.0 nm depending on the temperature. This illustrates very well the complexity involved when trying to understand the size scaling of cluster properties. From the graphs, it is also seen that the uncertainties are smaller at 1200 K than at 300 K. This is a consequence of the smearing of the cluster size effects by the temperature, which was also seen above.

The obtained values for the number of sites are quite low. It is approximately an order of magnitude lower than the rough estimates made by Honkala *et al.*[14] For example, for step site B (B_5), we get a peak value between 1.5 and 2.5 μmol/g at 3.5 nm in diameter where they find a peak value of 30 μmol/g at 2 nm diameter. However, our peak is a bit broader, so they would probably get approximately a factor 10 lower reaction rate, if our results for step site B was used in their work, which is a change in the wrong direction compared to experiments. However, they only include the contribution from the B_5 site and in the next section, we show that step sites A and D probably give significant contributions to the overall rate. Furthermore, it is not impossible that other factors, which are not included in the model, influence the presence of step sites. For example, it is likely that the presence of gas will increase the number of step sites since the adsorption energy typically is higher at step sites compared to flat surfaces, which would favor the presence of step sites. Furthermore, the presence of a substrate could influence the presence of step sites, at least through the limitations it would give on the topological freedom. This will be the topic of later publications.

B. Activity versus cluster size

In order to illustrate how these data on the occurrence of special sites can be used to get the catalytic activity, we have calculated the dissociation barrier of nitrogen on all four step sites since nitrogen dissociation is the rate limiting step in the ammonia synthesis. These calculations were done using density functional theory. Figure 12 shows the obtained initial, transition, and final states for all four step sites. The initial and final states have been obtained by keeping the surface atoms fixed and making a local minimization of the energy by changing the position of the nitrogen atoms. The initial states are not the lowest-energy molecular absorbed states. In all four cases, these states are found when the nitrogen molecule sticks out of the surface from the top of a surface atom. However, the energy barriers for going down to the shown initial states are much smaller than the barrier found for the actual splitting of the molecule. The barrier of dissociation is then found by making a local minimization of the energy by changing the position of the nitrogen molecule

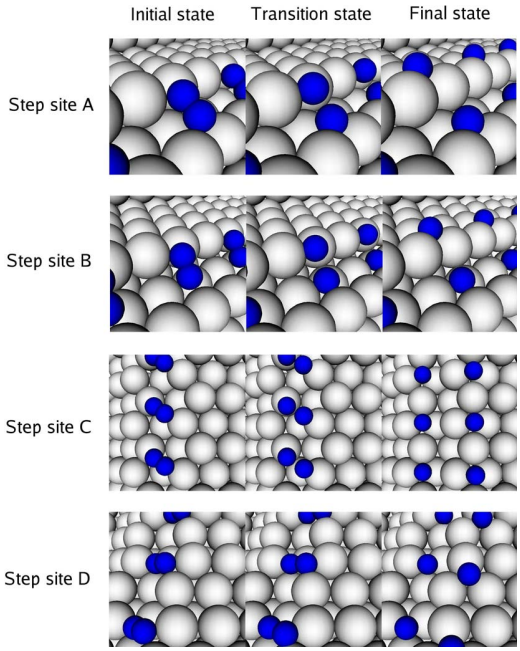

FIG. 12. (Color online) The splitting of a nitrogen molecule on the four different step sites defined in Fig. 8. The initial states are just local minima and not the lowest-energy absorption states. However, in all cases, the barrier between the lowest-energy absorption states and the initial state is lower than the barrier between the initial state and the final state, i.e., the energies of the transition states are the true barrier energies for the dissociation.

for different fixed values of the molecular bond length. From that, we get the energy as a function of bond length, which is shown on Fig. 13 for all the four different step sites.

All barrier heights are compared to the gas phase level since this is the relevant activation energy at relevant pressures and temperatures, where the coverage is low.[10] From this, we see that step site C has a large barrier of more than 2 eV with respect to the gas phase level, which means that it is practically catalytic inactive. The barrier height is even higher than the barrier on the flat close-packed surface (0001).[25] The barrier is approximately the same for step sites A and B, i.e., 0.59 eV, with respect to gas phase level. This is a bit higher than what has earlier been reported for step site B (Ref. 10), which is known as the B_5 site. This difference is due to the fact that we calculate the barrier for a step sitting on the edge of a cluster, whereas Ref. 10 calculates the barrier for a step sitting on a surface, i.e., the neighboring environment is a bit different. The energy barriers on the nonstepped edges in Fig. 8 are much higher, so they do not contribute to the activity.

A very simple approximation of the catalytic activity in the ammonia synthesis for the four different step sites can be obtained from the found barrier heights by writing the activity as

$$r = A \exp\left[-\frac{E_a}{k_B T}\right], \tag{2}$$

where E_a is the barrier height with respect to gas phase level. We do not include the adsorbed molecular state explicitly since it is in equilibrium with the gas phase and has a low coverage at relevant pressures and temperatures.[10] k_B and T are the Boltzmann constant and the temperature, respectively. A is the prefactor, which depends on the equilibrium constants of the other reaction steps and the gas pressures. However, we assume that the prefactor is the same on all the sites since we only need a rough estimate of the activity of the different cluster sizes relative to each other. In this way, we avoid making detailed calculations of all the elementary partial reactions in the ammonia synthesis for all the differ-

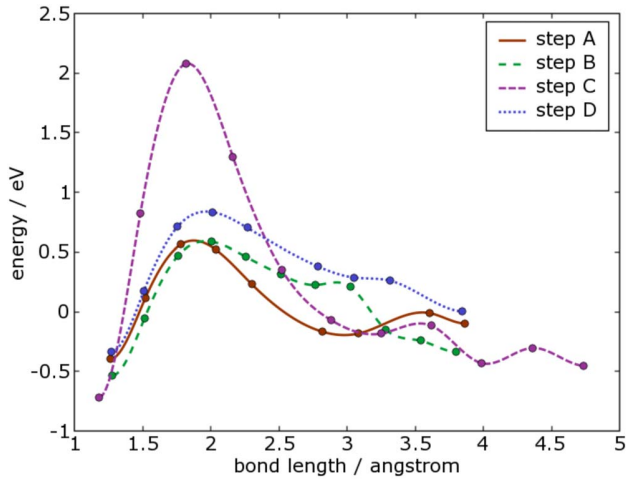

FIG. 13. (Color online) The energy as a function of the nitrogen bond length for the dissociation of a nitrogen molecule on the four different sites defined in Fig. 8. All energies are relative to the gas phase energy. The lines are cubic splines connecting the actual calculation points.

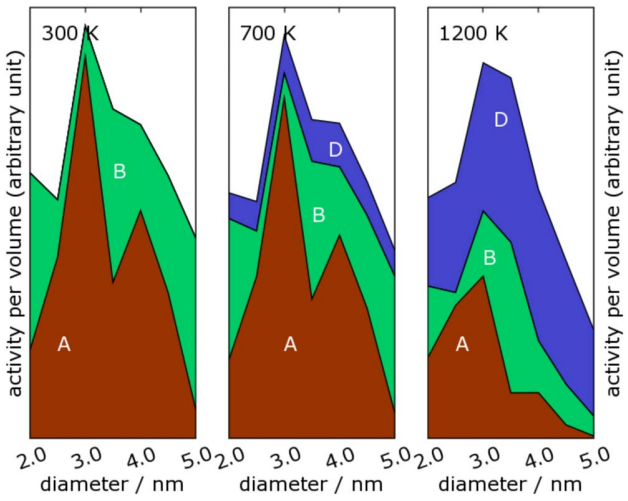

FIG. 14. (Color online) The total catalytic activity of ruthenium clusters in the ammonia synthesis as a function of the cluster diameter. The different colors indicate how much the different step sites contribute to the total activity. The activity peaks at a cluster size of 3 nm.

ent sites, as it was done for the B_5 site by Logadóttir and Nørskov.[10]

The catalytic activities obtained from Eq. (2) can then be multiplied by the number of sites present on the clusters to obtain the catalytic activity per volume catalyst as a function of cluster diameter, which is seen in Fig. 14. The graphs at 300 and 700 K indicate a maximum in the catalytic activity per volume catalyst at a cluster diameter of 3 nm, even though the curve is not so smooth. At 300 K, it is clearly seen that all the catalytic activity comes from step sites A and B, whereas step site D start contributing at 700 K. At 1200 K, the picture is a bit more clear and smooth. There still seems to be a optimal cluster diameter at 3 nm. The existence of such a maximum fits well with the experimental observation that the catalytic activity of a sample can increase after sintering the smallest Ru particles.[26] Furthermore, it is seen that step site D also contributes to the total activity at this higher temperature due to fact that it is more present on the clusters than the two others and the fact that the difference in barrier height becomes less important as temperature increases. The ammonia synthesis typically runs at a temperature around 700 K in industrial catalysts.

V. SUMMARY

We have developed a method to determine detailed structural information of ruthenium clusters in the diameter range from 1.5 to 5 nm. The method can directly be applied to other hcp metals and with minor modifications, it can be applied to other structures as well. We find that the number of catalytic active step sites does not change much with temperature within reasonable temperature ranges. The role of the temperature is more to smooth out some of the strong size dependence. At very small cluster sizes, the structure depends sensitively on the exact number of atoms. We find that this strong single atom dependence begin to cease at cluster sizes around 1000 atoms. We find that the dependence on the presence of step sites with respect to the cluster diameter is significantly different for the different types of step sites. This illustrates the complexity involved in understanding size dependencies. Finally, we made density functional theory calculations in order to get the barrier of dissociation for nitrogen on the different step sites. This barrier was used to estimate the ammonia synthesis activity of the different step sites. This information was combined with the structural information to obtain the catalytic activity versus cluster size. Here, we found that the optimal cluster diameter is approximately 3 nm.

ACKNOWLEDGMENTS

The authors wish to thank J. K. Nørskov and I. Chorkendorff for fruitful discussions and for reading this paper. The Center for Individual Nanoparticle Functionality (CINF) is sponsored by the Danish National Research Foundation. This work was supported by the Danish Center for Scientific Computing.

*schiotz@fysik.dtu.dk

[1] E. H. G. Backus, A. Eichler, M. L. Grecea, A. W. Kleyn, and M. Bonn, J. Chem. Phys. **121**, 7946 (2004).
[2] M. A. van Daelen, M. Neurock, and R. A. van Santen, Surf. Sci. **417**, 247 (1998).
[3] N. M. Galea, D. Knapp, and T. Ziegler, J. Catal. **247**, 20 (2007).
[4] B. Hammer, Surf. Sci. **459**, 323 (2000).
[5] S. Kandoi, J. Greeley, M. A. Sanchez-Castillo, S. T. Evans, A. A. Gokhale, J. A. Dumesic, and M. Mavrikakis, Top. Catal. **37**, 17 (2006).
[6] I. N. Remediakis, F. Abild-Pedersen, and J. K. Nørskov, J. Phys. Chem. B **108**, 14535 (2004).
[7] M. Mavrikakis, J. Rempel, J. Greeley, L. B. Hansen, and J. K. Nørskov, J. Chem. Phys. **117**, 6737 (2002).
[8] J. G. Wang and B. Hammer, J. Chem. Phys. **124**, 184704 (2006).
[9] Y. Zhu, Y. Dai, D. Chen, and W. Yuan, J. Mol. Catal. A: Chem. **264**, 299 (2007).
[10] Á. Logadóttir and J. K. Nørskov, J. Catal. **220**, 273 (2003).
[11] S. Linic and M. A. Barteau, J. Am. Chem. Soc. **125**, 4034 (2003).
[12] K. Reuter and M. Scheffler, Phys. Rev. B **73**, 045433 (2006).
[13] S. Dahl, Á. Logadóttir, R. C. Egeberg, J. H. Larsen, I. Chorkendorff, E. Törnqvist, and J. K. Nørskov, Phys. Rev. Lett. **83**, 1814 (1999).
[14] K. Honkala, A. Hellman, I. N. Remediakis, A. Logadottir, A. Carlsson, S. Dahl, C. H. Christensen, and J. K. Nørskov, Science **307**, 555 (2005).
[15] K. W. Jacobsen, P. Stoltze, and J. K. Nørskov, Surf. Sci. **366**, 394 (1996).
[16] K. W. Jacobsen, J. K. Nørskov, and M. J. Puska, Phys. Rev. B **35**, 7423 (1987).
[17] B. Hammer, L. B. Hansen, and J. K. Nørskov, Phys. Rev. B **59**, 7413 (1999).
[18] D. Vanderbilt, Phys. Rev. B **41**, 7892 (1990).
[19] G. Kresse and J. Furthmuller, Comput. Mater. Sci. **6**, 15 (1996).
[20] The DACAPO code is available as a part of the CAMPOS software (www.camp.dtu.dk/Software).
[21] We use the form of the EMT potential which is described by Jacobsen *et al.* (Ref. 15). The potential was optimized to give most accurate cohesive energy, lattice parameters, elastic constants, and surface energies possible for Ruthenium by changing six parameters defined by Jacobsen *et al.* (Ref. 15). We found these optimal values: $E_0=-6.3505$ eV, $V_0=12.3052$ eV, $s_0=1.4984$ Å, $\eta_2=3.9452$ Å^{-1}, $\kappa=6.5612$ Å^{-1}, and $\lambda=6.7015$ Å^{-1}.
[22] T. W. Hansen, J. B. Wagner, P. L. Hansen, S. Dahl, H. Topsøe, and C. J. H. Jacobsen, Science **294**, 1508 (2001).
[23] B. Hammer and J. K. Nørskov, Nature (London) **376**, 238 (1995).
[24] B. Hammer and J. K. Nørskov, Surf. Sci. **343**, 211 (1995).
[25] J. J. Mortensen, Y. Morikawa, B. Hammer, and J. K. Nørskov, J. Catal. **169**, 85 (1997).
[26] C. J. H. Jacobsen, S. Dahl, P. L. Hansen, E. Törnqvist, L. Jensen, H. Topsøe, D. V. Prip, P. B. Møenshaug, and I. Chorkendorff, J. Mol. Catal. A: Chem. **163**, 19 (2000).

Paper II

Δ self-consistent field method to obtain potential energy surfaces of excited molecules on surfaces

Jeppe Gavnholt, Thomas Olsen, Mads Engelund,* and Jakob Schiøtz†
Danish National Research Foundation's Center for Individual Nanoparticle Functionality (CINF), Department of Physics, Technical University of Denmark, DK-2800 Kongens Lyngby, Denmark
(Received 9 June 2008; revised manuscript received 15 July 2008; published 27 August 2008)

We present a modification of the Δ self-consistent field (ΔSCF) method of calculating energies of excited states in order to make it applicable to resonance calculations of molecules adsorbed on metal surfaces, where the molecular orbitals are highly hybridized. The ΔSCF approximation is a density-functional method closely resembling standard density-functional theory (DFT), the only difference being that in ΔSCF one or more electrons are placed in higher lying Kohn-Sham orbitals instead of placing all electrons in the lowest possible orbitals as one does when calculating the ground-state energy within standard DFT. We extend the ΔSCF method by allowing excited electrons to occupy orbitals which are linear combinations of Kohn-Sham orbitals. With this extra freedom it is possible to place charge locally on adsorbed molecules in the calculations, such that resonance energies can be estimated, which is not possible in traditional ΔSCF because of very delocalized Kohn-Sham orbitals. The method is applied to N_2, CO, and NO adsorbed on different metallic surfaces and compared to ordinary ΔSCF without our modification, spatially constrained DFT, and inverse-photoemission spectroscopy measurements. This comparison shows that the modified ΔSCF method gives results in close agreement with experiment, significantly closer than the comparable methods. For N_2 adsorbed on ruthenium (0001) we map out a two-dimensional part of the potential energy surfaces in the ground state and the 2π resonance. From this we conclude that an electron hitting the resonance can induce molecular motion, optimally with 1.5 eV transferred to atomic movement. Finally we present some performance test of the ΔSCF approach on gas-phase N_2 and CO in order to compare the results to higher accuracy methods. Here we find that excitation energies are approximated with accuracy close to that of time-dependent density-functional theory. Especially we see very good agreement in the minimum shift of the potential energy surfaces in the excited state compared to the ground state.

DOI: 10.1103/PhysRevB.78.075441 PACS number(s): 31.15.xr, 31.50.Df, 82.20.Gk

I. INTRODUCTION

Density-functional theory[1,2] (DFT) has proved to be a vital tool in gaining information on many gas-surface processes. This may be surprising, since DFT is only valid for relaxed systems in their ground state and therefore not directly applicable to dynamical situations. However, often the electrons relax much faster than the time scale of the atomic movement, such that the electron gas can be considered relaxed in its ground state at all times. Then potential energy surfaces (PES) of the ground state obtained by DFT, or any other method, can be used to describe the motion of atomic cores. This is the Born-Oppenheimer approximation.

In some situations, however, the Born-Oppenheimer approximation is not valid. This is for example the case when the electronic system is excited by a femtosecond laser[3,4] or hot electrons are produced with a metal-insulator-metal junction.[5] The Born-Oppenheimer approximation also breaks down if the time scales for the electronic and nuclear motions are comparable or if the separations between the electronic states are very small, such that transitions between the electronic states will occur. In these situations it is necessary to go beyond the Born-Oppenheimer approximation either by considering the coupling between electronic states[6,7] where it becomes necessary to obtain PESs of excited states, or by an electronic friction model.[8,9]

The problem of calculating excitation energies is being approached in many different ways, even within DFT. Time dependent density-functional theory[10] (TDDFT) gives, compared to the computational cost, good agreement with experiments for excitations in atoms and molecules.[11] However, TDDFT suffers some problems in excitations involving charge transfer.[12] The GW approximation[13,14] can be used to gain accurate excitation energies for molecules and clusters. The embedding method,[15,16] which combines high-accuracy quantum chemistry methods with DFT, makes it possible to handle larger periodic systems with great accuracy. The embedding theory has been applied to estimate PESs of excited molecules on surfaces.[17] However, the computational cost and involved complexity are still very high. Our aim has been to find a method, which at a computational cost close the level of ground-state DFT, can estimate excited-state energies of molecules on surfaces with reasonable accuracy. Such a method would make it more feasible to consider a large range of systems in search of systems with interesting or desired properties.

Constrained DFT (Refs. 7, 18, and 19) and Δ self-consistent field (ΔSCF) (Refs. 20 and 21) are two different approaches, which both can be considered as small extensions of ground-state DFT, such that the computational cost lies close to that of ground-state DFT. In constrained DFT an additional potential is introduced and varied until a certain constraint on the electrons is fulfilled. The simplest approach is to lower (or increase) the potential in a certain part of space until you have the desired number electrons in this area.[18] A different approach is to introduce potentials on the orbitals in a localized basis set, which depends on the orbitals' positions in space.[7] In Sec. III we will argue that when

 ©2008 The American Physical Society

considering molecular resonance states on surfaces it may be problematic with such a strict constraint on the electrons, since a part of the charge may return to the surface on a much shorter time scale than the lifetime of the resonance.

In the ΔSCF scheme the positions of the electrons are controlled by controlling the occupation of the Kohn-Sham (KS) states as the system reaches self-consistency. The ΔSCF scheme has for a long time been justified in cases, where the excited state corresponds to the lowest state of a given symmetry.[22] The scheme has, however, often been applied to more general cases. More recently, Görling[23] extended the KS formalism to include excited states, such that ΔSCF gets a formal justification in the general case, although a special unknown orbital-dependent exchange-correlation potential should be used for the excited states. In practical implementations standard exchange-correlation potentials from ground-state DFT are typically used.

This traditional way of just controlling the occupation of the KS orbitals has some limitations. For example when a molecule is placed on a metallic surface the molecular orbitals will hybridize with the orbitals in the surface, such that the molecular orbitals will be spread over several KS states. For such systems there is no good way of representing a resonance on the molecule as a change in the occupations of the KS orbitals. The optimal thing one can do within this scheme is to occupy the KS orbital with the largest overlap with the molecular orbital in question, but this overlap can be quite small and highly system size dependent. This problem was also pointed out by Hellman *et al.*[21] and Behler *et al.*[7]

In this paper we modify the ΔSCF approach, such that electrons are allowed to occupy arbitrary linear combinations of KS orbitals. In this way one achieves much better control on the position of the excited electron. As is the case for traditional ΔSCF some knowledge of the resonance is needed in order to apply the method. The method is especially relevant in Newns-Anderson-type[24,25] systems, where a resonance can be attributed to a known single level, which has been hybridized through interactions with other states. This includes systems with molecules adsorbed on metal surfaces and molecules trapped between to metal contacts.

The modification we propose only has minor implications on the way practical calculations are performed, which is very similar to performing an ordinary ground-state DFT calculation. In the following we will go through the details of the method and apply it to a few diatomic molecules on metallic surfaces. The obtained results will be compared to the ordinary ΔSCF method, spatially constrained DFT, and inverse-photoemission spectroscopy (IPES) measurements. Finally we present some tests on the performance of the ΔSCF approach on N_2 and CO in the gas phase.

II. METHOD

In the following we go through the differences between the linear-expansion ΔSCF method we propose, ordinary ΔSCF, and standard DFT. We start by stating the modification of the KS equations when considering an electron excited from the Fermi level to a higher lying state. Then we show how this affects the energy calculation. Finally we generalize the approach to other types of excitations.

A. Kohn-Sham equations

The fundamental KS equations[2] represent a practical way of finding the ground-state electron density for a given external potential and a given number of electrons through an iterative process

$$\left[-\frac{\nabla^2}{2}+v_{\mathrm{KS}}[n](\mathbf{r})\right]\psi_i(\mathbf{r})=\epsilon_i\psi_i(\mathbf{r}), \tag{1}$$

$$n(\mathbf{r})=\sum_{i=1}^{N}\psi_i^{\square}(\mathbf{r})\psi_i(\mathbf{r}), \tag{2}$$

$$v_{\mathrm{KS}}[n](\mathbf{r})=v_{\mathrm{ext}}(\mathbf{r})+\int d\mathbf{r}'\frac{n(\mathbf{r}')}{|\mathbf{r}-\mathbf{r}'|}+\frac{\delta E_{xc}}{\delta n(\mathbf{r})}, \tag{3}$$

where v_{KS} is the KS potential, E_{xc} is the exchange-correlation energy, and N is the number of electrons. As seen from Eq. (2) only the N orbitals with lowest energy contribute to the density, i.e., the electrons are placed in these orbitals.[26] In ordinary ΔSCF one estimates properties of excited states by placing the electrons differently. For example the HOMO-LUMO gap in a molecule could be estimated by replacing Eq. (2) with

$$n(\mathbf{r})=\sum_{i=1}^{N-1}\psi_i^{\square}(\mathbf{r})\psi_i(\mathbf{r})+\psi_a^{\square}(\mathbf{r})\psi_a(\mathbf{r}), \tag{4}$$

where $\psi_a(\mathbf{r})$ is the KS orbital resembling the LUMO from the ground-state calculation. Naturally, the KS orbitals found when solving these modified KS equations will differ from the ones found in an ordinary DFT calculation due to the change in the Hamilton through the change in the density when different orbitals are occupied.

In the linear-expansion ΔSCF method we propose, the excited electron is not forced to occupy a KS orbital, but can occupy any orbital that is a linear combination of empty KS orbitals

$$\psi^{\mathrm{res}}(\mathbf{r})=\sum_{i=N}^{M}a_i\psi_i(\mathbf{r}), \tag{5}$$

where M is the number of KS orbitals in the calculation. In practice this means that the KS many-particle wave function is no longer just a Slater determinant of N KS orbitals, but a Slater determinant of $N-1$ KS orbitals and $\psi^{\mathrm{res}}(\mathbf{r})$. Only empty KS orbitals are included in the linear expansion, since otherwise $\psi^{\mathrm{res}}(\mathbf{r})$ will not be orthogonal to the filled KS orbitals. Equation (2) is then replaced with

$$n(\mathbf{r})=\sum_{i=1}^{N-1}\psi_i^{\square}(\mathbf{r})\psi_i(\mathbf{r})+\sum_{i,j=N}^{M}a_i^{\square}a_j\psi_i^{\square}(\mathbf{r})\psi_j(\mathbf{r}). \tag{6}$$

Since the expansion coefficients a_i in principle could have any value some *a priori* knowledge are needed in order to choose good values. In the case of molecular resonances on surfaces the expansion coefficients are chosen such that

$\psi^{\mathrm{res}}(\mathbf{r})$ resembles the relevant molecular orbital as much as possible, i.e.,

$$a_i = \frac{\langle \psi_i | \phi \rangle}{\left(\sum_i |\langle \psi_i | \phi \rangle|^2 \right)^{1/2}}, \tag{7}$$

where ϕ is the molecular orbital. This is consistent with a Newns[24] and Anderson[25] picture, where the resonance corresponds to an electron getting in the molecular orbital, but the resonance broadening and energy shift are due to hybridization with the metallic bands and an image charge effect.

In calculations with k-point sampling the linear expansion is performed independently in all k points. In the linear-expansion ΔSCF one then avoids the difficulties one can encounter in choosing which KS state to occupy in each k point in the traditional way of performing ΔSCF calculations. For example, one may risk occupying different bands in each k point, when just choosing the KS orbital with the largest overlap with the molecular orbital in each k point.

B. Energy

The energy calculation, which is performed after the KS equations have reached self-consistency, is not significantly different in the linear-expansion ΔSCF scheme compared to ordinary DFT. The Hartree energy is evaluated directly from the density, which is also the case for the exchange-correlation energy if an orbital independent functional is used. So in linear-expansion ΔSCF these terms are evaluated exactly as in ordinary DFT. In ordinary DFT the kinetic energy is evaluated as

$$T[n(\mathbf{r})] = \sum_{i=1}^{N} \langle \psi_i | -\frac{\nabla^2}{2} | \psi_i \rangle = \sum_{i=1}^{N} \epsilon_i - \int v_{\mathrm{KS}}[n](\mathbf{r}) n(\mathbf{r}) d\mathbf{r}, \tag{8}$$

where the last equality is seen directly from Eq. (1). Similarly the expression for the kinetic energy in the linear-expansion ΔSCF is found to be

$$T[n(\mathbf{r})] = \sum_{i=1}^{N-1} \epsilon_i + \sum_{i=N}^{M} |a_i|^2 \epsilon_i - \int v_{\mathrm{KS}}[n](\mathbf{r}) n(\mathbf{r}) d\mathbf{r}. \tag{9}$$

For orbital-dependent exchange-correlation functionals some effort must be put into ensuring that the exchange-correlation energy is evaluated correctly. This should however be quite straightforward since all the occupied orbitals are known.

C. Gradients

Gradients of PESs are easily evaluated in ordinary DFT due to the Hellman-Feynman theorem. The Hellman-Feynman theorem, however, only applies to eigenstates and not linear expansions of eigenstates. Due to this there is no easy way of gaining the gradients in a linear-expansion ΔSCF calculation. In Sec. IV C we will show that the Hellman-Feynman gradients do in fact not match the true gradients.

D. Other excitations

Above we only considered excitations where an electron is removed from the Fermi energy and placed in some specified orbital. The method is, however, easily extended to other types of excitations by representing each removed and each added electrons as linear expansions of KS orbitals. Equation (6) then gains an extra sum for each extra linear expansion. In cases of removed electrons the sign should of course be negative and the sum be over KS states below the Fermi energy. Similarly Eq. (9) gains extra sums.

E. Implementation

We have implemented the method in GPAW,[27,28] which is a real-space DFT code that uses the projector-augmented waves[29,30] (PAW) formalism to represent the core electrons. The self-consistent electron density is determined by an iterative diagonalization of the KS Hamiltonian and Pulay mixing of the resulting density.[31] For calculations on single molecules we use the local-density approximation[32] (LDA) as well as revised Perdew-Burke-Ernzerhof (RPBE) (Ref. 33) to describe exchange and correlation effects. The LDA is used because we compare to TDDFT results obtained using the adiabatic local-density approximation (ALDA),[34] and RPBE is used to see whether or not the generalized gradient description improves results. For calculations on molecules at surfaces we only use RPBE because this is designed to perform well for molecules adsorbed on transition-metal surfaces.

The projection step described in Sec. II A can easily be approximated within the PAW formalism if the atomic orbitals are chosen as partial waves; see Appendix for details.

For reasons of comparison we have also made a few linear-response TDDFT (lrTDDFT) calculations. These have been made using the OCTOPUS code,[35,36] which is a real-space TDDFT code using norm-conserving pseudopotentials to represent core electrons.

III. MOLECULES ON SURFACES

The linear-expansion ΔSCF method is especially relevant for molecules on metallic surfaces because the molecular state, due to hybridization, is spread over many KS states, i.e., it is necessary to write the resonant state as a linear combination of KS states. In this section we will make a detailed investigation of the 2π resonance of N_2 on a ruthenium (0001) surface. Furthermore we apply the proposed method to several diatomic molecules on different metallic surfaces and compare the results to other methods and experiments. Finally we map out a part of the PESs for N_2 on ruthenium (0001) and use it to estimate how much energy could possibly be put into molecular motion from an electron hitting the resonance.

A. 2π resonance energy for N_2 on ruthenium

The two top panels in Fig. 1 show the 2π resonance energy for N_2 on a ruthenium (0001) surface as a function of the system size, i.e., the surface unit cell and the number of ruthenium layers.

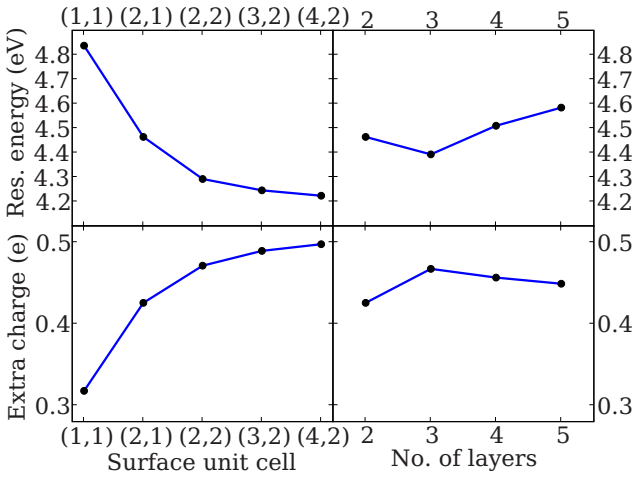

FIG. 1. (Color online) Upper row: The 2π resonance energy of N_2 molecule on a ruthenium surface. Lower row: The extra charge on the N_2 molecule in the resonance compared to a ground-state calculation. Left panels are for two layers and different surface cells, i.e., different N_2 coverages. Right panels are for a (2,1) surface cell and different number of layers. The extra amount of charge is estimated using Bader decomposition (Refs. 37 and 38).

The resonance energy is the total-energy difference between a resonant calculation and a ground-state calculation, both performed with atomic positions corresponding to the minimum of the ground-state PES (vertical resonance energies). We minimize the energy in the ground-state calculations by keeping all surface atoms frozen and found that the nitrogen molecule is placed on top with the two nitrogen atoms placed 2.084 and 3.201 Å above the surface. In the resonance calculation the $2\pi_y$ orbital of the N_2 molecule has been expanded on all KS states above the Fermi energy. This expansion has been used as ψ^{res} in Eq. (5). Although an extra electron is placed on the molecule we keep the total number of electrons unchanged, such that the unit cell is neutral. This is reasonable because a charged molecule will form an image charge in the surface, keeping the entire system neutral.

The resonance energy is converged to within 0.1 eV at a surface unit cell of (2,2). The rather large variation in energy for smaller unit cells is probably due to dipole interactions between periodic images. This is confirmed by a simple estimation of the dipol-dipol interaction energies. The resonance energy is not influenced significantly by the number of layers in the ruthenium, indicating that the charge redistribution only occurs very near to the surface. That the charge redistribution is local is confirmed by Fig. 2, which shows the change in charge between the resonance calculation and the ground-state calculation for four different surface unit cells.

For the larger unit cells, where the resonance energy has converged, a clearly localized image charge is seen below the nitrogen molecule and above the first layer of ruthenium atoms. The area with extra charge clearly resembles the 2π orbital of nitrogen, indicating that the 2π orbital is well represented by the linear expansion of KS orbitals. Figure 2 also reveals that some charges are redistributed within the molecule.

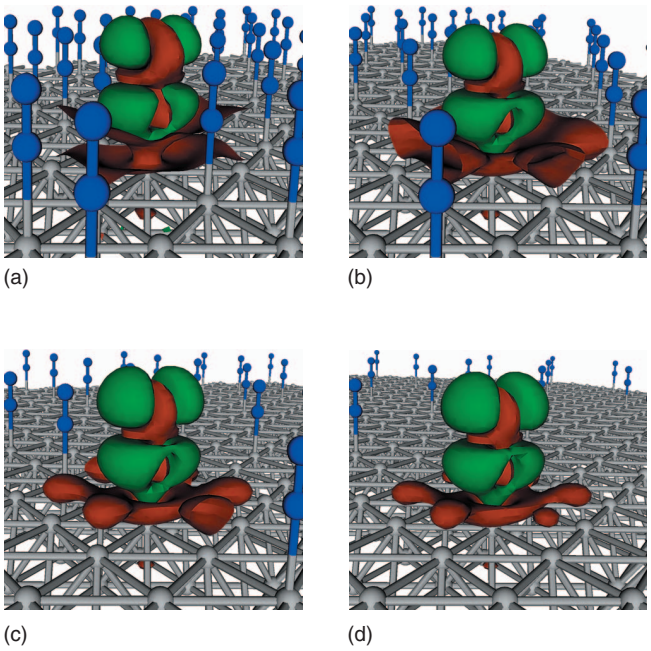

FIG. 2. (Color) The change in charge distribution due to the excitation. Green: more charge (0.01 a.u. contour), red: less charge (−0.01 a.u. contour). The four figures are for four different surface unit cells: (1,1), (2,1), (2,2), and (4,2). Gray atoms are ruthenium and blue atoms are nitrogen. The periodic images of the atoms are also shown, whereas the density changes are only shown in one unit cell.

In order to get an estimate of the size of the charge redistribution we also performed Bader decomposition[37,38] on the density found in the ground-state calculation and the resonance calculation. The two bottom panels in Fig. 1 show the extra charge assigned to the nitrogen molecule in the resonance calculation compared to the ground-state calculation as a function of system size. The converged value is close to 0.5 electron charge, i.e., only half of the electron is placed on the nitrogen molecule according to the Bader decomposition. This discrepancy could either be due to the ambiguity in the way one chooses to assign charge to the atoms or a more physical effect of charge going back into the surface when extra charge is placed on the molecule. The former reason is very likely, since the image charge is located very close to the molecule.

In order to investigate the effect of charge going back into the surface we start by considering the 2π orbital itself. Figure 3 shows the density of KS states and the projected density of states (PDOS) for the 2π orbital for the ground-state calculation and the resonance calculation. In the ground-state calculation a part of the long tail of the PDOS goes below the Fermi energy, i.e., a small part of the 2π orbital is occupied here. In the resonance calculation the PDOS has moved upward in energy such that the tail no longer goes below the Fermi energy, i.e., some charges go back into the surface as charge is placed on the molecule. Similar effects are seen for the other molecular orbitals as visualized in Fig. 4, which shows the PDOS for the 3σ, 4σ, 1π, and 5σ orbitals. Again it is seen that all the PDOSs are shifted up in energy as more

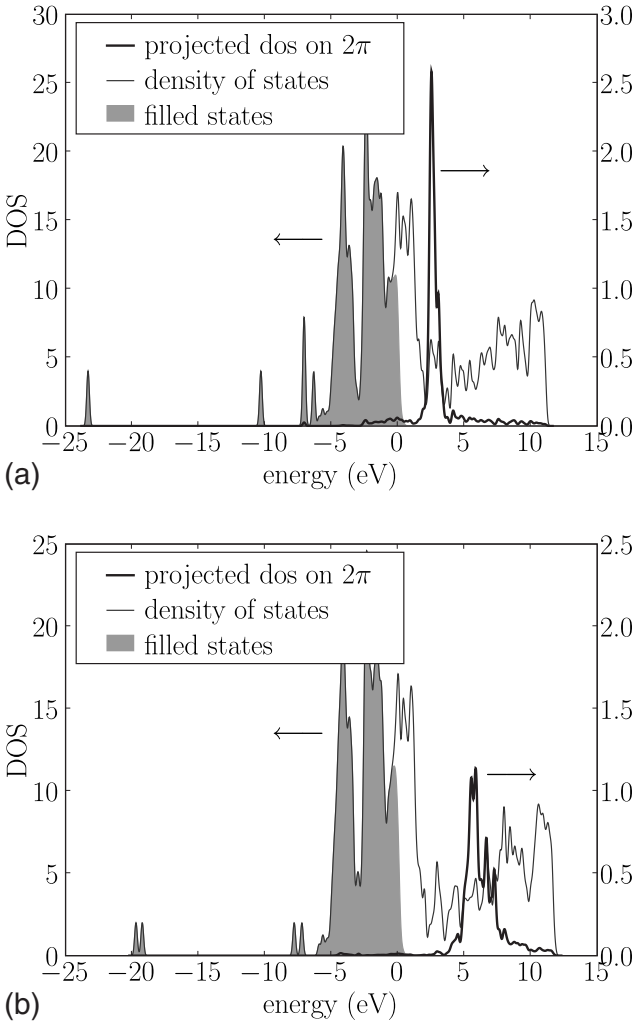

FIG. 3. The density of states for a N_2 molecule on a ruthenium slab and the projected density of states on the 2π orbital of the N_2 molecule. Top: Ground-state calculation. Bottom: Resonance calculation.

charge is placed on the molecule. Almost the entire PDOSs are still under the Fermi level, but small ripples can be seen above the Fermi level, also contributing to the amount of charge going back into the surface.

This backtransfer of charge is not an unwanted effect, since we try to model the long-lived resonance state, i.e., the reasonably localized peak in the PDOS in Fig. 3. The backtransfer of charge is due to some on the energy scale very delocalized bands, indicating a much shorter lifetime, i.e., the backtransfer is expected to happen on a much shorter time scale than the decay of the resonance. It is however clear from Figs. 3 and 4 that the charge backtransfer in this case is far from the 0.5 electron indicated by the Bader decomposition. We then conclude that the main part of the discrepancy in this situation can be assigned to the ambiguity in the way charge is assigned to the different atoms. We also find that one gets significant different results by assigning charge in a different manner, for example, by dividing the charge by a flat plane midway between the surface and the molecule.

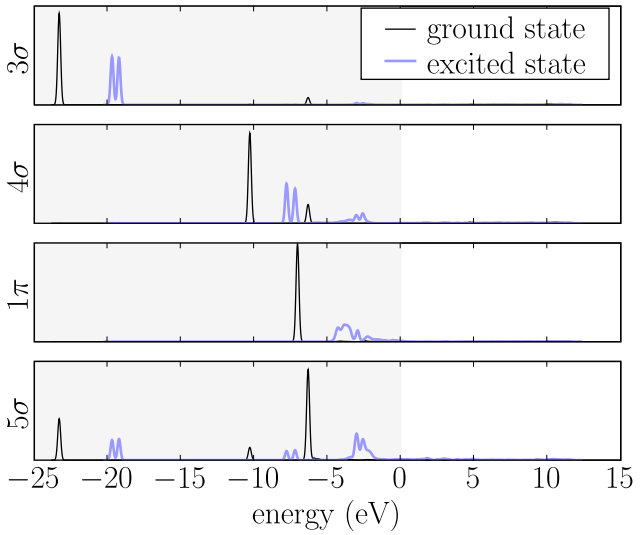

FIG. 4. (Color online) Projected density of states (PDOS) on the 3σ, 4σ, 1π, and 5σ orbitals of a N_2 molecule sitting on a ruthenium slab. The PDOSs are plotted for both the ground-state calculation and the resonance calculation. The gray area indicates energies below the Fermi level.

B. Comparison with inverse-photoemission spectroscopy experiments

In Table I we have tested the linear-expansion ΔSCF method against inverse-photoemission spectroscopy measurements and compared the results to spatially constrained DFT and ordinary ΔSCF calculations. The modified ΔSCF values are all calculated in exactly the same manner as for N_2 on ruthenium in Sec. III A. In all cases the molecules sit on top, and all surface atoms were kept fixed during the minimization of the molecular degrees of freedom. For the

TABLE I. Comparison of the 2π resonance energies for different diatomic molecules on different surfaces found by spatially constrained DFT, ordinary ΔSCF, our modified ΔSCF, and experiments. The experimental results have been obtained from inverse-photoemission spectroscopy measurements. All energies are in eV. We have not included lrTDDFT calculations, since it is not applicable to periodic systems.

System	Constrained DFT	ΔSCF (orig.)	ΔSCF (this work)	Experiment
N_2 on Ni(001)	2.2	3.5	4.0	4.4[a]
CO on Ni(001)	2.2	3.2	4.2	4.0[a]/4.5[b]
NO on Ni(001)	2.2	0.6	1.4	1.6[a]/1.5[c]
CO on Ni(111)	2.8	4.3	4.4	4.4[c]
NO on Ni(111)	2.7	0.5	1.4	1.5[b]
CO on Pd(111)	4.6	4.1	4.9	4.7[d]
CO on Pd step	2.8	3.2	4.5	4.0[d]

[a]Johnson and Hulbert (Ref. 39).
[b]Reimer *et al.* (Ref. 40).
[c]Reimer *et al.* (Ref. 41).
[d]Rogozik and Dose (Ref. 42).

TABLE II. The positions of the molecules in the systems from Table I. All positions are relative to the closest surface atom. The z direction is normal to the surface. At the Pd step the CO molecule is tilted over the step, which is the reason for the composant in the y direction. All numbers are in Angstroms.

Surface	Molecule	Pos. of 1. atom	Pos. of 2. atom
Ni(001)	N_2	N: (0,0,1.638)	N: (0,0,2.798)
	CO	C: (0,0,1.456)	O: (0,0,2.621)
	NO	N: (0,0,1.404)	O: (0,0,2.580)
Ni(111)	CO	C: (0,0,1.774)	O: (0,0,2.941)
	NO	N: (0,0,1.758)	O: (0,0,2.935)
Pd(111)	CO	C: (0,0,1.904)	O: (0,0,3.064)
Pd step	CO	C: (0,0.586,1.801)	O: (0,0.844,2.934)

Ni (001) surface we used three atomic layers, for the Ni (111) and Pd surfaces we used two atomic layers. The positions of the molecules in their minimized position are given in Table II. All resonance energies are vertical from the minimum of the ground-state PES. The relevant resonance for all the considered systems is the 2π resonance.

The spatially constrained DFT method was suggested by Wu and Van Voorhis.[18,19] In the calculations we perform here we divide the space into two areas divided by the flat plane mid between the surface and the lowest atom in the molecule. We the apply a potential $V=V_0[1+\exp(\frac{z_0-z}{\Delta z})]^{-1}$, with $\Delta z=0.2$ Å and z_0 being the z value of the dividing plane. V_0 is varied until an extra electron is placed on the molecules side of the dividing plane compared to the unconstrained calculation. The energy is then calculated as described by Wu and Van Voorhis.[18,19] The results using the original ΔSCF method have all been obtained by forcing an electron in the KS orbital with the largest overlap with the 2π orbital.

The results obtained with our proposed modification of the ΔSCF method are seen to agree quite well with the experimental results, better than the spatially constrained DFT and the original ΔSCF methods. All the results obtained by the original ΔSCF approach lie too low, which is due to the fact that the large hybridization of the molecular orbitals makes it impossible to place sufficient charge on the molecule. However, a significant problem with this method is that PESs often become discontinuous if one chooses to occupy the KS orbital with the largest overlap with the molecular orbital, since this can be different orbitals at different configurations.

The major problem with the spatially constrained DFT method seems to be that it in some cases is a too strict criterion to force an extra electron on the molecule, which reflects itself in similar resonance energies for CO and NO. We find that the backtransfer of charge discussed in Sec. III A is significant for adsorbed NO and essential to obtain the resonance energies we find with the modified ΔSCF method. This indicates that the spatially constrained DFT approach is more suited for systems with a smaller coupling than one has on the metallic surfaces considered here. The good agreement between our modified ΔSCF method and experiments indicates that this method is preferable for these kinds of systems and that the backtransfer effect is indeed physically reasonable.

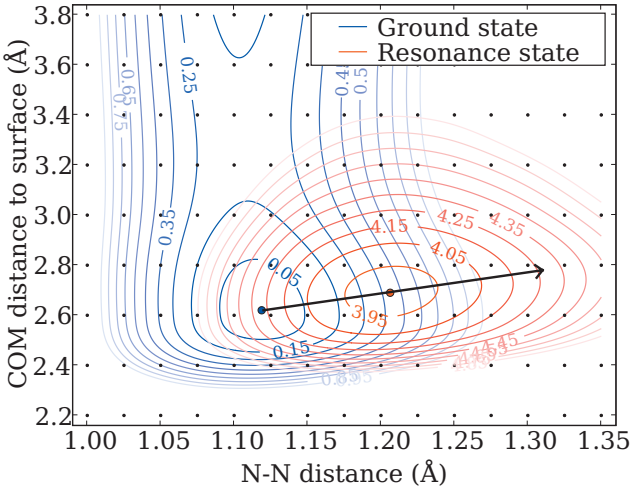

FIG. 5. (Color) Potential energy surfaces (PES) for a nitrogen molecule on a close-packed ruthenium surface in the ground state and the $2\pi_y$ resonance as a function of the distance between the two nitrogen atoms and the distance from the surface to the center of mass of the nitrogen molecule. The energies are in eV. The small dots represent the points where the energy has been calculated in order to generate the surfaces. The black arrow represents a possible trajectory of the system in the resonance state (see text).

C. Potential energy surfaces for N_2 on ruthenium

In Fig. 5 we have mapped out a part of the potential energy surfaces for a nitrogen molecule on a ruthenium (0001) surface in the ground state and the $2\pi_y$ resonances. We limit ourselves to two dimensions, which at least is reasonable in the ground state, since here it is well known that the molecule sits vertically on an on-top site. In the resonance state we have tried to rotate the molecule a small angle around the surface atom in the x and y directions at several points on the PES. In all cases this leads to an increase in energy, i.e., it also seems reasonable to stay within the two dimensions in the resonance state. Here we will only apply the PES to a simple estimate of the possible energy transfer into molecular motion from an electron hitting the resonance. For a more detailed analysis it is necessary to include other dimensions.

The ground-state PES looks as expected, with a small barrier for desorption and a local minimum corresponding to the adsorption configuration. The resonance PES has a shifted minimum, which indicates that an electron hitting this resonance could induce molecular motion, since a sudden shift between the PESs would leave the system far away from the minimum, such that the atoms would start to move. The maximum possible energy gain assuming classical ion dynamics from a single electron hitting the resonance can be roughly estimated by following the black arrow in Fig. 5. The system is most likely situated at the local minimum of the ground-state PES when the electron hits the resonance. The black arrow shows a possible trajectory of the system in

TABLE III. Vertical excitation energies for the N_2 molecule taken from the minimum-energy configuration of the ground state. All theoretical results are obtained using LDA as the *xc* potential (and ALDA for the *xc* kernel in the lrTDDFT calculations).

State	Transition	$\Delta\epsilon_{KS}$[a]	TDDFT[b] (ALDA)	ΔSCF (LDA)	ΔSCF (RPBE)	Exp.[c]
$a^1\Pi$			9.23	8.75	8.58	9.31
	$5\sigma\rightarrow 2\pi$	8.16				
$B^3\Pi$			7.62	7.55	7.52	8.04
Singlet-triplet splitting:			1.61	1.20	1.06	1.27
$w^1\Delta$			10.27	10.50	10.52	10.27
	$1\pi\rightarrow 2\pi$	9.63				
$W^3\Delta$			8.91	8.94	8.79	8.88
Singlet-triplet splitting:			1.36	1.56	1.73	1.39
$o^1\Pi$			13.87	11.97	12.40	13.63
	$4\sigma\rightarrow 2\pi$	11.21				
$C^3\Pi$			10.44	10.37	10.61	11.19
Singlet-triplet splitting:			3.43	1.60	1.79	2.44

[a]KS eigenvalue differences.
[b]Linear-response calculations taken from Grabo *et al.* (Ref. 44).
[c]Computed by Oddershede *et al.* (Ref. 45) using the spectroscopic constants of Huber and Herzberg (Ref. 46).

the resonance state until the resonance decays and the system returns to the ground-state PES. The potential energy after the electron event in this optimal situation is approximately 1.5 eV higher than before the event. This is seen to be more than enough to desorb the molecule. A more detailed analysis involving calculations of the possible vibrational excitations and the probabilities of exciting them will be the topic of a future publication. Such an analysis will have to take all six degrees of freedom of the molecule into account.

The PESs show that the center of mass is shifted away from the surface when the resonance is occupied. This may seem counterintuitive since the charged molecule is attracted to the generated image charge in the surface. However, the resonance weakens the bond between the nitrogen atoms, such that the distance between them increases, which shifts the center of mass outwards as the lower atom is not free to move closer to the surface. This effect is more significant than the decrease in the ruthenium-nitrogen distance due to the mentioned image charge effect.

IV. SMALL MOLECULES

In the following we present some small tests performed on N_2 and CO. These small systems have the advantage that they make it possible to compare to more accurate linear-response time-dependent density-functional theory calculations. When possible we also compare to experiments. The only advantage of our modified ΔSCF compared to ordinary ΔSCF for these molecules is the possibility of handling degenerate states without getting convergence problems, i.e., the following should be viewed as a test of the ΔSCF approach rather than a test of our modification. We are especially interested in confirming the ability to predict the shift of the minimum when going from the ground-state PES to the excited-state PES, which we in Sec. III C argued is very important when considering molecular motion induced by an electron hitting a molecular resonance.

A. Excitation energies

We have used the linear-expansion ΔSCF in combination with the multiplet sum method[43] to calculate excitation energies for different excitations in the N_2 and CO molecules. The results are presented in Tables III and IV, respectively. The 4σ and 5σ states are both represented by a single KS orbital. The 1π and 2π states are both double degenerate, so they are both represented as a linear combination of two KS orbitals: $|\pi\rangle=\frac{1}{\sqrt{2}}|\pi_{\mathrm{KS},a}\rangle+i\frac{1}{\sqrt{2}}|\pi_{\mathrm{KS},b}\rangle$, where $|\pi_{\mathrm{KS},a}\rangle$ and $|\pi_{\mathrm{KS},b}\rangle$ are the two degenerate KS orbitals. The imaginary unit i has been included in order to get the correct angular momentum of the excited states (Π and Δ). This would not be possible using traditional ΔSCF, where one only has the freedom to change occupation numbers of the KS states. Due to the rotational symmetry of the density found from these states the calculations do not suffer from any convergence difficulties. That is not the case if one just occupies one of the degenerate KS orbitals. Only the Δ states are included in the $1\pi\rightarrow 2\pi$ transitions in Tables III and IV, since the Σ states cannot be estimated by the multiplet sum method.[43] This is, however, not a problem for the kinds of systems for which

TABLE IV. Vertical excitation energies for the CO molecule taken from the minimum-energy configuration of the ground state. All theoretical results are obtained using LDA as the *xc* potential (and ALDA for the *xc* kernel in the lrTDDFT calculations).

State	Transition	$\Delta\epsilon_{KS}$[a]	TDDFT[b] (ALDA)	ΔSCF (LDA)	ΔSCF (RPBE)	Exp.[c]
$A^1\Pi$			8.44	7.84	7.81	8.51
	$5\sigma\rightarrow 2\pi$	6.87				
$a^3\Pi$			6.02	6.09	6.02	6.32
Singlet-triplet splitting:			2.42	1.75	1.79	2.19
$D^1\Delta$			10.36	10.82	10.73	10.23
	$1\pi\rightarrow 2\pi$	9.87				
$d^3\Delta$			9.24	9.72	9.55	9.36
Singlet-triplet splitting:			1.12	1.10	1.18	0.87
$C^1\Pi$				13.15	13.09	
	$4\sigma\rightarrow 2\pi$	11.94				
$c^3\Pi$			11.43	12.26	12.09	11.55
Singlet-triplet splitting:				0.89	1.00	

[a]KS eigenvalue differences.
[b]Linear-response calculations taken from Gonis *et al.* (Ref. 47).
[c]Computed by Nielsen *et al.* (Ref. 48).

this method is intended, such as molecules on surfaces where high-accuracy alternatives are still lacking.

In general the excitation energies found by the linear-expansion ΔSCF method look quite good for the low-lying excitations. The accuracy is only slightly worse than that of lrTDDFT and significantly better than just taking KS eigenvalue differences. The singlet triplet splittings are also rather close to the experimental values. The method however seems to struggle a bit more in the higher lying $4\sigma\rightarrow 2\pi$ transitions. This could indicate that the method should only be applied to low-lying excitations. Changing the exchange-correlation functional from LDA to RPBE does not affect the accuracy significantly although a small tendency toward better performance is seen for the higher lying excitations. We note, however, that the intended application of ΔSCF do not include simple diatomic molecules, where more accurate quantum chemical methods are available.

B. Excited potential energy surfaces

The shapes of the potential energy surfaces can in some cases be more important than the exact height of them, i.e., a constant error is not so critical. This is for example the case when considering chemistry induced by hot electrons.[5,49] In order to get an idea of the accuracy with which the linear-expansion ΔSCF method reproduces correct shapes of potential energy surfaces we have calculated the potential energy surfaces for the ground state and two excited states in the N_2 molecule. These are plotted in Fig. 6 together with results from lrTDDFT calculations.

The small differences between the two ground-state curves are due to the fact that they have been calculated with two different codes. Both codes are real-space codes, but gpaw uses the PAW formalism to represent the core electrons whereas OCTOPUS uses norm-conserving pseudopotentials. The calculations have been made with the same grid spacing

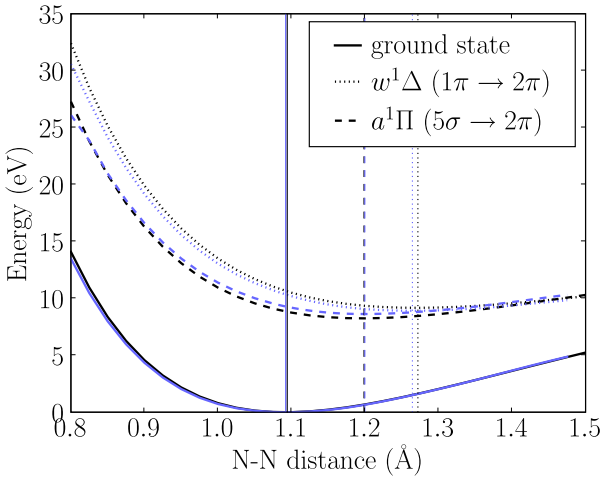

FIG. 6. (Color online) The energy as a function of bond length for the N_2 molecule in the ground state and two excited states. The black lines correspond to ΔSCF calculations, the gray (online: light blue) lines correspond to linear-response calculations. The linear-response calculations have been made using OCTOPUS (Refs. 35 and 36). The vertical lines indicate the positions of the minima.

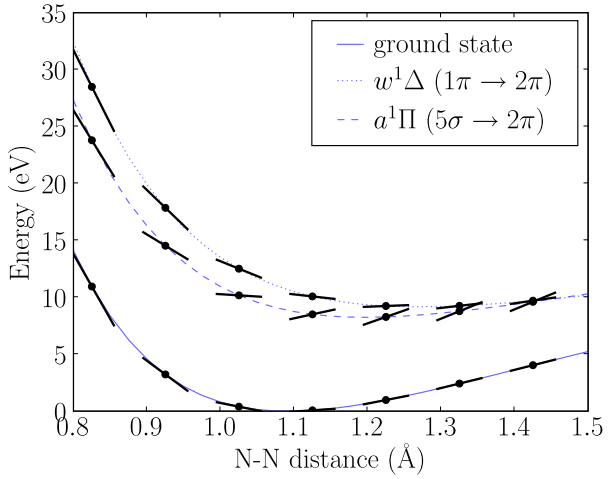

FIG. 7. (Color online) The energy as a function of bond length for the N_2 molecule in the ground state and two excited states. The short thick lines indicate the size of the gradients.

and unit-cell size and with the same exchange-correlation potential (LDA/ALDA).

The shapes of the potential energy surfaces found from the two different methods are seen to be very similar. Especially the predicted positions of the minima are seen to agree very well. The shifting of the minima toward larger bond lengths is also the expected behavior, since an electron is moved from a bonding orbital to an antibonding orbital. When going to bond lengths beyond 2 Å we start having problems with convergence problems in the ΔSCF calculations, since the 2π orbital ceases to exist. This is not a problem we have encountered in the systems with a molecule on a surface.

The good agreement between ΔSCF and lrTDDFT probably reflects that ΔSCF and ignoring the history dependence of the exchange-correlation potential in TDDFT are related approximations. For example, the density obtained in ΔSCF would be stationary if evolved in time with TDDFT.

C. Gradients

As mentioned in Sec. II C the Hellman-Feynman theorem does not apply in the linear-expansion ΔSCF method. This is verified by the calculations shown in Fig. 7. Here the energies of the ground state and two excited states in the N_2 molecule are plotted as a function of the bond length. The short thick lines indicate the gradient given by calculated Hellman-Feynman forces. For the ground state the agreement is as expected perfect, but for the excited states there is a clear mismatch. Unfortunately this implies that it is computationally heavy to do dynamics or minimizations in the excited states.

V. SUMMARY

We have extended the ΔSCF method of calculating excitation energies by allowing excited electrons to occupy linear combinations of KS states instead of just single KS states. This solves the problems encountered for molecules near surfaces, where the molecular orbitals hybridize, such that none of the KS orbitals can be used to represent an extra electron placed on the molecule. The method has been implemented in gpaw[27,28] and applied to several systems.

From calculated potential energy surfaces of N_2 on a ruthenium surface we concluded that an electron hitting the 2π resonance in this system can induce molecular dynamics due to the different positions of the minima of the ground-state PES and the resonance PES. Through a simple analysis we found that one electron can optimally place 1.5 eV in the atomic motion, more than enough to desorb the molecule.

We find good agreement between the model and inverse photoemission experiments for several diatomic molecules on different metallic surfaces. For the considered systems we find significantly better agreement with experiments using the modified ΔSCF method compared to spatially constrained DFT and traditional ΔSCF.

Finally we applied the method to N_2 and CO in their gas phases we found that excitation energies are estimated with quite good accuracy for the lower lying excitations, comparable to that of TDDFT. Especially the shape of the potential energy surfaces and the positions of the minima agree well with TDDFT results.

ACKNOWLEDGMENTS

The authors wish to thank Jens Jørgen Mortensen and Anders Hellman for fruitful discussions. The Center for Individual Nanoparticle Functionality (CINF) is sponsored by the Danish National Research Foundation. This work was supported by the Danish Center for Scientific Computing.

APPENDIX: OVERLAPS USING PAW PSEUDOWAVE FUNCTION PROJECTIONS

The projector augmented wave[29] method utilizes that one can transform single-particle wave functions $|\psi_n\rangle$ oscillating wildly near the atom core (all-electron wave functions) into smooth well-behaved wave functions $|\tilde{\psi}_n\rangle$ (pseudowave functions) which are identical to the all-electron wave functions outside some augmentation sphere. The idea is to expand the pseudowave function inside the augmentation sphere on a basis of smooth continuations $|\tilde{\phi}_i^a\rangle$ of partial waves $|\phi_i^a\rangle$ centered on atom a. The transformation is

$$|\psi_n\rangle = |\tilde{\psi}_n\rangle + \sum_{i,a} (|\phi_i^a\rangle - |\tilde{\phi}_i^a\rangle)\langle \tilde{p}_i^a|\tilde{\psi}_n\rangle, \tag{A1}$$

where the projector functions $|\tilde{p}_i^a\rangle$ inside the augmentation sphere a fulfills

$$\sum_i |\tilde{p}_i^a\rangle\langle\tilde{\phi}_i^a| = 1, \quad \langle \tilde{p}_i^a|\tilde{\phi}_j^a\rangle = \delta_{ij}, \quad |\mathbf{r} - \mathbf{R}^a| < r_c^a. \tag{A2}$$

Suppose we have an atom adsorbed on a metal surface and we wish to perform a ΔSCF calculation where a certain atomic orbital $|a\rangle$ is kept occupied during the calculation. If the orbital is hybridized with the metal states we need to find the linear combination which constitutes the orbital. This can

always be done if a sufficient number of unoccupied KS orbitals is included in the calculation

$$|i\rangle = \sum_n c_{ni}|\psi_n\rangle, \quad c_{ni} = \langle\psi_n|i\rangle. \tag{A3}$$

Since the partial waves are typically chosen as atomic orbitals we just need to consider the quantity

$$\langle\psi_n|\phi_i^a\rangle = \langle\tilde{\psi}_n|\phi_i^a\rangle + \sum_{j,a'}\langle\tilde{\psi}_n|\tilde{p}_j^{a'}\rangle(\langle\phi_j^{a'}|\phi_i^a\rangle - \langle\tilde{\phi}_j^{a'}|\phi_i^a\rangle) \approx \langle\tilde{\psi}_n|\tilde{p}_i^a\rangle. \tag{A4}$$

If we were just considering a single atom, the last equality would be exact inside the augmentation sphere since the partial waves would then be orthogonal and the pseudopartial waves are dual to the projectors in Eq. (A2). When more than one atom is present there are corrections due to overlap of partial waves from neighboring atoms and noncompleteness of projectors/pseudopartial waves between the augmentation spheres. However using $\langle\tilde{\psi}_n|\tilde{p}_i^a\rangle$ is a quick and efficient way of obtaining the linear combination, since these quantities are calculated in each step of the self-consistence cycle anyway. The method can then be extended to molecular orbitals by taking the relevant linear combinations of $\langle\tilde{\psi}_n|\tilde{p}_i^a\rangle$.

*Present address: Department of Micro- and Nanotechnology, Technical University of Denmark, DK–2800 Kongens Lyngby, Denmark.
†schiotz@fysik.dtu.dk

[1] P. Hohenberg and W. Kohn, Phys. Rev. **136**, B864 (1964).
[2] W. Kohn and L. J. Sham, Phys. Rev. **140**, A1133 (1965).
[3] A. C. Luntz, M. Persson, S. Wagner, C. Frischkorn, and M. Wolf, J. Chem. Phys. **124**, 244702 (2006).
[4] M. Bonn, S. Funk, C. Hess, D. N. Denzler, C. Stampfl, M. Scheffler, M. Wolf, and G. Ertl, Science **285**, 1042 (1999).
[5] J. W. Gadzuk, Phys. Rev. Lett. **76**, 4234 (1996).
[6] W. Lichten, Phys. Rev. **131**, 229 (1963).
[7] J. Behler, B. Delley, K. Reuter, and M. Scheffler, Phys. Rev. B **75**, 115409 (2007).
[8] K. Bohnen, M. Kiwi, and H. Suhl, Phys. Rev. Lett. **34**, 1512 (1975).
[9] M. Brandbyge, P. Hedegård, T. F. Heinz, J. A. Misewich, and D. M. Newns, Phys. Rev. B **52**, 6042 (1995).
[10] E. Runge and E. K. U. Gross, Phys. Rev. Lett. **52**, 997 (1984).
[11] M. Petersilka, E. K. U. Gross, and K. Burke, Int. J. Quantum Chem. **80**, 534 (2000).
[12] M. E. Casida, F. Gutierrez, J. Guan, F. Gadea, D. Salahub, and J. Daudey, J. Chem. Phys. **113**, 7062 (2000).
[13] L. Hedin, Phys. Rev. **139**, A796 (1965).
[14] G. Onida, L. Reining, and A. Rubio, Rev. Mod. Phys. **74**, 601 (2002).
[15] T. Klüner, N. Govind, Y. A. Wang, and E. A. Carter, J. Chem. Phys. **116**, 42 (2002).
[16] D. Lahav and T. Klüner, J. Phys.: Condens. Matter **19**, 226001 (2007).
[17] D. Kröner, I. Mehdaoui, H. Freund, and T. Klüner, Chem. Phys. Lett. **415**, 150 (2005).
[18] Q. Wu and T. Van Voorhis, Phys. Rev. A **72**, 024502 (2005).
[19] Q. Wu and T. Van Voorhis, J. Phys. Chem. A **110**, 9212 (2006).
[20] R. O. Jones and O. Gunnarsson, Rev. Mod. Phys. **61**, 689 (1989).
[21] A. Hellman, B. Razaznejad, and B. I. Lundqvist, J. Chem. Phys. **120**, 4593 (2004).
[22] O. Gunnarsson and B. I. Lundqvist, Phys. Rev. B **13**, 4274 (1976).
[23] A. Görling, Phys. Rev. A **59**, 3359 (1999).
[24] D. M. Newns, Phys. Rev. **178**, 1123 (1969).
[25] P. W. Anderson, Phys. Rev. **124**, 41 (1961).
[26] Often an electronic temperature is introduced to improve convergence, such that the electrons are distributed by a Fermi-Dirac distribution. This can also be done in the proposed method.
[27] J. J. Mortensen, L. B. Hansen, and K. W. Jacobsen, Phys. Rev. B **71**, 035109 (2005).
[28] The GPAW code including the implementation of ΔSCF is available as a part of the CAMPOS software, www.camp.dtu.dk/Software
[29] P. E. Blöchl, Phys. Rev. B **50**, 17953 (1994).
[30] P. E. Blöchl, C. J. Först, and J. Schimpl, Bull. Mater. Sci. **26**, 33 (2003).
[31] G. Kresse and J. Furthmuller, Comput. Mater. Sci. **6**, 15 (1996).
[32] D. M. Ceperley and B. J. Alder, Phys. Rev. Lett. **45**, 566 (1980).
[33] B. Hammer, L. B. Hansen, and J. K. Nørskov, Phys. Rev. B **59**, 7413 (1999).
[34] A. Zangwill and P. Soven, Phys. Rev. A **21**, 1561 (1980).
[35] OCTOPUS is a freely available real-space time-dependent density-functional theory code (see www.tddft.org/programs/octopus/).
[36] A. Castro, H. Appel, M. Oliveira, C. Rozzi, X. Andrade, F. Lorenzen, M. Marques, E. Gross, and A. Rubio, Phys. Status Solidi B **243**, 2465 (2006).
[37] G. Henkelman, A. Arnaldsson, and H. Jónsson, Comput. Mater. Sci. **36**, 354 (2006).
[38] R. F. W. Bader, *Atoms in Molecules: A Quantum Theory* (Oxford University Press, New York, 1990).
[39] P. D. Johnson and S. L. Hulbert, Phys. Rev. B **35**, 9427 (1987).
[40] W. Reimer, T. Fink, and J. Küppers, Surf. Sci. **186**, 55 (1987).
[41] W. Reimer, T. Fink, and J. Küppers, Surf. Sci. **193**, 259 (1988).
[42] J. Rogozik and V. Dose, Surf. Sci. **176**, L847 (1986).
[43] T. Ziegler, A. Rauk, and E. J. Baerends, Theor. Chim. Acta **43**, 261 (1977).
[44] T. Grabo, M. Petersilka, and E. Gross, J. Mol. Struct.: THEOCHEM **501-502**, 353 (2000).
[45] J. Oddershede, N. E. Grüner, and G. H. F. Diercksen, Chem. Phys. **97**, 303 (1985).
[46] K. P. Huber and G. Herzberg, *Molecular Spectra and Molecular Structure IV: Constants of Diatomic Molecules* (Van Nostrand Reinhold, New York, 1979).
[47] *Electron Correlations and Materials Properties*, edited by A. Gonis, N. Kioussis, and M. Ciftan (Plenum, New York, 1999).
[48] E. S. Nielsen, P. Jørgensen, and J. Oddershede, J. Chem. Phys. **73**, 6238 (1980).
[49] P. Saalfrank, Surf. Sci. **390**, 1 (1997).

Paper III

Hot-electron-mediated desorption rates calculated from excited-state potential energy surfaces

Thomas Olsen, Jeppe Gavnholt, and Jakob Schiøtz*
Department of Physics, Danish National Research Foundation's Center of Individual Nanoparticle Functionality (CINF), Technical University of Denmark, DK-2800 Kongens Lyngby, Denmark
(Received 13 October 2008; revised manuscript received 24 November 2008; published 6 January 2009)

We present a model for desorption induced by (multiple) electronic transitions [DIET (DIMET)] based on potential energy surfaces calculated with the delta self-consistent field extension of density-functional theory. We calculate potential energy surfaces of CO and NO molecules adsorbed on various transition-metal surfaces and show that classical nuclear dynamics does not suffice for propagation in the excited state. We present a simple Hamiltonian describing the system with parameters obtained from the excited-state potential energy surface and show that this model can describe desorption dynamics in both the DIET and DIMET regimes and reproduce the power-law behavior observed experimentally. We observe that the internal stretch degree of freedom in the molecules is crucial for the energy transfer between the hot electrons and the molecule when the coupling to the surface is strong.

DOI: 10.1103/PhysRevB.79.035403 PACS number(s): 31.15.xr, 71.15.Qe, 71.38.−k, 82.20.Gk

I. INTRODUCTION

The advent of femtosecond lasers has initiated major progress in the study of nonadiabatic surface dynamics on a wide range of systems. Photoinduced desorption had already been observed for a few adsorbate systems[1,2] using low-intensity nanosecond laser pulses, but high-intensity femtosecond laser pulses have been shown to induce desorption in a large class of adsorbate systems[3–10] and induce chemical reactions which cannot proceed by thermal heating.[11]

The mechanism attributed to these reactions is excitation of substrate electrons by the laser pulse. A single hot electron can then interact with an initially unoccupied adsorbate resonance, thus asserting a force on the adsorbate nuclei which may then lead to desorption induced by electronic transitions (DIET). Using femtosecond lasers, it is possible to reach high densities of excited electrons resulting in a different dominating mechanism—desorption induced by multiple electronic transitions (DIMET) (Ref. 12) where several hot electrons interact with the adsorbate.

A different method to produce hot electron based on a metal-insulator-metal (MIM) heterostructure was suggested by Gadzuk.[13] With an ideal MIM device, it is possible to tune hot electrons to any desired resonance of an adsorbate system and the approach thereby suggests the highly attractive possibility of performing selective chemistry at surfaces. Such devices have been constructed and characterized[14] and comprise a promising candidate for future hot-electron femtochemistry experiments.

The theoretical framework to describe the nonadiabatic dynamics resulting from a hot electron interacting with an adsorbate is usually based on the concept of potential energy surfaces (PESs). In the Born-Oppenheimer approximation the electrons are assumed to remain in their ground state and are thus decoupled from the nuclei. This allows one to map out a ground-state PES for the nuclei by calculating the electronic energy for each position of the nuclei. Similarly, when an initially unoccupied resonance becomes occupied, a new excited-state PES arises which has its minimum at a different location from the ground-state PES and a force is exerted on the adsorbate. Several models have emerged to deal with nonadiabatic dynamics at surfaces, but they are usually limited by the difficulty to obtain reliable excited-state PESs and most theoretical results are based on model potentials.[15–20]

An often used method to treat the extreme DIMET regime with many contributing electrons is using an electronic friction model.[21–23] The hot electrons are then assumed to thermalize rapidly and the influence of the electrons on the adsorbate is treated statistically using an electronic temperature which can be several thousands of Kelvins. The conceptual picture is that of a hot Fermi distribution with a tail partially overlapping an adsorbate resonance and thereby exerting a force on the adsorbate. However, correct calculation of the temperature-dependent friction still requires knowledge of the excited-state PES.

The subject of this paper will be the application of two-dimensional excited-state PESs to calculate desorption probabilities. We will be particularly interested in the DIET regime where the hot electron has a known energy as relevant for the MIM device and the few-electron DIMET regime. Although the friction models have enjoyed some success,[24,25] there is still a need of a microscopic nonstatistical model of DIMET to test the assumption of thermally equilibrated electrons and to bridge the gap to the DIET regime. Furthermore, the hot-electron femtochemistry relevant to the MIM device can certainly not be described using an electronic temperature since all electrons are tuned to a specific energy.

We start by summarizing the method of linear-expansion delta self-consistent field extension of density-functional theory (ΔSCF-DFT) (Ref. 26) used to calculate the excited-state PESs and note some qualitative features using CO on Pt(111) as an example. We then discuss the models used to obtain desorption probabilities based on the calculated potential energy surfaces. First an adiabatic model in which the adsorbate jumps between the ground- and excited-state potentials is presented. A general nonadiabatic Newns-Anderson-type[27,28] model is then introduced and the connection to potential energy surfaces is explained. This model with linear coupling has previously been solved[29] and applied to the one-dimensional desorption problem with model parameters.[16] We extend these results to a two-

 ©2009 The American Physical Society

dimensional adsorbate and obtain the nonadiabatic coupling parameters from calculated excited-state potential energy surfaces. In the DIET regime, the model will be used to show that for small excited-state lifetimes the main channel of energy transfer is the internal degree of freedom and we emphasize its importance in desorption dynamics. We compare the calculated desorption probabilities for CO and NO on four transition-metal surfaces and note some general features of the desorption dynamics. The scattering probabilities obtained in the model are then generalized to include adsorbates in any vibrationally excited state which allow us to extend the calculations to include a substrate temperature and to treat the DIMET regime within the model. In Appendix A it is shown how to expand excited states within the projector augmented wave (PAW) formalism, and in Appendix B the results and generalizations of scattering amplitude calculations are summarized.

II. POTENTIAL ENERGY SURFACES

The potential energy surfaces were obtained using the code GPAW (Refs. 30 and 31) which is a real-space density-functional theory (DFT) code that uses the projector augmented wave method.[32,33] In all our calculations we used the revised Perdew-Burke-Ernzerhof (RPBE) exchange-correlation functional[34] since this has been designed to perform well for molecules adsorbed on surfaces and has been shown to perform better than the original PBE functional[35] both for isolated molecules[36] and for adsorbed molecules. For each metal we set up a closed-packed surface consisting of three atomic layers with the top layer being relaxed. 10 Å of vacuum was then introduced above the slab and 0.25 monolayer of adsorbate molecules relaxed at either top or at hcp hollow site. We then mapped out two-dimensional ground-state potential energy surfaces in terms of the internal stretch and the center of mass (COM) to surface distance coordinate using 12 irreducible k points and a grid spacing of 0.2 Å.

To find the excited-state potential energy surfaces, we use the method of linear-expansion delta self-consistent field (ΔSCF) which we have published in a previous work[26] and implemented in GPAW. In the previous publication we have tested the method against inverse photoemission spectroscopy and found that it performed well for molecules chemisorbed on surfaces.[26] In each step of the self-consistency cycle an electron is removed from the Fermi level, the density of an excited state is added to the total density, and the band energy of this state is added to the total energy. To get the band energy right, we need to expand the excited state on the Kohn-Sham (KS) orbitals found in each iteration. The method is thus a generalization of the usual ΔSCF where occupations numbers are changed. Instead of changing occupation numbers we occupy an orbital which is not an eigenstate of the KS Hamiltonian but a superposition of eigenstates, in such a way that the state is as close as possible to the original molecular state. We refer to Appendix A for details on how to do this within the projector augmented wave formalism. The excited states used in this paper are the antibonding 2π orbitals of NO and CO.

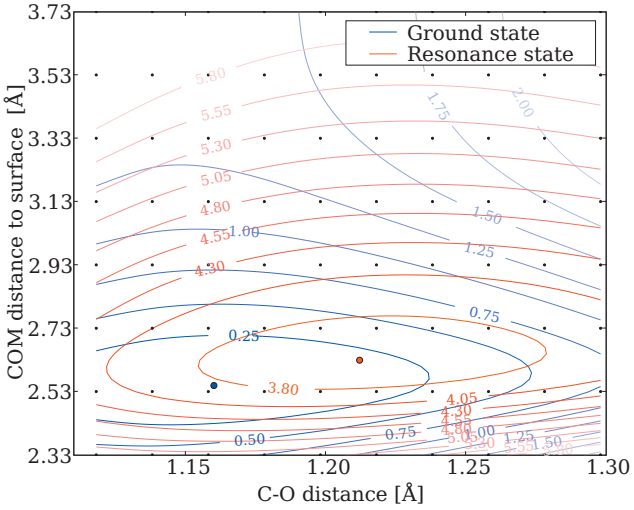

FIG. 1. (Color) Ground- and excited-state (2π) potential energy surfaces for CO adsorbed on Pt(111) top site. The coverage is 0.25 monolayer.

In the previous publication,[26] we investigated the influence of the interactions between neighboring supercells for different supercell sizes and found that the size dependency of the excitation energy is consistent with an electrostatic dipole-dipole interaction. Already for a (2×2) surface cell, the interaction energy has become small, and furthermore this interaction energy will have little influence on the slope of the excited-state PES and thus little influence on the calculated desorption rates. For this reason and to keep the calculations manageable, we use a (2×2) surface cell.

As an example we show the two-dimensional excited-state PES superimposed on a ground-state PES in the case of CO on Pt(111) top site in Fig. 1. The molecules adsorb with the molecular axis perpendicular to the surface with carbon closest to the top site. Due to the symmetry of the 2π orbital and the geometry at the ground-state minimum, we cannot induce forces parallel to the surface if the molecule is at the ground-state minimum when excited. The excited state could have unstable extremal points with respect to the degrees of freedom parallel to the surface; but the model we apply in this work only depends on the degrees of freedom with nonvanishing derivatives on the excited-state PES and we thus assume that the COM and internal stretch degrees of freedom should capture the essential desorption dynamics of the considered systems.

Since the excited molecule has an extra electron in an antibonding orbital the excited molecule is expected to have a larger equilibrium bond length and this is also what we observe. A popular and conceptually simple way of explaining desorption in one-dimensional models of DIET is the Antoniewicz mechanism,[37] where the excited molecule induces an image charge on the surface which results in an attractive force on the surface. The excited molecule is then accelerated toward the surface and eventually decays to the steep wall of the ground-state Morse potential. From Fig. 1 we observe a qualitatively different behavior: the COM of the excited molecules experience a repulsive force accelerating the COM of the molecule away from the surface. This is

due to the effect of the bond-length expansion and the fact that the 2π orbital has a large density in the vicinity of the carbon atom which gives a repulsion that dominates the image charge attraction. It will be shown below that for the considered systems, it is primarily excitation of the internal degree of freedom which is responsible for the large energy transfers leading to desorption. The potential energy surfaces for CO adsorbed on Pd, Rh, and Ru show very similar qualitative features.

III. MODELS

The time scale at which adsorbates dissipate energy to the substrate is typically on the order of picoseconds[38] and since the oscillation times for the two modes is ~15–50 fs (see Sec. IV A) we will assume that the molecule has plenty of time to desorb if it has absorbed the required energy from a hot electron. This is the major assumption we will impose and thus when we refer to desorption rates in the following, it is the rate of transferring at least of the energy needed for a molecule to desorb.

Assuming a Lorentzian resonance with full width at half maximum (FWHM) $\Gamma=\hbar/\tau$ centered at ϵ_a, the probability that a hot electron of energy ε desorbs the molecule becomes

$$P_{\mathrm{des}}^{\mathrm{ad}}(\varepsilon)=\frac{(\Gamma/2)^2}{(\varepsilon-\epsilon_a)^2+(\Gamma/2)^2}\frac{1}{\tau}\int_0^\infty P(t_d)e^{-t_d/\tau}dt_d, \tag{1}$$

where $P(t_d)$ is the probability of a desorption event when the molecule is excited at $t=0$ and decays at time $t=t_d$. Using classical dynamics, the probability $P(t_d)$ can be obtained by propagating the molecule on the excited-state PES according to the forces, evaluate the energy gain ΔE after time t_d, and set $P(t_d)=1$ if $\Delta E>E_{\mathrm{des}}$ and $P(t_d)=0$ if $\Delta E<E_{\mathrm{des}}$. However, the short lifetime of the excited electron implies that classical molecular propagation on the excited-state PES may not be a good approximation.

In fact, the classical limit is obtained when the action $S=\int dtL[\dot{x}(t),x(t)]$ on a representative path satisfies

$$|S|\gg\hbar. \tag{2}$$

Assuming a quadratic excited-state potential of frequency ω and initial potential energy E_0, we can evaluate the action on a classical path between initial time t_i and final time t_f. For generic time scales one just obtains the usual condition of high excitation numbers $E_0\gg\hbar\omega$, whereas for $\omega\Delta t\ll 1$, the additional condition of $E_0\Delta t\gg\hbar$ needs to be satisfied in order to apply classical dynamics. In the case of CO on Pt(111) we have $E_0\sim 0.3$ eV (Fig. 1) and $\tau\sim 1$ fs (Fig. 8) which gives $E_0\Delta t\sim\hbar$. Thus molecular propagation on the excited-state PES is not expected to follow the classical equations of motion. Below we will show an example where a classical analysis underestimates desorption probabilities by several orders of magnitude.

This scheme could be extended to a quantum dynamical treatment of the molecule by propagating the molecular wave function using a two-PES Hamiltonian. However, the method still rests on the Born-Oppenheimer approximation and the adiabatic concept of potential energy surfaces and thus cannot be expected to fully capture the nonadiabatic entangled dynamics of the resonant electron and adsorbate coordinates.

Instead we consider a Newns-Anderson-type[27,28] Hamiltonian with substrate states $|k\rangle$, a resonant state $|a\rangle$, adsorbate coordinates x_i, an adiabatic adsorbate ground-state potential $V_0(x_i)$, and a nonadiabatic coupling of the resonant electron to adsorbate coordinates $\varepsilon_a(x_i)$,

$$H=T(\dot{x}_i)+V_0(x_i)+\varepsilon_a(x_i)c_a^\dagger c_a+\sum_k\epsilon_k c_k^\dagger c_k+\sum_k(V_{ak}c_a^\dagger c_k+V_{ak}^\square c_k^\dagger c_a). \tag{3}$$

The strength of the electronic coupling is expressed through the function

$$\Gamma(\varepsilon)=2\pi\sum_k|V_{ak}|^2\delta(\varepsilon-\epsilon_k). \tag{4}$$

The model as such neglects the electron-electron interaction, but we assume that the important part of the electron-electron interactions is the restructuring of the metallic electrons when the resonance is occupied and that we can capture this effect in an effective nonadiabatic coupling. To do this we note that we can obtain $\varepsilon_a(x_i)$ as the expectation value differences of Eq. (3) with the adsorbate at x_i with and without an electron in the state $|a\rangle$. Applying this to an interacting problem leads us to identify $\varepsilon_a(x_i)=V_1(x_i)-V_0(x_i)$, where $V_1(x_i)$ and $V_0(x_i)$ are the potential energy surfaces of excited and ground states which we have obtained with linear-expansion ΔSCF-DFT.

In the following we will apply the wideband limit which means that the individual coupling coefficients V_{ak} are assumed to vary slowly in energy and the density of states $\rho(\varepsilon)$ is taken as constant in the vicinity of the resonance. This gives an energy-independent coupling $\Gamma=2\pi\rho(\epsilon_a)\Sigma_k|V_{ak}|^2$ and the resonance spectral function corresponding to the electronic part of Eq. (3) becomes a Lorentzian with FWHM Γ.

Even in the wideband limit it is quite difficult to handle model (3) analytically with arbitrary coupling function $\varepsilon_a(x_i)$. In particular, we would like to calculate the probability that an incoming substrate electron of energy ε_i scatters inelastically on the resonance and is reflected back into the substrate with final energy ε_f. Fortunately, the potential energy surfaces we are considering are close to being quadratic in the region of interest (see Fig. 1) and the ground- and excited-state potentials have approximately the same curvature. Taylor expanding $V_0(x_i)$ to second order and $\varepsilon_a(x_i)$ to first order in the vicinity of the ground-state equilibrium positions x_i^0 then gives

$$H=\epsilon_a c_a^\dagger c_a+\sum_k\epsilon_k c_k^\dagger c_k+\sum_k(V_{ak}c_a^\dagger c_k+V_{ak}^\square c_k^\dagger c_a)+\sum_i\hbar\omega_i\left(a_i^\dagger a_i+\frac{1}{2}\right)+\sum_i\lambda_i c_a^\dagger c_a(a_i^\dagger+a_i), \tag{5}$$

with $\epsilon_a=V_1(x_i^0)-V_0(x_i^0)$ and

$$\lambda_i = \frac{l_i}{\sqrt{2}} \frac{\partial}{\partial x_i} V_1 \Big|_{x_i = x_i^0}, \quad l_i = \sqrt{\frac{\hbar}{m_i \omega_i}}, \tag{6}$$

where we have assumed that an appropriate transformation to normal coordinates has been performed. Note that if the ground- and excited-state potentials are exactly quadratic with equal second derivatives, we can relate the coupling constants to the positions x_i^1 of the excited-state potential minimum as $\lambda_i^2 = \hbar \omega_i \Delta V_i$ with $\Delta V_i = \frac{1}{2} m_i \omega_i^2 |x_i^1 - x_i^0|$. The quantity $g_i = (\lambda_i / \hbar \omega_i)^2$ then corresponds to an "initial quantum number" on the excited-state surface and this becomes the effective dimensionless coupling constant in the model (see Appendix B). Hamiltonian (5) has previously been subjected to detailed analysis in the context of inelastic scattering[29] and applied to desorption dynamics[16] for the case of a one-dimensional adsorbate with model parameters.

Below we extend the results of Refs. 16 and 29 to a two-dimensional adsorbate and calculated the coupling parameters λ_i from excited-state potential energy surfaces. We also calculate scattering amplitudes for an adsorbate initially in a vibrationally excited state which enable us to apply the model to the DIMET regime.

A. DIET

In Eq. (B8) we show how to calculate the scattering probability $P_{n_i,n_j}(\varepsilon_i)$ that an incoming electron of energy ε_i excites the (n_i, n_j) mode of a two-dimensional harmonic oscillator. The probability of transferring E_R or more energy to the adsorbate can then be found by calculating

$$P_R(\varepsilon_i) = \sum_{n_i,n_j} P_{n_i n_j}(\varepsilon_i)\, \theta(\hbar \omega_i n_i + \hbar \omega_j n_j - E_R), \tag{7}$$

where $\theta(x)$ is the Heaviside step function. The desorption rate can then be calculated by integrating this expression with the current density of incoming hot electrons. One should note that the probability $P_{n_i n_j}$ of exciting the (n_i, n_j) modes in a two-mode model is not just given by the product of single mode probabilities P_n in a one-mode model. This is due to an indirect coupling of the two modes through the resonance. The result can be generalized to include the substrate temperature and we will examine the consequences of this below.

B. DIMET

If we assume that the time between individual inelastic-scattering events is much longer than the scattering time itself, it is possible to regard multiple-electron desorption events as sequence of single-electron-scattering events. Since we have extended the inelastic-scattering probabilities to include situations where the molecule is initially in a vibrationally excited state, it is also possible to treat DIMET events within model (5). As an example, let us assume a single vibrational mode which is initially unoccupied ($n=0$). When a hot electron with energy ε_1 scatters inelastically on the resonance the result will be a probability distribution $P_{n_1}(\varepsilon_1)$ for all vibrationally excited states n of the molecule. If a second electron with energy ε_2 now scatters on the resonance, the probability distribution will change to $P_{n_2}(\varepsilon_1, \varepsilon_2)$ and so forth. The probability $P_{n_2-n_1}(\varepsilon_2, n_1)$ of exciting the state n_2 given that the initial state was n_1 is calculated in Eq. (B6) and we can write

$$P_{n_2}(\varepsilon_1, \varepsilon_2) = \sum_{n_1=0}^{\infty} P_{n_2-n_1}(\varepsilon_2, n_1) P_{n_1}(\varepsilon_1), \tag{8}$$

for a two-electron event and similar expressions for multiple-electron events. Given an initial distribution of hot electrons, we may then calculate the probability of a desorption event with any number of contributing electrons.

TABLE I. Parameters for CO adsorbed at top site on four transition metals. All numbers are in eV.

Metal	ϵ_a	ω_z	ω_d	λ_z	λ_d
Pt(111)	3.89	0.054	0.255	−0.142	−0.145
Pd(111)	3.64	0.061	0.256	−0.082	−0.164
Rh(111)	3.80	0.048	0.247	−0.129	−0.132
Ru(0001)	3.74	0.054	0.255	−0.134	−0.120

IV. RESULTS

A. Parameters

The parameters in desorption model (5) are the width of the resonance Γ, the frequencies of the normal modes ω_i, the excitation energy ϵ_a, and the nonadiabatic coupling coefficients λ_i. We cannot calculate Γ from first principles but we estimate its value from the Kohn-Sham projected density of states. It is typically on the order of 1 eV, but it will be instructive to treat it as a free parameter and examine how it affects desorption probabilities.

The frequencies are obtained from a standard normal-mode analysis and ϵ_a is obtained as the excitation energy at the ground-state potential minimum. The coupling coefficients are determined by mapping out a small area of the excited-state potential energy surface in the immediate vicinity of the ground-state potential. In each of the considered systems, we optimize the area such that it is small enough to be linear but large enough to suppress numerical fluctuations in the excited-state energies. We then fit a linear function to this area and transform the derivatives to the normal modes.

In all the considered systems the calculated normal modes are similar but not identical to the standard COM and internal stretch modes. For example, with CO on Pt(111) the internal stretch and COM modes are, respectively, $\mathbf{d}=(-1, 0.75)$ and $\mathbf{z}=(1,1)$, whereas the calculated modes are in the directions $\mathbf{d}=(-1, 0.68)$ and $\mathbf{z}=(1, 1.11)$ with respect to the (x_C, x_O) coordinates normal to the surface. Since the desorption probabilities are quite sensitive to the value of the nonadiabatic coupling constants, it is important that we take the derivatives on the excited-state PES with respect to the correct normal modes.

Tables I and II below display the calculated parameters. We have only examined CO at on-top sites and NO at hcp hollow sites. NO is seen to have much lower nonadiabatic

TABLE II. Parameters for NO adsorbed at hcp hollow site on four transition metals. All numbers are in eV.

Metal	ϵ_a	ω_z	ω_d	λ_z	λ_d
Pt(111)	1.71	0.039	0.196	−0.050	−0.053
Pd(111)	1.48	0.055	0.201	−0.046	−0.053
Rh(111)	1.82	0.073	0.277	−0.042	−0.020
Ru(0001)	2.14	0.042	0.192	−0.052	−0.006

coupling coefficients and excitation energies than CO. The low excitation energies are due to the fact that NO already has one electron in the antibonding orbital and the resonance thus has to lie close to the Fermi level of the metal. The small coupling coefficients can also be traced to the ground-state occupation of the 2π orbital on NO. In the Kohn-Sham picture we can imagine the resonance corresponding to 2π lying right at the Fermi level being partially occupied. When an extra electron is put into the orbital, the resonance energy is increased due to the Hartree repulsion and the initial partial occupation is lost. In the true system things are more complicated, but the qualitative features are the same: exciting NO results in less charge being transferred to the molecule than exciting CO and thus a weaker nonadiabatic coupling. Thus it is much harder to transfer energy to adsorbed NO compared to CO in a one-electron event; but since the resonance is located much closer to the Fermi level a thermal distribution of hot electrons is likely to result in more frequent scattering events than for CO.

B. DIET desorption rates

The probability that a single electron with energy ε_i scatters inelastically and transfers the energy E_R to an adsorbate can be calculated in model (5) with Eq. (7). Our basic assumption is that rate of energy dissipation to the substrate is much longer than the time of a desorption event, and when we refer to desorption rates in the following it will mean the rates of transferring the energy needed for a molecule to desorb in a truncated quadratic potential.

In Fig. 2 we display the probability that an incoming electron will scatter with an energy loss in excess of the desorption energy ($\Delta E > 1.5$ eV) for three values of the resonance width. When only a single mode is considered we see the appearance of oscillator sidebands with an energy spacing of $\hbar\omega$. At larger resonance width the sidebands are washed out and the probability takes the form of a Lorentzian which is detuned by $\delta\epsilon_a \sim \Delta E/2$. A simple way to understand this detuning is as a compromise where both the incoming and outgoing electrons are closest to the resonance. Thus we see the emergence of an *effective* inelastic resonance with a center that is detuned dependent on the desorption energy and a shape which is highly dependent on the lifetime. Such a probability distribution could not have been obtained in a model where the transfer of energy to the adsorbate is decoupled from the probability of capturing the electron, and the desorption probability would always be a Lorentzian (in the wideband limit) centered at ϵ_a and multiplied by a factor

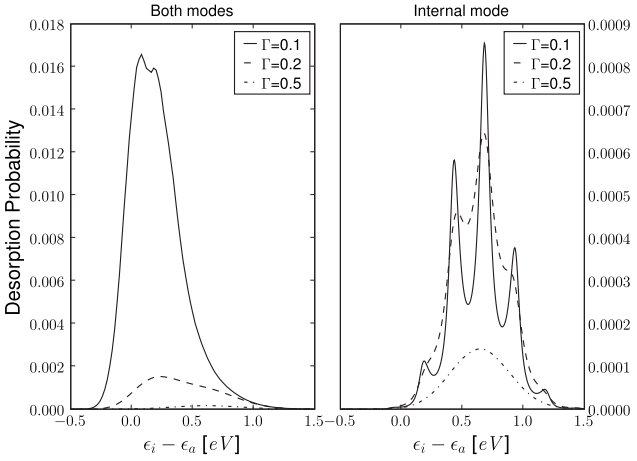

FIG. 2. Desorption probability for CO adsorbed on Pt(111) for three different values of the resonance width. For $\Gamma > 0.5$ the one- and two-mode probability distributions become identical Lorentzians with an integrated probability that decays exponentially with resonance width (see Fig. 3).

dependent on the details of the potential energy surfaces. For $\Gamma > 0.5$ eV the COM degree of freedom becomes unimportant and the desorption probabilities obtained using both modes and only the internal degree of freedom become identical.

Assuming an energy-independent current of hot electrons we can integrate the desorption probabilities in Fig. 2 to obtain a desorption rate normalized to the incident flux of electrons. In Fig. 3 we show how each of the two modes contributes to the desorption rate and compare with a calculation within the classical adiabatic model (1). The two single mode rates are obtained by setting g_d and g_z to zero in

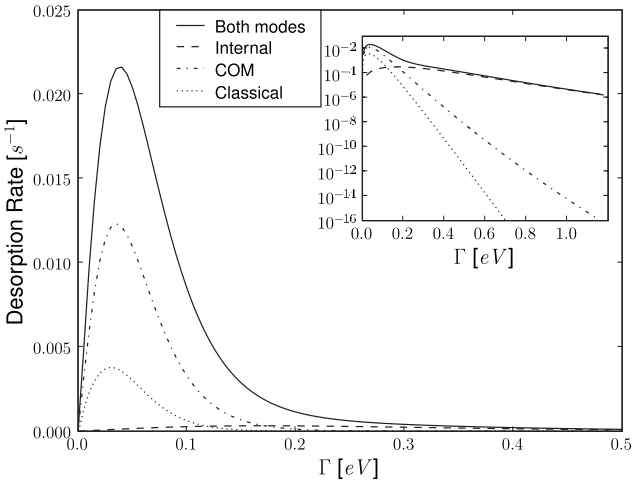

FIG. 3. Desorption rate for CO adsorbed on Pt(111) as a function of resonance width Γ. In the wide resonance (short lifetime) regime the rate is seen to be completely governed by the internal stretch excitation, whereas the COM excitation is governing the desorption rate in the narrow resonance (long lifetime) regime. The classical rate becomes several orders of magnitude smaller than the quantum rate at large resonance width. The inset shows the same data on a logarithmic scale.

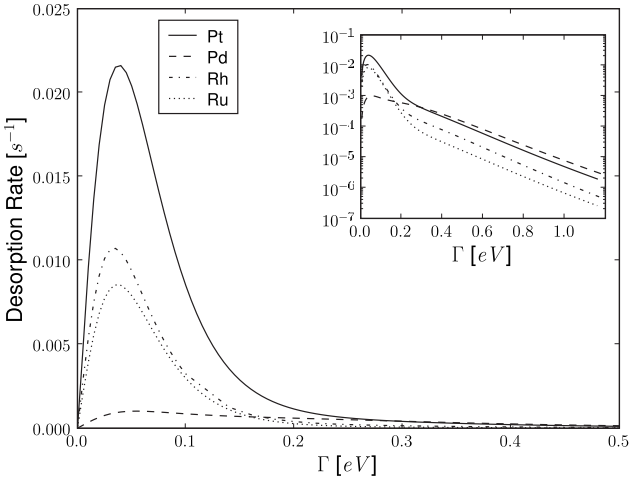

FIG. 4. Rates of transferring 1.5 eV to CO on four transition metals.

Eq. (B8). It is seen that it is the internal stretch mode that governs the energy transfer completely in the large width regime and the COM mode governs the energy transfer at low width. The reason for this partitioning is the time scale associated with the two different modes. As seen from Tables I and II the nonadiabatic coupling constants have approximately the same magnitude for the two modes. However, the period of oscillation is five times larger for the COM mode and for small lifetimes there is not enough time to transfer energy to the COM mode. From Fig. 3 we see that the maximum rate of energy transfer in each mode occurs when $\Gamma \sim \hbar\omega_i$. The desorption rate decreases at small resonance width, since the hot electron then becomes weakly coupled to the resonant state

In Figs. 4 and 5 we show a comparison of CO and NO adsorbed on the different transition metals. Again comparing with Tables I and II it is seen that it is the coupling to the internal mode alone which controls the magnitude of the desorption rate at large resonance width. Since the internal

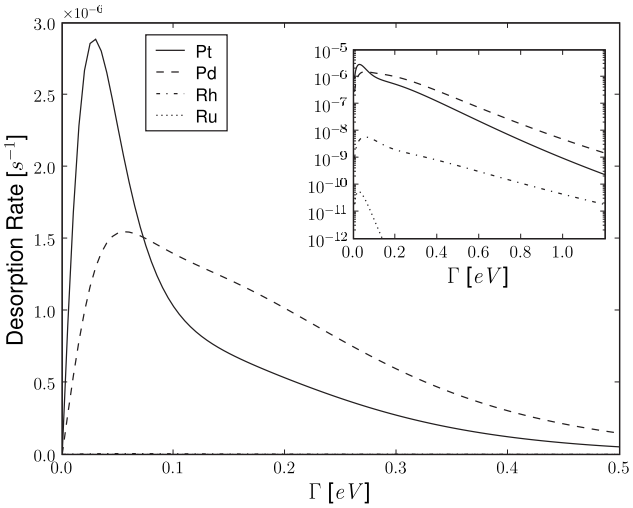

FIG. 5. Rates of transferring 1.0 eV to NO on four transition metals.

TABLE III. Desorption energies and calculated maximum desorption probability for CO adsorbed at top site on four transition metals. All numbers except $P_D^{\max}$ are in eV.

Metal	E_D	Γ	$\delta\varepsilon$	$P_D^{\max}$
Pt(111)	1.37[a]	1.0	0.6	2×10^{-5}
Pd(111)	1.48[a]	1.5	0.7	7×10^{-7}
Rh(111)	1.45[a]	1.2	0.7	1×10^{-6}
Ru(0001)	1.49[a]	0.9	0.7	2×10^{-6}

[a]Experimental values taken from Abild-Pedersen and Andersson (Ref. 39).

degree of freedom seems to control the rate of energy transfer in the physical range of the resonance width (typically $0.5<\Gamma<1.5$) we will ignore the COM degree of freedom in the following.

Comparison of CO and NO

So far we have analyzed some general features of desorption probabilities and their dependence on the nonadiabatic coupling parameters and the lifetime $\tau=\hbar/\Gamma$. Now we will compare the desorption probabilities of CO and NO on four transition-metal surfaces using experimentally determined desorption energies. Although substantial experimental data exist for various systems including CO and NO, a direct comparison to experimental data is difficult since experimental desorption yields are highly dependent on the distribution of hot electrons in the substrate which depends on the detailed physical properties of the metal and the applied laser pulse. The distribution of hot electrons resulting from a given laser pulse could in principle be calculated from first principles; however, we will make no attempt of such a calculation here but simply compare desorption probabilities of single-electron events as relevant for the MIM device.[13,14] In Tables III and IV we summarize the desorption energy E_d, the estimated resonance width Γ, the detuning of the energy at which the incoming electron has the maximum probability of transferring the desorption energy $\delta\varepsilon=\varepsilon_i^{\max}-\epsilon_a$, and the maximum desorption probability $P_D^{\max}=P_D(\varepsilon_i^{\max})$ for the four transition metals (the maximum probability is detuned from ϵ_a, as shown in Fig. 2). The detuning very nicely follows the rule of thumb that $\delta\varepsilon\sim E_D/2$ in accordance with the picture of a compromise between the incoming and outgoing elec-

TABLE IV. Desorption energies and calculated maximum desorption probability for NO adsorbed at hcp hollow site on four transition metals. All numbers except $P_D^{\max}$ are in eV.

Metal	E_D	Γ	$\delta\varepsilon$	$P_D^{\max}$
Pt(111)	1.29[a]	0.8	0.6	3×10^{-11}
Pd(111)	1.17[b]	0.6	0.6	5×10^{-9}
Rh(111)	1.68[b]	0.4	0.8	2×10^{-15}
Ru(0001)	1.49[c]	0.3	0.7	3×10^{-22}

[a]Croci *et al.* (Ref. 40).
[b]Vang *et al.* (Ref. 41).
[c]Butler *et al.* (Ref. 42).

trons both being as close as possible to the center of the resonance ϵ_a.

In general it is easier for a single electron at the right energy to mediate a desorption event involving CO than with NO from all the considered systems. However, in a femtosecond laser-pulse experiment the resulting hot-electron distribution would have much lower occupation numbers at the CO resonances than at a typical NO resonance. For example, taking platinum as an example with a thermal electron distribution at 5000 K and referring to Tables I and II, we see that the electronic occupation numbers at the resonance energy of CO and NO relates as $f(\epsilon_{NO})/f(\epsilon_{\mathrm{NO}}) \sim 150$. We should also note that the excited-state potential energy surfaces for adsorbed NO are only quadratic in a small region near the minimum and Hamiltonian (5) is thus not expected to describe NO as accurately as CO.

The desorption probabilities are highly dependent on the resonance width Γ which we can only estimate roughly from the Kohn-Sham projected density of states. In addition, the electronic lifetime of CO on Pt(111) has been shown to be highly dependent on coverage[3] since the 2π electrons become delocalized and quasistationary at certain coverages. Furthermore, both CO and NO are known to form adsorbate structures which is more involved[41,43] than the simple periodic coverage of 0.25 monolayer considered here and the dependence of nonadiabatic coupling coefficients on coverage certainly deserves a study of its own.

However, from Figs. 4 and 5 we do observe the general trends that NO has a much weaker nonadiabatic coupling to the surfaces than CO and that for both CO and NO the coupling to Pt and Pd is similar, whereas the coupling is weaker for Rh and very low for Ru. This decrease in nonadiabatic coupling could hint at a simple dependence on the number of d-band electrons. Investigating this will be the subject of future work.

C. DIMET desorption rates

To get an idea of desorption probabilities in the DIMET regime, we will start by examining how an initial excitation influences the probability of transferring a given number of vibrational quanta. When the oscillator is in an excited vibrational state there is also the possibility of stimulated emission of vibrational quanta where the incoming hot electron gains energy by the scattering event.

In Fig. 6 the maximum probability of transferring Δn quanta is shown for a range of initial quantum numbers n. We treat n as a continuous variable since in the case of a thermal ensemble of states the initial quantum number is simply replaced by a Bose distribution. There is a striking increase in the probabilities of transferring energy to the oscillator if the oscillator is already excited. For example, the probabilities of exciting $0 \rightarrow 3$ and $3 \rightarrow 6$ are 3×10^{-3} and 2×10^{-2}, respectively, although both transitions involve the same energy transfer. Thus if we compare the one-electron event $P_{0\rightarrow 6}=6 \times 10^{-6}$ with the product of the two probabilities $P_{0\rightarrow 3\rightarrow 6}=6 \times 10^{-5}$, we get an order-of-magnitude difference and we still need to include the other channels for transferring six quanta in a two-electron event.

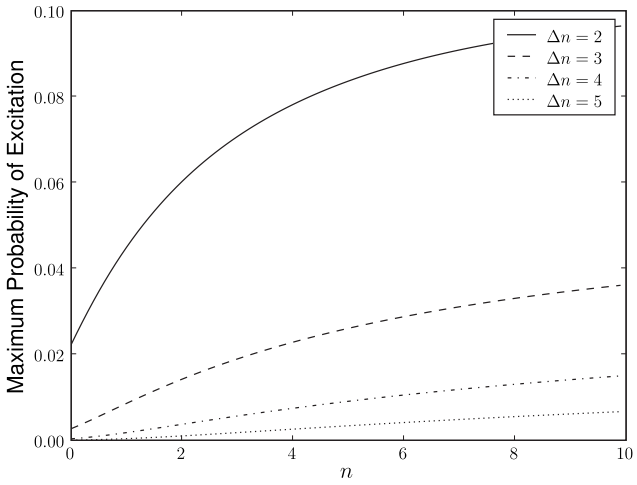

FIG. 6. Maximum probability of transferring Δn vibrational quanta given that the initial state is n with $\Gamma=1.0$ eV.

This also implies that the effect of a finite substrate temperature is twofold. The occupation numbers of excited vibrational states will be nonzero, meaning that less energy transfer is needed to desorb the molecule and the likelihood of a given energy transfer is increased if the molecule is thermally excited. However at room temperature the probability that the internal mode is in its first-excited state is on the order of 10^{-5} and we can safely neglect the effect of temperature.

A hallmark of the DIMET regime is the power-law dependence of the desorption rate on the laser fluence $R \sim F^n$ where n depends on the particular adsorbate/substrate system considered.[4] It is by no means trivial that the desorption rate should follow a power law and calculating the exponent of a particular system is a major challenge of any DIMET model.

It is reasonable to assume that the laser fluence is proportional to the flux of hot electrons hitting the molecule, since the desorption rate typically becomes linear[44] for small fluences corresponding to the DIET regime. As a simple model for the desorption rate we then consider a given flux J of hot electrons at a fixed energy ε_i hitting the resonance in equally spaced time intervals $\Delta t=1/J$. We assume that each vibrational quantum has a fixed lifetime T_{vib} and that desorption occurs immediately if the vibrational energy reaches the desorption energy E_D. The probability that one vibrational quantum survives the time interval Δt is $e^{-\Delta t/T_{\mathrm{vib}}}$ and the probability of decay is $(1-e^{-\Delta t/T_{\mathrm{vib}}})$. The probability that the first electron excites the nth vibrational state is then simply the DIET probability,

$$Q_1(n) = P_n(\varepsilon_i, 0), \tag{9}$$

where $P_n(\varepsilon_i,0)$ is given by Eq. (B6). The probability of the adsorbate being in the nth vibrational state after the second electron has scattered is

$$Q_2(n) = \sum_{m=0}^{\infty} p(m) P_{n-m}(\varepsilon_i, m), \tag{10}$$

where $P_{n-m}(\varepsilon_i,m)$ is the probability of the transition $m \rightarrow n$ [Eq. (B6)] and $p(m)$ is the probability that the adsorbate was initially in the state m given by

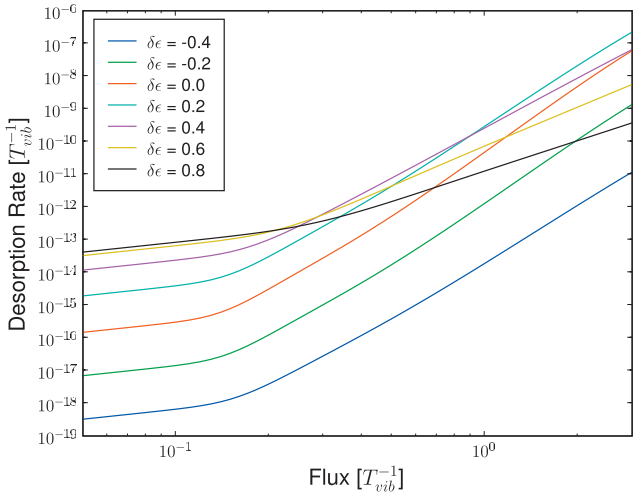

FIG. 7. (Color) Desorption rate as a function of electron flux per adsorption site. For small electron flux the rate is linear in the flux corresponding to the DIET regime, whereas for larger electron flux the rate obeys a power law ($R \sim J^n$ with $n > 1$) corresponding to the DIMET regime. In this figure we show the desorption rate of NO on Pt(111) using the parameters given in Table IV and in seven different values of detuning.

$$p(m) = \sum_{k=m}^{\infty} Q_1(k) \binom{k}{m} (e^{-\Delta t/T_{\mathrm{vib}}})^m (1 - e^{-\Delta t/T_{\mathrm{vib}}})^{k-m} \times \theta(E_d - \hbar\omega k). \quad (11)$$

Thus we only sum over values of k below the desorption energy since states above E_D would previously have been desorbed by assumption. Similarly the probability $Q_3(n)$ of being in the nth excited state after the third scattering event can be expressed in terms of $Q_2(n)$ and so forth. The desorption probability of the Nth electron is then

$$P_N^{\mathrm{des}} = \sum_n Q_N(n)\theta(\hbar\omega n - E_D). \quad (12)$$

When enough time intervals are included the probabilities converge such that $P_N^{\mathrm{des}} = P_{N-1}^{\mathrm{des}}$ and the desorption rate is $R(J) = JP_N^{\mathrm{des}}$ with $J = 1/\Delta t$.

In Fig. 7 we show the rate for NO on Pt(111) with $\Gamma = 0.8$ eV. The desorption energy corresponds to 8 vibrational quanta. Note that changing the lifetime T_{vib} in this model just corresponds to rescaling the flux. The similarity to similar experimental figures[44] is striking. At small flux the rate is linear whereas it obeys a power law ($R \sim J^n$ with $n > 1$) at higher fluences. The fit to a power law is very good for fluxes above 0.2 T_{vib}^{-1}. For small values of the detuning ($-0.4 < \delta\varepsilon < 0.2$ eV) we find that $5.5 < n < 6$, in good agreement with Ho.[44] For large positive values of the detuning the exponent decreases dramatically which is probably due the fact that fewer transitions dominate the dynamics in this region. This means that even though the results were obtained using the simple electron flux $J(\varepsilon_i) = J_0\delta(\varepsilon_i - \epsilon_a - \delta\varepsilon)$ we would most likely obtain the same exponent if we generalized the model to any flux localized within ± 0.2 eV of the resonance.

Although the correspondence with the experimentally found exponent may be fortuitous in such a simple model, the power law itself is very robust to changes in the parameters and we obtain similar power laws for CO on Pt(111). For example, changing the value of Γ results in an overall shift of the rates but the exponents are essentially unchanged. Indeed the exponents appear to be determined mainly by the number of vibrational quanta needed for desorption.

V. SUMMARY AND DISCUSSION

We have previously presented a method to obtain excited-state potential energy surfaces for molecules chemisorbed at metal surfaces.[26] In this paper the method has been applied and combined with a nonadiabatic quantum model to obtain desorption probabilities for CO and NO on four transition-metal surfaces.

The model we have applied allows us to predict the probability that a hot electron will transfer a given amount of energy to the different vibrational modes of an adsorbate. Our main conclusion is the significant role of the internal degree of freedom and the failure of classical mechanics to describe the excited-state adsorbate propagation. Combining the model with a simple picture of the decay and re-excitation of vibrational states reproduces the characteristic power laws of DIMET experiments and yields the exponent associated with a given adsorbate/substrate system.

The model we have used for calculating the energy-transfer rates obviously represents a very simplified view of the dynamics. First of all it is a model of noninteracting electrons. We assume that we can include the important part of the electron-electron interactions by using nonadiabatic coupling coefficients λ_i obtained from the interacting density with linear-expansion ΔSCF-DFT. The approximation amounts to assuming ballistic hot electrons and instantaneous restructuring of the electronic environment when occupying the resonance. Although this may be the case in some metallic systems, electron-electron interactions could have effects which go beyond a simple renormalization of the nonadiabatic coupling. The linear nonadiabatic coupling regime leading to Eq. (5) corresponds to an assumption of equal curvature on the ground- and excited-state PESs. This is a good approximation for CO but NO has a very shallow excited-state PES on some of the transition metals and there the approximation may not be as good.

Furthermore the model assumes that the ground-state potential is quadratic and that the excited-state potential is simply a shifted ground-state potential. At least in the COM direction it is clear from Fig. 1 that the ground-state potential deviates significantly from a quadratic potential and since we are concerned with high-lying vibrational excitations, this deviation could perhaps have an important effect. It may be possible to include anharmonic terms in the Hamiltonian and calculate different scattering amplitudes perturbatively but this will be left for future work.

We have focused on the molecules CO and NO, since they have a conceptually simple structure and a vast amount of experiments have been performed on these systems. However, it is well known that generalized gradient approxima-

tion (GGA)–DFT calculations of CO adsorbed an Pt(111) predict CO to bind at a hollow site in contradiction to the experimentally observed top site.[45] While the difference in adsorbtion energy appears to be less with GPAW than in the calculations presented in Ref. 45, possibly due to the use of the PAW method instead of ultrasoft pseudopotentials, the difference is still 80 meV and the inability to predict the correct binding site is worrying. On the other hand, the existence in the calculation of another adsorption site with a slightly lower energy is unlikely to change the local shape in the potential energy surface enough to *qualitatively* change the results obtained here. In addition, we see a very similar behavior for CO on Ru(0001), where DFT does predict the right adsorption site (the top site). We have thus chosen to put CO at the experimentally observed top site as the hollow site would lead to a smaller surface molecule distance and thus very different screening and desorption rate.

As previously mentioned the value of Γ is estimated from the Kohn-Sham projected density of states, but we do not know how well this estimate matches the true value and as such we have mostly treated Γ as a free parameter. In fact the object of interest in the problem is the spectral function of the resonant state; but even if we had a reliable way of determining this function we would have to make the wideband approximation (where the spectral function is a Lorentzian of width Γ) in order to calculate scattering rates. Nevertheless it would be very interesting to calculate this function to get an idea of the validity of the wideband approximation and to obtain a trustworthy value of Γ.

We have not made any attempt to predict how the distribution of energy evolves after a molecule returns to its electronic ground state, but assume that the dissipation of energy is slow enough that the adsorbate will desorb if the desorption energy has been transferred. This is of course a rather crude assumption and the rate of energy transfer should be accompanied by a detailed molecular propagation on the full-dimensional ground-state PES to improve the results. Ground-state molecular dynamics would also be necessary to obtain branching ratios when there is a possibility of different chemical reactions induced by hot electrons.

However the model we have presented captures some of the essential features of nonadiabatic dynamics. For example, the appearance of an effective inelastic resonance which is detuned from the electronic resonance by an amount depending on the energy transfer is a pure nonadiabatic result and would never have emerged from an adiabatic model. Furthermore the exponents in the DIMET power laws appear to be determined by the number of vibrational quanta needed for desorption and thus communicate the quantum nature of the dynamics.

ACKNOWLEDGMENTS

We would like to acknowledge the help and advice of Jens Jørgen Mortensen on implementing and using linear-expansion ΔSCF in GPAW. The Center for Individual Nanoparticle Functionality (CINF) is sponsored by the Danish National Research Foundation. This work was supported by the Danish Center for Scientific Computing.

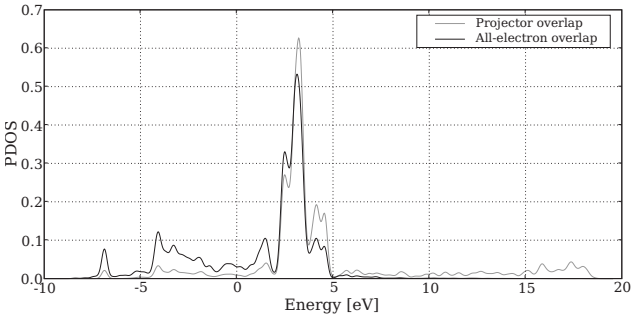

FIG. 8. Ground-state calculation of CO adsorbed on Pt(111) top site. The projected density of states of the 2π orbitals using the methods of projector or pseudowave-function overlap and all-electron wave-function overlap are compared. In the projector overlap method the orbital is defined by $|\tilde{p}_{2\pi}\rangle = \frac{1}{\sqrt{13}}(3|\tilde{p}_x\rangle_C - 2|\tilde{p}_x\rangle_O)$ which is the orbital most similar to the gas-phase calculation. The long high-energy tail of the projector overlap signals an inaccuracy of the method and makes excited-state calculations dependent on the number of unoccupied bands. Thus we use the all-electron overlaps to determine expansion coefficients in this work.

APPENDIX A: PROJECTING KS STATES ON A MOLECULAR ORBITAL IN PAW

The PAW method[32] utilizes that one can transform single-particle wave functions $|\psi_n\rangle$ oscillating wildly near the atom core (all-electron wave functions) into smooth well-behaved wave functions $|\tilde{\psi}_n\rangle$ (pseudowave functions) which are identical to the all-electron wave functions outside some augmentation sphere. The idea is to expand the pseudowave function inside the augmentation sphere on a basis of smooth continuations $|\tilde{\phi}_i^a\rangle$ of partial waves $|\phi_i^a\rangle$ centered on atom a. The transformation is

$$|\psi_n\rangle = |\tilde{\psi}_n\rangle + \sum_{i,a} (|\phi_i^a\rangle - |\tilde{\phi}_i^a\rangle)\langle\tilde{p}_i^a|\tilde{\psi}_n\rangle, \tag{A1}$$

where the projector functions $|\tilde{p}_i^a\rangle$ inside the augmentation sphere a fulfills

$$\sum_i \langle\tilde{p}_i^a|\tilde{\phi}_i^a\rangle = 1, \quad \langle\tilde{p}_i^a|\tilde{\phi}_j^a\rangle = \delta_{ij}, \quad |\mathbf{r} - \mathbf{R}^a| < r_c^a.$$

The method of linear-expansion ΔSCF involves expanding a molecular orbital $|\varphi_i\rangle$ in Kohn-Sham states $|\psi_n\rangle$ and does a self-consistent calculation with an additional density corresponding to the orbital.[26] The simplest way of getting the expansion coefficients is using the projector overlaps $\langle\psi_n|\varphi_i\rangle \sim \langle\tilde{\psi}_n|\tilde{p}_i^a\rangle$ which is calculated in each iteration anyway. However, this method turns out to be too inaccurate in the case of CO on Pt(111) due to nonvanishing projector overlaps for highly energetic Kohn-Sham states as shown in Fig. 8. This implies that the expansion coefficients depend on the number of unoccupied bands included in the calculation

To calculate the overlaps $\langle\psi_n|\varphi_i\rangle$ exactly, one should start by performing a gas-phase calculation of the molecule or atom which is to be used in the ΔSCF calculation. The pseudowave function $\tilde{\psi}_i(x)$ corresponding to the orbital to be occupied is then saved along with the projector overlaps

$\langle \tilde{p}_k^a | \tilde{\psi}_i \rangle$ and the ΔSCF calculation is initialized. In each step of the calculation we can then do a numerical integration to obtain the expansion coefficients by

$$c_{ni} = \langle \psi_n | \psi_i \rangle = \langle \tilde{\psi}_n | \tilde{\psi}_i \rangle + \sum_{a,j,k} \langle \tilde{\psi}_n | \tilde{p}_j^a \rangle (\langle \phi_j^a | \phi_k^a \rangle - \langle \tilde{\phi}_j^a | \tilde{\phi}_k^a \rangle) \times \langle \tilde{p}_k^a | \tilde{\psi}_i \rangle, \tag{A2}$$

where Eq. (A1) was used. Note that there is only a single sum over atoms (and only the ones in the molecule) and that the cross terms of pseudowave or all-electron wave function does not contribute. This can be seen using the arguments following Eq. 20 of Ref. 33.

APPENDIX B: CALCULATING THE INELASTIC-SCATTERING PROBABILITY

Here we briefly summarize the calculation leading to the inelastic-scattering probabilities in model (5).[29] An explicit expression for the probability has previously been obtained[29] for a single mode at initially in the ground state. Here we will extend the result to an explicit expression for any number of modes initially in a thermal ensemble of vibrationally excited states.

From Hamiltonian (3) the differential reflection matrix $R(\varepsilon_i, \varepsilon_f)$ which is defined as the probability per unit final-state energy that an incoming hot electron with energy ε_i scatters on the resonance into a final state of ε_f can be expressed in terms of the four-point Green's function. The inelastic part is contained in the expression,

$$R_{\mathrm{in}}(\varepsilon_i, \varepsilon_f) = \Gamma(\varepsilon_f)\Gamma(\varepsilon_i) \int\int\int \frac{d\tau ds dt}{2\pi\hbar^3} e^{i[(\varepsilon_i - \varepsilon_f)\tau + \varepsilon_f t - \varepsilon_i s]/\hbar} \times G(\tau, s, t), \tag{B1}$$

where the Green's functions is

$$G(\tau, s, t) = \theta(s)\theta(t)\langle c_a(\tau - s) c_a^\dagger(\tau) c_a(t) c_a^\dagger(0) \rangle,$$

$$c(t) = e^{iHt/\hbar} c(0) e^{-iHt/\hbar}, \tag{B2}$$

and $\langle\ \rangle$ denotes a thermal ensemble of oscillator states. The expression is valid for any nonadiabatic coupling function $\varepsilon_a(x)$, but in general it can be very hard to obtain an expression for the Green's function. An exception is the wideband limit with linear coupling corresponding to Hamiltonian (5).[29] The Green's function then becomes

$$G(\tau, s, t) = \theta(t)\theta(s) e^{-i\epsilon_a (t-s)/\hbar - \Gamma(t+s)/2\hbar} \times \exp\left(\sum_i g_i [i(t-s)\omega_i - (1+n_i) f_i - n_i f_i^\square] \right), \tag{B3}$$

where ϵ_a is center of the resonance, n_i is the Bose distribution, $g_i = (\lambda_i / \hbar\omega_i)^2$ is the effective coupling constant of the mode i, and

$$f_i(\tau, s, t) = 2 - e^{-i\omega_i t} - e^{i\omega_i s} + e^{-i\omega_i \tau}(1 - e^{i\omega_i t})(1 - e^{i\omega_i s}). \tag{B4}$$

The integrals in scattering matrix (B1) can be evaluated by writing the exponentials in Eq. (B3) as Taylor expansions and performing the τ integral. This leaves the remaining two integrals as complex conjugates which are evaluated by writing factors such as $(1 - e^{i\omega_i t})^m$ by their binomial expansions. For a single oscillator with thermal occupation n we obtain the inelastic reflection matrix,

$$R_{\mathrm{in}}(\varepsilon_i, \varepsilon_f, n) = \Gamma^2 e^{-2g(1+2n)} \sum_{m_1=0}^{\infty} \sum_{m_2=0}^{\infty} \frac{g^{m_1+m_2}(1+n)^{m_1} n^{m_2}}{m_1!\, m_2!} \times \delta(\varepsilon_i - \varepsilon_f - (m_1 - m_2)\hbar\omega) \times F(m_1, m_2), \tag{B5}$$

with

$$F(m_1, m_2) = \left| \sum_{i=0}^{m_1} \sum_{j=0}^{m_2} (-1)^{i+j} \binom{m_1}{i} \binom{m_2}{j} \times \sum_{k=0}^{\infty} \sum_{l=0}^{\infty} \frac{g^{k+l}(1+n)^k n^l}{k!\, l!} \times \frac{1}{\varepsilon_i - \epsilon_a - (i - j + k - l - g)\hbar\omega + i\Gamma/2} \right|^2.$$

Although the expression looks rather complicated it has a simple interpretation. Integrating over final-state energies in the vicinity of $\Delta n = m_1 - m_2$ gives the probability of transferring $\Delta E = \Delta n \hbar\omega$ to the oscillator if the energy of the incoming electron is ε_i,

$$P_{\Delta n}(\varepsilon_i, n) = \Gamma^2 e^{-2g(1+2n)} \left[\frac{g^{\Delta n}(1+n)^{\Delta n}}{\Delta n!} F(\Delta n, 0) + \frac{g^{\Delta n+1}(1+n)^{\Delta n+1} gn}{(\Delta n+1)!} F(\Delta n+1, 1) + \frac{g^{\Delta n+2}(1+n)^{\Delta n+2}(gn)^2}{(\Delta n+2)!\, 2!} F(\Delta n+2, 2) + \cdots \right], \tag{B6}$$

where the first term is the probability of adding Δn bosons, the second term is the probability for removing (coupling ng) one, and adding [coupling $(n+1)g$] $\Delta n+1$ bosons and so forth.

We can also evaluate the differential reflection matrix for N oscillators initially in the ground state with frequencies and coupling constants ω_i and g_i, respectively. The result is

$$R_{\mathrm{in}}(\varepsilon_i,\varepsilon_f)=\Gamma^2 e^{-2\Sigma_{i=1}^N g_i}\sum_{m_1=0}^{\infty}\cdots\sum_{m_N=0}^{\infty}\frac{g_1^{m_1}\cdots g_N^{m_N}}{m_1!\cdots m_N!}\delta\left(\varepsilon_i-\varepsilon_f-\sum_{i=1}^{N}m_i\hbar\omega_i\right)\left|\sum_{j_1=1}^{m_1}\cdots\sum_{j_N=1}^{m_N}(-1)^{\Sigma_{i=1}^N j_i}\binom{m_1}{j_1}\cdots\binom{m_N}{j_N}\right.$$

$$\left.\times\sum_{L_1=0}^{\infty}\cdots\sum_{l_N=0}^{\infty}\frac{g_1^{l_1}\cdots g_N^{l_N}}{l_1!\cdots l_N!}\frac{1}{\varepsilon_i-\epsilon_a+i\Gamma/2-\sum_{i=1}^{N}(j_i+l_i-g_i)\hbar\omega_i}\right|^2. \tag{B7}$$

It is amusing that result (B5) for a one-mode system with initial excitation number n follows from result (B7) if we regard Eq. (B5) as a two-mode system at $T=0$ with energies $\hbar\omega$ and $-\hbar\omega$ and coupling constants $g(n+1)$ and gn, respectively. For convenience we state the probability of exciting the (m_d,m_z) state from the ground state in the two-dimensional model with modes d and z,

$$P_{m_d m_z}(\varepsilon_i)=\Gamma^2 e^{-2(g_d+g_z)}\frac{g_d^{m_d}g_z^{m_z}}{m_d!\,n_z!}\left|\sum_{j_d=1}^{m_d}\sum_{j_z=1}^{m_z}(-1)^{j_d+j_z}\binom{m_d}{j_d}\binom{m_z}{j_z}\sum_{k=0}^{\infty}\sum_{l=0}^{\infty}\frac{g_d^k g_z^l}{k!\,l!}\frac{1}{\varepsilon_i-\epsilon_a-(j_d+k-g_d)\hbar\omega_d-(j_z+l-g_z)\hbar\omega_z+i\Gamma/2}\right|^2. \tag{B8}$$

Elastic scattering

The elastic part of the scattering matrix for a single oscillator with thermal occupation number n is

$$R_{\mathrm{el}}(\varepsilon_i,\varepsilon_f,n)=\delta(\varepsilon_i-\varepsilon_f)[1+2\ \mathrm{Im}\ G_R(\varepsilon_i)],$$

$$G_R(\varepsilon)=\int\frac{dt}{\hbar}e^{i\varepsilon t/\hbar}G_R(t),$$

$$G_R(t)=-i\theta(t)\langle n|c_a(t)c_a^{\dagger}(0)|n\rangle. \tag{B9}$$

We can use the linked cluster theorem to derive the retarded Green's function and get the result

$$G_R(t)=-i\theta(t)e^{-g(1+2n)}e^{(-i\epsilon_a-ig\hbar\omega-\Gamma/2)t/\hbar}\sum_{m_1=0}^{\infty}\sum_{m_2=0}^{\infty}\frac{g^{m_1}n^{m_1}g^{m_2}(1+n)^{m_2}}{m_1!\,m_2!}e^{-i(m_2-m_1)\omega t}. \tag{B10}$$

We can then calculate the elastic part of the scattering probability and get

$$P_{\mathrm{el}}(\varepsilon_i,n)=1-\Gamma^2 e^{-g(1+2n)}\sum_{m_1=0}^{\infty}\sum_{m_2=0}^{\infty}\frac{g^{m_1}n^{m_1}g^{m_2}(1+n)^{m_2}}{m_1!\,m_2!}\frac{1}{(\varepsilon_i-\epsilon_a-[m_2-m_1-g]\hbar\omega)^2+(\Gamma/2)^2}. \tag{B11}$$

When calculating the elastic-scattering probability one should also remember to include the $m_1=m_2$ terms in Eq. (B5).

The n in the expressions above denote the Bose distribution and not a specific state $|n\rangle$, but in the context of DIMET our main point of interest is the probability that a oscillator initially in the state $|n_i\rangle$ scatters inelastically to the state $|n_f\rangle$. However, the expression in the case of a pure state is very similar to the thermal ensemble, the only difference being that we should make the substitution

$$e^{-g_i n_i(f_i+f_i^{\square})}\rightarrow L_{n_i}[g(f_i+f_i^{\square})] \tag{B12}$$

in Eq. (B3), where $L_n(x)$ is the nth Laguerre polynomial. The expression involving Laguerre polynomials is somewhat more complicated to handle numerically and therefore we have chosen to work with the thermal ensemble expressions instead. In the range of parameters in the present work, the thermal ensemble expressions are very good approximations since $L_n(x)$ have the same first-order Taylor expansion as e^{-nx} and for $t<\hbar/\Gamma$ we get $g_i f_i<0.001$.

*schiotz@fysik.dtu.dk

[1] S. A. Buntin, L. J. Richter, R. R. Cavanagh, and D. S. King, Phys. Rev. Lett. **61**, 1321 (1988).
[2] S. A. Buntin, L. J. Richter, D. S. King, and R. R. Cavanagh, J. Chem. Phys. **91**, 6429 (1989).
[3] F. Fournier, W. Zheng, S. Carrez, H. Dubost, and B. Bourguignon, Phys. Rev. Lett. **92**, 216102 (2004).
[4] J. A. Prybyla, T. F. Heinz, J. A. Misewich, M. M. T. Loy, and J. H. Glownia, Phys. Rev. Lett. **64**, 1537 (1990).
[5] J. A. Prybyla, H. W. K. Tom, and G. D. Aumiller, Phys. Rev. Lett. **68**, 503 (1992).
[6] F. Budde, T. F. Heinz, M. M. T. Loy, J. A. Misewich, F. de Rougemont, and H. Zacharias, Phys. Rev. Lett. **66**, 3024 (1991).
[7] J. A. Misewich, A. Kalamarides, T. F. Heinz, U. Höfer, and D. M. Newns, J. Chem. Phys. **100**, 736 (1994).
[8] L. M. Struck, L. J. Richter, S. A. Buntin, R. R. Cavanagh, and J. C. Stephenson, Phys. Rev. Lett. **77**, 4576 (1996).
[9] P. T. Howe and H. L. Dai, Surf. Sci. **451**, 12 (2000).
[10] L. Cai, X. Xiao, and M. M. T. Loy, Surf. Sci. Lett. **464**, L727 (2000).
[11] M. Bonn, C. Hess, S. Funk, J. H. Miners, B. N. J. Persson, M. Wolf, and G. Ertl, Phys. Rev. Lett. **84**, 4653 (2000).
[12] J. A. Misewich, T. F. Heinz, and D. M. Newns, Phys. Rev. Lett. **68**, 3737 (1992).
[13] J. W. Gadzuk, Phys. Rev. Lett. **76**, 4234 (1996).
[14] L. B. Thomsen, G. Nielsen, S. B. Vendelbo, M. Johansson, O. Hansen, and I. Chorkendorff, Phys. Rev. B **76**, 155315 (2007).
[15] J. W. Gadzuk, L. J. Richter, S. A. Buntin, D. S. King, and R. R. Cavanagh, Surf. Sci. **235**, 317 (1990).
[16] J. W. Gadzuk, Phys. Rev. B **44**, 13466 (1991).
[17] J. W. Gadzuk, Surf. Sci. **342**, 345 (1995).
[18] S. M. Harris, S. Holloway, and G. R. Darling, J. Chem. Phys. **102**, 8235 (1995).
[19] J. W. Gadzuk, J. Vac. Sci. Technol. A **15**, 1520 (1997).
[20] P. Saalfrank, G. Boendgen, K. Finger, and L. Pesce, J. Chem. Phys. **251**, 51 (2000).
[21] A. Nourtier, J. Phys. (Paris) **38**, 479 (1977).
[22] D. M. Newns, T. F. Heinz, and J. A. Misewich, Prog. Theor. Phys. Suppl. **106**, 411 (1991).
[23] M. Brandbyge, P. Hedegård, T. F. Heinz, J. A. Misewich, and D. M. Newns, Phys. Rev. B **52**, 6042 (1995).
[24] A. C. Luntz and M. Persson, J. Chem. Phys. **123**, 074704 (2005).
[25] A. C. Luntz, M. Persson, S. Wagner, C. Frischkorn, and M. Wolf, J. Chem. Phys. **124**, 244702 (2006).
[26] J. Gavnholt, T. Olsen, M. Engelund, and J. Schiøtz, Phys. Rev. B **78**, 075441 (2008).
[27] P. W. Anderson, Phys. Rev. **124**, 41 (1961).
[28] D. M. Newns, Phys. Rev. **178**, 1123 (1969).
[29] N. S. Wingreen, K. W. Jacobsen, and J. W. Wilkins, Phys. Rev. B **40**, 11834 (1989).
[30] The GPAW code is available as a part of the CAMPOS software: www.camd.dtu.dk/Software
[31] J. J. Mortensen, L. B. Hansen, and K. W. Jacobsen, Phys. Rev. B **71**, 035109 (2005).
[32] P. E. Blöchl, Phys. Rev. B **50**, 17953 (1994).
[33] P. E. Blöchl, C. J. Först, and J. Schimpl, Bull. Mater. Sci. **26**, 33 (2003).
[34] B. Hammer, L. B. Hansen, and J. K. Nørskov, Phys. Rev. B **59**, 7413 (1999).
[35] J. P. Perdew, K. Burke, and M. Ernzerhof, Phys. Rev. Lett. **77**, 3865 (1996).
[36] S. Kurth, J. P. Perdew, and P. Blaha, Int. J. Quantum Chem. **75**, 889 (1999).
[37] P. R. Antoniewicz, Phys. Rev. B **21**, 3811 (1980).
[38] J. D. Beckerle, M. P. Casassa, R. R. Cavanagh, E. J. Heilweil, and J. C. Stephenson, Phys. Rev. Lett. **64**, 2090 (1990).
[39] F. Abild-Pedersen and M. P. Andersson, Surf. Sci. **601**, 1747 (2007).
[40] M. Croci, C. Felix, G. Vandoni, W. Harbich, and R. Monot, Surf. Sci. **307–309**, 460 (1994).
[41] R. T. Vang, J. G. Wang, J. Knudsen, J. Schnadt, E. Lægsgaard, I. Steensgaard, and F. Besenbacher, J. Phys. Chem. B **109**, 14262 (2005).
[42] D. A. Butler, B. Berenbak, S. Stolte, and A. W. Kleyn, Phys. Rev. Lett. **78**, 4653 (1997).
[43] M. Ø. Pedersen, M. L. Bocquet, P. Sautet, E. Lægsgaard, I. Stensgaard, and F. Besenbacher, Chem. Phys. Lett. **299**, 403 (1999).
[44] W. Ho, Surf. Sci. **363**, 166 (1996).
[45] P. J. Feibelman, B. Hammer, J. K. Nørskov, F. Wagner, M. Scheffler, R. Stumpf, R. Watwe, and J. Dumesic, J. Phys. Chem. B **105**, 4018 (2001).

Paper IV

Hot electron assisted femtochemistry at surfaces - a TDDFT approach

Jeppe Gavnholt,[1] Angel Rubio,[2] Thomas Olsen,[1] Kristian S. Thygesen,[3] and Jakob Schiøtz[1]

[1]*Danish National Researh Foundation's Center for Individual Nanoparticle Functionality (CINF), Department of Physics, Technical University of Denmark, DK–2800 Kongens Lyngby, Denmark*

[2]*European Theoretical Spectroscopy Facility (ETSF) Dpto. Fisica de Materiales, U. del Pais Vasco, E-20018 Donostia-San Sebastian, Spain*

[3]*Center for Atomic-scale Materials Design (CAMD), Department of Physics, Technical University of Denmark, DK–2800 Kongens Lyngby, Denmark*

(Dated: January 15, 2009)

Using time-evolution time-dependent density functional theory (TDDFT) we study the interactions between single electrons and molecular resonances at surfaces. We perform a number of calculations on an electron hitting an adsorbed molecule from inside the surface and establish a picture, where the resonance is being probed by the incoming electron. This enables us to extract the position of the resonance energy through a fitting procedure. It is demonstrated that with the model we can extract several properties of the system, such as the presence of resonance peaks, the time electrons stay on the molecule before returning to the surface when hitting a molecular resonance and the lowering of the resonance energy due to an image charge effect. Finally we apply the TDDFT procedure to only consider the decay of molecular excitations and find that it agrees quite well with the width of the projected density of Kohn-Sham states.

PACS numbers: 31.15.ee, 73.20.Hb, 82.20.Gk

I. INTRODUCTION

In most chemical processes the intrinsic barriers are overcome due to the randomly directed thermal energy of the atomic cores. This sets some limitations on the possibility of controlling chemical reactions, since the thermal energy will distribute itself among all degrees of freedom in the system, ie. the energy cannot be directed towards for example splitting of a certain molecule or desorption of another. Furthermore, in order to get a satisfactory turnover frequency, in some catalyzed reactions, the temperature may need to be so high that the catalyst becomes unstable and degrades over time.

In hot electron assisted femtochemistry at surfaces[1–8] the hot electrons (electrons with an energy significantly above the Fermi level) interact with molecular resonances, which gives rise to an electron-phonon coupling. This will initiate motion mainly in those vibrational modes where the coupling is high, ie. it is possible to direct energy towards certain vibrational modes. This has been demonstrated in an experiment by Bonn et al.,[8] who were able to form carbondioxide from carbonmonooxide and oxygen on a Ruthenium (0001) surface with the help of hot electrons. This is normally impossible because the carbonmonooxide desorbs before the carbondioxide formation, when the temperature is raised. The effect is explained by the hot electrons injecting energy into the vibrational modes of the adsorbed atomic oxygen, so that the barrier to forming carbonmonooxide can be overcome at a lower temperature.

In most femtochemistry experiments the hot electrons are generated using a femtosecond laser pulse. Each pulse excites a lot of electrons in the metal surface. Due to the high electron density the electron-electron scattering thermalize the hot electrons very rapidly, on a femtosecond timescale, giving rise to an electronic temperature, which is much higher than the phonon temperature. The phonons and electrons will equilibriate much slower, on a picosecond timescale, ie. for several picoseconds there are electrons present, which have sufficient energy to interact with otherwise unreachable molecular resonances. The high concentration of high-energy electrons even makes it possible to observe multi-electron processes, such as desorption induced by multiple electronic transistions (DIMET), which has been observed for a variety of systems.[9] However, the thermal distribution of electrons does not make it possible to target a specific molecular resonance, which lie above other resonances in energy.

Another approach to generating hot electrons, by the use of a Metal-Insulator-Metal (MIM) junction, has been suggested by Gadzuk.[7] If the insulating layer in the junction is sufficiently thin and a finite bias is applied, electrons will tunnel from near the Fermi level of the first metal into the other metal, where they can have an energy significantly above the Fermi level, ie. they will be hot electrons. If the second metal layer is also very thin, these electrons will be able to reach the surface of the other metal, and perhaps induce chemistry. The advantage of such a device is that it should, at least theoretically, be possible to target certain molecular resonances by tuning the energy of the hot electrons. The disadvantage being that it will probably not be possible to generate a high electron flux, ie. only single-electron processes can be observed. Such a MIM device, where the first metal has been substituted by a highly doped silicon layer, has recently been created,[10] and its ability to induce chemical reactions is currently being investigated.

We have previously investigated the hot electron interaction with different diatomic molecules on different tran-

sition metal surfaces, by applying an electron-phonon interaction model to potential energy surfaces, which are obtained from the delta self-consistent field method.[11,12] The purpose of this paper is to investigate a different approach, based on time-evolution time dependent density functional theory (TDDFT), to modelling hot electrons interacting with molecular resonances. TDDFT provides, in principle, an exact framework to describe non-equilibrium processes as the ones relevant in femtochemistry and transport. The price one has to pay in TDDFT is that all correlation effects are embedded in an exchange and correlation kernel that should be non-local in space and time. However, most functional in use nowadays are not designed to cope with non-equlibrium situations, but still it is common practice to apply local and semi-local functionals to those situations. Further work is needed in the development of non-local and frequency dependent exchange-correlation functionals, which would have impact beyond the present studies. The hope is, however, that such an approach with a simple exchange-correlation functional can still give supplementary information about the occuring processes. Of specific interest are the cross-section for exciting the resonance and the lifetime the molecular excitations, which are very important when considering the possiblity of hot electrons inducing chemistry.[12] Another nice feature of the time-evolution approach is that it offers the possibility of simulating the entire event of one hot electron hitting a molecule, ie. it offers a more physically intuitive picture. Finally it is also woth mentioning that TDDFT provides a multi-component approach,[13] where the electron and nuclei motion can be directly coupled. This provides the hope that the TDDFT approach presented here in the future can involve a direct calculation of the induced molecular motion.

In the following we will start by giving a description of how the time-evolution TDDFT calculation have been performed. After this we present the simulations of the entire event of a hot electron hitting a molecule at a surface. We start by considering a simple model system and then move on to a more realistic system. Finally we will investigate the lifetime of molecular excitations, by starting time-evolution TDDFT calculations from the excited state. All the way through we will focus on Nitrogen adsorbed on Ruthenium, although the methods presented of course are general.

II. METHOD

The main type of calculation performed in this paper is a time-evolution TDDFT calculation, which we have done with the freely available OCTOPUS code.[14,15] We use an Adiabatic Local-Density Approximation (ALDA)[16] description of the exchange-correlation functional. Non-adiabatic effects and initial state dependence of the exchange-correlation functional are not accounted for by the simple LDA-type functional. However, this is not a serious drawback for the present work where we are more interested in getting a qualitative rather than a quantitative picture of the process of hot-electron induced femtochemistry at metal surfaces. To describe core electrons we use norm-conserving pseudopotentials from the Fritz-Haber-Institute (FHI),[17] generated using the Troullier-Martins scheme.[18] OCTOPUS uses a real-space grid to represent wavefunctions and densities. After some convergence tests we found that a grid-spacing of 0.18 Å gives sufficient accuracy. The Kohn-Sham equations are propagated using a combination of the exponential midpoint rule[19] and a Krylov subspace approximation to the exponential matrix operator.[20] The optimal timestep for the type of systems considered here was found to be 0.001 fs, so this timestep has been used in all calculations presented in this paper.

The time-evolution TDDFT calculations have not been started from the ground state, but still ground state calculations have been used in the generation of the initial states as it will be clear from Secs. III and IV. Unless otherwise specified the ground state calculations have been made using the OCTOPUS code, with a Local-Density Appoximation (LDA)[21] description of the exchange-correlation interactions to maintain consistency with the TDDFT calculations. In each cycle towards self-consistency in the Kohn-Sham equations a Broyden mixing[22] of the 7 preceeding densities is performed and the Hamiltonian is diagonalized iteratively using the conjugate-gradient method. The occupations of the Kohn-Sham states follow a Fermi-Dirac distribution with an electronic temperature of 0.1 eV, which is necessary in order to get convergence.

III. EXCITING AN ADSORBED MOLECULE

In this section we consider the entire event of a single electron hitting a molecule adsorbed at a surface. We will start from a situation, where an electron is placed inside the surface and has a momentum towards the molecule sitting on the surface. This means that we do not consider the creation of the hot electron, but the simulated situation is very similar to that found in the MIM device, where hot electrons come from inside the surface with a sufficiently low rate, such that the hot electrons do not affect each other. Naturally, we expect the interaction between the hot electron and the molecular resonance to depend on the starting state of the hot electron, so in order to get some information on this dependence we will start by considering a very simple system. After this we will go to a more realistic system, consisting of a Nitrogen molecule adsorbed on a Ruthenium cluster.

A. Nitrogen on a fictitious surface

In this section we consider a very simple representation of a molecule adsorbed on a surface. As the adsorbed

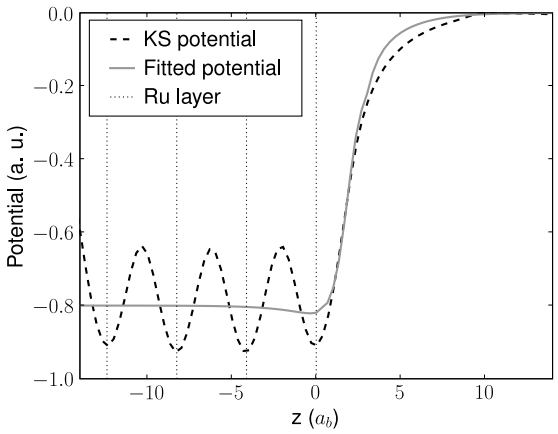

FIG. 1: A fit of the Kohn-Sham potential at a Ruthenium surface. The dotted curve shows the self-consistent ground state Kohn-Sham potential of a 4 layer Ruthenium (0001) slab averaged over the directions parallel to the surface. The solid curve shows our fit from Eq. (1). The vertical lines indicate the positions of the layers in the slab. The DFT calculation was made with the GPAW code.[23,24]

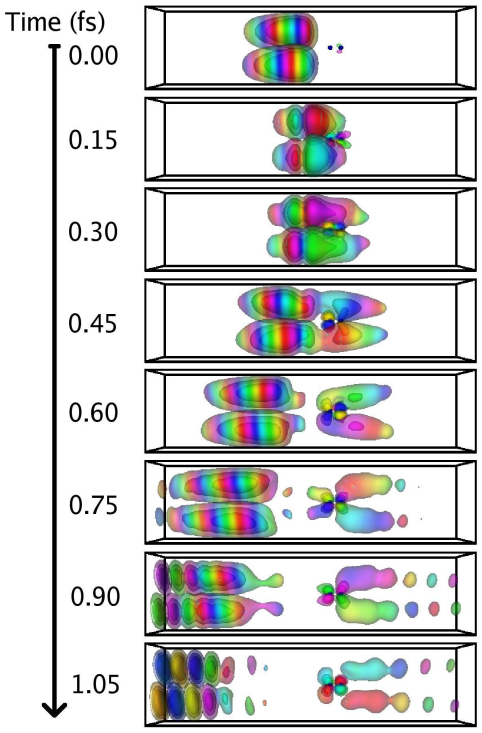

FIG. 2: An example of the evolution over time of a hot electron with a momentum directed towards the molecule. The hot electron orbital is shown at times: 0 fs, 0.15 fs, 0.30 fs, 0.45 fs, 0.60 fs, 0.75 fs, 0.90 fs and 1.05 fs. The grey scale (online: color grading) indicates the phase of the orbital. The two dots, which are visible at $t = 0$ fs, indicate the positions of the Nitrogen atoms. The unit cell is cylindrical with a radius of 4 Å and a length of 40 Å and is exactly contained in the shown boxes.

molecule we use the diatomic Nitrogen molecule and instead of representing the surface with a lot of individual atoms, we use a simple external potential. One could just use a step-function, but in order to avoid any spurious effects due to the hard edges, we make a fit to the Kohn-Sham potential of a Ruthenium slab DFT calculation, which is shown on Fig. 1. The slap consists of 4 atomic layers and the exposed surfaces are close-packed (0001) surfaces. The shown Kohn-Sham potential has been averaged over the directions parallel to the surface. The fitted potential is in atomic units[25] given by the expression

$$V_{fit}(z) = -0.8\frac{1}{1+e^{4(z-1)}} - 0.16e^{-|z-1.55|}, \qquad (1)$$

where z is the coordinate perpendicular to the surface and $z = 0$ corresponds to the position of the outermost layer of atoms in the surface. The expression of Eq. (1) only respresents the surface, ie. the entire system of a surface and a molecule is handled by applying an external potential of $V_{fit}(z) + \sum_a V^a_{cent}(\mathbf{r})$, where V^a_{cent} is the central potential of atom a in the molecule. Furthermore the valence electrons of the molecule are included in the calculations, whereas no electrons of the surface are included.

This simple representation of the surface has the advantage that it is easy to generate an starting orbital for the hot electron inside the surface, which is orthogonal to the other occupied orbitals, since all other electrons are located on the molecule outside the surface. Furthermore the computational effort is significantly lowered by the fact that only a few electrons are included in the calculation.

Figure 2 shows an example of how the orbital of a hot electron evolves over time, when it starts inside the surface with a momentum towards the surface. Before the time-evolution calculation the states of the valence electrons of the Nitrogen molecule was found by performing a ground state calculation with just these electrons. The starting orbital of the hot electron is an unoccupied eigenfunction of this ground-state Hamiltonian multiplied by $e^{i0.8z}$, in order to give it a momentum of 0.8 a.u. towards the surface. This eigenfunction was chosen because it is almost entirely located inside the surface and it has the Π symmetry needed in order for it to interact with the $2\pi^*$ states of the molecule.

Figure 2 shows several interesting features. When hitting the surface a large fraction of the electron is reflected due to the workfunction of the surface, but some of the electron ends up in the $2\pi^*$ states of the molecule, indicating a non-zero probability of exciting the molecule. In this calculation some of the electron is apparently also transmitted by the molecule, which indicates that some of the electron has an energy above the vacuum level. From the figure it is also obvious that it does not make

Wf. no.	Picture	Specifications
1	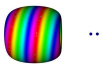	**Radial direction:** 1. order Bessel function **z direction:** Gaussian wavepacket with $p_0 = 0.8$, $\Delta p = 0.1$
2		**Radial direction:** 1. order Bessel function **z direction:** Gaussian wavepacket with $p_0 = 0.8$, $\Delta p = 0.2$
3		**Radial direction:** 1. order Bessel function **z direction:** Gaussian wavepacket with $p_0 = 0.8$, $\Delta p = 0.4$
4		Eigenfunction for the ground state Hamiltonian (eigenfunction no. 7) times $e^{ip_0 x}$, $p_0 = 0.8$
5		Eigenfunction for the ground state Hamiltonian (eigenfunction no. 13) times $e^{ip_0 x}$, $p_0 = 0.8$

TABLE I: The five different types of wavefunctions we use as starting orbitals for the hot electron in section III. The 1. order Bessel function used in the radial direction for wavefunction 1-3 is scaled such that the first node coincides with the unit cell boundary. The grey scale (online: color grading) indicates the phase of the wavefunctions. The unit cells are cylindrical with a radius of 6 Å and a length of 80 Å.

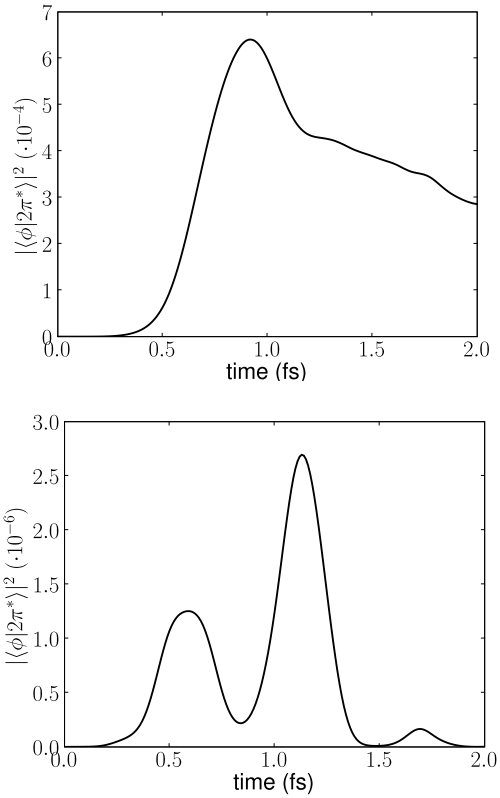

FIG. 3: The difference between an electron that hits resonance and one that does not. The y-axes are the orbital of the hot electron, ϕ, projected to the subspace spanned by the two $2\pi^*$ orbitals of the molecule squared. The x-axes show the time. Top panel is an example of an electron hitting resonance (Wf. no. 1 from Table I with $p_0 = 0.8$) . Bottom panel is an example of an electron not hitting resonance (Wf. no. 1 from Table I with $p_0 = 0.4$). Please notice the more than two orders of magnitude difference in the y-axis scales.

sense to continue the calculation much further, since the reflections of the electron at the unphysical unit cell edges start to interfer with the molecule after approximately 1 fs.

For the calculation displayed on Fig. 2 we chose the starting orbital of the hot electron rather randomly. In order to get an idea of how the obtained results vary with the starting orbital we have carried out calculations with the hot electron starting in a number of different starting orbitals as illustrated in Table I. Each of the orbitals shown in Table I have an average momentum in the z-direction of 0.8 a.u., but we also made several calculations on the same orbitals, but with different average momenta, ie. multiplied with a different exponential factor ($e^{ip_0 z}$). The unit cells have been made twice as long as the unit cell in Fig. 2 in order to prolong the time it takes before reflected waves reach the molecule.

The fraction of the electron that gets into the $2\pi^*$-orbitals of the molecule varies a lot from calculation to calculation. The upper and lower panel on Fig. 3 illustrate the situations where a rather large part and a rather small part, respectively, of the electron goes into the $2\pi^*$-orbitals. The y-axes show the projection of the orbital of the hot electron onto the subspace spanned by the two $2\pi^*$-orbitals of the molecule and the x-axes are time. In the top panel the electron seems to hit resonance, since a rather large part of it gets into the $2\pi^*$-orbital. Furthermore it is seen that the excitation is quite long-lived compared to the small fluctuations in the off-resonance calculation shown on the lower panel.

The results of all the calculations have been collected in Fig. 4, which shows the maximum overlap between the hot electron orbital and the $2\pi^*$-orbitals of the molecule squared, $|\langle\phi|2\pi^*\rangle|^2$, as a function of the average momentum for each of the 5 different starting orbitals from Table I. By maximum overlap we mean the maximum overlap within the first 2 fs, which is time enough for the wavefunction to fully hit the molecule, but not enough

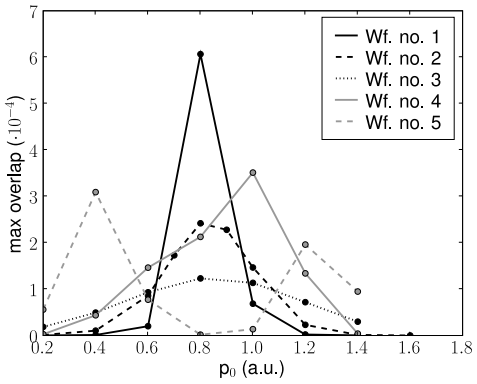

FIG. 4: The amount of electron that gets into the $2\pi^*$-orbitals of the molecule within the first two femtoseconds plotted as a function of the average momentum of the hot electron, p_0. The five different curves are for the five different orbitals given in Table I.

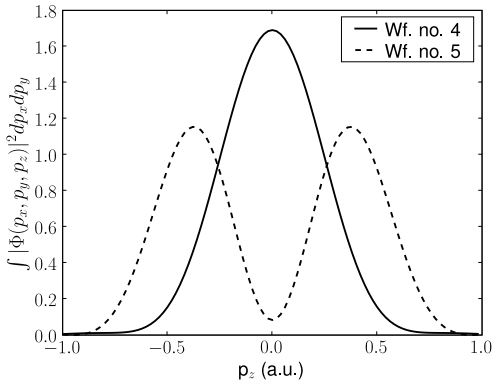

FIG. 5: The Fourier transform of wavefunction 4 and 5 from Table I integrated over the momenta parallel to the surface. The horizontal axis indicate the momentum in the direction perpendicular to the surface, p_z.

time for the reflections at unit cell boundaries to interfer with the results. For all the curves there is a large dependence on the momentum, ie. there are certain values of p_0 which are at resonance and others which are off-resonance. The curves are, however, also quite different. Curve 1-3 all have the maximum at the same momentum, but it is also clear that the more well-defined momentum the wavefunction has, the more well-defined is the resonance peak. This indicates that the shape of the resonance peaks are reflected by the Fourier transforms of the wavefunctions. This is supported by Fig. 5, which shows the Fourier transforms of wavefunction 4 and 5 integrated over the axes parallel to the surface. These curves resemble the resonance curves on Fig. 4 a lot. One interpretation of this is that the wavefunction, which is sent towards the molecule, is just probing the resonance. In an energy picture this means that the maximal overlap, MO, which we interpret as the excitation probability, can be written as

$$MO = \int R(\epsilon) W(\epsilon) d\epsilon, \tag{2}$$

where $W(\epsilon)$ is the amount of the hot electron that has the energy ϵ, ie.

$$W(\epsilon) = \sum_i |\langle \phi | \psi^i_{KS} \rangle|^2 \delta(\epsilon - \epsilon^i_{KS}). \tag{3}$$

ϕ is the hot electron orbital and ψ^i_{KS} is the i'th Kohn-Sham orbital, which has the energy ϵ^i_{KS}. $R(\epsilon)$ is the energy representation of the resonance. The difference of the Kohn-Sham eigenvalues do not describe excitation energies, therefore in Eq. (3) we are neglecting the renormalisaton of the Kohn-Sham eigenvalues by the exchange-correlation kernel. For resonances as in the case of molecular systems in front of metallic surfaces this renormalisation can be accounted for.[26]

For the resonance we will assume a Lorentzian shape

$$R(\epsilon) = \alpha_{res} \frac{(\Gamma/2)^2}{(\epsilon - \epsilon_{res})^2 + (\Gamma/2)^2}, \tag{4}$$

which corresponds to an exponentially decaying excitation. Γ is the Full-Width at Half Maximum (FWHM) of the resonance and is related to the lifetime of the resonance. ϵ_{res} is the mid-point of the resonance, which we will refer to as the resonance energy. The excitation probability is proportional to α_{res}, so it is closely related to the resonance cross-section.

We estimate the three parameters, Γ, ϵ_{res} and α_{res}, in Eq. (4) by performing a least squares fit of the maximum overlaps obtained by inserting Eqs. (4) and (3) in Eq. (2) to the maximum overlaps shown on Fig. 4. This gives the values $\Gamma = 1.4$ eV, $\epsilon_{res} = 9.8$ eV above the Fermi level and $\alpha_{res} = 5.4 \cdot 10^{-3}$. The value of $\epsilon_{res} = 9.8$ eV may seem high, but one should keep in mind that for this system the Fermi level lies at the Highest Occupied Molecular Orbital (HOMO) of the Nitrogen molecule and that the surface cannot create an image charge, which would lower the resonance energy. The 9.8 eV also seem reasonable, when comparing to the lowest excitation energies of the Nitrogen molecule, which are at the same level. In Sec. III B we will calculate the equivalent number for a molecule sitting at a more realistic cluster surface. Here we do indeed find that the presence of electrons in the surface and the possibility of an image charge will lower this number.

The resulting Lorentz distribution is shown on Fig. 6, where $W(\epsilon)$ from Eq. (3) is also plotted for different momenta of the hot electron orbital. From this it is evident that the resonance features from Fig. 4 arise because the energy distribution of the hot electron passes the resonance as the momentum of the hot electron is increased.

Figure 7 shows how close the true maximum overlaps fits with the ones obtained by inserting the optimal values

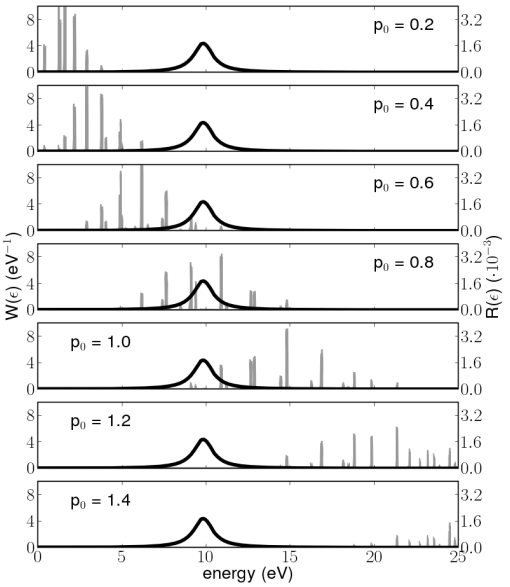

FIG. 6: The grey peaks show $W(\epsilon)$ from Eq. (3), where the delta functions have been replaced by gaussians with a spread of 0.1 eV, for wf. no. 1. in Table I. The different subplots are for different average momenta, p_0. The black curves show the fitted Lorentzian, $R(\epsilon)$, from Eq. (4) with the values $\Gamma = 1.4$ eV, $\epsilon_{res} = 9.8$ eV above the Fermi level and $\alpha_{res} = 5.4 \cdot 10^{-3}$. The left y-axes indicate $W(\epsilon)$ and the right $R(\epsilon)$.

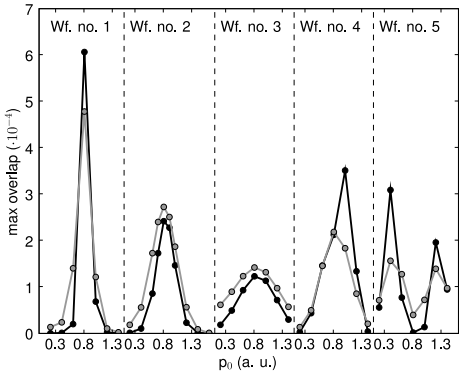

FIG. 7: The black lines show the same maxium overlaps depicted on Fig. 4. The grey lines are obtained by inserting Eqs. (3) and (4) in Eq. (2) and varying Γ, ϵ_{res} and α_{res} until the best least squares fit is obtained. We find this to be at $\Gamma = 1.4$ eV, $\epsilon_{res} = 9.8$ eV above the Fermi level and $\alpha_{res} = 5.4 \cdot 10^{-3}$.

of Γ, ϵ_{res} and α_{res} into Eqs. (2)-(4). It is seen that they agree quite well, especially it should be noted that the double-peaked feature at Wf. no. 5 is reproduced. This indicates that the assumptions made in Eqs. (2)-(4) are reasonable and that Γ, ϵ_{res} and α_{res} are truly properties

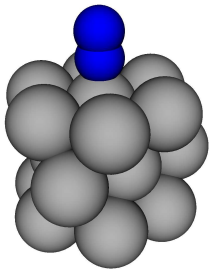

FIG. 8: The Ruthenium cluster with adsorbed Nitrogen, which we perform calculations on in section III B. The grey atoms are Ruthenium and the blue Nitrogen. The cluster has 20 Ruthenium atoms.

of the system and not the arbitrarily chosen orbitals for the hot electrons.

B. Nitrogen on a Ruthenium cluster

The system considered in section III A is only a very crude approximation to a real system. First of all, in a real system the surface will be build from individual atoms and, perhaps more importantly, the other electrons in the surface will feel the hot electron, giving rise to a screening effect.

The intention of this section is to utilize the experiences gained in section III A on a more realistic system, ie. we want to probe the resonance with some wavefunction for the hot electron, and then perform the fitting of Eqs. (2)-(4) in order to extract the values of Γ, ϵ_{res} and α_{res}. We will consider the cluster shown on Fig. 8, which consists of 20 Ruthenium atoms and a Nitrogen molecule adsorbed on it. The cluster is a simple model of a Nitrogen molecule adsorbed on a close-packed (0001) Ruthenium surface and includes the first three layers. We use a cluster instead of a slab in order to avoid all the difficulties that arise when applying periodic boundary conditions in a time-evolution TDDFT calculation.[15] A possible intermediate system to consider would be a jellium surface, where the external step potential is made deeper and combined with extra electrons inside the surface. One would not gain much compared to the cluster calculation with respect to the calculational complexity and effort needed, so we have not done this here.

Some extra care has to put into finding a suitable starting orbital of the hot electron in this system, because of the other electrons present in the cluster, which the orbital of the hot electron must be orthogonal to. Furthermore the Fourier transform of the hot electron orbital should be quite simple, preferably with just one peak, such that we can expect that the fitting described in section III A can be done easily. The procedure we choose is to first perform an ordinary ground state DFT calculation on the 20 atoms Ruthenium cluster without the

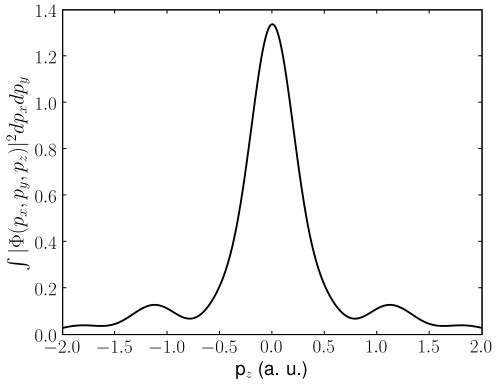

FIG. 9: The momentum space representation of the hot electron wavefunction squared and integrated over the directions parallel to the surface.

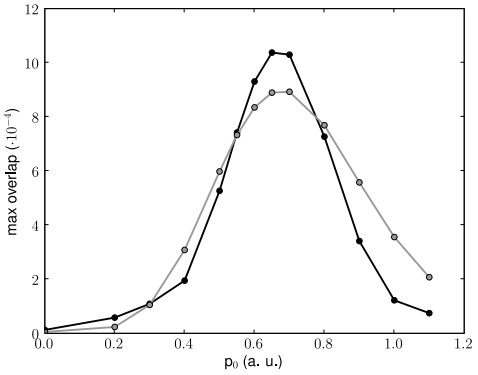

FIG. 10: The black curve shows the amount of electron that gets into the $2\pi^*$-orbital of the molecule within the first three fs plotted as a function of the average momentum of the hot electron, p_0. The grey lines are obtained by inserting Eqs. (3) and (4) in Eq. (2) and varying Γ, ϵ_{res} and α_{res} until the best least squares fit is obtained. We find this to be at $\Gamma = 0.36$ eV, $\epsilon_{res} = 4.9$ eV and $\alpha_{res} = 1.9 \cdot 10^{-3}$.

Nitrogen molecule. We then project the function

$$\Psi(r, \theta, z) = J_1(\tfrac{r}{r_0}) e^{i\theta} e^{-\frac{(z+3.3)^2}{3.3^2}} \qquad (5)$$

onto the space spanned by the 116 lowest lying Kohn-Sham orbitals. $J_1(r)$ is a Bessel function of the first kind, r, θ and z are the usual semipolar coordinates and the equation is in atomic units. r_0 is chosen such that the first node of $J_1(\frac{r}{r_0})$ lies at $r = 8\ a_0$. $z = 0$ corresponds to the z-value of the highest lying layer of atoms in the cluster. We normalize this projected version of $\Psi(r, \theta, z)$ and multiply it with $e^{ip_0 z}$, where p_0 is the average momentum, and use it as the starting orbital for the hot electron. With this choice we ensure that the Fourier transform of the starting orbital only has one significant peak, as it can be seen from Fig. 9, and we ensure that the orbital is nicely localized within the cluster. The choice of $\Psi(r, \theta, z)$ in Eq. 5 is made because it only has a single peak in the Fourier representation and the $e^{i\theta}$ factor gives it the Π symmetry required in order for the electron to interact with the $2\pi^*$ orbitals of the Nitrogen molecule. Other than that the exact choice of $\Psi(r, \theta, z)$ is not so critical. We have tried both varying the number of included KS orbitals and the parameters of the gaussian in Eq. (5).

Finally a groundstate DFT calculation is performed on the cluster with the Nitrogen molecule attached and all the occupied Kohn-Sham orbitals are othogonalized to the starting orbital of the hot electron through an ordinary Gram-Schmidt orthogonalization procedure. Furthermore one spin-up electron is removed at the Fermi level and placed in the orbital of the hot electron, still with spin-up. This is then used as the starting point for the time-evolution TDDFT calculation. Spins are treated using an ordinary spin-polarization procedure.

As it was also done in section III A the time-evolution calculations are performed for different values of the average momentum, p_0. Figure 10 shows the maximum projection of the hot electron orbital onto the subspace

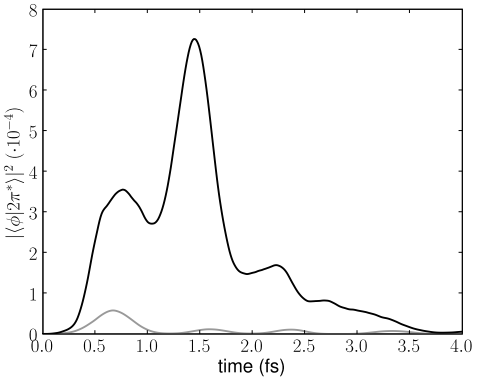

FIG. 11: The orbital of the hot electron, ϕ, projected to the plane spanned by the two $2\pi^*$ orbitals of the molecule squared as a function of time. The black curve is at a momentum of $p_0 = 0.8$ a.u. and the grey curve is at $p_0 = 0.2$.

spanned by the $2\pi^*$ orbitals of the Nitrogen molecule within the first 3 fs. as a function of p_0. Again a clear resonance peak is found. From Fig. 11 it is also seen that the difference between an electron hitting resonance and an off-resonance electron is not only the size of the overlap with the molecular orbital, but also the time the electron stays there. An electron hitting resonance will stay on the molecule for some time before returning to the surface, which seems physically reasonable. This was also what we saw in section III A.

Figure 10 shows also the least squares fit we obtain by varying Γ, ϵ_{res} and α_{res} in Eqs. (2)-(4). The optimal values we find are $\Gamma = 0.36$ eV, $\epsilon_{res} = 4.9$ eV above the Fermi energy and $\alpha_{res} = 1.9 \cdot 10^{-2}$. The Γ value

is quite uncertain, because $R(\epsilon)$ is much more localized than $W(\epsilon)$ in Eq. 2, ie. we try to determine the shape of a very thin function by probing it with a very wide. The 4.9 eV resonance energy is significant lower than the 9.8 eV found in section III A, which was also expected as the Fermi level is now raised by the electrons in the surface and as the resonance energy is lowered by an image charge effect with the surface. Inverse photo-emission experiments for N_2 on an Nickel surface give an energy of approximately 4.4 eV.[27] When we perform ΔSCF calculations in the manner described in Ref. 11 we find that there is only a minor difference in energy between having a Nickel and a Ruthenium surface. This indicates that the value of 4.9 eV is quite reasonable. It is also worth noticing that the projected density of states for the 2π states has its maximum between 2 and 3 eV above the Fermi level as we will show in Sec. IV. This means that the optimal value of ϵ_{res} cannot be explained as a mere matching in energy between the hot electron and the 2π Kohn-Sham states.This is probably because the energy of the Kohn-Sham states will change as the density changes, which fits well with a ΔSCF picture of the situation. In the next section we will consider the value of Γ.

We expect that the found α_{res} values will depend on the cross-section areas of the considered systems, ie. the unit cell cross-section in section III A and the cluster cross-section in this section, since the hot electron orbital is spread over these areas. It will probably be reasonable to assume that α_{res} is inversely proportional to the cross-section area of the system, ie.

$$A_{res} = \alpha_{res} \cdot A_{system}, \tag{6}$$

where A_{res} is the resonance cross section and A_{system} is the cross section of the system. With this crude approximation we can make a very rough estimate of the resonance cross section. As the system cross section we use the area that 7 atoms fill in a Ruthenium (0001) surface, because there are 7 atoms in the top layer of the cluster. We then get $A_{res} = 0.88\ \mathring{A}^2$. By performing calculations for different system cross sections it would be possible to test the assumption of Eq. (6). However, this is beyond the scope of this paper.

IV. DECAY OF AN EXCITATION

In section III we simulated the entire event of an electron hitting a molecular resonance and then returning to the surface. It is, however, also interesting to just consider the decay of an excited molecule, in order to gain some information on the lifetime, which is a very important parameter when trying to calculate the probability that the electron will induce some chemistry.[12] Again we consider a Nitrogen molecule adsorbed on a Ruthenium cluster.

The decay is considered by exciting an electron to the Nitrogen molecule and then monitor the overlap between the electron and the molecular $2\pi^*$ orbitals as time

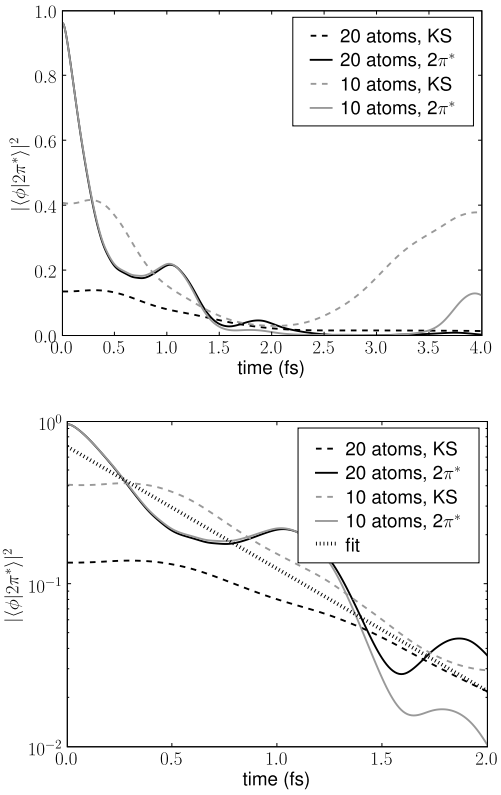

FIG. 12: The orbital of the excited electron projected plane spanned by the $2\pi^*$ orbitals of the Nitrogen molecule squared as a function of time for four different calculations. The only difference between upper and lower panel is that they use a normal and a logaritmic scale, respectively, on the y-axes. Two of the calculations are performed on the 20 atoms cluster from Fig. 8 and the other two on the 10 atoms cluster from Fig. 13. The difference between the two calculations on each cluster is the state of the excited electron. Either the Kohn-Sham orbital with the largest overlap with the $2\pi^*$ orbitals of the molecule is used or simply one of the $2\pi^*$ orbitals found from a gas phase calculation is used.

passes. Figure 12 shows this overlap as a function of time for four different calculations. The difference between the calculations is the state the electron has started in and/or the size of the cluster considered. The electron is either started in the Kohn-Sham eigenfunction with the largest overlap with the $2\pi^*$ orbitals of the Nitrogen molecule or simply in one of the $2\pi^*$ orbitals of the Nitrogen molecule found from a gas phase calculation. The cluster is either the 20 atoms Ruthenium cluster shown on Fig. 8 or the 10 atoms Ruthenium cluster shown on Fig. 13.

From the semilogaritmic plot in the lower panel of Fig. 12 it is seen that the lifetime is quite similar for all four calculations, indicating that the arbitrary choice of a starting orbital for the excited electron and the size of the cluster is not too critical, when estimating the lifetime. From the linear fit on the semilogaritmic plot we get a lifetime of $\tau = 0.6$ fs. With the use of Heisenbergs uncer-

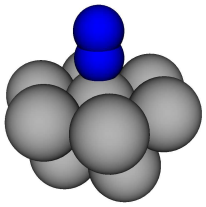

FIG. 13: One of the Ruthenium clusters used in section IV. The grey atoms are Ruthenium and the dark (online: blue) are an adsorbed Nitrogen molecule. The cluster has 10 Ruthenium atoms.

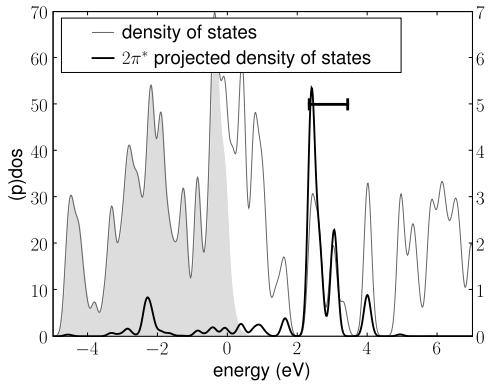

FIG. 14: The density of states for the 20 atoms cluster of Fig. 8 and the density of states projected onto the plane spanned by the $2\pi^*$ orbitals of the Nitrogen molecule. The inserted bar has a length of 1.1 eV, which corresponds to the expected uncertainty in energy of the $2\pi^*$ resonance (see text). The light grey filling indicates the occupied states. Left axis is the density of states and the right the projected density of states.

tainty relation, $\Delta t \Delta E \approx \hbar$, we can associate this lifetime with an uncertainty in the resonance energy: $\Delta E \approx 1.1$ eV. By comparing this with the density of states projected onto the plane spanned by the $2\pi^*$ orbitals of the Nitrogen molecule, as it is done on Fig. 14, we see that it fits quite well with the spread of the projected density of states. This indicates that estimating excitation lifetimes from the projected density of Kohn-Sham states is reasonable. In section III B we found a value of $\Gamma = 0.36$ eV, which is approximately a factor of 3 different from the ΔE found here. This difference is consistent with the large uncertainty attached to the Γ value determined in the fitting procedure.

From the upper panel of Fig. 12 it is also seen that the electron returns to the $2\pi^*$ orbitals after a few femtoseconds for the 10 atoms cluster, when the electron is placed in a Kohn-Sham orbital. This looks like a two-level oscillation and in fact a more careful analysis reveals that the electron oscillates between two Kohn-Sham orbitals, ie. the couplings to the other Kohn-Sham orbitals are very low. Similar effects can also be seen in the other calculations if they are continued, and is a consequence of the fact that it does not make sense to continue the calculations too far, because the system cannot dissipate the electronic energy as it would when connected to a large surface.

V. SUMMARY

We have applied time-evolution TDDFT to model the interaction of electrons with molecular resonances at surfaces. More specifically we have considered systems consisting of a Nitrogen molecule adsorbed either on a simple fictive surface or a more realistic Ruthenium cluster. We found that this TDDFT approach can be used to to extract several physical properties of the systems:

- When an electron collides with a molecule from inside the surface, some of the orbital is reflected, some places itself in a molecular state and in some case some of it passes the molecule. This can be associated with the probabilities of reflection, excitation and transmission.
- When the momentum (or energy) of the incoming electron is varied a resonance feature is observed.
- An electron hitting the resonance will stay on the molecule for some time in contrast to an electron hitting off-resonance.
- We obtain reasonable values for the resoance energies. As expected the resonance energy is lowered by the contact with a realistic surface.
- The decay of the electronic excitation fits an exponential quite well.

Furthermore we have established a picture, where the incoming hot electron can be considered as a probe, which probes the resonance. Using a fitting procedure we have been able to extract resonance properties, which apparently are system specific and not dependent on the exact nature of the incoming electron orbital. We have shown how this picture can be applied to a more realistic system consisting of a molecule adsorbed on a cluster of atoms.

Finally we compared the lifetime observed in a time-evolution TDDFT calculation with a simple projected density of states analysis. We found that they agree quite well.

Acknowledgments

The Center for Individual Nanoparticle Functionality CINF is sponsored by the Danish National Research

Foundation. This work was supported by the Danish Center for Scientific Computing. A. R. acknowledges funding by the Spanish MEC (FIS2007-65702-C02-01), "Grupos Consolidados UPV/EHU del Gobierno Vasco" (IT-319-07), CSIC, and the European Community through e-I3 ETSF project (INFRA-2007-1.2.2: Grant Agreement Number 211956). We acknowledge support by the Barcelona Supercomputing Center, "Red Espanola de Supercomputacion" and SGIker ARINA (UPV/EHU). The Center for Atomic-scale Materials Design CAMD is sponsored by the Lundbeck Foundation.

[1] H.-L. Dai and W. Ho, eds., *Laser Spectroscopy and Photochemistry on Metal Surfaces* (World Scientific, Singapore, 1995).
[2] J. W. Gadzuk, Phys. Rev. B **44**, 13466 (1991).
[3] R. E. Palmer and P. J. Rous, Rev. Mod. Phys. **64**, 383 (1992).
[4] R. R. Cavanagh, D. S. King, J. C. Stephenson, and T. F. Heinz, J. Phys. Chem. **97**, 786 (1993).
[5] X.-Y. Zhu, Annu. Rev. Phys. **45**, 113 (1994).
[6] D. G. Busch and W. Ho, Phys. Rev. Lett. **77**, 1338 (1996).
[7] J. W. Gadzuk, Phys. Rev. Lett. **76**, 4234 (1996).
[8] M. Bonn, S. Funk, C. Hess, D. N. Denzler, C. Stampfl, M. Scheffler, M. Wolf, and G. Ertl, Science **285**, 1042 (1999).
[9] J. A. Misewich, T. F. Heinz, and D. M. Newns, Phys. Rev. Lett. **68**, 3737 (1992).
[10] L. B. Thomsen, G. Nielsen, S. B. Vendelbo, M. Johansson, O. Hansen, and I. Chorkendorff, Phys. Rev. B **76**, 155315 (2007).
[11] J. Gavnholt, T. Olsen, M. Engelund, and J. Schiøtz, Phys. Rev. B **78**, 075441 (2008).
[12] T. Olsen, J. Gavnholt, and J. Schiøtz, Phys. Rev. B **79**, 035403 (2009).
[13] T. Kreibich and E. K. U. Gross, Phys. Rev. Lett. **86**, 2984 (2001).
[14] Octopus is a freely available real space time-dependent density functional theory code (see `www.tddft.org/programs/octopus/`).
[15] A. Castro, H. Appel, M. Oliveira, C. Rozzi, X. Andrade, F. Lorenzen, M. Marques, E. Gross, and A. Rubio, Phys. Status Solidi B **243**, 2465 (2006).
[16] A. Zangwill and P. Soven, Phys. Rev. A **21**, 1561 (1980).
[17] Pseudopotentials from the Fritz-Haber institute are available on the website `www.abinit.org/Psps/?text=../Psps/LDA_FHI/fhi`.
[18] N. Troullier and J. L. Martins, Phys. Rev. B **43**, 1993 (1991).
[19] M. Hochbruck and C. Lubich, SIAM J. Numer. Anal. **41**, 945 (2003).
[20] M. Hochbruck and C. Lubich, SIAM J. Numer. Anal. **34**, 1911 (1997).
[21] D. M. Ceperley and B. J. Alder, Phys. Rev. Lett. **45**, 566 (1980).
[22] C. G. Broyden, Math. Comput. **19**, 577 (1965).
[23] The `gpaw` code including the implementation of ΔSCF is available as a part of the CAMPOS software: `www.camp.dtu.dk/Software`.
[24] J. J. Mortensen, L. B. Hansen, and K. W. Jacobsen, Phys. Rev. B **71**, 035109 (2005).
[25] Lengths in Bohr radii and energies in Hartree.
[26] K. S. Thygesen, Phys. Rev. Lett. **100**, 166804 (2008).
[27] P. D. Johnson and S. L. Hulbert, Phys. Rev. B **35**, 9427 (1987).